DOCTOR OF PHILOSOPHY

Mathematical modelling of cancer cell invasion of tissue
discrete and continuum approaches to studying the central role of adhesion

Andasari, Vivi

Award date:
2011

DOCTOR OF PHILOSOPHY

Mathematical modelling of cancer cell invasion of tissue

discrete and continuum approaches to studying the central role of adhesion

Vivi Andasari

2011

University of Dundee

Mathematical Modelling of Cancer Cell Invasion of Tissue: Discrete and Continuum Approaches to Studying the Central Role of Adhesion

By

Vivi Andasari

A Thesis Submitted for the Degree of Doctor of Philosophy

Division of Mathematics

University of Dundee

Dundee

May 2011

In the Name of God, the Entirely Merciful, the Especially Merciful

All praise, gratitude and thanks are to the Almighty God, the One and Only God, the Eternal Refuge, Who Begets Not nor Was He Begotten, Nor is there to Him any equivalent. He is the Creator of everything, to Him belongs whatever is in the heavens and whatever is in the earth, and to Him we all will return. Master of the Day of Judgment. He is the Most High, the Greatest, the All-Hearing, the All-Seeing, the All-Knowing, the All-Powerful, Whose Power controls every single creature, and Whose Will dominates every single event.

God the Most Wise, says in His Final Revelation sent down to his servant and final Messenger, Muhammad (Peace and Blessing of God be upon him), which is the Qur'aan in surah (chapter) Al-Qamar (the Moon) ayah (sign/verse) 49:

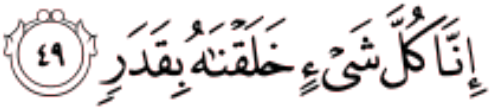

where the translation of the meaning in English would be

"*Verily, all things have We created in proportion and measure*."

O Lord, certainly You Have not Created all this without reason. Glory be to You. Protect us from the torment of the Fire. I surrender to Your Will. I acknowledge Your Love, Mercy, and Blessing, without which I am nothing and this work would have not been possible.

Contents

List of Figures

List of Tables

Acknowledgements

I would like to express my deep and sincere gratitude to my supervisor, Prof. Mark Chaplain, FRSE, who is an extraordinary person, and has been very supportive and nice since the first day I arrived in Dundee. Prof. Chaplain has made my PhD life worthwhile and unforgettable. I am very blessed to have been given the opportunity to work on a very interesting topic, mathematical modelling of cancer, which is meant to serve the humanity. The projects that I have been working on for this PhD thesis would not have been possible without Prof. Chaplain's guidance and help.

I also would like to thank collaborators who have contributed their expertise and spent their time to help me with numerical programming: Dr. Alf Gerisch from Technische Universität Darmstadt in Germany, Dr. Maciej Swat from Biocomplexity Institute, Indiana University in the USA, and Ryan Roper from Computational Systems Biology Lab, University of Washington in the USA.

Family, friends, and colleagues surely have provided support that I can never thank enough. I am very grateful with this life that I have been bestowed with, in which I have and know you all in my life.

To my late father, this thesis is dedicated to you. I have found a way to combine your passion for medicine that you wanted me so much to be a (medical) doctor to serve the humanity as you always advised me to do good to others and my passion for mathematics. I miss you so much.

Declaration

I declare that the following thesis is my own composition and that it has not been submitted before in application for a higher degree.

Vivi Andasari

Certification

This is to certify that Vivi Andasari has complied with all the requirements for the submission of this Doctor of Philosophy thesis to the University of Dundee.

Prof. Mark Chaplain, FRSE

Publications

1. V. Andasari, A. Gerisch, G. Lolas, A.P. South, M.A.J. Chaplain. Mathematical modelling of cancer cell invasion of tissue: biological insight from mathematical analysis and computational simulation. *Journal of Mathematical Biology*, $63(1):141-171, 2011$. http://dx.doi.org/10.1007/s00285-010-0369-1

2. V. Andasari and M.A.J. Chaplain. Intracellular Modelling of Cell-Matrix Adhesion during Cancer Cell Invasion. Mathematical Modelling of Natural Phenomena. *Submitted*, 2011.

3. V. Andasari, R. Roper, M. Swat, M.A.J. Chaplain. Integrating Intracellular Dynamics in Cell-Based Systems using CompuCell3D and Bionetsolver with an Application to Multiscale Mathematical Modelling of Cancer Cell Growth and Invasion, *In preparation*.

4. V. Andasari, A. Gerisch, G. Lolas, A.P. South, M.A.J. Chaplain. The Role of Cell Adhesion in uPA System for Cancer Cell Invasion of Tissue, *In preparation*.

Abstract

Adhesion, which includes cell-to-cell and cell-to-extracellular-matrix adhesion, plays an important role in cancer invasion and metastasis. After undergoing morphological changes malignant and invasive tumour cells, i.e., cancer cells, break away from the primary tumour by loss of cell-cell adhesion, degrade their basement membrane and migrate through the extracellular matrix by enhancement of cell-matrix adhesion. These processes require interactions and signalling cross-talks between proteins and cellular components facilitating the cell adhesion. Although such processes are very complex, the necessity to fully understand the mechanism of cell adhesion is crucial for cancer studies, which may contribute to improving cancer treatment strategies. We consider mathematical models in an attempt to understand better the roles of cell adhesion involved in cancer invasion. Using mathematical models and computational simulations, the underlying complex biological processes can be better understood and their properties can be predicted that might not be evident in laboratory experiments. Cancer cell migration and invasion of the extracellular matrix involving adhesive interactions between cells mediated by cadherins and between cell and matrix mediated by integrins, are modelled by employing two types of mathematical models: a continuum approach and an individual-based approach. In the continuum approach, we use Partial Differential Equations in which cell adhesion is treated as non-local and formulated by integral terms. In the individual-based approach, we first develop pathways for cell-cell and cell-matrix adhesion using Ordinary Differential Equations and later incorporate the pathways in a simulation environment for multiscale computational

modelling. The computational simulation results from the two different mathematical models show that we can predict invasive behaviour of cancer cells from cell adhesion properties. Invasion occurs if we reduce cell-cell adhesion and increase cell-matrix adhesion and vice versa. Changing the cell adhesion properties can affect the spatio-temporal behaviour of cancer cell invasion. These results may lead to broadening our understanding of cancer cell invasion and in the long term, contributing to methods of patient treatment.

"*We will show them Our signs in the Universe and within themselves until it becomes clear to them that it is the Truth. Is it not sufficient concerning your Lord that He is, over all things, a Witness?*"

(Qur'aan 41:53)

Chapter 1

Introduction

Computational models of complex biomedical phenomena, such as cancer development and progression, now have become an integral part of building our understanding of underlying cancer biology. Well-engineered models which are generated from biological models and experiments, *e.g.*, *in vivo* or *in vitro*, through observations in real patients can help explain mechanisms in the complex phenomenon. When being successful in predicting experimental results the models can be used to significantly improve biomedical research throughput by allowing virtual, *in silico* modelling.

In healthy tissues, cells work in perfect order. They collaborate and follow the rules governing normal tissue structure and maintenance, such as whether to divide, differentiate, or to die. But in cancer, which starts from mutations at the genetic level, cells acquire novel, often abnormal phenotypes which cause the cells to ignore the governing rules. The cells grow uncontrollably, they may invade surrounding tissue (which is the topic of this thesis) and eventually spread throughout the body or metastasise. When metastasis happens, cancer can cause the death of individuals. We discuss the biology of cancer invasion, specifically cancer of epithelial tissue origin or carcinoma, in Chapter 2.

Mathematical modelling of the various phases of cancer, in particular solid tumour growth, has itself been developing and expanding over the years. Selected publications

in the field of mathematical modelling of cancer invasion of tissue in connection with the topic of this thesis is discussed in Chapter 3.

A common agreement between experimentalists and theoreticians recently is that cancer progression involves processes that interact with one another and occur at multiple scales of time and space. The time scales involved vary from nanoseconds to years: the signalling events in the cell typically occur over fractions of a second to a few seconds, the transcriptional events may take hours, it takes days for cell division and growth and tissue remodelling, months for tumour doubling times, and years for tumour growth, etc. The spatial scales range from nanometres for protein-DNA interactions to centimetres for tumour mass development, angiogenesis, tissue invasion, etc. These scales are strongly linked with each other. A phenomenon cannot be considered using a single scale, fully isolated, without taking into account what happens at other smaller or larger scales.

In general when incorporating the temporal and spatial scales, there are three commonly used viewpoints: the subcellular level, the cellular level, and the tissue level. Or, from a modelling point of view those levels can also be referred to as the microscopic scale, the mesoscopic scale, and the macroscopic scale, respectively. Cancer usually starts at the subcellular level marked by events that occur within the cell, such as genetic mutations, transduction of chemical signals between proteins and a large number of intracellular components that regulates activities at the cellular level such as uncontrolled cell division, cell detachment that leads to epithelial-mesenchymal transition (EMT), etc. Interactions between tumour cells and host cells, intravasation and extravasation processes are viewed from a larger scale, that is the mesoscopic scale. The macroscopic scale concerns activities that occur at the tissue level such as cell migration, convection and diffusion of chemical factors, which are all typical for continuum processes (Preziosi, 2003).

In modelling the various stages of cancer progression, certain computational and

mathematical methodologies are more suitable than others. For example, in the case of solid avascular tumour growth, simple continuum models are well-suited since they capture bulk properties of tissues. Instead of explicitly treating individual cells, collective properties of the tumour tissue are modelled, such as cell density and oxygen concentration. An advantage of such an approach is that systems with a large number of cells, on the order of 10^6 or higher, can be handled. We present continuum models of cancer cell invasion of tissue that focus on the role of the urokinase plasminogen activation (uPA) system in Chapter 4 and integrate the uPA system with cell adhesion mechanisms in Chapter 5.

On the other hand, explicit representation of individual cells and their properties (*e.g.*, locations, radii, morphology, surface area, volume, etc.) can become computationally burdensome when trying to model systems on the order of 10^4 to 10^6 cells. Nevertheless, such individual cell-based modelling approaches are capable of capturing phenomena and behaviour in multicellular systems that continuum strategies cannot capture. A multiscale individual cell-based approach focusing on the role of intracellular proteins E-cadherin and β-catenin in mediating adhesion between cells is presented in Chapter 6. A pathway model for interactions between cell and extracellular matrix and the mathematical model is proposed in Chapter 7.

The main aim of this thesis is to understand the roles of cell adhesion which include cell-cell and cell-matrix adhesion in cancer invasion of tissue using two mathematical approaches: a continuum approach and an individual cell-based approach.

For the continuum approach, first we look at a model of cancer invasion of tissue developed by Chaplain and Lolas (2005), where the locomotion of cancer cells is governed by random motility, directional migration towards gradients of soluble chemoattractants or chemotaxis, and directional movement up gradients of substratum-bound extracellular matrix components or haptotaxis. We use this model as a basic model for cancer cell invasion of surrounding tissue and extend the model by incorporating cell

adhesion that accounts for cell motility, which is an important event in cancer invasion.

In summary, the key results of our continuum models in this thesis are: (i) comprehensive computational simulations of our mathematical model of cancer invasion and the observation of interesting spatio-temporal irregular patterns; (ii) the linking of these patterns to results of a linear stability analysis of unique positive uniform steady states of the system, and, (iii) a comparison of the computational simulations with experimental results and identification of weakness of the model for future work.

For the individual cell-based approach, we use a pathway developed by Ramis-Conde et al. (2008) for multiscale modelling of cell detachment based on a cell-cell adhesion mechanism for implementation in a lattice-based simulation methodology. We present a case study on model cross-validation. We simulate, reproduce, and compare the cancer invasion model described in Ramis-Conde et al. (2008) (which uses off-lattice methodology) in a simulation environment CompuCell3D for cellular modelling (using lattice-based methodology) and incorporate Bionetsolver for the intracellular modelling.

Chapter 2

Biological Background of Cancer Invasion

2.1 Introduction

About 90% of cancer-related illnesses and deaths are caused by malignant tumour cells, *i.e.*, cancer cells, that have left the primary tumour, spread to anatomically distant sites far from the locations in the body where their primary tumours first arose, and formed secondary tumours at the new sites. Metastasis, the term given to this disseminating process, depends on complex biochemical and biological changes in cancer cells and in the associated stroma, and the interactions between them.

When cells have successfully undergone metastasis and established new colonies at distant sites, they often produce considerable harm. Bone is the most common site of recurrence of metastatic breast cancer cells, where they affect the spine, ribs, pelvis, and proximal long bones. The breast cancer metastatic colonies in the bone can cause localised erosion of bone tissue, resulting in severe pain and skeletal collapse. Breast cancer cells also metastasise to vital organs such the lungs, liver, and to the brain, posing life threatening effects (Weinberg, 2007).

2.2 General Mechanisms of Invasion and Metastasis

Metastasis involves complex molecular cascades comprising many interconnected steps. The steps are connected to each other through a series of adhesive interactions, invasive processes, and responses to chemotactic stimuli. The major steps can be summarised as follows: (1) the detachment of tumour cells from the primary tumour mass, by down-regulation of cell-cell adhesion components such as cadherins and catenins; (2) invasion of the basement membrane and the extracellular matrix (ECM) components by over-expression of proteolytic enzymes such as matrix metalloproteinases (MMPs) and urokinase-type plasminogen activator (uPA), and migration through the ECM mediated by cell-matrix adhesion components such as integrins and fibronectin; (3) intravasation of the tumour cells into the blood vessels and lymphatic vessels which gives them access to the circulatory system to travel to distant anatomical sites; (4) extravasation or escape from the circulatory system and penetration into the surrounding tissue of new sites by adhesion of the circulating tumour cells to the endothelial cell lining at the capillary bed of the target organ site; (5) invasion of the basement membrane and target organ tissue; and (6) the growth of secondary tumours at the target organ site (Guo and Giancotti, 2004; Brooks et al., 2010). Tumour-induced angiogenesis also provides a route for metastatic spread.

The metastatic cascade that we are mathematically investigating and modelling in this thesis is the local invasion of normal or host tissues which involves steps (2) and (3) as well as step (6) of the above mentioned complex sequence of steps critical for metastasis. Typically for carcinomas (cancer of epithelial tissue origin) invasion indicates penetration of cancer cells into the stromal compartment and their occupation. Cancer cells invade beyond the constraints of the normal tissue where they originate. Invasive cells acquire genetic and epigenetic changes that give rise to an aggressive phenotype. Carcinoma cells must discard many of their epithelial phenotypes, detach from epithelial sheets, and undergo a drastic alteration which is referred to as the

epithelial-mesenchymal-transition (EMT). Two properties that are necessary for successful invasion are increased cell motility through cell adhesion properties and the ability to release proteolytic enzymes. These are associated with decreased cell-cell adhesion, degradation of basement membranes and tissue, and enhanced cell-matrix adhesion for migration across the tissue as well as enhanced local growth of tumour cells. The process of invasion with cell detachment and migration (which may start after angiogenesis takes place) is illustrated in plot (d) of Fig. 2.1.

2.3 Detachment

Many of the activities of mammalian cells *in vivo*, such as embryogenesis, mitosis, morphogenesis, shape maintenance, cell orientation, survival, and motility depend on the attachment of cells to their surroundings such as the extracellular matrix (ECM) and other neighbouring cells. Most cells possess multiple mechanisms that enable them to bind to other neighbouring cells (cell-cell adhesion) and to the extracellular matrix (cell-matrix adhesion).

The maintenance, formation or disruption of cell-cell and cell-matrix adhesion are particularly important cellular events in cancer invasion and metastasis. Cell-cell adhesion functions to maintain a tumour's compactness. Loss of cell-cell adhesion facilitates the detachment of tumour cells from the primary tumour mass. This event is then followed by the formation of cell-matrix adhesion that mediate the migration of tumour cells through the ECM (Guo and Giancotti, 2004).

Recent studies have shown that cell-cell and cell-matrix adhesion play a significant role in the invasive and metastatic potential of many types of cancer, such as colorectal cancer (Kirkland and Ying, 2008; Paschos et al., 2009), breast cancer (Kowalski et al., 2003; Sloan et al., 2006; Havaki et al., 2007), cervical cancer (Maity et al., 2009), ovarian cancer (Ahmed et al., 2005; Sawada et al., 2008), pancreatic cancer (Sawai et al., 2006), lung cancer (Lee et al., 2002; Zhu et al., 2007), carcinomas (Schlippe

et al., 2000; Brockbank et al., 2005; Heyder et al., 2005; Janes and Watt, 2006), and melanomas (Kuphal et al., 2005).

Cell adhesion is mediated by cell adhesion molecules (CAMs) expressed on the cell surface. Cell adhesion molecules (CAMs) are specialised membrane (glyco)proteins, also called transmembrane receptors, that mediate chemical and mechanical interactions between the intracellular and extracellular compartments. For these interaction purposes, they all have cytoplasmic, transmembrane, and extracellular domains.

There are four major groups of cell adhesion molecules (CAMs) that have been identified: the integrin family, the immunoglobulin superfamily, selectins, and cadherins. Two groups that are considered to be generally involved in cell adhesion of epithelial tissue are cadherins and integrins.

Cadherins are the main adhesion molecules that are thought to be responsible for the binding of a cell to neighbouring cells or cell-cell adhesion. Cadherins of one cell bind to cadherins of adjacent cells in a calcium-dependent manner. Cadherins mediate cell-cell adhesion mainly by homotypic interactions, although there are also heterotypic bindings between different cadherin molecules. The cytoplasmic tail of cadherins binds to the proteins of the catenin family to form cadherin/catenin complexes mediating connection to the actin cytoskeleton that provides tensile strength for the cell. The group of intracellular anchor proteins, catenins, consists of p120-catenin, α-catenin, γ-catenin, and β-catenin (Jiang, 1996; Alberts et al., 2002). Classical cadherins are named based on the types of the main tissues where they are found, *e.g.*, E-cadherin is found in epithelial tissues, N-cadherin is expressed predominantly in the nervous system, and P-cadherin is present in cells in the placenta and epidermis, etc. Of all types of cadherins, E-cadherin is the most well-studied cell-cell adhesion protein, as it is thought to be a key molecule for cell-cell adhesion. Cells without E-cadherin expression may not aggregate or adhere to each other.

E-cadherin is mainly distributed at the cell membrane, particularly at cell-cell adhesion areas. The function of E-cadherins is highly dependent on the functional activity of catenins as a provider of mechanical linkage between E-cadherin and the cytoskeleton (Garrod, 1993; Tsutsui et al., 1996). After being synthesised, E-cadherin binds to both β-catenin and γ-catenin in the cytoplasm, before being transported to the cell membrane. α-catenin binds to E-cadherin or β-catenin-γ-catenin-E-cadherin complexes at the cell membrane (Jiang, 1996). Cells with normal E-cadherin expression, but lacking in catenins, are not able to adhere to each other.

Disruption of cell-cell adhesion is essential for the first step of local invasion of cancer, in which malignant cells detach and break free from the primary tumour mass. This mechanism is frequently associated with the abnormality of either E-cadherin expression or function, the latter being related with loss of expression of α-catenin (Shimoyama et al., 1992) or mutations in β-catenin (Kawanishi et al., 1995) that cause disturbance in E-cadherin-catenin interaction. *In vitro* studies have suggested a linear relation between disruption of E-cadherin-catenin complexes and the invasive phenotype (Wijnhoven et al., 2000; Aken et al., 2001). The loss of E-cadherin-catenin complex bindings is followed by reduced expression of E-cadherin on the cell surface, while catenins accumulate in the cell nucleus. Down-regulation of E-cadherin is sometimes accompanied by up-regulation of N-cadherin, with which cancer cells form homotypic interactions with various types of mesenchymal cells like fibroblasts and endothelial cells that reside in the matrix/stroma (Weinberg, 2007).

It remains unclear whether the loss of E-cadherin-mediated cell adhesion is a prerequisite for cancer invasion or is a consequence of dedifferentiation during cancer progression *in vitro*. However, Perl et al. (1998) demonstrated that the loss of E-cadherin-mediated cell-cell adhesion is involved in the transition from adenoma to invasive carcinoma. And there is also evidence that the up-regulation of N-cadherin as exchange with down-regulation of E-cadherin occurs when melanocytes become

transformed into melanoma cells (Weinberg, 2007).

Reduction of E-cadherin expression on the cell surface is accompanied by a marked increase in proteolytic enzyme urokinase-type plasminogen activator (uPA). This increase probably involves RNA and protein synthesis. E-cadherin is also associated with the distribution of uPA from the perinuclear region to the cell surface (Jiang, 1996).

2.4 Degradation of the Extracellular Matrix

Extracellular matrix (ECM) has a dual role: as the substratum on which the cells move and as the physical barrier that the cells have to surpass. One of the first steps in cancer invasion is the remodelling of the matrix and a major part of this process involves the over-expression of proteolytic enzymes, such as the urokinase-type plasminogen activator (uPA) and matrix metalloproteinases (MMPs), by the cancer cells to degrade the physical obstacle by breaking down matrix proteins/components. The inherent ability of cancer cells to invade because of the over-expression of uPA has been experimentally demonstrated in several human cancers including breast cancer (Duffy, 2002), prostate cancer (Webber and Waghray, 1995), murine lung carcinoma (Henneke et al., 2010), pleural mesothelioma (cancer that develops in the lining of the lungs) (Tucker et al., 2010), gastric carcinoma (Alpízar-Alpízar et al., 2010), pancreatic cancer (Gibbs et al., 2009), bladder, kidney, colorectal, stomach, brain, ovary, endometrium and melanoma (Markus, 1988). High levels of uPA expression in cancer are correlated with poor cancer prognosis.

The plasminogen activation system consists of two plasminogen activators, tissue-type plasminogen activator (tPA) and urokinase-type plasminogen activator (uPA). tPA mainly plays a role in the generation of plasmin for fibrinolysis in blood vessels, while uPA is thought to play a more dominant role in tissue remodelling process specifically in cancer.

The serine protease uPA is implicated in the catalysis of the proteolytic conversion of the inactive zymogen plasminogen to the active proteinase plasmin. Plasmin is an important enzyme that catalyses degradation of major proteins in basement membranes and extracellular matrix, facilitating cancer cell invasion of the surrounding tissue. The activity of uPA to generate plasmin is inhibited by serpins plasminogen activator inhibitor-1 or PAI-1 and the activity of plasmin is inhibited by α_2-antiplasmin (Andreasen et al., 1997, 2000; Duffy and Duggan, 2004; Danø et al., 2005).

uPA is secreted as a single polypeptide chain pro-enzyme, pro-uPA, which is inactive and has a very low intrinsic proteolytic activity. Pro-uPA is activated to active uPA by plasmin. Active uPA proteolytically converts the inactive zymogen plasminogen to plasmin, which then degrades directly or indirectly matrix components, or activates latent growth factors such as transforming growth factor 1 (TGF-1). Pro-uPA and uPA bind with high affinity to a cell surface uPA receptor, uPAR, a multidomain glycoprotein tethered to the cell membrane with a glycosylphosphotidylinositol (GPI) anchor. The binding of uPA by uPAR restricts plasminogen activation to the immediate vicinity of the cell membrane (Andreasen et al., 1997, 2000; Duffy and Duggan, 2004; Danø et al., 2005). The concerted action of these plasminogen activation system members is more prevalent at the leading edge of migrating cells, contributing to the invasive properties and metastatic potential of malignant tumour cells or cancer cells. In addition to matrix degradation, the migration of cancer cells requires cell attachment to the matrix.

2.5 Cell Motility

After having been detached from the primary tumour mass followed by secretion of proteolytic enzymes to degrade the barrier in front of them, invasive cancer cells now are on their way to embark on their journey migrating across the tissue before gaining access to any nearby blood or lymph vessel that transports them to distant sites. For

the purpose of migration, invasive cells need adhesive interaction between them and the matrix (components) or cell-matrix adhesion. It is a vital process in invasion of the basement membrane and the tissue at primary site, and in penetration of the tissue of the target organ at the secondary site, when metastasis has eventually formed. In the interactions between cell and matrix, the intracellular compartment of a cell is connected with the extracellular environment by binding of cell surface receptors with proteins of the ECM. The major groups of proteins mediating cell-matrix adhesion are a family of cell surface receptors known as integrins, named for their role in integrating the intracellular cytoskeleton with the ECM (Ojaniemi and Vuori, 1997). Aside from migration, cell-matrix adhesion also plays an important role in cell survival and proliferation.

Integrins are heterodimeric cell-surface receptors that consist of two transmembrane subunits, α and β, and each $\alpha\beta$ combination has its own binding specificity and signalling properties which form distinct integrin sub-types linking extracellular matrix components, such as fibronectin, vitronectin, laminin and collagen, to the intracellular actin cytoskeleton. The binding of integrins to the matrix components induces discrete cell surface structures mediating direct interactions of cells with the extracellular matrix (Giancotti and Ruoslahti, 1999; Berrier and Yamada, 2007).

There are many structural molecules involved that bind or link integrins to actin, regulate signalling from integrins to the actin cytoskeleton, and also activate integrins. The cytoplasmic tails of integrins are generally short and always devoid of enzymatic features. Hence, integrins transduce signals by associating with adapter proteins that connect the integrin to the cytoskeleton, cytoplasmic kinases, and transmembrane growth factor receptors (Giancotti and Ruoslahti, 1999).

Cancer cells spread within the tissues using similar migration mechanisms occurring in normal, non-neoplastic cells during physiological processes such as embryonic morphogenesis, wound healing and immune-cell trafficking. The principles of cancer

cell migration show that they retain the same basic strategies as those initially investigated in non-neoplastic fibroblasts, keratinocytes and myoblasts (Friedl and Wolf, 2003). The mechanisms require multi-nodal control that ensure continuous, coordinated assembly and disassembly of adhesions depending on the requirements of a given situation (Webb et al., 2002; Vicente-Manzanares et al., 2005).

Cancer cells possess a broad spectrum of motility mechanisms, depending importantly on cell type and matrix structure. They can migrate as individual cells, referred to as individual cell migration, or expand in solid cell strands, sheets, files or clusters, called collective migration (Friedl and Wolf, 2003). Migration can be viewed as a multiple cycle. The basic migratory cycle includes:

1. Extension of a protrusion $\rightarrow$ polymerization of the actin cytoskeletal network drives the initial extension of the plasma membrane at the cell front.

2. Formation of stable attachments near the leading edge of the protrusion $\rightarrow$ the interaction of the integrin family of transmembrane receptors with the ECM stabilises the adhesions by recruiting signalling and cytoskeletal proteins.

3. Translocation of the cell body forward $\rightarrow$ these small, nascent adhesions may transmit strong forces, and serve as traction points for the propulsive forces that move the cell body forward.

4. Release of adhesions and retraction at the cell rear completes the migratory cycle allowing net translocation of the cell in the direction of movement.

All the stages above are happening continuously as the cell moves on the matrix. In connection with proteolysis, degradation of extracellular matrix occurs while the advancing cell body gains volume towards the matrix scaffold. This is perhaps meant to provide the space required for cell expansion and migration, leaving behind defects in the matrix that look like tubes along the migration track.

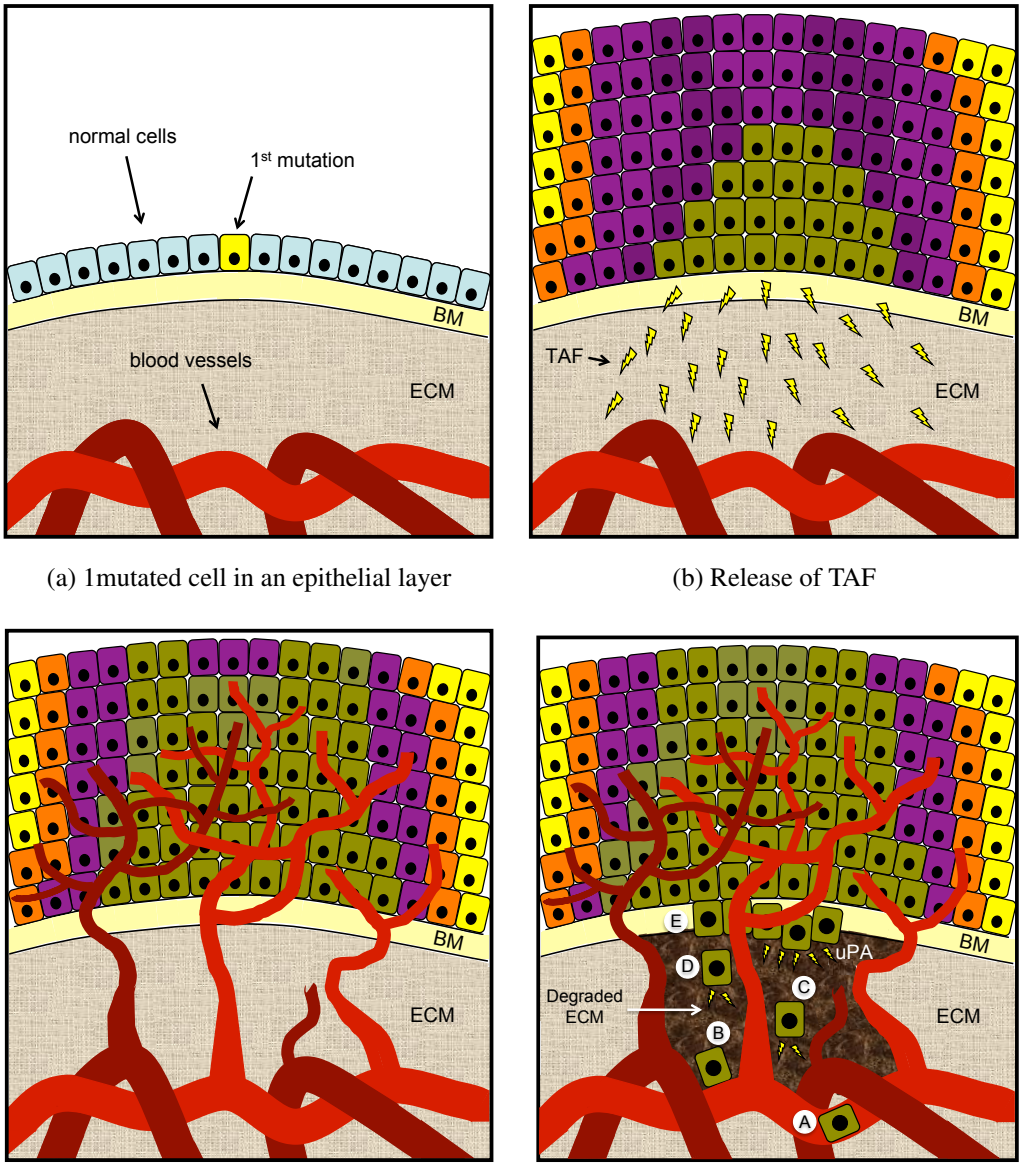

(a) 1mutated cell in an epithelial layer

(b) Release of TAF

(c) Angiogenesis

(d) Invasion with loss of adhesion and migration

Figure 2.1: Illustration of typical growth and invasion of carcinomas from a layer of epithelial cells sitting on a basement membrane (BM) that separates the epithelial layer from extracellular matrix (ECM). (a) One cell (yellow) in a layer of epithelial cells undergoes the 1st mutation. (b) The mutated cell divides uncontrollably replacing normal cells (blue), and new levels of mutations continue to occur determined by the colours of the cells. Orange cells have undergone a second mutation, purple cells with a third mutation, and the last mutation yielding more aggressive cells is faced by green cells. (c) Tumour cells release Tumour Angiogenesis Factor (TAF) to stimulate new blood vessels for oxygen and food supplies. (c) Angiogenesis takes place. (d) Invasion takes place. A group of cells E breach the basement membrane, with some detaching from the primary tumour mass and secreting uPA. Cells C and D have completely detached and perform individual migration on the matrix that has been degraded by proteolysis through secretion of uPA. Cell B has reached the main blood vessel, invading endothelial cells of blood vessel for intravasation. Cell A is travelling in the blood vessel. The invasive cells have abnormally large nuclei (Weinberg, 2007).

Chapter 3

Mathematical Modelling of Cancer Invasion

3.1 Introduction

Mathematical modelling of cancer growth and development in the 20th century dates back at least as far as the 1950s, where Thomlinson and Gray (1955) carried out examinations of sections of human lung cancer and from it formulated a mathematical model for diffusion and consumption of oxygen. The examined histological sections were assumed to be in the shape of a cylinder and the model was based on a theory developed by Hill (1928) for diffusion of oxygen into plane and cylindrical elements of tissue. It was then followed by other mathematical models of cancer growth over the next thirty years. During that period, research papers in cancer modelling appeared slowly – on average about 2 research papers published per year in the 1970s and 1 paper per year in the 1980s.

With advances in computing technology since the 1990s until the present we have witnessed the steady increase in the number of mathematical models everywhere in cancer research. These models have diverse approaches. We could say that there has

been a greater need for the cancer research field to embrace mathematics and computation. In this chapter we present a literature review of the progression of mathematical models of cancer invasion of tissue as it is the focus of our research. We divide the review into two sections: in section 3.2 we discuss the literature review of mathematical models that use a continuum approach, while models based on a multiscale individual cell-based approach are discussed in section 3.3.

3.2 Continuum Models

Mathematical modelling of the various phases of solid tumour growth has itself been developing and expanding over the years. For comprehensive reviews of the modelling in this area, see the books by Adam and Bellomo (1996); Preziosi (2003); Bellomo et al. (2008). Early mathematical models of cancer focused on growth dynamics of solid tumours. Some of these models were based on oxygen distribution and consumption as factors that drive tumour growth, such as the models proposed by Burton (1966); Greenspan (1972); McElwain and Ponzo (1977). It was not until the 1970s after a series of experimental studies on metastasis by Liotta and co-workers (Araujo and McElwain, 2004) that the modelling on tumour invasion started to appear, when Saidel et al. (1976) developed a deterministic model of the metastatic process of a solid tumour through blood vessels. They used a compartmental model that consisted of tumour cells in the tumour mass, tumour vessels, tumour cells penetrating the vessels, tumour cells arrested in the target organ, and metastatic foci in the target organ as model variables. As their model aimed at providing a theoretical framework for analysis and simulation, it was in good agreement with the general dynamics of the process.

A myriad of experimental studies that have been performed since the 1970s and are still ongoing up to date disclose that cancer progression is a very complex process which involves many different subcellular or intracellular and extracellular phenomena

that are related to each other. To unravel the complexities, it is necessary to dissect the "black box" and study the components part by part. There are many aspects that have been implicated in cancer progression and have been studied so far, such as angiogenesis, acidity-dependence, proteolysis, cell adhesion, modes of motility (based on tissue rigidity), etc.

The transition of solid tumour growth from the avascular phase (which is relatively harmless) to the invasive and malignant vascular phase depends upon the crucial process of angiogenesis since it is necessary for the tumour to attain nutrients and dispose of waste products (Folkman, 1974, 1976). To achieve vascularisation, tumour cells secrete diffusible substances known as Tumour Angiogenesis Factors (TAF) into the surrounding tissue (Folkman and Klagsbrun, 1987). This has the effect of stimulating nearby capillary blood vessels to grow towards and penetrate the tumour, resupplying the tumour with vital nutrient, and then, the invasion and metastasis take place. Several TAF substances have now been identified, such as members of the fibroblast growth factor (FGF) family, vascular permeability factor/vascular endothelial growth factor (VPF/VEGF), angiogenin, transforming growth factor alpha and beta (TGF-α and TGF-β), platelet-derived growth factor (PDGF), platelet-derived endothelial cell growth factor (PDECGF), tumour necrosis factor alpha (TNF-α), interleukins, chemokines, and angiopoietins (angs) (Ribatti et al., 2002). Mathematical modelling of tumour-induced angiogenesis started in the early 1990s with a model of the diffusion of TAF into surrounding tissue by Chaplain and Stuart (1991). It was expanded and followed by other models of tumour-induced angiogenesis such as by Chaplain et al. (1995); Maggelakis (1996); Orme and Chaplain (1996a,b); Chaplain (1996); Orme and Chaplain (1997); McDougall et al. (2002); Plank and Sleeman (2003); Valenciano and Chaplain (2003); Mantzaris et al. (2004); Plank et al. (2004); Zheng et al. (2005); McDougall et al. (2006); Stéphanou et al. (2006); Stamper et al. (2007); Macklin et al.

(2009). In particular mathematical models of tumour-induced angiogenesis for invasion of tissue that include degradation/invasion of tissue or tissue components are those proposed by Chaplain (2000); Zheng et al. (2005). A model of invasion in the lymphatic vascular system was proposed by Pepper and Lolas (2008). The model consists of a coupled system of eight partial differential equations describing the evolution in time and space of tumour cell density, LEC (lymphatic endothelial cells) density, extracellular matrix protein density, urokinase plasminogen activator concentration (uPA) secreted by LECs and by cancer cells, plasmin concentration activated by LECs and by cancer cells, and vascular endothelial growth factor-C concentration (VEGF-C).

Human tumours have long been considered acidic. Measurement of pH in tissue has shown that the microenvironment in tumours is generally more acidic (lower pH) than in normal tissues. Tumour cells produce a high concentration of H^+ ions that diffuse along concentration gradients into the adjacent normal tissue, exposing the normal tissue to an extracellular pH that is significantly lower than normal. This chronically acidic environment causes normal cells to die due to the activation of p53-dependent apoptosis pathways and loss of function of critical pH-sensitive genes. While normal cells die, tumour cells exhibit maximum proliferation in the acidic medium. The progressive loss of normal tissue at the tumour-host interface then facilitates tumour invasion (Gatenby and Gawlinski, 2003). Mathematical models of acid-mediated tumour invasion have been proposed by Gatenby and Gawlinski (1996); Webb et al. (1999); Smallbone et al. (2005). On their hypothesis that the alteration of microenvironmental pH induced by tumour may provide a mechanism for cancer invasion, Gatenby and Gawlinski (1996) developed an invasion model describing the interactions between tumour tissue, normal tissue, and excess of H^+ ion concentration. The model consists of a system of reaction-diffusion equations of Lotka-Volterra type for the population competition between normal and tumour tissue. Their model predicts a pH gradient extending from the tumour-host interface, which is confirmed by reanalysis of their

experimental data. Smallbone et al. (2005) develop an invasion model for multicellular tumour spheroid to examine the role of acidosis in the interaction between normal and tumour cell populations. A model by Webb et al. (1999) proposed the involvement of proteolytic activity (they considered matrix metalloproteinases or MMPs) in tumour acidity and suggested that changes in MMP activity at low pH do not have significant effects on the stimulation of a more metastatic phenotype or invasive behaviour.

During local invasion, the basement membrane and components of surrounding extracellular matrix or tissue must be degraded through proteolytic activities of several hydrolytic enzymes such as the urokinase-type plasminogen activator (uPA) and matrix metalloproteinases (MMPs), released either by the tumour cells themselves or by cells surrounding the tumour. Mathematical models by Perumpanani et al. (1996, 1998, 1999); Anderson et al. (2000); Marchant et al. (2001); Stewart et al. (2002); Chaplain and Lolas (2005, 2006) emphasise the roles of proteolysis in cancer invasion of tissue. Perumpanani et al. (1996) derived a model to describe the interactions of invasive cells with normal cells, noninvasive tumour cells, ECM proteins, and proteases. Their model also includes changes in cell adhesion that transform noninvasive tumour cells into invasive tumour cells and changes in the protease-antiprotease axis for excessive matrix degradation. The model suggests the occurrence of noninvasion with high protease expression on the basis of chemotactic gradients that prevent invasion. A model of human fibrosarcoma cell line HT1080 by Perumpanani et al. (1998) shows that matrix metalloproteinase-2 (MMP-2)-digested fragments of fibronectin exert a chemotactic pull stronger than that of undigested fibronectin. In their other model, Perumpanani et al. (1999) combine proteolysis and haptotaxis that can be produced by contact with the extracellular matrix through the mediation of cell surface receptors (integrins). Unlike the previous model (Perumpanani et al., 1998), diffusion terms for cells and MMP-2 are absent in Perumpanani et al. (1999). In the continuum model

proposed by Anderson et al. (2000), cancer invasion is described by interactions between tumour cell density, matrix degrading enzyme concentration, and extracellular matrix density. A model by Marchant et al. (2001) looks at the influence of diffusion in the invasion profiles, which stabilises the shock-like step at the invading front. Stewart et al. (2002) develop a model for the early stages of malignant tumour invasion due to random motility, cellular proliferation, proteolysis and haptotaxis. Their model demonstrates that invasion profiles asymptotically evolve to travelling wave solutions and are also influenced by cell diffusion. Numerical simulations (in 1D) of the above mentioned models produce results that behave like travelling wave solutions, which suggest that the invading cancer cell density always maintains a uniform solution. Experimentally, invasive cancer cells that invade and penetrate the extracellular matrix exhibit heterogeneity in their spatial patterns of spreading, as shown by experimental data in Fig. 4.14 and studies by Nyström et al. (2005). Models that particularly focus on the role of specific proteolytic enzyme such as urokinase-type plasminogen activation system or uPA developed by Chaplain and Lolas (2005, 2006) produce rich and dynamic heterogeneous spatio-temporal solution profiles of cancer cell invasion. Their models describe the interactions between cancer cells, host tissue, and uPA (Chaplain and Lolas, 2006) and additionally the inhibitor of uPA and plasmin (Chaplain and Lolas, 2005). Motility of cells is governed by cell random motion, chemotaxis in response to gradients of diffusible uPA and PAI-1, and haptotaxis in response to gradients of matrix density which is not diffusible. Mathematically, chemotaxis and haptotaxis take the same form and it means that movement of cells is directed towards high concentrations of the substance in question. The chemotactic (and haptotactic) function that was introduced by Patlak in 1953 and later by Keller and Segel (1970) has been characterised experimentally and studied intensively from a theoretical standpoint since it was first introduced. Mathematical models of chemotaxis have been developed in order

to predict aggregation patterns of cells by establishing conditions leading to the instability of homogeneous or spatially uniform steady states (see for example, the books by Murray (2003); Edelstein-Keshet (2005)). Studies have suggested that chemotaxis in a system consisting of reaction-diffusion-taxis terms may destabilise spatially uniform steady states, resulting in some new state where spatial variations predominate. We perform a linear stability analysis of the uPA system model by Chaplain and Lolas (2005) in Chapter 4, and show that destabilisation of the spatially uniform steady state in the uPA system is taxis-driven. The results obtained from computational simulations carried out on the model equations produce dynamic heterogeneous spatio-temporal solutions.

Another phenotypic alteration that must occur for the successful invasion of neighbouring tissue is changes in cell adhesion. Although a model that implicitly includes changes in cell adhesion has been implemented by Perumpanani et al. (1996), a continuum approach model that explicitly describes cell-cell adhesion leading to directed cell movement due to adhesive forces was first developed by Armstrong et al. (2006). The model consists of a term for the gradient of adhesive movement due to adhesive force between cells. The cell adhesion term is nonlocal in space and was derived based on cell sorting mechanisms. The adhesive force is considered to be the sum of local forces between adjacent cells, hence depending on a so-called "cell sensing radius" which gives the nonlocal term (integral term). This model has been extended for use in cancer invasion models by (Gerisch and Chaplain, 2008; Painter et al., 2010) where the cell adhesion term is expanded into interactions between cell-cell and cell-matrix and can drive invasive behaviour. Invasion is controlled by reducing cell-cell adhesion and enhancing cell-matrix adhesion, which is the hallmark for epithelial-mesenchymal transition (EMT). Painter et al. (2010) show that the adhesive movement term alone (without cell random motion term) could produce directed movement of cells driven by low cell-cell adhesion and high cell-matrix adhesion. Gerisch and Chaplain (2008)

show that in the limit of the sensing radius going to zero, the nonlocal model with integral term converges to a "standard" related system of reaction-diffusion-taxis equations. Convinced by the generality, simplicity, and convenient use of the cell adhesion mechanism developed by Armstrong et al. (2006), we extend our uPA model in Chapter 4 by incorporating cell adhesion in the equation for cancer cell density. This is to complement the model of cancer invasion by covering more phenotypic alterations, as discussed in Chapter 5. Using a volume filling effect as developed by Hillen and Painter (2001); Painter and Hillen (2002); Gerisch and Chaplain (2008); Painter et al. (2010), numerical solutions of our nonlocal model exhibit rich patterns of spatial heterogeneity by varying cell-cell and cell-matrix adhesion parameters. The boundedness of solutions of the model by Armstrong et al. (2006) has been proven by Sherratt et al. (2009) and the global existence has been proven by Szymańska et al. (2009).

Aside from what has been mentioned above, there are other aspects of invasion that have been modelled, enriching the field of cancer research. Kim and Friedman (2009) develop a model for the early development of transformed epithelial cells (TECs) in the presence of fibroblasts in the tumour microenvironment. Their model is used to generate several hypotheses on how to slow tumour growth and invasion. It also has been revealed experimentally that cancer cells exhibit biphasic dependence of invasion speed on matrix density, where the maximum speed of invasion is attained at an intermediate level of the physical distribution of matrix proteins, density or adhesiveness (Huttenlocher et al., 1996; Lauffenburger and Horwitz, 1996; Choquet et al., 1997; Palecek et al., 1997; Stahl and Mueller, 1997; Maheshwari et al., 1999, 200; Cox et al., 2001; Gobin and West, 2002; Hocking and Chang, 2003; Li et al., 2005; Peyton and Putnam, 2005; Khatiwala et al., 2006; Zaman et al., 2006; Silvestre et al., 2009). A mathematical model of malignant invasion that consists of equations for cancer cell density, extracellular matrix (collagen) density, and protease by Marchant et al. (2006) produces this biphasic dependence on the density of surrounding normal tissue. The

biphasic behaviour that they explained using nonstandard phase plane analysis is suggested to have appeared because of the inclusion of competition for space between the collagen gel and the malignant cells. In our numerical simulations, we apply a biphasic dependence of cell speed on matrix density and cell-matrix adhesion strength to our nonlocal model by tuning the cell diffusion parameter (which governs cell speed and movement) to be a maximum at intermediate matrix density and cell-matrix adhesion strength. Proliferation and migration of brain tumour cells are mutually exclusive phenotypes that do not occur at the same time (Giese et al., 1996). The exact cellular mechanisms that dictate whether the cells either migrate or proliferate are not known. Although Athale et al. (2005) have developed a deterministic approach for the phenotypic switch by using epidermal growth factor receptor- or EGFR-mediated signalling pathway, their model involves a lot of signalling cascades within the network of genes and proteins and is cumbersome to be implemented in our uPA and nonlocal models. Fedotov and Iomin (2007) propose a two-component reaction-transport model for the migration-proliferation dichotomy in the spreading of tumour cells which was written as a system of integro-differential equations employing Laplace transform and in which (Fedotov and Iomin, 2008) they propose a stochastic approach. Different modes or strategies of tumour cell movement depending on extracellular matrix structure are also an interesting aspect to be modelled. Hillen (2006) develops mesoscopic and macroscopic models for mesenchymal motion in a time-varying network tissue, directed and undirected orientation tissue. Adding to mesenchymal motion, amoeboid motion of cells with application to cancer invasion is also modelled by Painter (2009) in various matrix density and orientation. With their reaction-diffusion model, Cristini et al. (2005) manage to get simulations that result in heterogeneous cell proliferation and migration of cells in a tumour mass in the presence of heterogeneous distribution of oxygen and nutrients. The microenvironmental substrate gradients are thought to drive morphologic instability with separation of cell clusters from the tumour edge and

infiltration into the surrounding normal tissue.

Although the mathematical models presented in this thesis can be applied in general for any type of cancer of epithelial origin, some mathematical models of cancer invasion are dedicated to specific types of cancer, such as modelling of glioma invasion by Swanson et al. (2000, 2003); Frieboes et al. (2006); Stein et al. (2007); Swanson (2008) and breast cancer by Gavaghan et al. (2002); Enderling et al. (2007). Glioma is a type of tumour that starts in the brain or spine, but is more common in the brain. The tumour originates from glial cells. Unlike other types of tumours, human malignant gliomas are exceedingly motile. Experiments showed that within 7 days of implantation, glioma cells can be identified throughout the central nervous system (CNS), see Chicoine and Silbergeld (1995) and references therein. Swanson et al. (2000, 2003); Swanson (2008) model the growth and invasion of a glioma in different parts of the human CNS. To account for spatial heterogeneity of the brain tissue that consists of white and grey matter, they employ nonlinear diffusion coefficient for tumour cells, where the diffusion coefficient is a function of the spatial variable x and the different regions of grey and white matter. This is to reflect experimental observations which show that glioma cells exhibit higher motility in white matter than in grey matter. Simulations of Frieboes et al. (2006) show that tumour morphogenesis *in vivo* may be a function of marginally stable environmental conditions caused by spatial variations in cell nutrients, oxygen, and growth factors, while a mathematical model by Stein et al. (2007) uses experimental data of U87 glioblastoma tumour spheroids in a three-dimensional collagen gel. For breast cancer modelling, Enderling et al. (2007) develop a mathematical model to simulate the stepwise development of breast cancer cells from normal stem cells via mutations in two tumour suppressor genes (TSGs) and Gavaghan et al. (2002) review mathematical models of cancer that can be used for modelling of breast carcinoma to aid detection.

3.3 Multiscale Individual Cell-based Models

Perhaps the earliest individual cell-based modelling was started in 1980 with a computational model of cancer invasion developed by Düchting and Dehl (1980a,b) to determine the spatial structure and temporal behaviour of tumour spread. They developed an algorithm for the transformation of normal cells into tumour cells in 2D.

During the last decade or so many of approaches to multicell, multiscale modelling of cancer evolution and treatment therapy that have been developed, have been driven by a large number of computational advances and progresses in individual or single cell-based modelling. Most of the multiscale models describe interactions between variables that occur on the microscopic and mesoscopic scales, such as interactions between cells that are driven by intracellular processes, interactions between cells and extracellular matrix, interactions between cells and gradients of external stimuli (proteolytic enzymes, oxygen, glucose, etc). Generally, individual cell-based models are classified into lattice-based and off-lattice models. In the lattice-based modelling, each biological cell is represented as either a single lattice site or a set of many contiguous sites on a lattice through spatial discretisation. Models that fall into the category of lattice-based modelling generally use approaches that include cellular automata models, some hybrid discrete-continuum or HDC (combination between continuum and discrete cellular automata like) models, Glazier-Graner-Hogeweg or GGH models, and the invariants and extensions of these models. On the other hand, in the off-lattice modelling each biological cell is often treated as a unit of finite volume with arbitrary locations whose motion is not restricted to lattice points and has shapes that are restricted to spheres, ellipsoids, or Delaunay-decomposition-based shapes (or Voronoi polygons or Thiessen polygons) (Galle et al., 2005; Kim et al., 2007). For off-lattice modelling there are many approaches that have been developed, such as by Galle et al. (2005); Kim et al. (2007); Ramis-Conde et al. (2008, 2009), models in Sections III and IV of the book Anderson et al. (2007). Agent-based models by Athale et al. (2005);

Athale and Deisboeck (2006); Zhang et al. (2007, 2009) belong to lattice-based category, while other agent-based models (Bearer et al., 2009; Frieboes et al., 2010) are categorised into off-lattice models. Here we only review selected articles related to the multiscale modelling of cancer. The reader may refer to Drasdo (2003); Lowengrub et al. (2010); Rejniak and Anderson (2010) for comprehensive reviews on these two main types of individual cell-based models. van Leeuwen et al. (2007), in particular, review a range of mathematical models of colorectal cancer (CRC) that provide insight into different aspects of its development for potential multiscale modelling that could advance our understanding of CRC. A review by Bellomo et al. (2003) provides a survey of mathematical models and methods dealing with the analysis and simulation of tumour dynamics in competition with the immune system.

Cellular automata (CA) models have been proposed to describe avascular and vascular growth of tumour invasion and angiogenesis. For more extensive reviews of CA modelling of tumour growth in particular see Moreira and Deutsch (2002). Cellular automata for multiscale modelling of tumour growth and invasion has been used to a large extent, for example, in models by Alarcón et al. (2004, 2005); Betteridge et al. (2006); Byrne et al. (2006b,a); Deroulers et al. (2009). In their model Alarcón et al. (2004) couple cell growth to the (complex) environmental conditions and intracellular processes. They used a hybrid cellular automaton as a basic theoretical framework to combine and couple models from the tissue scale, such as vascular structural adaptation, to the intracellular scale, such as the cell cycle. Intercellular processes are represented by ordinary differential equations, extracellular processes by partial differential equations and cell processes by rules in a cellular automaton, as developed earlier (Alarcón et al., 2003). Their model predicts that inhomogeneity in the environmental conditions may restrict the ability of malignant colonies to grow and invade healthy tissue. Using the same methodology, in their other models more intracellular processes (cell-cycle, VEGF production, and apoptosis) and tissue level phenomena

(vascular structural, adaptation, and blood flow) were coupled into the model to investigate the effects of nutrient heterogeneity, growth and invasion of cancerous tissue, and emergent growth laws (Alarcón et al., 2005; Byrne et al., 2006b,a). In Betteridge et al. (2006) the CA model incorporates cell movement, over-crowding, and dynamics for haematocrit distribution. Computational simulations of all these CA models were confined to 2-dimensional space.

The use of a lattice-based HDC technique for multiscale modelling of tumour growth and progression has developed over the years. The technique used in multiscale models by Anderson (2005); Ayati et al. (2006); Anderson (2007); Anderson et al. (2009) couples continuum equations that model the dynamics of diffusible external stimuli or chemical substances (such as glucose, matrix degrading enzymes, oxygen concentration, etc) or non-diffusible substrates (such as extracellular matrix) with a discrete cellular automaton-like model based on a biased random-walk technique that models discrete cell migration and interactions. These models use finite difference approximations to discretise cell density (of a partial differential equation) and then generate the probability of movement, based on a biased random-walk model (Anderson, 2003). Anderson (2005) studies the importance of cell adhesion in cancer invasion. However, we note that the model does not explicitly describe components of adhesion (intracellular components for cell-cell adhesion and extracellular components for cell-matrix adhesion) that significantly affect cellular phenotype.

Gerlee and Anderson (2007, 2008); Anderson et al. (2009) extend the HDC technique by modelling the regulatory pathways of each cancer cell with an artificial neural network, which they call an evolutionary hybrid cellular automata (EHCA) model. Each cell is equipped with a genotype that determines the cell phenotype, that is they provide each cell with a micro-environment response network that determines the behaviour of the cell based on the local environment. The network is modelled using a feed-forward artificial neural network, that takes environmental variables as an input

and from these determines the cellular behaviour as the output. The response network is inherited by the daughter cells under mutations. Using this approach Gerlee and Anderson (2007) model the impact of the tissue oxygen concentration on the growth and evolutionary dynamics of the tumour and Gerlee and Anderson (2008) investigate the influence of the tissue oxygen concentration and extracellular matrix density on the growth dynamics of the tumour. Another variation of the cellular automata technique that has been used for the modelling of tumour growth and invasion is the lattice-gas cellular automata Dormann and Deutsch (2002); Ghaemi and Shahrokhi (2006); Hatzikirou et al. (2010); de Franciscis et al. (2011).

Agent-based models are also widely used in multiscale cancer modelling. Athale et al. (2005) develop a model to simulate the cellular decision-process for either the proliferating or migrating phenotype based on a molecular interaction network of genes and proteins. The model is based on a 2-dimensional spatial cellular automaton model where each cell can only occupy one lattice site or grid point at a time. The network of genes and proteins is modelled using ordinary differential equations. The same modelling methodology is also used in Athale and Deisboeck (2006) to study the effects of epidermal growth factor receptor (EGFR) density on tumour growth dynamics, both at the sub- and the multi-cellular level.

Zhang et al. (2007) present a 3-dimensional multiscale agent-based model to simulate the cellular decision process to either proliferate or migrate in the context of brain tumours. Each agent on cell is equipped with an EGFR gene-protein interaction network module that is also connected to a simplified cell-cycle description. The same cell modelling technique used in Athale et al. (2005) is adopted and each 3-dimensional fixed grid point can be occupied by only one cell at each time step. The results show that proliferative and migratory cell populations directly impact the spatio-temporal expansion patterns of the cancer. This was later refined by Zhang et al. (2009) to incorporate mutations representing a simplified tumour progression pathway.

Another lattice-based modelling technique that is also one of the subjects of our research is the GGH model, which is an extension of the large-q Potts model. The large-q Potts model itself is an extension of the *Ising model*, a simple early model of ferromagnetism based on the magnetic moments, or spins, of individual atoms and their interaction energies. Spins interact via an energy minimisation function called a *Hamiltonian* (Balter et al., 2007; Glazier et al., 2007). The GGH model is also known as the Cellular Potts Model or CPM and was initially used to simulate the sorting of a mixture of two cell types based on differential adhesion (Graner and Glazier, 1992; Glazier and Graner, 1993). The technique gained popularity and has been widely used in modelling systems based on individual cells. Glazier and co-workers implemented the GGH model into a simulation environment called **CompuCell3D** or **CC3D**, which is what we are using for our multiscale modelling in Chapter 6. CC3D implementations are described using combination of CompuCell3D Markup Language (CC3DML) and Python scripting. Such a combined approach allows us to build complex biomedical models because CC3D contains description of objects (cells, ECM, diffusible external stimulus), interactions (cell-cell adhesion, morphogen-dependent cell mitosis), initial conditions (initial configuration of cells based on time-lapse microscopy image), and the description of the time evolution of cell properties (concentration dynamics of intracellular component of cells driving adhesive cell properties or rule-based cell type differentiation). Each biological cell is represented by many lattice sites and the system evolves in time through the Hamiltonian. For computational simulations we implement the model in 3-dimensional space where one cell may contain between 300 to 400 cubic lattice sites. The open source software CC3D is developed by collaborators at the Biocomplexity Institute, Indiana University, Bloomington, Indiana, USA and it can be downloaded from the CC3D website (`http://www.compucell3d.org`).

It is our aim to broaden the use of the GGH model implemented in the CC3D

simulation environment for multiscale modelling of cancer by incorporating the intracellular programming library **Bionetsolver** developed by our collaborators at the Computational Systems Biology/Sauro Lab, University of Washington, Seattle, Washington, USA. Bionetsolver is a C++ library with a high-level Python API. It makes use of the SBML ODE Solver Library (SOSlib) to implement reaction-kinetic network dynamics which can regulate the cell dynamics generated by the Hamiltonian. Further details about Bionetsolver and the implementation with CC3D into multiscale modelling is discussed in Chapter 6 of this thesis.

Jiang et al. (2005) use the extended large-q Potts model for their multiscale model of avascular tumour growth that spans three scales, subcellular, cellular, and extracellular level. They use a Boolean network for regulation of the expression of proteins that control the cell cycle at the subcellular scale, a discrete lattice Monte Carlo model for modelling cell growth, proliferation, death, and intracellular adhesion at the cellular scale, and reaction-diffusion equations for modelling chemical dynamics (nutrient, waste, growth promoter, and inhibitor concentrations) at the extracellular scale. Rubenstein and Kaufman (2008) also employ the large-q Potts model for their multiscale modelling of glioma invasion. The Potts model is used to model glioma invasiveness from cell-cell adhesion and cell-matrix adhesion

It is also necessary to briefly review some off-lattice models that are used in multiscale modelling of cancer, particularly the model by Ramis-Conde et al. (2008), since we are using it as our centre-based model for modelling cancer invasion driven by kinetics of intracellular components, discussed in Chapter 6. Ramis-Conde et al. (2008) develop a pathway describing the interactions between E-cadherin, a family of cell surface glycoproteins responsible for regulation cell-cell adhesion, and β-catenin, an intracellular protein that is associated with E-cadherin. The pathway inside each individual cell is translated into a set of ordinary differential equations that model the intracellular dynamics of E-cadherin and β-catenin depending on signalling, either for

attachment or detachment. The dynamics or movement of the cells is described by a stochastic equation of motion and each cell behaves as an elastic sphere. Cell-cell interaction is approximated through cell-cell contact areas using the radii of neighbouring cells and the distance between their centre. The technique used is similar to that in Galle et al. (2005). The computational simulation results of this model are in a good agreement with experiments by Brabletz et al. (2001) that show higher concentration of nuclear β-catenin in cells at the outer layer of the tumour mass due to fewer binding neighbours as compared with the concentration of nuclear β-catenin in cells inside the tumour mass. The same authors also developed a multiscale model of cancer cell intravasation (Ramis-Conde et al., 2009) to study the influence of different protein pathways in forming transendothelial migration (TEM), which is the disruption of the VE-cadherin-mediated bonds between the endothelial cells forming the last cell layer that a cancer cell needs to cross to reach the vasculature, blood or lymph vessel. Aside from the same methods used for intracellular pathway and cell movement in their previous work, the model in Ramis-Conde et al. (2009) uses a mathematical force-based multiscale model for the biophysical properties of the cells and simplified protein pathways involved in TEM.

Kim et al. (2007) have developed an off-lattice individual cell-based model combined with a continuum model for multicellular tumour spheroid growth. They used the technique developed by Dallon and Othmer (1997) where the cells are modelled as deformable ellipses and the movement is modelled using an equation of motion. The continuum model is used to describe nutrients (oxygen and glucose) and the mechanical response of the gel outside the tumour, and for the quiescent and necrotic regions of the tumour. Agent-based off-lattice modelling is used to study nonlinear tumour growth in 3-dimensional space (Frieboes et al., 2010) and to study how tumour growth and invasion are governed by biophysical laws and regulated by heterogeneity in phenotypic, genotypic, and microenvironmental parameters (Bearer et al., 2009). In

these models the discrete cells are assumed to have zero size. In order for two cells not occupy the same position in space, a circular random walk model that incorporates chemotaxis, haptotaxis and volume exclusion is used.

In this chapter we have presented a review of the main models that have been developed to study cancer invasion. The list of papers is very long, and it is still growing, particularly with advances of computer power enabling to reduce computational cost as the numerical complexity and number of cells increase. Each approach has their own advantage and limitation. Nevertheless they all enrich the field of cancer biology modelling with the ultimate goal to be able to first of all replicate observations from *in vivo* and/or *in vitro* experiments, and then eventually to contribute to cancer treatment strategies.

Chapter 4

A Mathematical Model of Cancer Invasion of Tissue Involving the uPA System

4.1 Introduction

One of the first steps of invasion is the remodelling of the surrounding tissues or extracellular matrix or ECM and a major part of this process is the over-expression of proteolytic enzymes, such as the urokinase-type plasminogen activator (uPA) and matrix metalloproteinases (MMPs), by the cancer cells to break down matrix proteins. Degradation of the matrix enables the cancer cells to migrate through the tissue and subsequently to spread to distant anatomical sites in the body, a process known as metastasis.

In order to understand the process of invasion of surrounding tissues by cancer cells, we begin with an invasion model that describes the interactions between cancer cells, the proteolytic enzymes and the host tissue. Because the phenomena that occur in this model are typical of continuum systems, where the proteolytic enzymes are

diffusible chemical substance and the movement of cancer cells can also be described by random motility or diffusion, macroscopic scale modelling or continuum approach is appropriate for this purpose.

In this chapter, we undertake an analysis of a mathematical model of cancer cell invasion of tissue which focuses on the role of the urokinase plasminogen activation (uPA) system for matrix degradation. We focus on the model that was first developed by Chaplain and Lolas (2005) and discuss its role in tissue invasion, tumour heterogeneity and its biological and clinical implications.

In the model under consideration, the interactions of cancer cells and l chemicals are described by a system of $l+1$ reaction-diffusion-taxis equations of the form

$$\frac{\partial c}{\partial t} = D_c \nabla^2 c - \nabla \cdot \left(c \sum_{j=1}^{l} p_j(c,\mathbf{n}) \nabla n_j \right) + f(c,\mathbf{n}), \qquad (t,\mathbf{x}) \in (0,T] \times \Omega \tag{4.1a}$$

$$\frac{\partial \mathbf{n}}{\partial t} = \mathbf{D}\nabla^2 \mathbf{n} + \mathbf{g}(c,\mathbf{n}), \tag{4.1b}$$

where we denote the time (t) and space $(\mathbf{x})$ dependent concentrations of the chemical species by the vector valued function $\mathbf{n}(t,\mathbf{x})$ and the density of the cancer cells by $c(t,\mathbf{x})$,

$$c : [0,T] \times \bar{\Omega} \to \mathbb{R} \qquad \text{and} \qquad \mathbf{n} : [0,T] \times \bar{\Omega} \to \mathbb{R}^l.$$

Here, $\Omega \subset \mathbb{R}^d$, $d = 1$ or $d = 2$, is a bounded domain and $[0,T]$ is the time interval of interest. Furthermore, the cancer cell random motility coefficient $D_c \geq 0$ and the diagonal matrix $\mathbf{D} \geq 0$ of chemical diffusion coefficients, the taxis functions $p_j, j = 1,\ldots,l$, associated with each chemical n_j, as well as the reaction terms f and $\mathbf{g}$ are given. The temporal derivative is denoted by $\dfrac{\partial}{\partial t}$, the spatial gradient operator by ∇, and the Laplace operator by ∇^2. The partial differential equation (PDE) system (4.1) is supplied with appropriate initial and boundary conditions.

4.2 Cancer Invasion: the uPA System and its Role in ECM Proteolysis

The prognosis of a cancer is primarily dependent on its ability to invade and metastasise, and a crucial component of these processes is the degradation of extracellular matrix. A major constituent of matrix are proteins and their directed degradation by cellular enzymes (proteolytic enzymes or *proteases* for short) is called *proteolysis*.

Many steps that occur during tumour invasion and the formation of metastases (as well as in a number of distinct physiological events in the healthy organism) require the regulated turnover of matrix macromolecules. It is now widely believed that the breakdown of these barriers is catalysed by proteases released from the invading cancer cells. Most of these proteases belong to one of two general classes: *matrix metalloproteases* (MMPs) (Parsons et al., 1997; Pepper, 2001) or *serine proteases* (Andreasen et al., 1997, 2000). Proteases give cancers their defining deadly characteristic—the ability of malignant cells to break out of tissue compartments.

The enzymatic system we will focus on in this chapter is the *urokinase plasminogen activation system* (uPA system) which consists of:

uPA,	the urokinase plasminogen activator,
uPAR,	the urokinase plasminogen activator receptor,
plasmin,	the matrix degrading enzyme,
VN,	the ECM protein vitronectin, and
PAI-1,	the plasminogen activator inhibitor type-1.

A schematic diagram of the key interactions of the system is given in Fig. 4.1.

uPA is an extracellular serine protease. Cells secrete its enzymatically inactive form pro-uPA into the extracellular space. pro-uPA is activated by plasmin to its active form uPA. In the model below, we do not distinguish between pro-uPA and uPA, which both bind to uPA receptors (uPAR) located on the cell membrane. Two major

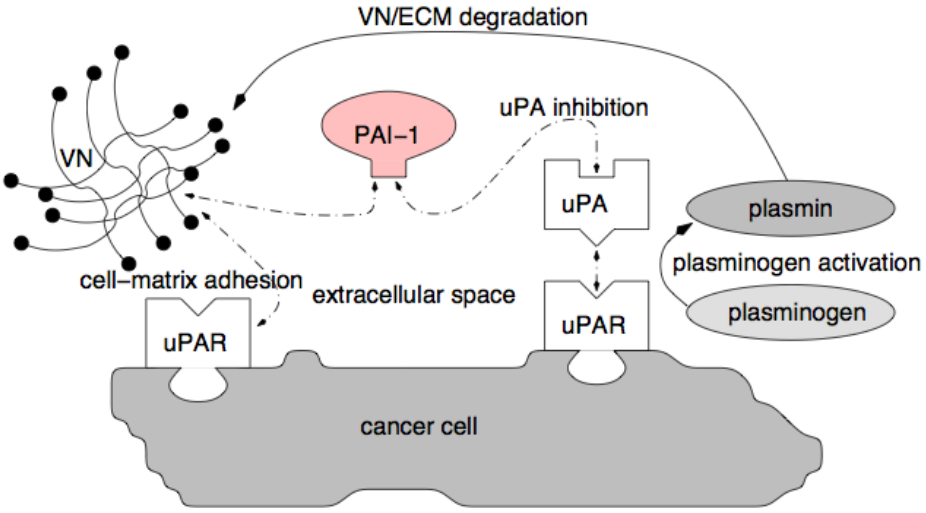

Figure 4.1: A schematic diagram of the uPA system showing its main components and their interactions.

functional domains make up the uPA molecule: the protease domain and the growth factor domain (not discussed here). The protease moiety in uPAR-bound uPA activates the pro-enzyme plasminogen to its active form plasmin. Plasminogen is a ubiquitous protein produced mainly in the liver and present in blood and the matrix. Plasmin itself is a broadly acting serine protease that, either directly or through the activation of other proteases, catalyses the breakdown of many of the known extracellular matrix and basement membrane molecules, such as vitronectin (VN), fibronectin, fibrin, laminin, thrombospondin, and collagens. Therefore, to maintain tissue *homeostasis* and to avoid unrestrained tissue damage, the process of plasminogen activation in a healthy organism is strictly controlled through the availability of uPA, localised activation, and interaction with specific inhibitors (PAIs). One of these inhibitors, PAI-1, is believed to be the most abundant fast-acting inhibitor of uPA *in vivo* (Andreasen et al., 1997, 2000). In other words, for cells to protect themselves they must secrete a surplus of inhibitors to guarantee restraint of pericellular proteolysis. Indeed secreted uPA is often associated with PAI-1 and remains inactive. PAI-1 has a high affinity to the matrix constituent VN and VN-bound PAI-1 remains in an active conformation for

prolonged periods of time.

These facts suggest that the five molecules uPA, PAI-1, plasmin, uPAR and VN constitute the core of an integrated dynamical system which allows spatial and temporal rearrangements of its components at cell surfaces during cell migration and invasion. Moreover, it has become clear that this system has a multi-functional role in cancer biology. The system seems to function not only in cancer cell migration and invasion, but also in remodelling of the tissue surrounding the cancer cells, which may contribute decisively to the overall process of metastasis.

4.3 Mathematical Model

In this section we present the mathematical model of the uPA system and cancer cell invasion of tissue. The model explicitly considers the production of plasmin and the interactions between cancer cells (with uPAR located on their surface), uPA, PAI-1, plasmin, and the extracellular matrix component VN. In the model we assume an unrestricted supply of plasminogen. Furthermore, we assume a fixed average number of uPARs located on each cancer cells surface. This implies that the concentration of uPAR is proportional to the cancer cell density and we do not explicitly model the evolution of uPAR. We denote the cancer cell density by $c(t,\mathbf{x})$, the uPA concentration by $u(t,\mathbf{x})$, the PAI-1 concentration by $p(t,\mathbf{x})$, the plasmin concentration by $m(t,\mathbf{x})$, and the VN concentration by $v(t,\mathbf{x})$. We briefly describe the main interactions between all the variables before writing the system of equations. A fuller description may be found in Chaplain and Lolas (2005).

Cancer Cells The dominating factors governing cancer cell migration are random motion, chemotaxis due to uPA and PAI-1 as well as haptotaxis due to VN and other matrix components. Besides migration, cancer cell proliferation is also included in the model in the form of a logistic growth law.

Extracellular Matrix It is known that extracellular matrix does not diffuse

and therefore we omit any diffusion term (or other "migration" terms) from its model equation. Furthermore, based on the experimental evidence that uPA activates plasminogen to its cancer cell-surface associated form plasmin, which in turn catalyses the breakdown of VN (and other matrix molecules), we model the fact that plasmin degrades VN upon contact at a (degradation) rate δ. The inhibitor PAI-1 also binds to VN and in this way inhibits VN from binding to cell-surface receptors (such as uPAR and/or integrins) and promoting its own production through the regulation of cell-matrix-associated signal transduction pathways. This effect is accounted for by the degradation term $-\phi_{22}vp$. Furthermore, it is assumed that the latter process is reversed by PAI-1 binding to uPA and the production term $\phi_{21}up$ is added to the model. Finally, a logistic growth term accounts for the remodelling of the extracellular matrix by the cells present in the tissue such as fibroblasts. We assume the secretion of extracellular matrix components by fibroblasts to be spatially limited, and therefore a logistic growth term is considered to be appropriate to model this process.

Urokinase Plasminogen Activator The spatio-temporal evolution of the concentration of uPA is assumed to occur through diffusion, cancer cells acting as sources, while its binding to PAI-1 and uPAR dominates its removal from the system.

Plasminogen Activator Inhibitor-1 The conservation equation for the concentration of PAI-1 is similar to that of uPA. Thus, we assume it diffuses, with its production being a result of plasmin activation and its neutralisation in the system occurs by its binding to VN and to uPA.

Plasmin In examining spatio-temporal evolution of the plasmin concentration, we assume that it also diffuses. Furthermore, we assume that binding of uPA to uPAR provides the cell surface with a potential proteolytic activity via activation and cell-surface co-localisation of plasminogen and thus leads to plasmin formation. Additionally, the binding of PAI-1 to VN indirectly results in the binding of uPA to uPAR

and therefore in enhanced plasmin formation. Finally, the term $-\phi_{54}m$ models the deactivation of plasmin either by degradation or by the action of the plasmin inhibitor α_2-antiplasmin.

The mathematical model depicting the interactions between all variables described above, in its full dimensional form, is given by

$$\begin{aligned}
\frac{\partial c}{\partial t} &= \underbrace{D_1\nabla^2 c}_{\text{random motility}} - \nabla\cdot\Big[\underbrace{\xi_u c\nabla u}_{\text{uPA-chemo}} + \underbrace{\xi_p c\nabla p}_{\text{PAI-1-chemo}} + \underbrace{\xi_c c\nabla v}_{\text{VN-hapto}}\Big] \\
&\quad + \underbrace{\sigma_1 c(1-\frac{c}{c_0})}_{\text{proliferation}}, && \text{(4.2a)}\\
\frac{\partial v}{\partial t} &= -\underbrace{\beta vm}_{\text{degradation}} + \underbrace{\Phi_{21}up}_{\text{uPA/PAI-1}} - \underbrace{\Phi_{22}vp}_{\text{PAI-1/VN}} + \underbrace{\sigma_2 v(1-\frac{v}{v_0})}_{\text{remodelling}}, && \text{(4.2b)}\\
\frac{\partial u}{\partial t} &= \underbrace{D_3\nabla^2 u}_{\text{diffusion}} - \underbrace{\Phi_{31}pu}_{\text{uPA/PAI-1}} - \underbrace{\Phi_{33}cu}_{\text{uPA/uPAR}} + \underbrace{\gamma_{31}c}_{\text{production}}, && \text{(4.2c)}\\
\frac{\partial p}{\partial t} &= \underbrace{D_4\nabla^2 p}_{\text{diffusion}} - \underbrace{\Phi_{41}pu}_{\text{PAI-1/uPA}} - \underbrace{\Phi_{42}pv}_{\text{PAI-1/VN}} + \underbrace{\gamma_{41}m}_{\text{production}}, && \text{(4.2d)}\\
\frac{\partial m}{\partial t} &= \underbrace{D_5\nabla^2 m}_{\text{diffusion}} + \underbrace{\Phi_{52}pv}_{\text{PAI-1/VN}} + \underbrace{\Phi_{53}uc}_{\text{uPA/uPAR}} - \underbrace{\Phi_{54}m}_{\text{degradation}}. && \text{(4.2e)}
\end{aligned}$$

These model equations coincide with those given in Chaplain and Lolas (2005) (Equation (9)), except for some minor details. In this thesis we replace the degradation of plasmin term due to binding of uPA and PAI-1 in Chaplain and Lolas (2005) ($-\Phi_{51}pu$) with a natural degradation term $-\Phi_{54}m$. To nondimensionalise the system, we rescale distance with the maximum distance of the cancer cells at this early stage of invasion $L := 0.1\,\text{cm}$ and time with $\tau := L^2 D^{-1}$, where $D := 10^{-6}\text{cm}^2\,\text{s}^{-1}$ is a representative chemical diffusion coefficient. The dependent variables v, u, p, m are rescaled with appropriate reference concentration values v_0, u_0, p_0, m_0 in the nanomolar range, $1\text{nM} \equiv 10^{-9}\text{mol/l}$ taken from Chaplain and Lolas (2005), while the reference cancer

cell density n_0 is taken from Gerisch and Chaplain (2008). The full set of scaling parameters is given by

$$L = 0.1\,\mathrm{cm}, \qquad \tau = \frac{L^2}{D} = 10^4\mathrm{s}, \qquad c_0 = 6.7\times 10^7 \mathrm{cell\,cm^{-3}}, \qquad v_0 = 1\mathrm{nM},$$
$$u_0 = 1\mathrm{nM}, \qquad p_0 = 1\mathrm{nM}, \qquad m_0 = 0.1\mathrm{nM},$$

from which the nondimensional variables are obtained,

$$\tilde{x} = \frac{x}{L}, \qquad \tilde{t} = \frac{t}{\tau} \quad \text{or} \quad \tilde{t} = \frac{tD}{L^2}, \qquad \tilde{c} = \frac{c}{c_0}, \qquad \tilde{v} = \frac{v}{v_0},$$
$$\tilde{u} = \frac{u}{u_0}, \qquad \tilde{p} = \frac{p}{p_0}, \qquad \tilde{m} = \frac{m}{m_0},$$

as well as nondimensional parameters,

$$D_c = \frac{D_1}{D}, \quad \chi_u = \xi_u \frac{u_0}{D}, \quad \chi_p = \xi_p \frac{p_0}{D}, \quad \chi_v = \xi_v \frac{v_0}{D}, \quad \mu_1 = \sigma_1 \tau,$$
$$\delta = \beta \frac{m_0 \tau}{v_0}, \quad \phi_{21} = \Phi_{21} \frac{u_0 p_0}{v_0}\tau, \quad \phi_{22} = \Phi_{21} p_0 \tau, \quad \mu_2 = \sigma_2 \tau,$$
$$D_u = \frac{D_3}{D}, \quad \phi_{31} = \Phi_{31} p_0 \tau, \quad \phi_{33} = \Phi_{33} c_0 \tau, \quad \alpha_{31} = \gamma_{31} \frac{c_0}{u_0}\tau,$$
$$D_p = \frac{D_4}{D}, \quad \phi_{41} = \Phi_{41} u_0 \tau, \quad \phi_{42} = \Phi_{42} v_0 \tau, \quad \alpha_{41} = \gamma_{41} \frac{m_0}{p_0}\tau,$$
$$D_m = \frac{D_5}{D}, \quad \phi_{52} = \Phi_{52} \frac{v_0 p_0}{m_0}\tau, \quad \phi_{53} = \Phi_{53} \frac{u_0 c_0}{m_0}\tau, \quad \phi_{54} = \Phi_{54}\tau.$$

Inserting the nondimensional variables and parameters above into the system (4.2)

we obtain the nondimensionalised form of the system of PDEs given by

$$\frac{\partial c}{\partial t} = \underbrace{D_c\nabla^2 c}_{\text{random motility}} - \nabla\cdot\Big[\underbrace{\chi_u c\nabla u}_{\text{uPA-chemo}} + \underbrace{\chi_p c\nabla p}_{\text{PAI-1-chemo}} + \underbrace{\chi_c c\nabla v}_{\text{VN-hapto}}\Big] + \underbrace{\mu_1 c(1-c)}_{\text{proliferation}} \quad (4.3a)$$

$$\frac{\partial v}{\partial t} = -\underbrace{\delta vm}_{\text{degradation}} + \underbrace{\phi_{21}up}_{\text{uPA/PAI-1}} - \underbrace{\phi_{22}vp}_{\text{PAI-1/VN}} + \underbrace{\mu_2 v(1-v)}_{\text{remodelling}}, \quad (4.3b)$$

$$\frac{\partial u}{\partial t} = \underbrace{D_u\nabla^2 u}_{\text{diffusion}} - \underbrace{\phi_{31}pu}_{\text{uPA/PAI-1}} - \underbrace{\phi_{33}cu}_{\text{uPA/uPAR}} + \underbrace{\alpha_{31}c}_{\text{production}}, \quad (4.3c)$$

$$\frac{\partial p}{\partial t} = \underbrace{D_p\nabla^2 p}_{\text{diffusion}} - \underbrace{\phi_{41}pu}_{\text{PAI-1/uPA}} - \underbrace{\phi_{42}pv}_{\text{PAI-1/VN}} + \underbrace{\alpha_{41}m}_{\text{production}}, \quad (4.3d)$$

$$\frac{\partial m}{\partial t} = \underbrace{D_m\nabla^2 m}_{\text{diffusion}} + \underbrace{\phi_{52}pv}_{\text{PAI-1/VN}} + \underbrace{\phi_{53}uc}_{\text{uPA/uPAR}} - \underbrace{\phi_{54}m}_{\text{degradation}}. \quad (4.3e)$$

In this work we consider a default set of model parameters referred to as *parameter set* $\mathscr{P}$. The majority of the values of the parameters are taken from Chaplain and Lolas (2005), except for the values of the new parameter ϕ_{54}, and also for parameters μ_1 and μ_2 which are cell proliferation and matrix remodelling terms, respectively. We consider here the rate of matrix remodelling slower than cell proliferation (Perentes et al., 2009). The values of the nondimensional parameter set $\mathscr{P}$ are given in Table 4.1.

Table 4.1: Parameter set $\mathscr{P}$ for the uPA model

$D_c = 3.5\cdot 10^{-4}$	$D_u = 2.5\cdot 10^{-3}$	$D_p = 3.5\cdot 10^{-3}$	$D_m = 4.91\cdot 10^{-3}$
$\chi_u = 3.05\cdot 10^{-2}$	$\chi_p = 3.75\cdot 10^{-2}$	$\chi_v = 2.85\cdot 10^{-2}$	$\mu_1 = 0.25$
$\delta = 8.15$	$\phi_{21} = 0.75$	$\phi_{22} = 0.55$	$\mu_2 = 0.15$
$\phi_{31} = 0.75$	$\phi_{33} = 0.3$	$\alpha_{31} = 0.215$	
$\phi_{41} = 0.75$	$\phi_{42} = 0.55$	$\alpha_{41} = 0.5$	
$\phi_{52} = 0.11$	$\phi_{53} = 0.75$	$\phi_{54} = 0.5$	

The above dimensionless parameters are taken from Chaplain and Lolas (2005).

The dimensional values of the parameters can be recovered using the scalings detailed above *e.g.* D_c (dimensional) $= 3.5 \times 10^{-4} \times 10^{-6}\text{cm}^2\text{s}^{-1} = 3.5 \times 10^{-10}\text{cm}^2\text{s}^{-1}$. In particular for the diffusion coefficient of the cancer cells, although based on *in vivo* measurements of human colon adenocarcinomas diffusion coefficients range between the order of 10^{-7} to $10^{-8}\text{cm}^2\text{s}^{-1}$ (Brown et al., 2004), we choose a small diffusion coefficient because here our focus is on the motility of cancer cells due to chemotaxis by the components of the urokinase plasminogen activation system. Also, as will be revealed in the computational simulation results in Section 4.5, smaller diffusion coefficients give rise to heterogeneity of the solutions.

We consider system (4.3) to hold for times $t \in (0,T]$ and on a bounded spatial domain $\Omega \subset \mathbb{R}^d$, for $d = 1$ or $d = 2$, representing a region of tissue. We use two different cases of domains, each parameterised by a positive parameter M: the one-dimensional domain $\Omega_1 := (-M,M) \subset \mathbb{R}$ and the two-dimensional square domain $\Omega_2 := (-M,M) \times (-M,M) \subset \mathbb{R}^2$. For reasons of symmetry, in our computational simulations in Sect. 4.5 we take $\Omega_1 := (0,M) \subset \mathbb{R}$ for the one-dimensional domain and $\Omega_2 := (0,M) \times (0,M) \subset \mathbb{R}^2$ for the two-dimensional square domain.

System (4.3) must be closed by appropriate initial and boundary conditions for each of the dependent variables. For the two cases of domains we use different initial conditions for cancer cell density and matrix/VN concentration. For the 1-dimensional domain case we assume that initially there is a cluster of cancer cells already present at $\mathbf{x} = \mathbf{0}$ and that they have penetrated a short distance into the extracellular matrix, while the remaining space is occupied by the matrix alone. Additionally, we assume that the uPA protease as well as the PAI-1 inhibitor initial concentration are proportional to the initial cancer cell density while the plasmin protease is not yet produced by the cancer cells. Specifically, the initial conditions for system (4.3) in 1-dimensional

spatial domain are taken to be

$$\begin{aligned} c(0,\mathbf{x}) &= \exp(-|\mathbf{x}|^2\,\varepsilon^{-1})\,, \\ v(0,\mathbf{x}) &= 1-\frac{1}{2}\exp(-|\mathbf{x}|^2\,\varepsilon^{-1})\,, \\ u(0,\mathbf{x}) &= \frac{1}{2}\exp(-|\mathbf{x}|^2\,\varepsilon^{-1})\,, \qquad \text{for} \quad \mathbf{x}\in\bar{\Omega}_1\,, \\ p(0,\mathbf{x}) &= \frac{1}{20}\exp(-|\mathbf{x}|^2\,\varepsilon^{-1})\,, \\ m(0,\mathbf{x}) &= 0\,, \end{aligned} \tag{4.4}$$

where throughout this chapter we have taken $\varepsilon = 0.01$.

For the 2-dimensional square domain case, the cancer cells are initially placed to form a strip along the top of the domain. The strip of cancer cells takes about 20% of the domain and is at a uniform initial density of 1, while the matrix/VN concentration uniformly occupies the rest of 80% of the domain also at initial concentration 1. The uPA, PAI-1, and plasmin at $t = 0$ follow those in Eq. 4.4, *i.e.*,

$$\begin{aligned} u(0,\mathbf{x}) &= 0.5\,c(0,\mathbf{x})\,, \\ p(0,\mathbf{x}) &= 0.05\,c(0,\mathbf{x})\,, \qquad \text{for} \quad \mathbf{x}\in\bar{\Omega}_2\,, \\ m(0,\mathbf{x}) &= 0\,. \end{aligned} \tag{4.5}$$

We assume that cancer cells, and as a consequence uPA, PAI-1 and plasmin, remain within the domain of tissue under consideration and therefore zero-flux boundary conditions are imposed on $\partial\Omega$, the boundary of Ω. For the matrix density, $v(t,\mathbf{x})$ satisfies an ordinary differential equation (ODE) and so no boundary conditions can be prescribed.

4.4 Linear Stability Analysis

4.4.1 Positive, Spatially Uniform Steady States

We first write the solution components of the model (4.3) as a vector $\mathbf{w}(t,\mathbf{x})$

$$\mathbf{w}(t,\mathbf{x}) := (c(t,\mathbf{x}), v(t,\mathbf{x}), u(t,\mathbf{x}), p(t,\mathbf{x}), m(t,\mathbf{x}))\,.$$

We are interested in the existence of spatially uniform steady states $\mathbf{w}^* = (c^*, v^*, u^*, p^*, m^*)$ of the system (4.3), where the values can be derived by setting the spatial and temporal variations to zero

$$\frac{\partial \mathbf{w}}{\partial t} = \frac{\partial \mathbf{w}}{\partial \mathbf{x}} = 0$$

to get

$$\begin{aligned}
0 &= \mu_1 c^*(1-c^*) && \text{(4.6a)}\\
0 &= -\delta v^* m^* + \phi_{21} u^* p^* - \phi_{22} v^* p^* + \mu_2 v^*(1-v^*) && \text{(4.6b)}\\
0 &= -\phi_{31} p^* u^* - \phi_{33} c^* u^* + \alpha_{31} c^* && \text{(4.6c)}\\
0 &= -\phi_{41} p^* u^* - \phi_{42} p^* v^* + \alpha_{41} m^* && \text{(4.6d)}\\
0 &= \phi_{52} p^* v^* + \phi_{53} u^* c^* - \phi_{54} m^* && \text{(4.6e)}
\end{aligned}$$

From Eq. 4.6a we infer that $c^* = 0$ or $c^* = 1$. The first case leads to non-positive steady states and is not discussed. So in the following we investigate the case $c^* = 1$.

Solving the steady state conditions for Eqs. (4.6c) to (4.6e) for u^*, m^*, v^* results in expressions for u^*, m^*, v^* in terms of p^*. First, from solving Eq. 4.6c we get

$$u^*(p^*) = \frac{\alpha_{31}}{\phi_{31} p^* + \phi_{33}}. \tag{4.7}$$

Rearranging Eq. 4.6e into

$$p^* v^* = \frac{\phi_{54}}{\phi_{52}} m^* - \frac{\phi_{53}}{\phi_{52}} u^*,$$

and substituting it into Eq. 4.6d yields

$$m^*(p^*) = \frac{(-\phi_{41}\phi_{52} p^* + \phi_{53}\phi_{42}) u^*(p^*)}{\phi_{42}\phi_{54} - \alpha_{41}\phi_{52}}. \tag{4.8}$$

Further, substituting Eq. 4.8 into (4.6d) gives

$$v^*(p^*) = \frac{(-\phi_{41}\phi_{54} p^* + \phi_{53}\alpha_{41}) u^*(p^*)}{p^*(\phi_{42}\phi_{54} - \alpha_{41}\phi_{52})}. \tag{4.9}$$

Inserting the expressions (4.7), (4.8), and (4.9) into the steady state condition for Eq. 4.6b results in a rational equation for p^*. Its denominator

$$p^{*2}(p^*\phi_{31} + \phi_{33})^2 (\phi_{42}\phi_{54} - \alpha_{41}\phi_{52})^2,$$

a polynomial of degree four, has no zeros $p^* > 0$. Its numerator, also of degree four, has four different zeros. This leads to potentially four positive steady states $\mathbf{w}^*$. However, in all our tests we always have observed the existence of a unique positive, spatially uniform steady state $\mathbf{w}^*$ for a specific set of parameters. In the case of the parameter set $\mathscr{P}$ as given in Table 4.1, the one positive and unique steady state $\mathbf{w}^*$ is given by

$$\mathbf{w}^* := (c^*, v^*, u^*, p^*, m^*) \approx (1, 0.047, 0.222, 0.889, 0.343)\,. \tag{4.10}$$

(Indeed, we note that for all parameter sets used in this chapter, it was verified using both *Mathematica* and *Maple* that a unique positive steady state existed.) This steady state is linearly stable which can be seen by evaluating the Jacobian matrix $J_R(\mathbf{w})$ of the reaction terms, given by

$$J_R(\mathbf{w}) = \begin{pmatrix} \mu_1(1-2c) & 0 & 0 & 0 & 0 \\ 0 & -\delta m - \phi_{22} p + \mu_2(1-2v) & \phi_{21} p & \phi_{21} u - \phi_{22} v & -\delta v \\ -\phi_{33} u + \alpha_{31} & 0 & -\phi_{31} p - \phi_{33} c & -\phi_{31} u & 0 \\ 0 & -\phi_{42} p & -\phi_{41} p & -\phi_{41} u - \phi_{42} v & \alpha_{41} \\ \phi_{53} u & \phi_{52} p & \phi_{53} c & \phi_{52} v & -\phi_{54} \end{pmatrix} \tag{4.11}$$

at $\mathbf{w}^*$ and observing that its eigenvalues have a maximum real part of ≈ -0.24.

4.4.2 Dispersion Curves and Taxis-driven Instability

Here we investigate the linear stability of system (4.3) in the vicinity of a spatially uniform steady state $\mathbf{w}^*$. To this end, we write the solutions $\mathbf{w}(t, \mathbf{x})$ of this system as small perturbations of $\mathbf{w}^*$,

$$\mathbf{w}(t, \mathbf{x}) := \mathbf{w}^* + \varepsilon \tilde{\mathbf{w}}(t, \mathbf{x})\,,$$

where $\varepsilon > 0$ is small and $\tilde{\mathbf{w}}(t,\mathbf{x})$ is bounded. We consider the PDE systems for $\mathbf{x} \in (-M,M)^d$ with periodic boundary conditions and assume that the perturbations can be written as d-dimensional Fourier series for all $t \geq 0$, that is

$$\tilde{\mathbf{w}}(t,\mathbf{x}) = \sum_{\mathbf{k}\in\mathbb{Z}^d} \mathbf{a}_{\mathbf{k}}(t)\exp(\mathrm{i}\mathbf{k}\pi M^{-1}\cdot\mathbf{x})$$

with coefficient functions $\mathbf{a}_{\mathbf{k}} : [0,T] \to \mathbb{C}^5$ for each $\mathbf{k} \in \mathbb{Z}^d$. In the following we use the notation $\tilde{\mathbf{k}} \equiv \mathbf{k}\pi M^{-1}$. This allows for the visualisation of dispersion relations independent of the domain size parameter M.

Linearising system (4.3) around a spatially uniform steady state $\mathbf{w}^*$ leads, upon dropping terms of order ε^2 or higher and dividing by ε, to

$$\frac{\partial\tilde{\mathbf{w}}}{\partial t} = J_T(\mathbf{w}^*)\nabla^2\tilde{\mathbf{w}} + J_R(\mathbf{w}^*)\tilde{\mathbf{w}}\,. \tag{4.12}$$

Here, the reaction Jacobian $J_R(\mathbf{w}^*)$ is given by (4.11). Furthermore, the transport Jacobian $J_T(\mathbf{w}^*)$, accounting for diffusion and taxis, is

$$J_T(\mathbf{w}^*) = \begin{pmatrix} D_c & -\chi_v c^* & -\chi_u c^* & -\chi_p c^* & 0 \\ 0 & 0 & 0 & 0 & 0 \\ 0 & 0 & D_u & 0 & 0 \\ 0 & 0 & 0 & D_p & 0 \\ 0 & 0 & 0 & 0 & D_m \end{pmatrix}. \tag{4.13}$$

We arrive at these entries by observing, for the first row, that

$$D_c\nabla^2 c = D_c\nabla^2(c^* + \varepsilon\tilde{c}) = \varepsilon D_c\nabla^2\tilde{c}$$

and accordingly for the diffusion terms in rows three, four, and five. The linearisation of the taxis terms is as

$$\begin{aligned} -\nabla\cdot(\chi_u c\nabla v) &= -\nabla\cdot(\chi_u(c^*+\varepsilon\tilde{c})\nabla(v^*+\varepsilon\tilde{v})) \\ &= -\varepsilon\chi_v c^*\nabla^2\tilde{v} - \varepsilon^2\chi_v\nabla\cdot(\tilde{c}\nabla\tilde{v}) \end{aligned}$$

which, upon dropping the ε^2-term and dividing by ε leads to the entry in column 2 in the first row of $J_T(\mathbf{w}^*)$. The remaining entries in that first row follow accordingly.

Inserting the Fourier series representation of $\tilde{\mathbf{w}}$ into (4.12) leads to

$$\sum_{\mathbf{k}\in\mathbb{Z}^d}\left[\frac{\partial \mathbf{a}_{\mathbf{k}}(t)}{\partial t}+\left(\|\tilde{\mathbf{k}}\|_2^2 J_T(\mathbf{w}^*)-J_R(\mathbf{w}^*)\right)\mathbf{a}_{\mathbf{k}}(t)\right]\exp(\mathrm{i}\tilde{\mathbf{k}}\cdot\mathbf{x})=0\,. \tag{4.15}$$

Furthermore, expanding the initial perturbation $\tilde{\mathbf{w}}(0,\mathbf{x})$ of the PDE system in a Fourier series defines coefficients $\mathbf{a}_{\mathbf{k},0}$ via

$$\tilde{\mathbf{w}}(0,\mathbf{x})=\sum_{\mathbf{k}\in\mathbb{Z}^d}\mathbf{a}_{\mathbf{k},0}\exp(\mathrm{i}\tilde{\mathbf{k}}\cdot\mathbf{x})\,.$$

Both relations imply that the Fourier coefficients $\mathbf{a}_{\mathbf{k}}(t)$ satisfy the linear ODE systems

$$\frac{\partial \mathbf{a}_{\mathbf{k}}(t)}{\partial t}=-\left(\|\tilde{\mathbf{k}}\|_2^2 J_T(\mathbf{w}^*)-J_R(\mathbf{w}^*)\right)\mathbf{a}_{\mathbf{k}}(t)\,,\quad \mathbf{a}_{\mathbf{k}}(0)=\mathbf{a}_{\mathbf{k},0}\,.$$

A growth of $\mathbf{a}_{\mathbf{k}}(t)$ then indicates a growth of the perturbation due to mode $\exp(\mathrm{i}\tilde{\mathbf{k}}\cdot\mathbf{x})$ whereas this perturbation is damped away with time if $\mathbf{a}_{\mathbf{k}}(t)\to 0$ for $t\to\infty$. Which type of behaviour takes place for a given perturbation mode is determined by the linear stability of the zero steady state of the above ODE. In more detail, a perturbation due to mode $\exp(\mathrm{i}\tilde{\mathbf{k}}\cdot\mathbf{x})$ grows if

$$\lambda_{\mathbf{k}}(\mathbf{w}^*):=\max\{\text{real part of the eigenvalues of } J_R(\mathbf{w}^*)-\|\tilde{\mathbf{k}}\|_2^2 J_T(\mathbf{w}^*)\}>0\,.$$

If $\lambda_{\mathbf{k}}(\mathbf{w}^*)<0$ then the perturbation is damped away. (The case $\lambda_{\mathbf{k}}(\mathbf{w}^*)=0$ can be treated as usual for linear ODE systems and leads to either growth or damping.)

We are interested in deciding whether there exist non-trivial perturbation modes $\exp(\mathrm{i}\tilde{\mathbf{k}}\cdot\mathbf{x})$ which grow with time, *i.e.* destabilise the linearly stable fixed point $\mathbf{w}^*$ of the reaction system. To this end, we plot for the 1D case ($d=1$, $\tilde{\mathbf{k}}=\tilde{k}$) and a given spatially uniform steady state $\mathbf{w}^*$ the quantity $\lambda_k(\mathbf{w}^*)$ against the (domain size scaled) wave number $\tilde{k}$. This gives the so-called *dispersion relation*. For the parameter set $\mathscr{P}$ and the variations of it, these dispersion relations for system (4.3) are given in Fig. 4.2. For parameter set $\mathscr{P}$ (see the solid line in Fig. 4.2) we observe that there is a range of

$\tilde{k}$-values for which $\lambda_k(\mathbf{w}^*)$ is positive and hence the corresponding perturbations are growing in time. This means that the unique positive, spatially uniform steady state $\mathbf{w}^*$, which is linearly stable for the reaction system itself, is destabilised due to the transport terms (diffusion and taxis).

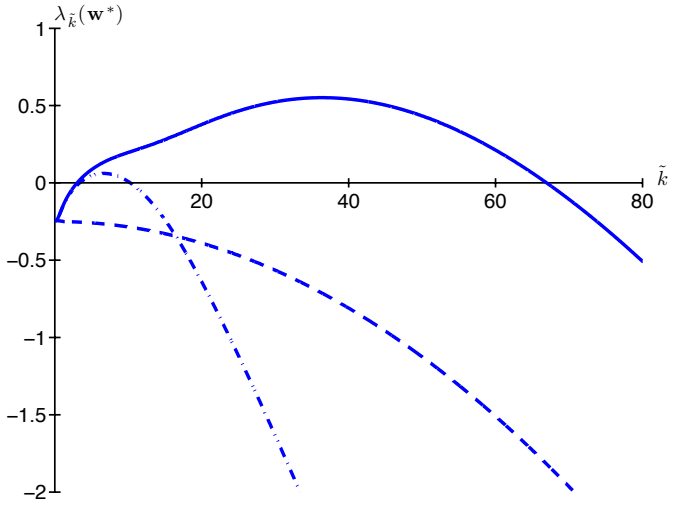

Figure 4.2: Plots of the dispersion relations for the unique positive, spatially uniform steady state $\mathbf{w}^*$ of system (4.3) with (i) parameter set $\mathscr{P}$ (*solid line*); (ii) with parameter set $\mathscr{P}$ but all taxis coefficients set to zero (*dashed line*), and (iii) with parameter set $\mathscr{P}$ but the cell random motility coefficient increased to $D_c = 0.00425$ (*dash-dotted line*).

Furthermore, setting all taxis coefficients in parameter set $\mathscr{P}$ to zero, there exist no values $\tilde{k} \in [0,80]$ for which $\lambda_k(\mathbf{w}^*) > 0$ (dashed line in Fig. 4.2). This observation implies that the destabilisation of the steady state $\mathbf{w}^*$ in system (4.3) is taxis-driven. To see the effect of varying cell random motility coefficient, increasing D_c more than ten times higher, that is to $D_c = 0.00425$, decreases the range of $\tilde{k}$-values for positive $\lambda_k(\mathbf{w}^*)$ (dash-dotted line in Fig. 4.2). The influence of varying cell random motility towards stability of the system is explained further in Fig. 4.3.

It is of interest to see how the range of k-values, for which perturbations grow, changes if key parameters of the model are modified. One such parameter is the random motility of the cancer cells, D_c. We again take the parameter set $\mathscr{P}$ but now vary parameter D_c in the range $[0, 0.01]$. For each value of D_c we compute the set of $\tilde{k}$-values for which $\lambda_k(\mathbf{w}^*) > 0$. The grey area in Fig. 4.3, top left, visualises this

set (with $\tilde{k}$ in the range $[0,80]$). We observe that up to a maximum value of D_c there are always some values $\tilde{k}$ with $\lambda_k(\mathbf{w}^*) > 0$. For decreasing cancer cell random motility D_c, the range of such $\tilde{k}$-values increases. This implies that increased cell random motility has a smoothing effect and leads to damping of, in particular, high frequency perturbations.

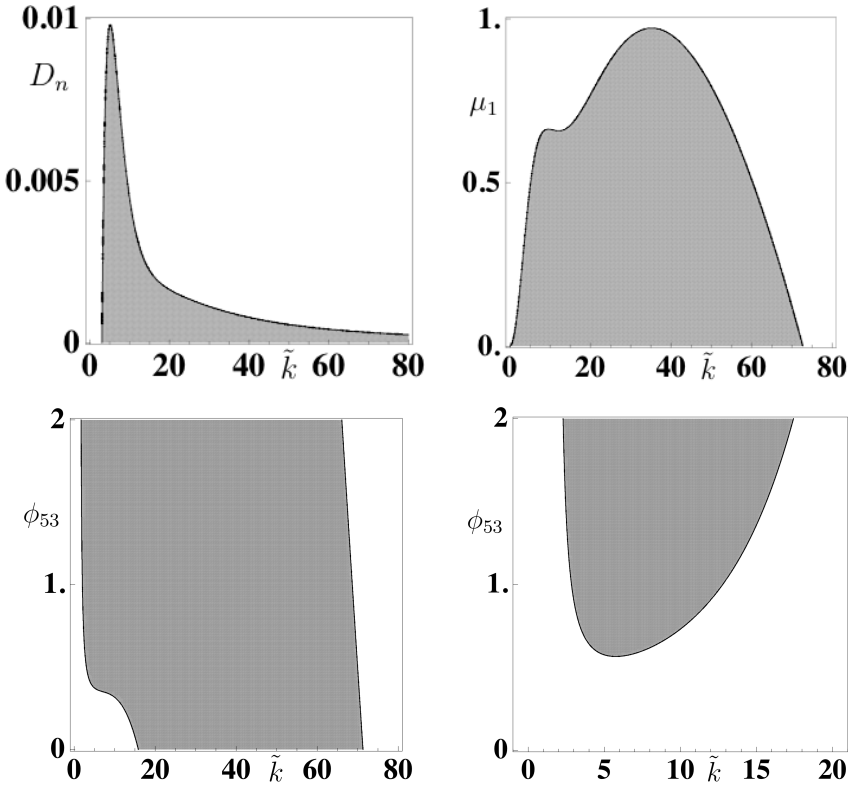

Figure 4.3: Dispersion relation of system (4.3) with parameters taken from set $\mathscr{P}$ and (i) D_c varying in $[0,0.01]$ (top left), (ii) μ_1 varying in $[0,1]$ (top right), (iii) ϕ_{53} varying in $[0,2]$ (bottom left), and (iv) ϕ_{53} varying in $[0,2]$ with $D_c = 0.00425$ (bottom right) for their respective unique positive, spatially uniform steady states. The grey area indicates the $\tilde{k}$-values for which $\lambda_k(\mathbf{w}^*) > 0$.

Besides the random motility coefficient D_c of the cancer cells, there are two other key parameters in the model: the proliferation rate μ_1 of cancer cells and the rate ϕ_{53} of plasmin production due to uPA/uPAR binding. Varying $\mu_1 \in [0,1]$ but keeping parameter set $\mathscr{P}$ otherwise unchanged, leads to the dispersion relations as shown in Fig. 4.3, top right plot. Here we observe that increasing cell proliferation leads to less

and less amplified modes and hence eventually to the damping of all perturbations. Varying $\phi_{53} \in [0,2]$ and keeping all other parameters as in set $\mathscr{P}$ gives no stability area for $\tilde{k}$ within the range $[15,70]$, (see bottom left Fig. 4.3). If the cancer cell random motility is increased to $D_c = 0.00425$ and all other parameters as in set $\mathscr{P}$, this leads to the dispersion relations as shown in Fig. 4.3, bottom right plot. It tells us that at lower values of ϕ_{53} with $D_c = 0.00425$, there are no $\tilde{k}$-values for which $\lambda_k(\mathbf{w}^*) > 0$; all perturbations are damped. But as ϕ_{53} is increased the grey area that determines instability starts to appear and the range of frequency perturbations becomes bigger at higher values of ϕ_{53}.

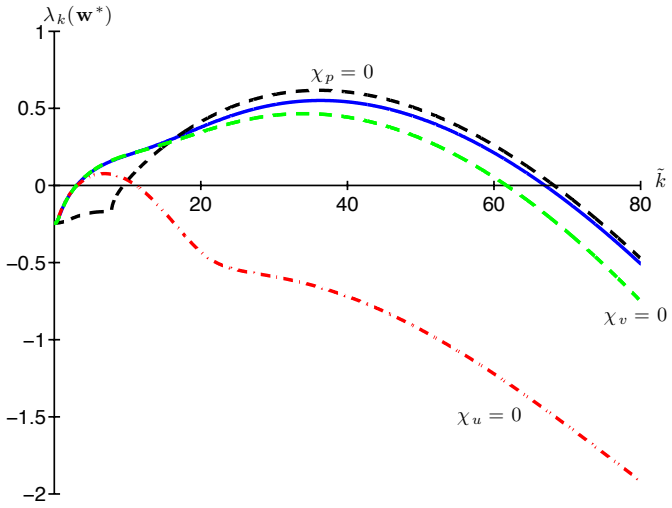

Figure 4.4: Plots of the dispersion relations for the system (4.3) with parameter set $\mathscr{P}$ taking (i) $\chi_u = 0$ (*dash-dotted red line*); (ii) $\chi_p = 0$ (*dashed black line*), and (iii) $\chi_v = 0$ (*dashed green line*). The *blue solid line* represents the dispersion relation with all parameter values as in parameter set $\mathscr{P}$.

In order to see which chemotactic term drives the instability, we plot the dispersion relation by switching off one chemotactic term (or making the chemotactic parameter equal to zero) at a time. Fig. 4.4 shows that taking $\chi_u = 0$ (dash-dotted red line) significantly reduces the range of $\tilde{k}$-values for positive $\lambda_k(\mathbf{w}^*)$, while by taking either $\chi_v = 0$ (dashed green line) or $\chi_p = 0$ (dashed black line) the range of $\tilde{k}$-values for positive eigenvalues remains large, almost the same as using the default values of parameter set $\mathscr{P}$. From these dispersion relations we can see that chemotaxis due to uPA mostly

causes the instability to arise in the system.

4.5 Computational Simulation Results

In this section we present computational simulation results for the model (4.3), together with the initial conditions and zero-flux boundary conditions, given in Sect. 4.3. The parameters are taken from parameter set $\mathscr{P}$ unless otherwise stated. These simulations firstly show the typical behaviour of the model solutions and, secondly, illustrate the theoretical results on taxis-driven instability as obtained in Sect. 4.4. The majority of the simulations presented are in a 1-dimensional spatial domain, Sub Sect. 4.5.2. However, we also perform 2-dimensional simulations, where the results are compared with experimental data taken from an organotypic gel culture system quantifying squamous cell carcinoma invasion. We begin with a few comments on the numerical method employed in obtaining the simulation results.

4.5.1 Numerical Technique

All simulation results are obtained with a custom-made code for the numerical solution of reaction-diffusion-taxis systems, see Gerisch and Chaplain (2006) and the references therein. The code is based on the method of lines. The approach makes use of a finite volumes discretisation in space which employs, for the taxis term, a higher-order, upwind-biased discretisation with nonlinear limiter function. This dedicated treatment of the taxis terms ensures, in general, second-order accuracy of the spatial discretisation and leads to a large positive ODE system, the MOL-ODE system. Here *positive* means that the exact and unique solution of the ODE system with arbitrary non-negative initial data remains non-negative for all later times. Conditions which ensure this property of an ODE system are, for instance, given in Horváth (1998). We note that negative solution values are often the result of unphysical oscillations near

steep fronts in the solution when the taxis terms of the PDE problem are discretised in a standard way, *e.g.*, by central finite differences. These negative values feed back into the reaction kinetics of the system which becomes unstable and we observe a subsequent blow-up of the numerical solution within a short time. So the approach taken here does not lead to negative solution values in the exact solution of the MOL-ODE and all the problems which go with them. This particularly desirable property is achieved automatically by the spatial discretisation by locally introducing just the amount of *numerical diffusion* which is required to ensure the property of positivity. No user intervention is needed. With these measures taken, the code also allows for reliable computations also in the case of zero cell random motility, *i.e.*, $D_c = 0$. The code has been tested with a simple diffusion equation, linear advection, and a simple 2D taxis problem with exact solution. The validation of the code is shown by the convergence of the simulation results as is explained in subsection 4.5.2 below.

After the discretisation in space a large ODE system is obtained which needs to be solved numerically. In particular, simulations of 2D problems lead to a very large dimension of the MOL-ODE system and suitable numerical schemes have to be employed. Due to the stiffness of the equations, the method selected must be implicit for computational efficiency. We have opted here for using the linearly-implicit Runge–Kutta method ROWMAP (Weiner et al., 1997). ROWMAP is designed for the efficient numerical solution of stiff initial value problems of large ODE systems. One of its particular strengths is that it requires a subroutine for the evaluation of the right-hand side of the ODE only; no explicit subroutine for the evaluation of the Jacobian matrix is required. The linear systems in the stages of the method are then solved using a multiple Arnoldi process (Weiner et al., 1997). The automatic time-step selection based on a local error control further increases the efficiency and reliability of the method.

4.5.2 Computational Simulation Results in 1D

The simulations in this section are obtained with the custom-made finite volume code, see Sect. 4.5.1. We use an equidistant covering of the spatial domain with finite volumes of length $1/50$ or $\Delta x = 0.02$. For the time integration we prescribe an absolute and relative tolerance of 10^{-6} (variable time step sizes). Numerical convergence tests have shown that these choices of discretisation parameters are appropriate for the problems at hand and give sufficiently accurate solutions. We ran all simulations up to a final time $t = 500$ unless indicated otherwise. This corresponds to a real time span of about 58 days. We have performed simulations on the domain $\Omega = (-10, 10)$ with zero-flux as well as with periodic boundary conditions. The results are qualitatively and quantitatively similar and also similar to the results obtained with $\Omega = (0, 10)$ and zero-flux boundary conditions. In particular the same conclusions can be drawn. In the interest of a clearer presentation we show simulation results obtained with $\Omega = (0, 10)$ (and $\Omega = (0, 15)$ for certain simulations) and zero-flux boundary conditions only.

Fig. 4.5 captures the dynamic heterogeneity of cancer cell density that evolves over time by interacting with components of the uPA system. The solution profile for the cancer cell density, which is in the form of spikes, varies in height and reaches above 3 dimensionless units of density. Initially, at $t = 0$, we assume a cluster of cancer cells are already present and they have penetrated a small area in the extracellular matrix. By $t = 75$ (~ 8.5days), several clusters of cancer cells that are composed of the primary tumour occupied half of the domain. At $t = 150$ (~ 17.5days) cancer cells have invaded the remaining of the extracellular matrix. In order to see whether the solutions converge, we performed numerical tests by using finer grids of grid spacings $\Delta x = 0.005$ and $\Delta x = 0.0025$. We measured the width of the spikes of cell density at density height 1 at $t = 500$ and compared the results with the width of the spikes from simulations using the default grid spacing of $\Delta x = 0.02$. We can confirm that the width of the spikes remains (approximately) constant at about $0.03-0.04$ length units for all

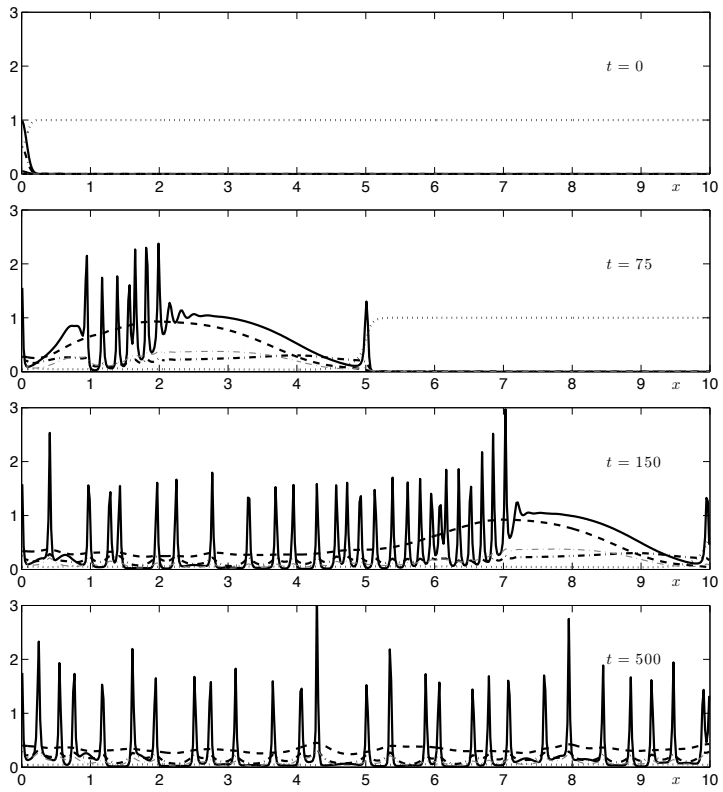

Figure 4.5: Sequence of profiles showing the spatio-temporal evolution of cancer cells c (solid black line) invading the extracellular matrix v (dotted black line) along with the other components of the model: uPA protease concentration u (dash-dotted black line), PAI-1 concentration p (dashed black line), and plasmin concentration m (dash-dotted grey thin line) for model (4.3) with parameter set $\mathscr{P}$ at dimensionless times $t = 0$, $t = 75$, $t = 150$, and $t = 500$.

grid sizes, shown in Fig. 4.6

The spatio-temporal dynamic heterogeneity of the cancer cell density over time can also be appreciated from the plot shown in Fig. 4.7. The solutions are as expected from the linear stability analysis carried out in the previous section and also in line with the results obtained by Chaplain and Lolas (2005). We note that for parameter set $\mathscr{P}$ the spatially uniform, positive steady state $\mathbf{w}^*$ is unstable (due to the taxis, as previously shown). The initial data given by (4.4) allow the spread of the cancer cells into the domain in a "wave-like" manner. Of course in this case (*i.e.* with parameter set $\mathscr{P}$) no travelling wave exists since the underlying steady state has been destabilised. We note that these results show a spatio-temporal pattern that is very similar to previous simulation results obtained by Wang and Hillen (2007) in a simpler chemotaxis system

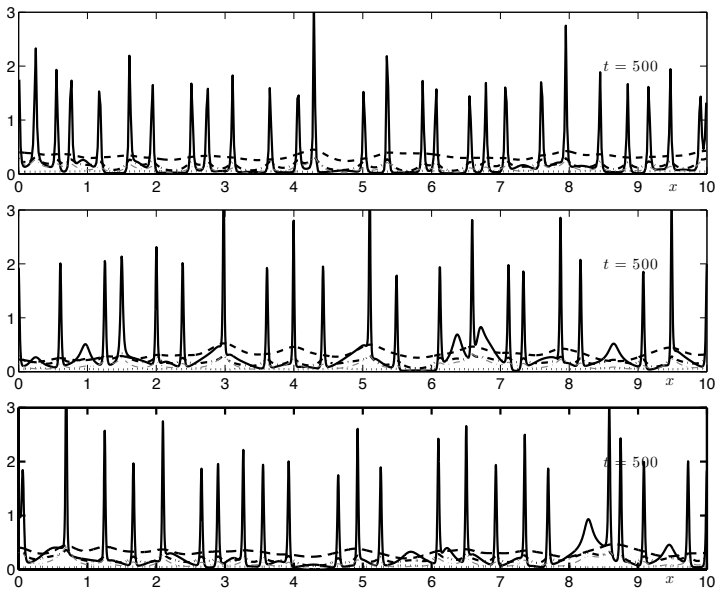

Figure 4.6: Convergence test for the simulation results using different grid spacings taken at time $t = 500$, where (i) top figure is for a simulation with grid spacing $\Delta x = 0.02$, (ii) middle figure with $\Delta x = 0.005$, and (iii) bottom figure with $\Delta x = 0.0025$. The spikes of all simulations have width $0.03 - 0.04$ length units.

where a volume filling term was included in a Keller-Segel model. This approach employed a "squeezing probability" with nonzero cell kinetics that resulted in merging and emerging local peaks. More recently, Hillen and Painter (2009) also obtained a similar pattern of merging and emerging peaks in one of their chemotaxis models incorporating logistic growth for the cell kinetics.

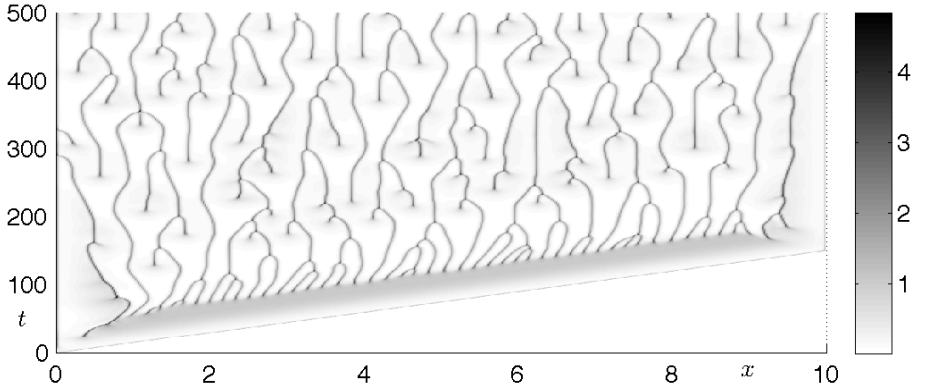

Figure 4.7: Plots showing the spatio-temporal evolution of the cancer cell density c for model (4.3) with parameter set $\mathscr{P}$.

It is useful to compare certain features of these simulations with other simulations where a travelling wave does exist *e.g.*, (furthest) distance travelled into the domain at a given point in time - see, for example, Fig. 4.8. In the case of parameter set $\mathscr{P}$ we note that any initial data that can be considered a perturbation of the steady state will evolve into the observed spatio-temporal heterogeneity.

Effect of Varying the Parameter D_c

During the growth of a solid tumour, over time the cancer cells become more malignant through increased mutations. One important phenotypic consequence of this is that the cancer cells become more motile. This can be reflected in the model by increasing the parameter D_c. In Fig. 4.8, we show the solution profiles of all five solution components of model (4.3) at the fixed time point $t = 70$ for four different values of D_c. As can be seen from the figure plots, increasing the cancer cell random motility parameter D_c leads to smoother solution profiles with less steep "wave" fronts. The increased speed of propagation of the leading edge of the invasive front with increasing D_c is also obvious *i.e.* the higher the value of D_c, the faster into the tissue the cancer cells penetrate.

In Fig. 4.9 we show the evolution of the cancer cell density c over time. In the top and middle plot D_c has a value of 0.014 and 0.00425, respectively, *i.e.*, increased with respect to its base value in parameter set $\mathscr{P}$. In the bottom plot, we have set the cell random motility to zero. Recall that the corresponding plot for D_c as given in $\mathscr{P}$ is shown in Fig. 4.7.

From the top plot in Fig. 4.9, *i.e.*, with $D_c = 0.014$, we observe a travelling wave like solution converging to the homogeneous steady state of the system. Decreasing D_c to a value of 0.00425, we observe that the solution approaches a spatially heterogeneous steady state. When the value of $D_c = 0.00035$ is used, as given in parameter set $\mathscr{P}$, see Fig. 4.7, then a strong and persistent emerging and merging behaviour is

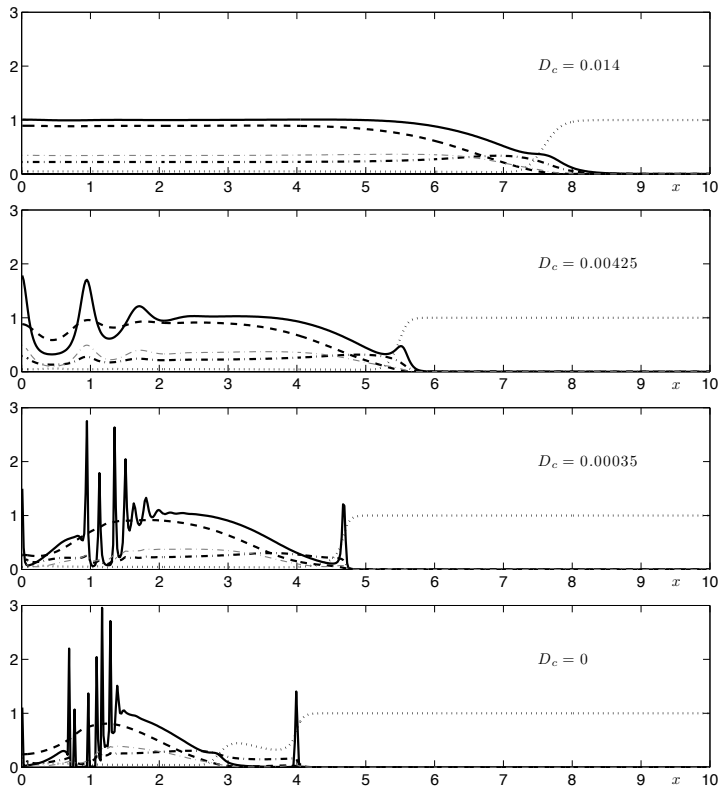

Figure 4.8: Plots showing the profiles of all variables obtained from numerical solutions of model (4.3) at time $t = 70$ with Neumann BCs with parameter set $\mathscr{P}$ but varying cell random motility coefficient D_c. Shown are the cell density c (solid black line), the matrix density v (dotted black line), the uPA concentration u (dash-dotted black line), the PAI-1 concentration p (dashed black line), and the plasmin concentration m (dash-dotted grey thin line). With increasing D_c, the profiles lose heterogeneity and eventually take on a travelling-wave-like solution.

present and no steady state is attained. This type of behaviour is even more pronounced for the case $D_c = 0$, as can be seen from the bottom plot of Fig. 4.9. We also note that the speed of propagation of the "invading wave" decreases with decreasing D_c.

Some insight into the range of spatio-temporal behaviour described above may be provided by the stability/instability diagrams presented in Fig. 4.3 (top left). For smaller D_c values more and more Fourier modes, in particular ones with higher frequencies, are growing with time, *i.e.,* are excited. More precisely, for $D_c = 0.014$ all perturbations of the corresponding spatially homogeneous steady state are damped since this steady state is stable. According to the initial condition chosen, we obtain

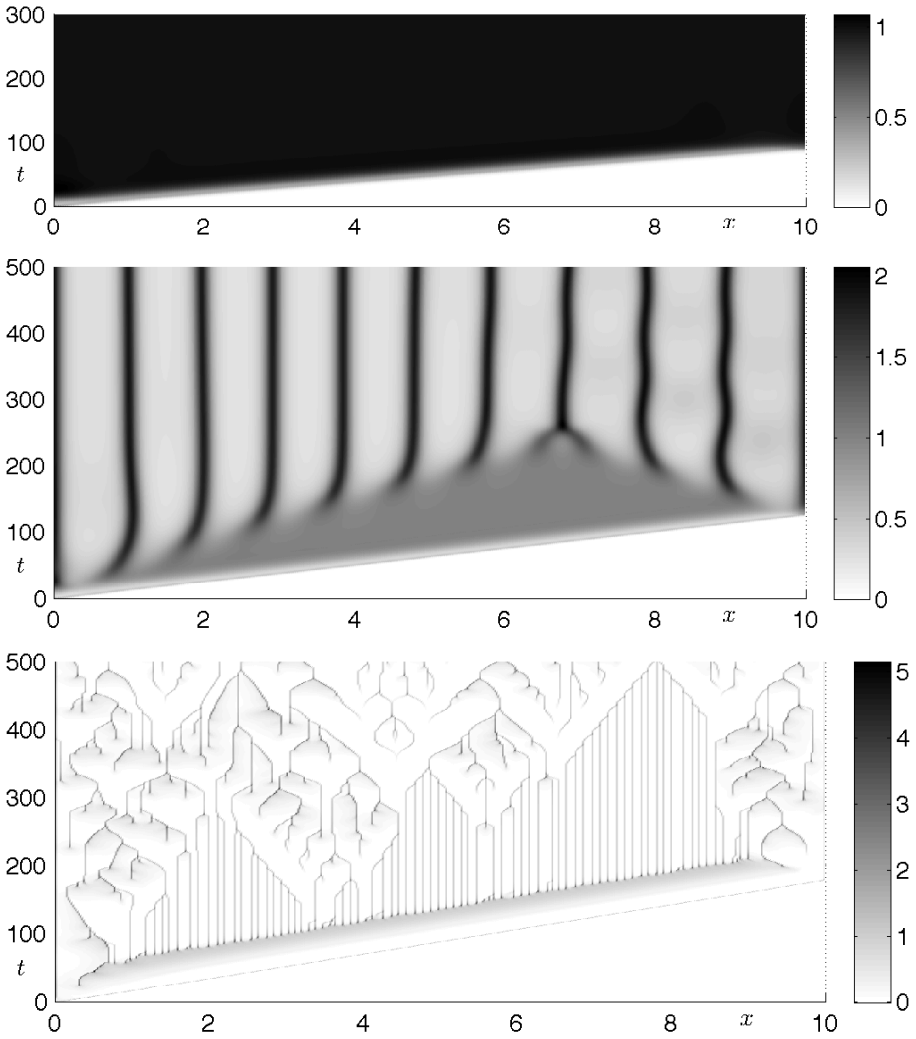

Figure 4.9: Plots showing the spatio-temporal evolution of the cancer cell density c for model (4.3) with parameter set $\mathscr{P}$ and a cancer cell random motility coefficient of (i) $D_c = 0.014$ (top); (ii) $D_c = 0.00425$ (middle) and (iii) $D_c = 0$ (bottom). For $D_c = 0.014$, the solution is shown up to a final time $t = 300$ when the spatially homogeneous steady state has been reached and continues to persist. For $D_c = 0.00425$ and $D_c = 0$, the solution is shown up to a final time $t = 500$.

a travelling wave solution leading to the stable homogeneous steady state of the system. For $D_c = 0.00425$, we observe, for large times, a pattern of equally spaced peaks in the domain $(0,10)$. This is the case of the onset of instability, which is a transition from a heterogeneous solution to travelling wave solution. This transition case is reminiscent of the cosine wave $\cos(20\pi/10 \cdot x)$. By examining the appropriate dispersion relation in Fig. 4.2, small dashed line, we note that the dominating mode is

the one with $\tilde{k} \approx 6.3$, which corresponds, for $M = 10$, to $k = 20$ and hence nicely explains the observed behaviour, *i.e.*, the initial data evolves to a spatially heterogeneous steady state. For $D_c = 0.00035$, the dispersion relation given in Fig. 4.2, solid line, shows a wide range of excited modes. We observe a much more heterogeneous solution and no steady state is reached. An analysis of the relation between the number of excited modes and the observed heterogeneous solution has been provided by Aida et al. (2006). Such a refined analysis has not been attempted for the model under study in this chapter. Nevertheless, the numerical results strongly suggest that an increased number of unstable modes leads to a stronger heterogeneity in the solution.

Effect of Varying the Parameter ϕ_{53}

As was noted in the previous subsection, during the growth of a solid tumour, over time, the cancer cells become more malignant through increased mutations. Another important phenotypic consequence of this is that the cancer cells secrete more matrix degrading enzymes. We reflect this here in our model by increasing the parameter ϕ_{53} of model (4.3) which prescribes the rate of plasmin production due to uPA/uPAR binding (a similar effect is achieved by varying the parameter α_{31}). To avoid the numerical effects of boundaries, we performed the simulations in the domain (0,15).

To see the effect of varying the parameter ϕ_{53} on the evolution of the cancer cell density, initially, at $t = 0$, we set the value $\phi_{53} = 0.1$. This low level of production rate of plasmin is kept until just before $t = 300$, after which we increase the value of ϕ_{53} smoothly to its default value 0.75 (via a smooth step-function) for the rest of the simulation. The corresponding spatio-temporal evolution of the cell density is shown in the top plot of Fig. 4.10. We note that the linear stability analysis carried out in Sect. 4.4 (and corresponding dispersion relations) indicates the changes to be expected by varying ϕ_{53} while keeping other parameters as in parameter set $\mathscr{P}$ and seen in the bottom left plot of Fig. 4.3.

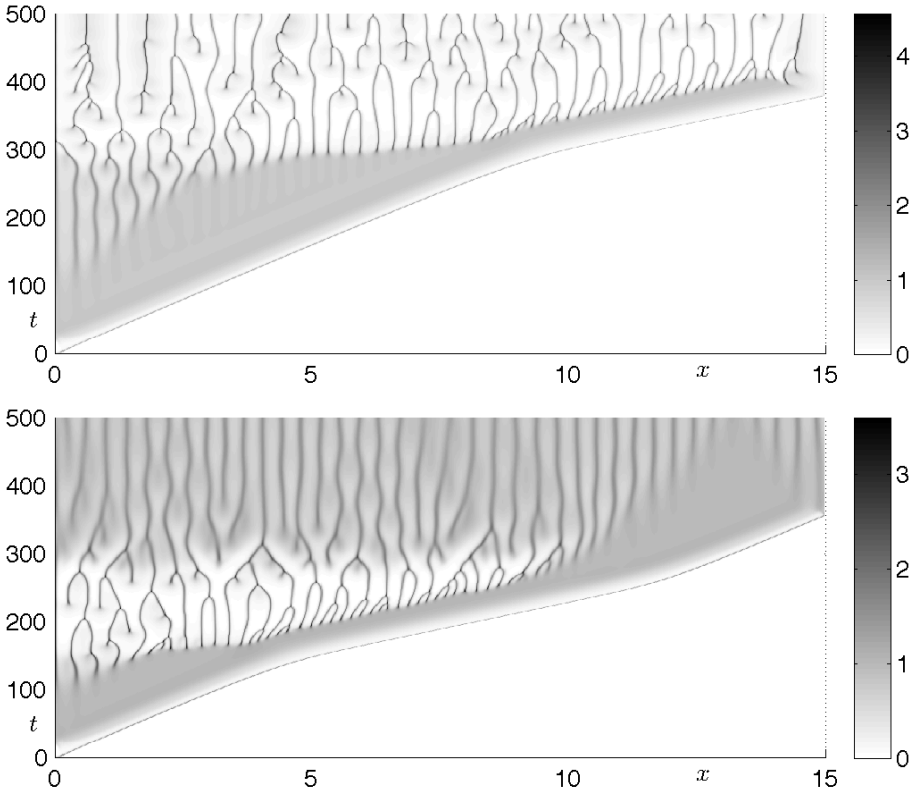

Figure 4.10: Plots showing the spatio-temporal evolution of the cancer cell density c for model (4.3) with parameter set $\mathscr{P}$ in the domain $(0,15)$. (i) Top plot, the parameter ϕ_{53} is increased from 0.1 to 0.75 around $t = 300$. (ii) Bottom plot, the parameter ϕ_{53} is increased from 0.1 to 0.75 around $t = 150$ and then decreased down to 0.1 again at around $t = 250$.

The cancer cell density evolves from the initial data and begins to invade the extracellular matrix. Between $t = 100$ and $t = 200$ we can see equally spaced peaks of cancer cell density appearing in the wake of the invasive front (this corresponds with the prediction of the dispersion relation from the linear stability analysis). At around $t = 300$ (and all subsequent times) we note that the cancer cell density in the wake of the invading front is now highly heterogeneous. Again this computational result confirms the prediction from the dispersion relation, since now $\phi_{53} = 0.75$. We also note a change in the speed of the invasive front when the value of ϕ_{53} is increased from low (0.1) to high (0.75). At lower values of ϕ_{53} the speed of the invasive front is faster than that at higher values of ϕ_{53}. The change in the invasive speed occurs around the switching time of $t = 300$ and can clearly be seen in the top plot of Fig. 4.10.

In the bottom plot of Fig. 4.10, the initial value of $\phi_{53} = 0.1$ is increased smoothly around $t = 150$ until it reaches the default value 0.75 (as prescribed by the parameter set $\mathscr{P}$). After $t = 250$ the value of ϕ_{53} is then smoothly reduced back to 0.1. The figure shows the corresponding change in the nature of the cancer cell density profile. The change of the speed of the invasive front from high to low and back to high again (for the appropriate values of ϕ_{53}) is also observed here.

To see the effects of higher cell random motility in varying ϕ_{53}, we performed simulations with D_c increased to 0.00425. The results are shown in Fig. 4.11. With the smaller values of parameter ϕ_{53}, in the top plot, we see an initial travelling wave solution evolving. At around $t = 40$, we smoothly increase the value of ϕ_{53} to its default value 0.75, where it stays for the remainder of the simulation. From the linear stability analysis, we would expect the underlying spatially homogeneous steady-state to be destabilised and this is indeed what is observed with eventually a final profile the same as that shown in Fig. 4.9 (middle) being attained. This process is then reversed

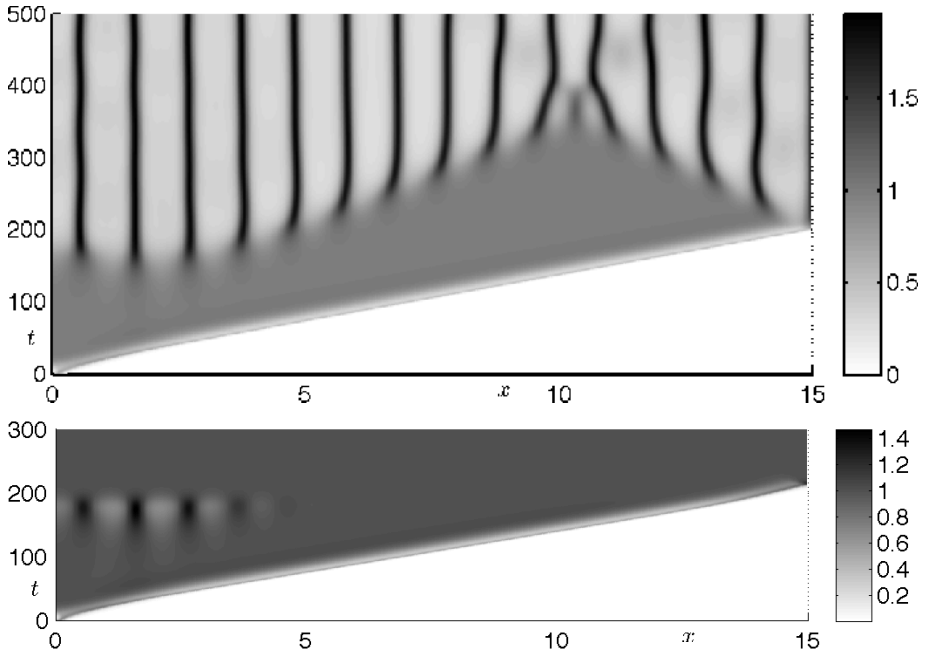

Figure 4.11: Plots showing the spatio-temporal evolution of the cancer cell density c for model (4.3) with parameter set $\mathscr{P}$ and $D_c = 0.00425$ in domain (0,15). In these plots, the parameter ϕ_{53} is (i) increased from 0.01 to 0.75 around $t = 40$ (top) and (ii) then decreased down to 0.01 again at around $t = 180$ (bottom).

by reducing the value of ϕ_{53} smoothly back to 0.01 at around $t = 180$. The resulting solution is visualised in Fig. 4.11 (bottom). From the linear stability analysis, we would expect the spatially homogeneous steady state to have been re-stabilised and this is indeed what we observe from the figure. In this case, *locally in time and space* we see growing perturbations shortly after the switching time $t = 40$. These then decay when ϕ_{53} is reduced again and have disappeared immediately after $t = 180$, leaving a smooth travelling wave profile behind, which drives the solution to its steady state. These simulations confirm the dispersal relation curve shown in the bottom right plot of Fig. 4.3.

Effect of Varying the Parameter μ_1

Similar computational experiments to the previous sub-section can be carried out by varying the cell proliferation parameter μ_1. An increase in the cancer cell proliferation rate is yet another important phenotypic consequence of increased malignancy. In Fig. 4.12 we show the evolution of the cancer cell density c when μ_1 is changed with time (otherwise parameter set $\mathscr{P}$ is used). Initially, we use $\mu_1 = 1.0$, *i.e.* above the threshold for the destabilisation of the steady state, see Fig. 4.3 (middle), and then decrease its value smoothly to $\mu_1 = 0.25$, its default value, around $t = 100$. Accordingly, we observe at first a travelling wave of cancer cells invading the domain. This is followed, after $t = 100$, by the appearance of cancer cell density heterogeneity in the wake of the wave front. The spatio-temporal structure of these solutions would persist for increasing time (not shown) if μ_1 were not changed again. Instead, at around $t = 180$, the value of μ_1 is increased to $\mu_1 = 1.0$ again, leading to a (re-)stabilisation of the steady state. Correspondingly, we observe that the peaks in the cell density are damped away quickly and the solution becomes homogeneous again.

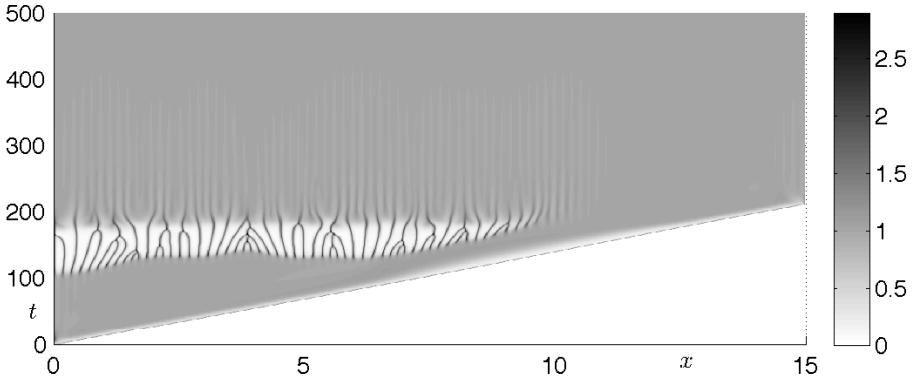

Figure 4.12: Plot showing the spatio-temporal evolution of the cancer cell density c for model (4.3) with parameter set $\mathscr{P}$. The parameter μ_1 is decreased from 1.0 to 0.25 around $t = 100$ and then increased back to 1.0 at around $t = 180$.

Simulation Results for Modified Proliferation Terms

The interactions between cancer cells and the extracellular matrix due to cell movement and proliferation and matrix remodelling result in competition for physical space between the cancer cells and matrix. Since it is considered more realistic biologically and in order to take the effect into account, in this section we modify the proliferation term of cancer cells and remodelling term of the extracellular matrix in (4.3) obeying the spatial restrictions. The equations for cancer cells and the extracellular matrix now become

$$\frac{\partial c}{\partial t} = \underbrace{D_c\nabla^2 c}_{\text{random motility}} - \nabla\cdot\Big[\underbrace{\chi_u c\nabla u}_{\text{uPA-chemo}} + \underbrace{\chi_p c\nabla p}_{\text{PAI-1-chemo}} + \underbrace{\chi_v c\nabla v}_{\text{VN-hapto}}\Big] + \underbrace{\mu_1 c(1-c-v)}_{\text{proliferation}}, \tag{4.16a}$$

$$\frac{\partial v}{\partial t} = -\underbrace{\delta v m}_{\text{degradation}} + \underbrace{\phi_{21} u p}_{\text{uPA/PAI-1}} - \underbrace{\phi_{22} v p}_{\text{PAI-1/VN}} + \underbrace{\mu_2(1-c-v)}_{\text{remodelling}}, \tag{4.16b}$$

subject to the boundary and initial conditions given by (4.4). The modified proliferation terms model the competition for space between cancer cells and matrix. The

cancer cells will grow as long as there is enough space available. The same effect applies to the extracellular matrix, where if the space is limited the extracellular matrix then will remodel back to a normal, healthy level of density.

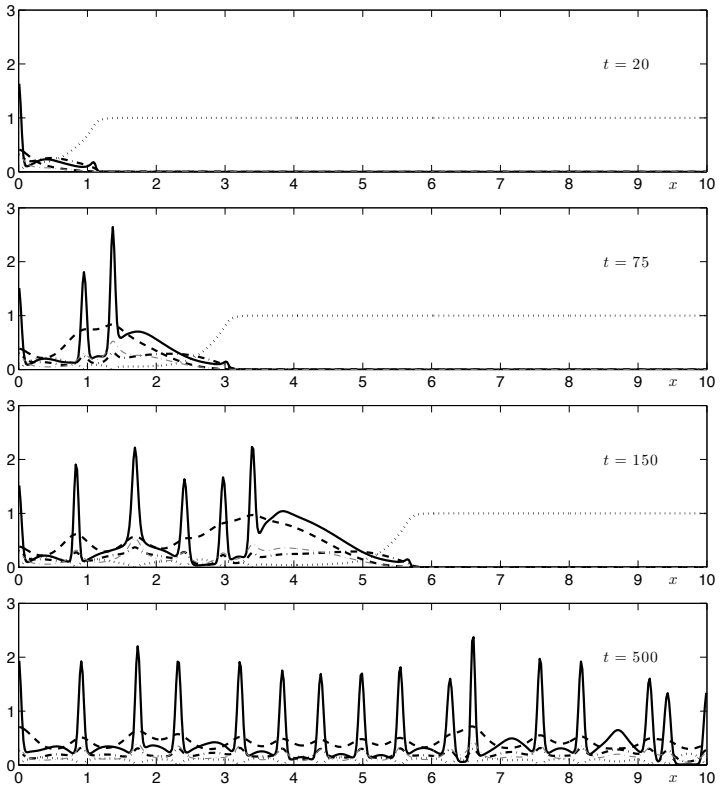

Figure 4.13: Plots showing the spatio-temporal evolution of the cancer cell density c for model (4.3) with modified proliferation and remodelling terms (4.16) on domain $(0, 10)$ with Neumann BCs.

The use of these functional forms of carrying capacity for cell proliferation and matrix remodelling specifically in cancer invasion modelling has been considered previously by Gerisch and Chaplain (2008). We note that the matrix remodelling term here is slightly different to that used in Eq. (4.3b). However, both are qualitatively similar in the sense that, in the absence of cancer cells (*i.e.* normal conditions), matrix will tend to a steady-state value of 1. We have also carried out extensive simulations using both remodelling terms and the precise form does not make any significant difference to the results.

The simulations of the modified system is shown in Fig. 4.13. We observe similar

dynamics as in the previous section. However, comparing solutions in Fig. 4.13 with solutions in Fig. 4.5 we see, for example, that in Fig. 4.5, at $t = 75$ (~ 8.5 days) the cancer cells have already migrated through half of the domain, while in Fig. 4.13 they have migrated appreciably less.

4.5.3 Computational Simulation Results in 2D

In this section we present computational simulation results of our model (4.3) with parameter set $\mathscr{P}$ on a two-dimensional square domain with finite volumes of length $1/50$ for each side of the domain. One of the reasons for doing this was to qualitatively compare our simulation results with experimental data obtained from an *in vitro* organotypic culture model developed to examine the invasiveness of cancer cells into a collagen:matrigel assay (Nyström et al., 2005; Martins et al., 2009). Although our model is formulated in terms of cancer cell invasion of matrix envisaged *in vivo*, it is very difficult to obtain data from *in vivo* systems. Such *in vitro* experimental systems as the collagen:matrigel assay provide an important first step at a qualitative comparison with our model.

Fig. 4.14 shows the results of cancer cell invasion *in vitro* using such an organotypic culture model. The figures show different penetration depths of the extracellular matrix by cancer cells of varying grade. In the top left figure, we have the result using normal cells. The remaining three figures (top right, bottom left and bottom right) show the results using cells isolated from varying grade of tumour *i.e.*, of increasing malignancy. As can be seen from the figures, as the cancer cells increase in malignancy, the depth of penetration into the extracellular matrix increases as does the extent of fragmentation *i.e.*, heterogeneity.

In Fig. 4.15, we present simulation results obtained using the finite volume code for the model (4.3) on the square domain $\Omega = (0,5)^2$ with no-flux boundary conditions. The two figures in the top plots show the initial conditions for the cancer cells and

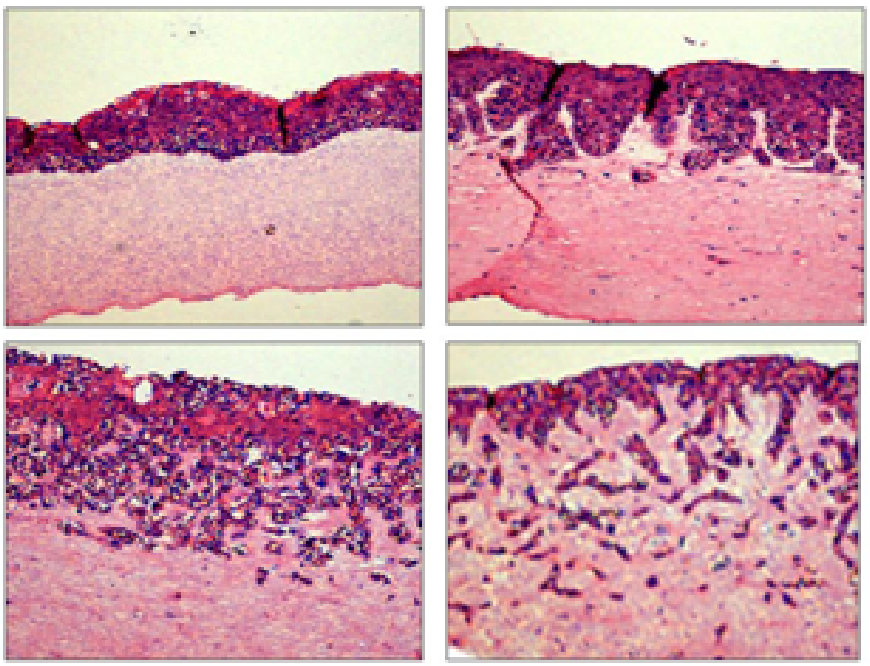

Figure 4.14: Modelling tumour cell invasion *in vitro* using an organotypic culture model reveals the varying extent of tumour mass fragmentation and extracellular matrix penetration. The figures show the depth of penetration into the extracellular matrix and the degree of fragmentation (heterogeneity) of tumour cells of increasing malignancy. Normal cells (top left figure) or cells isolated from varying grade of tumour (top right, bottom left and bottom right figures respectively) were cultured in contact with an extracellular matrix populated with normal stromal cells over a 14 day period. The figures show H&E stained sections from the 3-dimensional culture, highlighting epithelial cells (tumour and normal) forming a multi-layered epithelia with or without extracellular matrix invasion.

matrix - a strip of cancer cells (at a uniform initial density of 1) is placed along the top 20% of the square domain (cf. Fig. 4.14) and the matrix takes up the remaining 80% of the domain. The initial conditions for uPA, PAI-1 and plasmin are as given in (4.5) of Sect. 4.3, *i.e.*, $u(0,\mathbf{x}) = 0.5n(0,\mathbf{x})$, $p(0,\mathbf{x}) = 0.05n(0,\mathbf{x})$, and $m(0,\mathbf{x}) = 0$.

The middle plots of Fig. 4.15 show the simulation results for the cancer cells and matrix using parameter set $\mathscr{P}$. The left hand plot shows the distribution of cancer cells which have invaded most of the domain at $t = 200$ and are heterogeneously distributed throughout *i.e.*, a lot of fragmentation. Matrix distribution (right hand plot) is correspondingly fragmented and heterogeneous. These results may be compared with the

experimental data for the most malignant cancer cells shown in Fig. 4.14, bottom right plot, where we observe a large degree of cancer cell invasion and extracellular matrix degradation and heterogeneity.

Finally, the bottom plots of Fig. 4.15 show the simulation results for the cancer cells and matrix using a modified parameter set, reflecting a less malignant cancer cell population *i.e.*, the diffusion coefficient $D_c = 2.5 \cdot 10^{-4}$, haptotactic coefficient $\chi_v = 0.01425$, cell proliferation rate $\mu_1 = 0.1$, matrix degradation rate $\delta = 4.15$, and production of plasmin $\phi_{53} = 0.45$. The left hand plot shows the distribution of cancer cells at $t = 200$. In contrast with the middle plot, in this case the cancer cells have penetrated the extracellular matrix to a lesser degree and there is less heterogeneity (fragmentation). Correspondingly the extracellular matrix is less degraded. Once again, these results may be compared with the experimental data for the less malignant cancer cells shown in Fig. 4.14, bottom left plot, where we observe lesser cancer cell and matrix heterogeneity. Although our computational results qualitatively match the experimental data, we cannot be certain objectively of the mechanism responsible for the pattern. For example, a diffusion-driven instability may well play some role or reduced cell-cell adhesion.

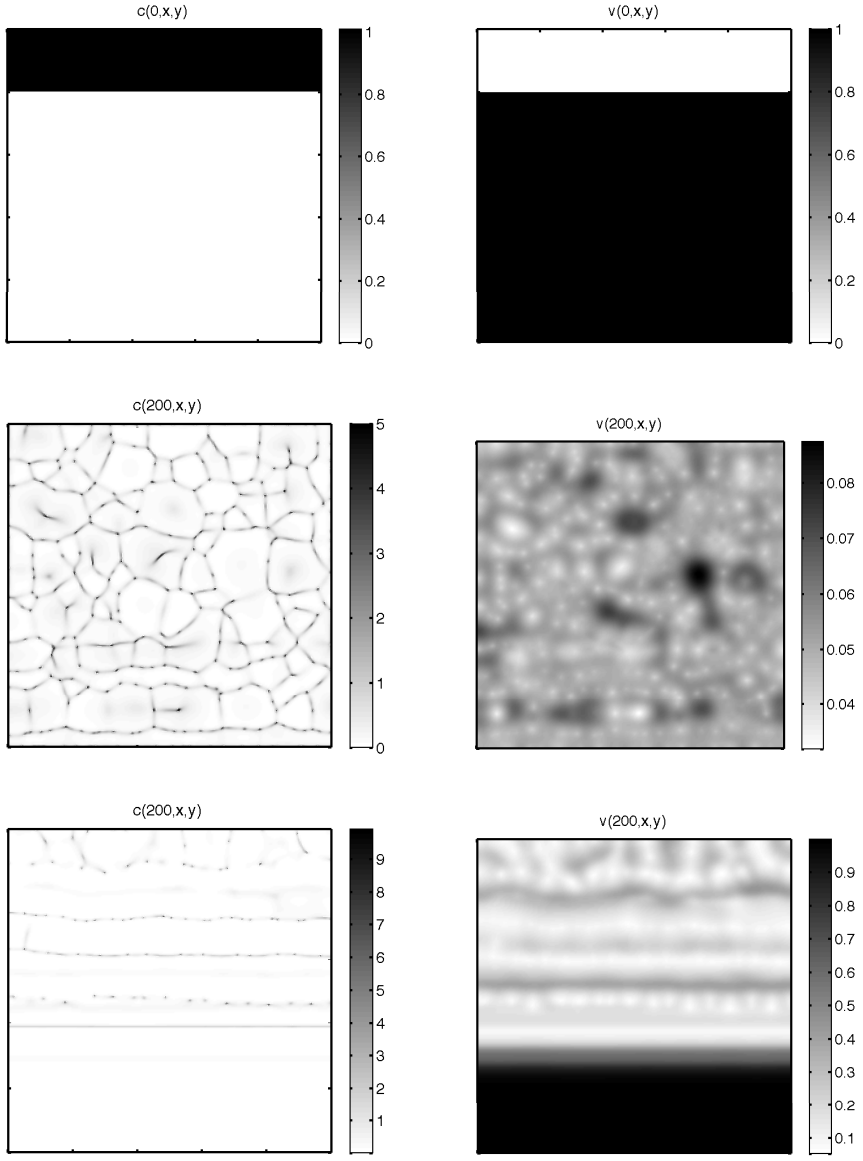

Figure 4.15: Plots showing the distribution of the cancer cell density $c(t,x,y)$ and matrix density $v(t,x,y)$ in a square domain $\Omega = (0,5)^2$. The top plots show the initial conditions, with cancer cells taking up one fifth of the domain (top left) and matrix occupying the rest of the domain (top right). The middle plots show the cancer cell (left) and matrix (right) densities at $t = 200$ using parameter set $\mathscr{P}$. The cancer cells have invaded the extracellular matrix in a very heterogeneous (fragmented) manner and penetrated almost to the lower boundary. The bottom plots show the cancer cell (left) and matrix (right) densities at $t = 200$ using a modified parameter set reflecting a less aggressive cancer cell phenotype – $D_c = 2.5 \cdot 10^{-4}$, $\chi_v = 0.01425$, $\mu_1 = 0.1$, $\delta = 4.15$, $\phi_{53} = 0.45$ (all other parameters unchanged from parameter set $\mathscr{P}$). In this case, the cancer cells have penetrated the extracellular matrix to a lesser degree and there is less heterogeneity (fragmentation). These simulations qualitatively mirror the experimental results shown in Fig. 4.14.

4.6 Discussion and Conclusions

In this chapter we have investigated, analytically and numerically, a mathematical model of cancer cell invasion of tissue (extracellular matrix) first presented in Chaplain and Lolas (2005). The biological focus of the model is the urokinase plasminogen activation (uPA) system but it is conceivable that similar results could be obtained by focusing on alternative matrix/protease dependent remodelling systems such as those associated with transforming growth factor-β activation (Jenkins, 2008). Our main contribution and finding is the observation of a very rich ("dynamic") spatio-temporal heterogeneity of the solutions. The linear stability analysis and computational simulations suggest that this may be due to a taxis-driven instability of the spatially homogeneous, positive steady state of the model, cf. (Keller and Segel, 1970; Pearce et al., 2007) (although we have not proved this). This in turn, leads to a very interesting and challenging open question to understand fully these "merging and emerging" dynamics. Furthermore, in this chapter we have shown that by varying key parameters of the model, the qualitative character of the solution—either of travelling-wave-like form or heterogeneous dynamics—can be changed. The prevalent character of the solution for a given parameter set can be predicted by examining dispersion relations (such as those shown in this chapter) derived from a linear stability analysis of the system.

Examples of the two different "types" of invasion by cancer cells observed here can be seen not only using laboratory based experimental models of cancer cell invasion, but also directly in clinical samples and certainly have implications for cancer treatment. In the case of "dynamic heterogeneity", a surgical removal of the tumour is made considerably more complicated and difficult due to the dissemination of small and individual tumour cell clusters in the tissue space, *i.e.*, a breakup of an initially compact tumour mass. Here the danger is that surgery leaves some of those tumour cell clusters behind which then are the starting point for a re-establishment of the disease or that this departure of cells from the primary tumour mass leads directly to

metastasis (Lindemann et al., 1992; Izbicki et al., 1997).

In the second type of behaviour, the travelling-wave-like regime, the tumour mass remains compact and can be more easily recognised as a whole and removed as such by the surgeon. However, with the parameters considered here, the tumour is still growing in this regime. We also note that in this case, although the tumour remains as a compact mass, the distance penetrated into the tissue is greater (since the wave speed is greater cf. Figure 4.8). One may draw the general conclusion that manipulation of the tumour microenvironment (Sutherland, 1988; Anderson et al., 2006), for example through the oxygen/nutrient supply to the tumour (and with a subsequent effect on cancer cell proliferation, migration, and enzyme production), may have a major impact on invasion. Different tumour types may possess varying abilities to maintain growth in the absence of oxygen/nutrient supply and different tumour types may evolve the ability to vascularise and re-supply the growing tumour mass. Rapid tumour growth either in a dynamic heterogeneic or a traveling-wave-like manner has the potential to lead to further evolution of the tumour but it is metastasis, not proliferation which results in cancer mortality (Sporn, 1996). The act of cells breaking out and leaving the primary tumour site remains the most deadly trait. The extent of invasion depth has long been correlated with poor prognosis (Breslow, 1970) and laboratory modelling and measurement of invasion tend to describe data more similar to the dynamic heterogeneic regime of invasion as "more aggressive" (Nyström et al., 2005) and Fig. 4.14.

In terms of future work and model development, we note that the model considered in this chapter has some limitations. Future work will deal with these and now we comment on these briefly.

In the original paper of Chaplain and Lolas (2005) an additional proliferation term $+\phi_{13}cu$ is present in the cancer cell equation of the model but is not considered here. This term models additional cancer cell proliferation as a result of signal pathways that are activated by uPA/uPAR binding. Such a dependence could be included in the

model by allowing the cancer cell proliferation rate μ_1 to depend on the uPA concentration u. Other effects of the uPA system which are observed biologically will also be considered for inclusion in the model. This critical review is expected to lead to a more focused/streamlined model of the kinetics. Other extensions of the present model would be to include explicitly an equation for oxygen/nutrient supply to the cancer cells (Sherratt and Chaplain, 2001) and to account in detail for effects of both cell-cell and cell-matrix adhesion. Although this effect has been modelled previously using discrete techniques (Anderson, 2005; Turner and Sherratt, 2002), an interesting approach using PDEs and continuum models has recently been developed by Gerisch and Chaplain (2008) building on initial work of Armstrong et al. (2006). In this approach, nonlocal terms in the PDE system are used to model the cell-cell and cell-matrix interactions, resulting in a system of integro-differential equations (Gerisch and Chaplain, 2008; Painter et al., 2010).

Using this refined approach, coupled with accurate parameter estimation, it should be possible to develop a mathematical model of cancer invasion that assesses invasion objectively and provides a numerical "Invasion Index" (Nyström et al., 2005; Martins et al., 2009). The simulations presented in Fig. 4.15 show that such a mathematical model can provide information regarding both the depth and pattern of invasion, two key features of cancer cell invasion. By varying parameter values, the mathematical model is capable of indicating how various factors influence invasion. Future work in this direction will require a careful estimate of parameter values in the collagen:matrigel assay and a more detailed experimental investigation of the biochemical processes involving the matrix degrading enzymes.

Finally, we note that since cancer is a progressive disease (Hanahan and Weinberg, 2000; MacSween, 2003), with the cancer becoming more malignant as the cancer cells

undergo successive mutations, an interesting development of the model would be to reflect this important aspect by introducing a "mutation pathway" into the model at a phenotypic level, whereby different sub-populations of increasingly malignant cells appear over time, Spremulli and Dexter (1983); Heppner (1984); Enderling et al. (2007). An indication of how a model of this type with two cancer cell sub-populations, having densities c_1 and c_2, respectively, might be implemented is given below:

$$\frac{\partial c_1}{\partial t} = \underbrace{D_{c_1}\nabla^2 c_1}_{\text{random motility}} - \nabla\cdot\Big[\underbrace{\chi_{u1}c_1\nabla u}_{\text{uPA-chemo}} + \underbrace{\chi_{p1}c_1\nabla p}_{\text{PAI-1-chemo}} + \underbrace{\chi_{v1}c_1\nabla v}_{\text{VN-hapto}}\Big] + \underbrace{\mu_{1,1}c_1(1-c)}_{\text{proliferation}} - \underbrace{\lambda c_1 F(t,v)}_{\text{conversion to } c_2}, \tag{4.17a}$$

$$\frac{\partial c_2}{\partial t} = \underbrace{D_{c_2}\nabla^2 c_2}_{\text{random motility}} - \nabla\cdot\Big[\underbrace{\chi_{u2}c_2\nabla u}_{\text{uPA-chemo}} + \underbrace{\chi_{p2}c_2\nabla p}_{\text{PAI-1-chemo}} + \underbrace{\chi_{v2}c_2\nabla v}_{\text{VN-hapto}}\Big] + \underbrace{\mu_{1,2}c_2(1-c)}_{\text{proliferation}} + \underbrace{\lambda c_1 F(t,v)}_{\text{conversion from } c_1}, \tag{4.17b}$$

where c denotes the total cell density, $c := c_1 + c_2$, and the conversion function F is a product of two Heaviside functions,

$$F(t,v) = H(t-50)\cdot H(v-0.3)\,. \tag{4.18}$$

In the above model, we have assumed that the cancer cells of sub-population 1 are converted into cancer cells of sub-population 2 after $t = 50$ and only in regions with sufficiently high matrix density $v > 0.3$. The differences between the two sub-populations are (i) in the diffusion coefficients – cancer cells of sub-population 2 diffuse faster than cancer cells of sub-population 1, *i.e.* $D_{c_2} > D_{c_1}$ (ii) in the proliferation rates – cells of sub-population 2 proliferate more rapidly than cells of sub-population 1, *i.e.* $\mu_{1,2} > \mu_{1,1}$, (iii) in the chemotactic and haptotactic constants – more aggressive cancer cells migrate more quickly *i.e.* $\chi_{u2} > \chi_{u1}$, $\chi_{up} > \chi_{p1}, \chi_{v2} > \chi_{v1}$. The other equations for the extracellular matrix, uPA, PAI-1, and plasmin remain unchanged from

system (4.3).

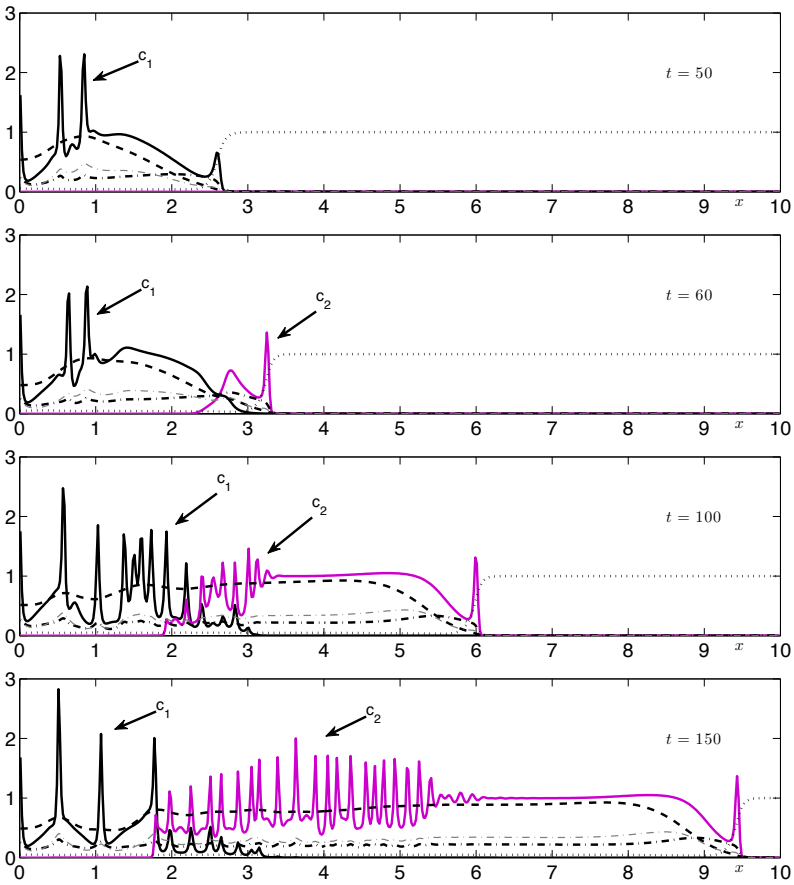

Figure 4.16: Plots showing the spatio-temporal evolution of the solution profiles of all variables of our extended model with two sub-populations of cancer cells c_1 and c_2. Solution profiles are shown for times $t = 50, 60, 100$, and 150 using parameter set $\mathscr{P}^*$. The density of cancer cells of sub-population 1 is denoted by the solid black line, the density of the more aggressive cancer cells of sub-population 2 by the solid magenta line, the matrix density by dotted black line, the uPA concentration by dash-dotted black line, PAI-1 concentration by dashed black line, and plasmin concentration by dash-dotted grey thin line.

Fig. 4.16 shows the results of a computational simulation of the above 2 equations along with the uPA-system equations from model (4.3) using new values of the

following parameters, we refer to as parameter set $\mathscr{P}^*$

$$
\begin{aligned}
&D_{c_1} = 3.5 \cdot 10^{-4}, && D_{c_2} = 2.5 \cdot 10^{-4}, \\
&\mu_{1,1} = 0.25, && \mu_{1,2} = 0.75, \\
&\chi_{u1} = 2.05 \cdot 10^{-2}, && \chi_{u2} = 3.05 \cdot 10^{-2}, \\
&\chi_{p1} = 2.75 \cdot 10^{-2}, && \chi_{p2} = 3.75 \cdot 10^{-2}, \\
&\chi_{v1} = 1.85 \cdot 10^{-2}, && \chi_{v2} = 2.85 \cdot 10^{-2}, \\
&\lambda = 0.3,
\end{aligned}
$$

and the rest of parameter values remains the same as parameter set $\mathscr{P}$ given in Table 4.1.

As is to be expected, for $t < 50$ the solutions evolve as in Fig. 4.16, first plot. After $t = 50$ there is some conversion from sub-population 1 to sub-population 2 at the leading edge of the invading front and so by $t = 60$ cancer cells of sub-population 2 are visible (second plot). As time increases, the more aggressive sub-population 2 gradually replaces the less aggressive sub-population (third and fourth plots). Furthermore, we observe an increase in the speed of invasion of the matrix by the more aggressive sub-population 2.

The results of the proposed model extension shown above indicate the potential for predicting the spatio-temporal evolution of an invasive cancer consisting of several heterogeneous sub-populations that differ in many phenotypic characteristics. Clinically, the different sub-populations within a primary tumour may give an impact on the design of treatment protocols to predict individual chemotherapy for cancer patients (Spremulli and Dexter, 1983).

Chapter 5

Modelling the Role of Cell Adhesion in Cancer Invasion

5.1 Introduction

Intercellular adhesion has long been recognised to be a fundamental biological process in many aspects of developmental biology. The binding and unbinding mechanisms are also particularly important in cancer progression by which the malignant cells detach from the primary tumour mass and spread throughout the surrounding tissues and to anatomically distant parts of the body. There is growing evidence that cell adhesion through cell adhesion proteins is implicated in cancer invasion and metastasis (Yamada, 1983; Jiang, 1996; Pignatelli, 1998; Mizejewski, 1999; Hazan et al., 2000; Kase et al., 2000; Aken et al., 2001; Irby and Yeatman, 2002; Kowalski et al., 2003; Cavallaro and Christofori, 2004; Heyder et al., 2005; Sawada et al., 2008; Paschos et al., 2009; Schmalhofer et al., 2009; Brooks et al., 2010; Hsu et al., 2010; Huang et al., 2010; Mao et al., 2010).

After undergoing genetic and epigenetic changes, malignant and invasive tumour cells, *i.e.*, cancer cells, break away from the primary tumour mass by losing adhesion

with one another and dissociating from any adjacent cells. Cancer cells then need to, (i) push their way through the basement membrane, which is a meshwork of protein that creates a barrier for cell movement and, (ii) migrate through the ECM surrounding the tumour epithelium. The degradation of the basement membrane and the ECM is necessary for removing any physical obstacles in the direction of cell movement. This process is performed by the activity of proteolytic enzymes, and the major one responsible for ECM degradation (and remodelling) is the urokinase-type plasminogen activator (uPA). Following ECM degradation, cancer cells are now able to migrate through the extracellular matrix mediated by adhesion between other cells and matrix.

After analysing the model of cancer cell invasion tissue based on the uPA system that we presented in the previous chapter (Chapter 4), here we discuss the incorporation of cell-cell and cell-matrix adhesion processes in the uPA model. The extended model consists of a system of partial differential equations with reaction-diffusion taxis terms accounting for uPA system and new non-local (integral) terms for cell-cell and cell-matrix adhesion.

5.2 Cell Adhesion in the uPA System

Molecular interactions are clinically proven to be critical in the metastatic cascade, defined as the progression from a primary, single tumour to secondary tumours at anatomically distant sites throughout the body. The interactions in the metastatic cascade consist of several major steps: (1) the development of capillary blood vessels nearby a primary tumour that crucially supply the tumour with vital nutrient and help to dispose of waste product; (2) the detachment of tumour cells from the primary tumour mass; (3) destruction of the basement membrane and invasion of the extracellular matrix (ECM) components by over-expression of proteolytic enzymes such as urokinase-type plasminogen activator (uPA), and migration through the matrix; (4) intravasation of the tumour cells into the blood vessels and lymphatic vessels which gains them access

to the circulatory system to travel to distant anatomical sites; (5) adhesion of the circulating tumour cells to the endothelial cell lining at the capillary bed of the target organ site; (6) invasion of the basement membrane and target organ tissue; and (7) the growth of secondary tumours at the target organ site (Guo and Giancotti, 2004; Brooks et al., 2010).

For cells of epithelial tissue origin, several steps in this cascade are dependent on cell adhesion mechanisms and proteolytic activities for local invasion of malignant cells of basement membrane and matrix around them. Tumour cells that have gained invasive properties start to detach from the primary tumour mass triggered by loss of cell-cell adhesion, particularly adhesion between cells at the edge or outer layer of the tumour body. The next step for the cells is migration through the tissue before reaching the vascular or lymphatic system for further circulation. To enable migration, the matrix must be degraded, as well as be remodelled, and there must be attachment of cells to the matrix. These processes requires pericellular proteolytic activities of matrix components mainly carried out by uPA and enhancement of cell-matrix adhesion for cell movement (Ellis et al., 1992). The association of uPAR with cell-matrix adhesion components integrins has been studied by Xue et al. (1997) in connection with directional proteolysis for cancer cell migration in fibrosarcoma. Stahl and Mueller (1997) studied the influence of the uPA and its receptor (uPAR) on melanoma cell adhesion to, and migration on, the extracellular matrix protein vitronectin (VN). Their experimental data showed the involvement of the components of the uPA system in direct regulation of cell adhesion and migration, modulating the behaviour of malignant tumour cells.

5.3 Mathematical Model

Continuum mathematical models incorporating (in some way) cell adhesion that describe the interactions either between cells or between cells and extracellular matrix have been proposed by Greenspan (1976); Bell et al. (1984); Evans (1985a,b); Bell

and Torney (1985); Hammer and Lauffenburger (1987); DiMilla et al. (1991); Xiao and Truskey (1996); Byrne and Chaplain (1996); Byrne (1997); Byrne and Chaplain (1997); Palecek et al. (1999); Cristini et al. (2005); Zheng et al. (2005); Macklin and Lowengrub (2007); Cristini et al. (2009); Macklin et al. (2009); Frieboes et al. (2010). A comprehensive review of some of these papers may be found in Lowengrub et al. (2010). However, in most of these models adhesion was incorporated via a boundary condition as a surface tension-like force. A model that used a continuum approach to model the role of adhesion in cell sorting behaviour was developed by Armstrong et al. (2006). The model describes the movement of cells as a result of adhesive forces generated due to binding and unbinding events of a cell to neighbouring cells. The adhesive forces are presented in the partial differential equations themselves in a (non-local) term explicitly describing cell adhesion. The idea was then used by Gerisch and Chaplain (2008) to model cancer invasion of tissue incorporating cell-cell and cell-matrix adhesion. Later Painter et al. (2010) used the model for modelling processes such as cancer invasion and development on heterogeneous matrix, where the movement is only driven by cell-cell and cell-matrix adhesion.

As it has been clear that cellular invasion depends on cooperation between adhesive and proteolytic mechanisms, it is our aim here to account for cell adhesion in the cancer cell invasion model, where cell motility is now also governed by movement due to cell adhesion. We do this by replacing the haptotactic term in Eq. 4.2a of Chapter 4 with a term that incorporates adhesive movement caused by forces that are generated when there occurs binding or unbinding events between cell-cell and between cell-matrix. The factors that drive cancer cell migration now consist of random motion, chemotaxis due to uPA and PAI, and adhesive movement. The rate of change of cell density in full

dimensional form is given by,

$$\frac{\partial c}{\partial t} = \underbrace{D_1\nabla^2 c}_{\text{random motility}} - \underbrace{\nabla\cdot(c\mathscr{A}\{\mathbf{w}(t,\cdot)\})}_{\text{adhesive movement}} - \underbrace{\nabla\cdot(c\xi_u(\mathbf{w})\nabla u)}_{\text{uPA-chemotaxis}} - \underbrace{\nabla\cdot(c\xi_p(\mathbf{w})\nabla p)}_{\text{PAI-1-chemotaxis}} + \underbrace{\sigma_1 c\left(1-\frac{c}{c_0}\right)}_{\text{proliferation}}. \tag{5.1}$$

The advection term $\mathscr{A}\{\mathbf{w}(t,\cdot)\}$ represents the so-called adhesion velocity and is referred to as "nonlocal". For our continuum approach we adapt the form for $\mathscr{A}\{\mathbf{w}(t,\cdot)\}$ introduced by Armstrong et al. (2006). This form has been studied and applied in various cancer models (Gerisch and Chaplain, 2008; Sherratt et al., 2009; Painter et al., 2010), and is given by

$$\mathscr{A}\{\mathbf{w}(t,\cdot)\} := \frac{1}{R}\int_S \frac{\mathbf{r}}{|\mathbf{r}|}\, g(\mathbf{w}(t,\mathbf{x}+\mathbf{r}))\Omega(r)d\mathbf{r}. \tag{5.2}$$

The integrand consists of three components: (i) the direction of the force denoted by the unit outer normal vector $\frac{\mathbf{r}}{|\mathbf{r}|}$, (ii) the radial dependency function $\Omega(r)$, and (iii) a function $g(\mathbf{w}(t,\mathbf{x}+\mathbf{r}))$ that describes the nature of the forces and depends on the vector concentration $\mathbf{w}$.

For 1D spatial domains the forces generated through adhesive binding affect the points in the right ($\frac{\mathbf{r}}{|\mathbf{r}|}=1$) or left ($\frac{\mathbf{r}}{|\mathbf{r}|}=-1$) direction of the Cartesian coordinate axis. In 2D domains the force is sensed by points within a circle or radius r, hence the position vector $\mathbf{r}$ in polar coordinates $\mathbf{r} = r(\cos\theta,\sin\theta)^T$ and its magnitude $|\mathbf{r}| = r$.

The function $\Omega(r)$ describes how strong the adhesion velocity $\mathscr{A}\{\mathbf{w}(t,\cdot)\}$ is influenced by points of the sensing region at $\mathbf{x}$ depending on their distance $\mathbf{r}$ from $\mathbf{x}$. Adhesive bindings are strong nearer to $\mathbf{x}$ and become weaker at distances further away. Therefore, in 1D $\Omega(r)$ should be an odd function of $\mathbf{r}$ with $\Omega(r) > 0$ for $\mathbf{r} > 0$ and $\Omega(r) < 0$ for $\mathbf{r} < 0$ (Armstrong et al., 2006). The simplest form $\Omega(r)$ that can be considered is a step function describing a constant magnitude of the force sensed by cells, either closer or further away from the force-generating cells within a sensing radius

(Armstrong et al., 2006; Painter et al., 2010), *i.e.*,

$$\Omega_1(r) = 1 \quad \text{for} \quad -R < r < R, \tag{5.3}$$

where $R = \max(r)$ is the sensing radius of the cells.

Gerisch and Chaplain (2008) consider normalised forms of $\Omega(r)$ in which its integral over the sensing region is one, *i.e.*,

$$\int_0^R 2\Omega(r)d\mathbf{r} = 1 \qquad \text{or} \qquad \int_0^R 2\pi r\Omega(r)d\mathbf{r} = 1\,,$$

for 1D and 2D, respectively. This leads to the constant form in 1D

$$\Omega_2(r) = \frac{1}{2R}\,, \tag{5.4}$$

and for 2D

$$\Omega_2(r) = \frac{1}{\pi R^2}\,. \tag{5.5}$$

The second form of $\Omega(r)$ considered in Gerisch and Chaplain (2008) is a function that linearly decreases to $\Omega(R) = 0$ with increasing distance from the centre. For 1D

$$\Omega_3(r) = \frac{1}{R}\left(1 - \frac{r}{R}\right)\,, \tag{5.6}$$

and for 2D is given by

$$\Omega_3(r) = \frac{3}{\pi^2 R}\left(1 - \frac{r}{R}\right)\,. \tag{5.7}$$

Since the adhesion involves forces between cancer cells (cell-cell adhesion) and between cancer cells and extracellular matrix (cell-matrix adhesion), we take $g(\mathbf{w}(t, \mathbf{x} + \mathbf{r}))$ as function of c and v. For convenience, we write $g(c, v)$. At its simplest, it could take a linear form,

$$g(c, v) = S_{cc}c(\mathbf{x} + \mathbf{r}) + S_{sc}v(\mathbf{x} + \mathbf{r})\,, \tag{5.8}$$

where S_{cc} and S_{cv} are constants that account for the strength of cell-cell and cell-matrix adhesion, respectively. The linear forms imply continuous generation of stronger adhesive force even at higher densities, eventually leading to movement of cells at very

high density. This scenario cannot be supported from an experimental point of view, as at high densities cells may form steady colonies or clusters that keep growing in size rather than conducting migration (Zantek and Kinch, 2001). This suggests that at high densities the cells are prevented from moving due to crowding and lack of space for cells to perform orientation. Therefore we consider a form for $g(c,v)$ that is more realistic by including a spatial restriction, where the cells aggregate and move only if there is space locally available. In our model the cells share the physical space with other components like the ECM, uPA, PAI-1, and plasmin. We assume that the chemical substances uPA, PAI-1, and plasmin subsume into the space occupied by the ECM. Now in one unit volume of the physical space there are cells that occupy a fraction ϑ_1 of the space and the ECM that takes another fraction ϑ_2,

$$f_s \approx \vartheta_1 c + \vartheta_2 v\,.$$

The total fraction f_s should be positive and must not be higher than a threshold density. An appropriate choice is $0 \leq f_s \leq 1$. If the space is densely occupied (either by the cells or ECM or by both combined) with $\vartheta_1 c + \vartheta_2 v \approx 1$, the self-limiting process should operate, giving

$$g(c,v) = (S_{cc}c + S_{sc}v)\,(1 - \vartheta_1 c - \vartheta_2 v)^+\,, \tag{5.9}$$

where the new form with a factor $(1-\vartheta_1 c-\vartheta_2 v)^+ := \max\{0,(1-\vartheta_1 c-\vartheta_2 v)\}$ ensures that the force that is generated is limited by densities of cells and matrix.

In the basic cancer invasion model analysed in Chapter 4 we consider a constant form for the chemotactic sensitivity coefficients $\xi_u(\mathbf{w}) = \xi_u$ and $\xi_p(\mathbf{w}) = \xi_p$. The chemotactic function was introduced by Patlak in 1953 and later by Keller and Segel (1970) to describe the aggregation of slime mould amoebae towards high concentrations of a chemical substance using two coupled parabolic equations. The model has been intensively studied in mathematical biology since then. The constant form of ξ_u means that the gradient of ∇u is multiplied by a linear instead of a nonlinear function.

This is similar to the linear form of the function $g(c,v)$ in Eq. 5.8. A feature of this choice is the fact that it may lead to mathematically finite time blow-up or "overcrowding" scenarios, where the solutions become unbounded. Whether the blow-up situations occur or not typically depends on the initial conditions and the space dimension d. The conditions for blow-up as well as the existence and uniqueness of solutions for specific forms of chemotactic sensitivity coefficient $\xi(\cdot)$ have been derived by a large number of authors, for example Jäger and Luckhaus (1992); Herrero and Velázquez (1996); Hortsmann and Wang (2001).

Although many have tried to interpret blow-up situations from a biological point of view, the linear form can also pose difficulty for numerical simulations. Therefore we opt for a form that includes assumptions for spatial restrictions, such as by limiting the movement of cells at relatively high densities. One of the possibilities to achieve this is by switching off the chemotactic response if the cell density becomes high, preventing cells from moving into dense regions. Such a mechanism, also called "overcrowding prevention" or "volume filling", has been studied by Hillen and Painter (2001); Painter and Hillen (2002) and references therein. This takes the same form as for the $g(c,v)$ function as in Eq. 5.9 and the chemotactic sensitivity coefficients $\xi_u(\mathbf{w})$ and $\xi_p(\mathbf{w})$ are now given by:

$$\xi_u(\mathbf{w}) = \xi_u(1-\vartheta_1 c - \vartheta_2 v) \qquad \text{and} \qquad \xi_p(\mathbf{w}) = \xi_p(1-\vartheta_1 c - \vartheta_2 v)\,. \tag{5.10}$$

We write down the system of equations in full dimensional form as

$$\begin{aligned}
\frac{\partial c}{\partial t} &= \underbrace{D_1\nabla^2 c}_{\text{random motility}} \underbrace{-\nabla\cdot\left(\frac{c}{R}\int_S \frac{\mathbf{r}}{|\mathbf{r}|}(S_{cc}c+S_{cv}v)(1-\vartheta_1 c-\vartheta_2 v)\Omega(r)d\mathbf{r}\right)}_{\text{adhesive movement}} \\
&\quad \underbrace{-\nabla\cdot(\xi_u c(1-\vartheta_1 c-\vartheta_2 v)\nabla u)}_{\text{uPA-chemotaxis}} \underbrace{-\nabla\cdot(\xi_p c(1-\vartheta_1 c-\vartheta_2 v)\nabla p)}_{\text{PAI-1-chemotaxis}} \\
&\quad \underbrace{+\sigma_1 c\left(1-\frac{c}{c_0}\right)}_{\text{proliferation}}, \qquad (5.11a)
\end{aligned}$$

$$\frac{\partial v}{\partial t} = \underbrace{-\beta v m}_{\text{degradation}} \underbrace{+\Phi_{21}up}_{\text{uPA/PAI-1}} \underbrace{-\Phi_{22}vp}_{\text{PAI-1/VN}} \underbrace{+\sigma_2 v(1-\frac{v}{v_0})}_{\text{remodelling}}, \qquad (5.11b)$$

$$\frac{\partial u}{\partial t} = \underbrace{D_3\nabla^2 u}_{\text{diffusion}} \underbrace{-\Phi_{31}pu}_{\text{uPA/PAI-1}} \underbrace{-\Phi_{33}cu}_{\text{uPA/uPAR}} \underbrace{+\gamma_{31}c}_{\text{production}}, \qquad (5.11c)$$

$$\frac{\partial p}{\partial t} = \underbrace{D_4\nabla^2 p}_{\text{diffusion}} \underbrace{-\Phi_{41}pu}_{\text{PAI-1/uPA}} \underbrace{-\Phi_{42}pv}_{\text{PAI-1/VN}} \underbrace{+\gamma_{41}m}_{\text{production}}, \qquad (5.11d)$$

$$\frac{\partial m}{\partial t} = \underbrace{D_5\nabla^2 m}_{\text{diffusion}} \underbrace{+\Phi_{52}pv}_{\text{PAI-1/VN}} \underbrace{+\Phi_{53}uc}_{\text{uPA/uPAR}} \underbrace{-\Phi_{54}m}_{\text{degradation}}. \qquad (5.11e)$$

We nondimensionalise the system of equations the same way as in Chapter 4. For the additional nonlocal and nonlinear chemotactic terms we nondimensionalise with the parameters $\vartheta_1 := c_0^{-1}$ and $\vartheta_2 := v_0^{-1}$, where ϑ_1 is the space fraction per unit cancer cell density ($1.5\times10^{-8}\,\mathrm{cm}^3\,\mathrm{cell}^{-1}$) and ϑ_2 is the space fraction per unit density of ECM ($10\,\mathrm{nM}^{-1}$) (Gerisch and Chaplain, 2008), and we take

$$\tilde{R}=\frac{R}{L}, \qquad \tilde{r}=\frac{r}{L}, \qquad \tilde{S_{cc}}=\frac{S_{cc}c_0}{D}, \qquad \tilde{S_{cv}}=\frac{S_{cv}v_0}{D}.$$

The maximum size of cells (including protrusion or sensing radius) is approximately in the range of $10-100\mu$m, and so the dimensionless $\tilde{R}\approx 0.01-0.1$.

Upon nondimensionalisation, combining the equation for cell density with the equations for matrix density, uPA, PAI-1, and plasmin concentrations all together, the mathematical model of cancer cell invasion of tissue incorporating cell adhesion in nondimensional form, after dropping the tildes for notational convenience, is given by:

$$\begin{aligned}
\frac{\partial c}{\partial t} &= \underbrace{D_c\nabla^2 c}_{\text{random motility}} \underbrace{-\nabla\cdot\left(\frac{c}{R}\int_S \frac{\mathbf{r}}{|\mathbf{r}|}(S_{cc}c+S_{cv}v)(1-c-v)\Omega(r)d\mathbf{r}\right)}_{\text{adhesive movement}} \\
&\quad \underbrace{-\nabla\cdot(\chi_u c(1-c-v)\nabla u)}_{\text{uPA-chemotaxis}} \underbrace{-\nabla\cdot(\chi_p c(1-c-v)\nabla p)}_{\text{PAI-1-chemotaxis}} \\
&\quad \underbrace{+\mu_1 c(1-c)}_{\text{proliferation}}, \qquad (5.12a)\\
\frac{\partial v}{\partial t} &= \underbrace{-\delta v m}_{\text{degradation}} \underbrace{+\phi_{21}pu}_{\text{uPA/PAI-1}} \underbrace{-\phi_{22}pv}_{\text{PAI-1/VN}} \underbrace{+\mu_2 v(1-v)}_{\text{remodelling}}, \qquad (5.12b)\\
\frac{\partial u}{\partial t} &= \underbrace{D_u\nabla^2 u}_{\text{diffusion}} \underbrace{-\phi_{31}pu}_{\text{uPA/PAI-1}} \underbrace{-\phi_{33}cu}_{\text{uPA/uPAR}} \underbrace{+\alpha_{31}c}_{\text{production}}, \qquad (5.12c)\\
\frac{\partial p}{\partial t} &= \underbrace{D_p\nabla^2 p}_{\text{diffusion}} \underbrace{-\phi_{41}pu}_{\text{PAI-1/uPA}} \underbrace{-\phi_{42}pv}_{\text{PAI-1/VN}} \underbrace{+\alpha_{41}m}_{\text{production}}, \qquad (5.12d)\\
\frac{\partial m}{\partial t} &= \underbrace{D_m\nabla^2 m}_{\text{diffusion}} \underbrace{+\phi_{52}pv}_{\text{PAI-1/VN}} \underbrace{+\phi_{53}cu}_{\text{uPA/uPAR}} \underbrace{-\phi_{54}m}_{\text{degradation}}. \qquad (5.12e)
\end{aligned}$$

The system (5.12) is closed with appropriate initial and boundary conditions. For 1D cases we use the spatial domain $D_{1D} := (0,M) \subset \mathbb{R}$ where M is a positive parameter

for domain length. We choose the following initial conditions

$$\begin{aligned} c(0,\mathbf{x}) &= \left(1+\exp\left(\frac{\mathbf{x}-a}{\varepsilon}\right)\right)^{-1}, \\ v(0,\mathbf{x}) &= 1-\frac{1}{2}\left(1+\exp\left(\frac{\mathbf{x}-a}{\varepsilon}\right)\right)^{-1}, \\ u(0,\mathbf{x}) &= \frac{1}{2}\left(1+\exp\left(\frac{\mathbf{x}-a}{\varepsilon}\right)\right)^{-1}, \qquad \text{for} \quad \mathbf{x}\in\bar{D}_{1D}, \\ p(0,\mathbf{x}) &= \frac{1}{20}\left(1+\exp\left(\frac{\mathbf{x}-a}{\varepsilon}\right)\right)^{-1}, \\ m(0,\mathbf{x}) &= 0, \end{aligned} \tag{5.13}$$

in which we take $\varepsilon = 0.1$ and $a = 1$. We assume that initially there is already some amount of cancer cells present in the domain in which they occupy $\frac{a}{M}$ of the domain length and the extracellular matrix takes the remaining domain. The initial conditions that we use for the 1D simulations are smooth type of initial conditions. We have observed that the initial conditions affect the speed of cancer cell movement of invasion across the extracellular matrix – the smoother the initial conditions, the faster the invasion process. For a 2D spatial domain $D_{2D} := (0,M_x)\times(0,M_y)\subset\mathbb{R}$ with positive parameters M_x (the length of domain in x-direction) and M_y (the length of domain in y-direction), we choose the same 2D initial conditions as described in Chapter 4, where the cancer cells of uniform initial density of 1 are placed to form a strip along one side of the domain, that is along $(0,M_y)$. The cell strip takes up about 25% of the domain while the rest of the domain is taken up by the extracellular matrix. The initial conditions for the other variables are

$$\begin{aligned} u(0,\mathbf{x}) &= 0.5\,c(0,\mathbf{x}), \\ p(0,\mathbf{x}) &= 0.05\,c(0,\mathbf{x}), \qquad \text{for} \quad \mathbf{x}\in\bar{D}_{2D}. \\ m(0,\mathbf{x}) &= 0. \end{aligned} \tag{5.14}$$

In this chapter we implement symmetry boundary conditions on one of the boundaries for the computational simulations. We assume that the $x = 0$ line is a (mirror)

symmetry line for the solutions (and parameters) and hence we can consider the problem on a reduced domain, namely only for $x > 0$ values (as everything for $x < 0$ follows from symmetry. For the opposite boundaries of $x = 0$, that is at $x = M$ for the 1D domain and $x = M_x$ for the 2D domain, we apply zero-flux boundary conditions. At the other boundaries $y = 0$ and $y = M_y$ for 2D we apply periodic boundary conditions. These conditions are explained further in Section 5.5.2.

5.4 Linear Stability Analysis

Intuitively we would expect that using the volume filling mechanism would stabilise the uniform steady state from some inhomogeneous perturbations, resulting in a homogeneous spatial pattern, or a pattern that evolves like a travelling wave. We carry out a linear stability analysis to determine which parameters can be varied for the possible generation of instability of the spatially uniform steady state or close to instability from system 5.12. We do this to highlight the key elements necessary for the system to generate spatial patterns. We use the same approach in this chapter as the linear stability analysis for the uPA system model presented in Chapter 4.

Since the reaction kinetics in (5.12) are similar to those in (4.3), in which $c^*(1 - c^*) = 0$ and we infer $c^* = 1$, the spatially uniform steady state $\mathbf{w}^*$ for the nonlocal system by using parameter set $\mathscr{P}$ is the same as the steady state that has been calculated in (4.10) given in section 4.4, which is,

$$\mathbf{w}^* := (c^*, v^*, u^*, p^*, m^*) \approx (1, 0.047, 0.222, 0.889, 0.343)\,. \tag{5.15}$$

We linearise the system (5.12) about the spatially uniform steady state $\mathbf{w}^*$ in the usual way by setting

$$\mathbf{w}(t, \mathbf{x}) := \mathbf{w}^* + \varepsilon \tilde{\mathbf{w}}\,,$$

where $0 < \varepsilon \ll 1$. Substituting into (5.12) and after dropping the terms of order ε^2 or

higher and dividing by ε we get the linearised equations written in the vector form

$$\frac{\partial \tilde{\mathbf{w}}}{\partial t} = J_T(\mathbf{w}^*)\nabla^2\tilde{\mathbf{w}} + J_{NL}(\mathbf{w}^*)\nabla\cdot\left(\int \tilde{\mathbf{w}}\Omega(r)d\mathbf{r}\right) + J_R(\mathbf{w}^*)\tilde{\mathbf{w}}. \tag{5.16}$$

The reaction Jacobian $J_R(\mathbf{w}^*)$ has the same components as $J_R(\mathbf{w})$ given in (4.11), which, upon evaluation around the steady state

$$J_R(\mathbf{w}^*) = \begin{pmatrix} \mu_1(1-2c^*) & 0 & 0 & 0 & 0 \\ 0 & -\delta m^* - \phi_{22}p^* + \mu_2(1-2v^*) & \phi_{21}p^* & \phi_{21}u^* - \phi_{22}v^* & -\delta v^* \\ -\phi_{33}u^* + \alpha_{31} & 0 & -\phi_{31}p^* - \phi_{33}c^* & -\phi_{31}u^* & 0 \\ 0 & -\phi_{42}p^* & -\phi_{41}p^* & -\phi_{41}u^* - \phi_{42}v^* & \alpha_{41} \\ \phi_{53}u^* & \phi_{52}p^* & \phi_{53}c^* & \phi_{52}v^* & -\phi_{54} \end{pmatrix} \tag{5.17}$$

The transport Jacobian $J_T(\mathbf{w}^*)$ now becomes

$$J_T(\mathbf{w}^*) = \begin{pmatrix} D_c & 0 & c^*\chi_u(\mathbf{w}^*) & c^*\chi_p(\mathbf{w}^*) & 0 \\ 0 & 0 & 0 & 0 & 0 \\ 0 & 0 & D_u & 0 & 0 \\ 0 & 0 & 0 & D_p & 0 \\ 0 & 0 & 0 & 0 & D_m \end{pmatrix}, \tag{5.18}$$

where the forms for the linearised chemotactic terms $\chi_u(\mathbf{w}^*)$ and $\chi_p(\mathbf{w}^*)$ depend on our choice of chemotactic linear sensitivity coefficients. Since here we use the form that incorporates volume filling mechanism $1-c-v$, which, from using $1-c^*=0$,

$$\chi_u(\mathbf{w}^*) = \chi_u v^* \qquad \text{and} \qquad \chi_p(\mathbf{w}^*) = \chi_p v^*.$$

The nonlocal Jacobian is given by

$$J_{NL}(\mathbf{w}^*) = \begin{pmatrix} g_1(\mathbf{w}^*) & g_2(\mathbf{w}^*) & 0 & 0 & 0 \\ 0 & 0 & 0 & 0 & 0 \\ 0 & 0 & 0 & 0 & 0 \\ 0 & 0 & 0 & 0 & 0 \\ 0 & 0 & 0 & 0 & 0 \end{pmatrix}, \tag{5.19}$$

where it consists of functions derived from adhesive force $g_1(\mathbf{w}^*)$ and $g_2(\mathbf{w}^*)$, where for the form with volume filling:

$$g_1(\mathbf{w}^*) = \frac{c^*}{R}(S_{cc}c^* + S_{cv}v^*) + \frac{c^*v^*S_{cc}}{R}, \tag{5.20}$$

and

$$g_2(\mathbf{w}^*) = \frac{c^*}{R}(S_{cc}c^* + S_{cv}v^*) + \frac{c^*v^*S_{cv}}{R}. \tag{5.21}$$

Now we look for solutions of the perturbations (5.16) in the usual way by setting

$$\tilde{\mathbf{w}}(t,\mathbf{x}) = \mathbf{W}\exp(\sigma t + \mathrm{i}\tilde{\mathbf{k}}\cdot\mathbf{x}), \tag{5.22}$$

where $\tilde{\mathbf{k}}$ is the wavevector and $\mathbf{W}$ is a vector of constants. Substituting this form into (5.16) we get

$$\left[\sigma\mathrm{I} + \|\tilde{\mathbf{k}}\|_2^2 J_T(\mathbf{w}^*) - \mathrm{i}\tilde{\mathbf{k}}J_{NL}(\mathbf{w}^*)\int \exp(\mathrm{i}\tilde{\mathbf{k}}\mathbf{r})\Omega(r)d\mathbf{r} - J_R(\mathbf{w}^*)\right]\mathbf{W} = \mathbf{0}. \tag{5.23}$$

The nonlocal Jacobian has a factor $\int \exp(\mathrm{i}\tilde{\mathbf{k}}\mathbf{r})\,\Omega(r)d\mathbf{r}$ that depends on the choice of $\Omega(r)$, where for 1D cases:

- if $\Omega(r) = 1$,
$$\int \exp(\mathrm{i}\tilde{\mathbf{k}}\mathbf{r})\,\Omega(r)d\mathbf{r} = \frac{2(\cos(\tilde{\mathbf{k}}R) - 1)}{i\tilde{\mathbf{k}}},$$
- if $\Omega(r) = \dfrac{1}{2R}$,
$$\int \exp(\mathrm{i}\tilde{\mathbf{k}}\mathbf{r})\,\Omega(r)d\mathbf{r} = \frac{\cos(\tilde{\mathbf{k}}R) - 1}{i\tilde{\mathbf{k}}R}, \text{ and}$$

- if $\Omega(r) = \dfrac{1}{R}\left(1 - \dfrac{r}{R}\right)$,

$$\int \exp(\mathrm{i}\tilde{\mathbf{k}}\mathbf{r})\,\Omega(r)d\mathbf{r} = \frac{2(\cos(\tilde{\mathbf{k}}R) - 1)}{i\tilde{\mathbf{k}}R} + \frac{2(1 - \cos(\tilde{\mathbf{k}}R))}{\tilde{\mathbf{k}}^2R^2}\,.$$

We use the radial dependency function $\Omega(r) = 1/2R$ for 1D and $\Omega(r) = 1/\pi R^2$ for 2D, as have been used in Gerisch and Chaplain (2008).

Going back to the equation (5.23), it has nontrivial solutions if and only if the determinant of the coefficient matrix equals zero, *i.e.*,

$$|\sigma\mathrm{I} + \|\tilde{\mathbf{k}}\|_2^2 J_T(\mathbf{w}^*) - \mathrm{i}\tilde{\mathbf{k}}J_{NL}(\mathbf{w}^*)\int \exp(\mathrm{i}\tilde{\mathbf{k}}\mathbf{r})\Omega(r)d\mathbf{r} - J_R(\mathbf{w}^*)| = 0\,. \tag{5.24}$$

We are interested in the dispersion relation for the unique positive, spatially uniform steady state $\mathbf{w}^*$ from the solutions of the matrix determinant above which give the eigenvalues of the solutions $\sigma_{\tilde{\mathbf{k}}}(\mathbf{w}^*)$ as a function of $\tilde{\mathbf{k}}$, where $\tilde{\mathbf{k}} = \mathbf{k}\pi M^{-1}$, for each $\mathbf{k} \in \mathbb{Z}$ and M is the domain size parameter. The characteristic polynomial equation (5.24) cannot be solved analytically. Therefore we resort to use a numerical package, such as *Matlab*, to find the eigenvalues.

In our base model of cancer invasion explained in Chapter 4, the dispersion relation in Fig. 4.2 suggests that the use of the parameter set $\mathscr{P}$ may lead to a wide range of unstable modes. This is generally true for the linear form of the terms that govern cell motility, which, for system (4.3), are heavily driven by chemotaxis and diffusion. For the extended model in system (5.12) the cell motility is also governed by a nonlocal term that accounts for aggregation/movement due to adhesive force. As we have stated before, we use volume filling form for all motility terms. In order to see the difference between the linear form and volume filling, in Fig.. 5.1 we plot dispersion relations for the largest of the eigenvalues of the solutions of (5.24) using parameter set $\mathscr{P}$ listed in Table 4.1 given in Chapter 4. The solid line represents the largest of the eigenvalues with linear form for $\chi_u(\mathbf{w}) = \chi_u$, $\chi_p(\mathbf{w}) = \chi_p$, and $g(c,v) = S_{cc}c + S_{cv}v$ and the dash-dotted line represents the largest of the eigenvalues with volume filling form

for $\chi_u(\mathbf{w}) = \chi_u(1-c-v)$, $\chi_p(\mathbf{w}) = \chi_p(1-c-v)$, and $g(c,v) = (S_{cc}c + S_{cv}v)(1-c-v)^+$. Since the haptotactic term in (4.3a) is replaced by the adhesive movement term, the haptotactic coefficient χ_v is replaced by cell-matrix adhesion coefficient S_{cv} and its value in the dispersion relations in Fig. 5.1 is set to $2.85 \cdot 10^{-2}$, which is the value of χ_v. Other nonlocal parameters such as the cell-cell adhesion coefficient is set to $S_{cc} = 0$, the sensing radius $R = 0.1$, and $\Omega(r) = \dfrac{1}{2R}$. We see that the dispersion relation with linear form of the system (5.12) in Fig. 5.1 is qualitatively and quantitatively comparable with the dispersion relation of our base model (4.3), except that the dispersion relation of the base model in Fig. 4.2 has slightly larger range of unstable modes.

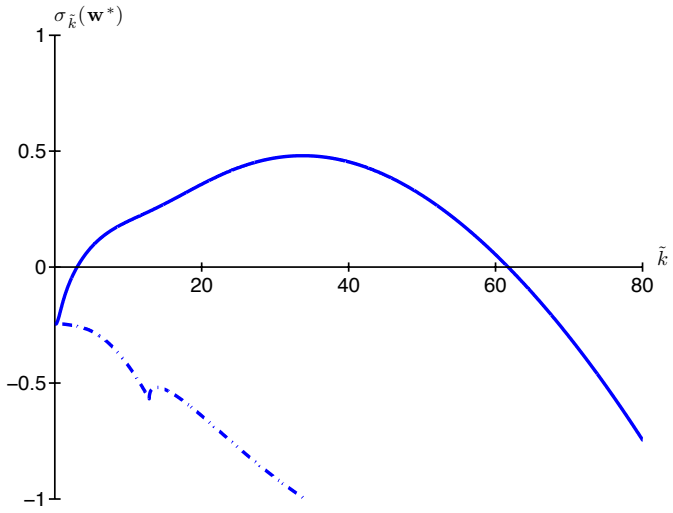

Figure 5.1: Plots of dispersion relations of the largest of the real part of eigenvalues $\sigma_{\tilde{k}}(\mathbf{w}^*)$ from the system (5.12) where (i) solid line is for equations with linear forms of $\chi_u(\mathbf{w}) = \chi_u$, $\chi_p(\mathbf{w}) = \chi_p$, and $g(c,v) = S_{cc}c + S_{cv}v$, resembling the dispersion relation in Fig. 4.2 (solid line) of Chapter 4, and (ii) dash-dotted line is for equations with volume filling forms of $\chi_u(\mathbf{w}) = \chi_u(1-c-v)$, $\chi_p(\mathbf{w}) = \chi_p(1-c-v)$, and $g(c,v) = (S_{cc}c + S_{cv}v)(1-c-v)$, all using parameter set $\mathscr{P}$ with additional $S_{cc} = 0$, $S_{cv} = 2.85 \cdot 10^{-2}$, sensing radius $R = 0.1$, and $\Omega(r) = 1/2R$.

One important use of the dispersion relation is that it may tell us the possibility of spatial pattern generation and the sizes of the patterns. We can expect from the dispersion relation with linear form for motility terms (solid line) that the patterns of the solutions for the system (5.12) using the parameter values stated will exhibit heterogeneity with merging and emerging peaks, qualitatively similar to the patterns

that have been shown and explained in full detail in Section 4.5. On the other hand, using the nonlinear form or volume filling form for motility terms results in the real part of eigenvalues $\sigma_{\tilde{k}}(\mathbf{w}^*)$ that are negative for all $\tilde{\mathbf{k}}$ (dash-dotted line), indicating stability of the spatial uniform steady state to some inhomogeneous perturbations.

In order to see the influence of adhesive movement in our model, particularly the effects of cell adhesion parameters, in the following we use non-zero cell-cell adhesion. The appropriate choice of nonlocal parameter values that resemble an invasive situation is when the cell-matrix adhesion coefficient S_{cv} is higher than the cell-cell adhesion coefficient S_{cc}. Biologically this means that the cells increase their attachment to matrix for movement across the matrix and reduce their attachment to other cells in order to set them free for movement. We set $S_{cv} = 0.1$ and $S_{cc} = 0.01$, and keep $R = 0.1$ and $\Omega(r) = 1/2R$ for the 1D domain.

For the linear stability analysis of the extended nonlocal model (5.12) we concentrate on how the dispersion relation varies with diffusion coefficients by 'tuning' the values of all diffusion coefficients at the same ratio. As we decrease the diffusion coefficient parameters for cells (D_c), uPA (D_u), PAI-1 (D_p), and plasmin (D_m), the dispersion curve rises until it rises above the axis with a finite range of $\tilde{\mathbf{k}}$. This is seen in Fig. 5.2, where we plot the maximum eigenvalues using different ranges of diffusion parameters: (i) D_1 is the curve using all default diffusion coefficients as given in parameter set $\mathscr{P}$ in Table 4.1; (ii) D_2 is the curve with the values of all diffusion coefficients 10 times lower than the values of of D_1; (iii) D_3 with the all diffusion coefficients 100 times lower than D_1, and (iv) D_4 with 1000 times lower than D_1. We have verified that the dispersion relation for all diffusion coefficients set to zero also lies on the same line as the dispersion relation curve D_4.

In Fig. 5.2 we see there is a range of diffusion parameters that generates a small band of unstable modes ($60 < \tilde{\mathbf{k}} < 70$) which grow into spatial patterns, that is with dispersion relation curve D_4, where $D_c = 3.5 \cdot 10^{-7}$, $D_u = 2.5 \cdot 10^{-6}$, $D_p = 3.5 \cdot 10^{-6}$, and

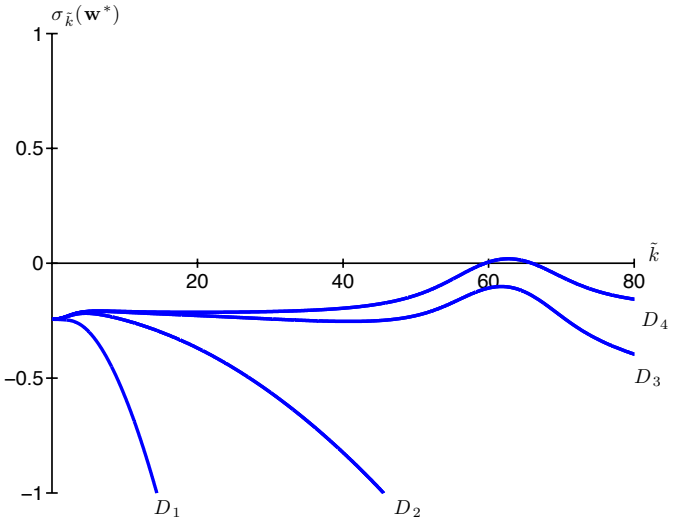

Figure 5.2: Plots showing the dispersion relation for different set of diffusion coefficients: (i) D_1 with all default diffusion coefficient values as given in parameter set $\mathscr{P}$ in Table 4.1, (ii) $D_2 = D_1 \times 10^{-1}$, (iii) $D_3 = D_1 \times 10^{-2}$, and (iv) $D_4 = D_1 \times 10^{-3}$. All plots are with volume filling forms of chemotactic sensitivity coefficients $\chi_u(\mathbf{w}) = \chi_u(1-c-v)$ and $\chi_p(\mathbf{w}) = \chi_p(1-c-v)$, and nonlocal $g(c,v) = (S_{cc}c + S_{cv}v)(1-c-v)$. The nonlocal parameters are $S_{cv} = 0.1$, $S_{cc} = 0.01$, $R = 0.1$, and $\Omega(r) = 1/2R$.

$D_m = 4.91 \cdot 10^{-6}$. These values of diffusion parameters are too small for our numerical code, thus we use the next diffusion parameter set D_3 that is 10 times higher. As we have seen in Chapter 4 in Fig. 4.8 where diffusion could affect cell speed and heterogeneity, in this chapter we choose even smaller diffusion coefficient values because we want to focus on the role of cell adhesion in the system that drives the movement or invasion of cancer cells. By using smaller diffusion coefficients we mainly focus on adhesion-driven movement and also to get heterogeneity in the solutions since the volume filling mechanism incorporated in adhesive and chemotaxis movement terms may keep stabilising the homogeneous steady state resulting in travelling wave-like solutions. There are diverse patterns that emerge in the solutions if we vary cell-cell adhesion and cell-matrix adhesion parameters, which is our aim in this chapter. It is also observed that varying cell-cell and cell-matrix adhesion can affect the speed of cell dispersion or invasion. This is supported by a hypothesis that adhesive properties of cancer cells may influence the patterns of spread and growth (Fidler, 1978). The

precise patterns that evolve are governed by the full nonlinear system, hence a nonlinear stability analysis perhaps could give us insight into these effects. We do not carry out a nonlinear analysis in this chapter, but leave it as future work.

In most of computational simulations in Chapter 5.5 we use the diffusion parameter set D_3 to see the spatial patterns that may emerge by varying nonlocal parameters, such as cell-cell adhesion S_{cc} and cell-matrix adhesion S_{cv}, and chemotactic parameters χ_u and χ_p. Thus we consider two new parameter sets to be used in the numerical simulations presented in the next section. The first parameter set is $\mathscr{P}_{NL1}$ and the parameter values are listed in Table 5.1. The other parameter set with varied values of diffusion and chemotactic coefficients is $\mathscr{P}_{NL2}$ and the values are listed in Table 5.2

Note that we only list parameter values in Tables 5.1 and 5.2 for diffusion coefficients, chemotactic coefficients, and nonlocal parameters. All other parameter values for reaction kinetics terms remain the same as in parameter set $\mathscr{P}$ listed in Table 4.1 in Chapter 4.

Table 5.1: Parameter set $\mathscr{P}_{NL1}$

$D_c = 3.5 \cdot 10^{-6}$	$D_u = 2.5 \cdot 10^{-5}$	$D_p = 3.5 \cdot 10^{-5}$
$D_m = 4.91 \cdot 10^{-5}$	$\chi_u = 3.05 \cdot 10^{-2}$	$\chi_p = 3.75 \cdot 10^{-2}$
$R = 0.1$	$S_{cv} = 0.1$	$S_{cc} = 0.01$

Table 5.2: Parameter set $\mathscr{P}_{NL2}$

$D_c = 1.3 \cdot 10^{-5}$	$D_u = 5 \cdot 10^{-5}$	$D_p = 7 \cdot 10^{-5}$
$D_m = 9.82 \cdot 10^{-5}$	$\chi_u = 3.05 \cdot 10^{-3}$	$\chi_p = 3.75 \cdot 10^{-3}$
$R = 0.1$	$S_{cv} = 0.1$	$S_{cc} = 0.01$

5.5 Computational Simulation Results

Here we solve the nonlocal system (5.12) numerically using the initial conditions and mixed boundary conditions as we have explained in section 5.3. The numerical simulations were performed using the same numerical technique for simulations in Chapter 4 that has been explained in full detail in section 4.5.1 with an additional evaluation for the integral terms. The numerical scheme follows the method of lines where, for the discretisation in space, a second-order finite volume approach is used to make use of flux-limiting for an accurate discretisation of the chemotaxis and nonlocal terms. Particularly for the nonlocal term, the spatial discretisation is done by using the Fast Fourier Transform (or FFT) technique. Full details of the numerical scheme are given in Gerisch and Chaplain (2006, 2008). The parameters are taken from parameter sets $\mathscr{P}_{NL1}$ listed in Table 5.1 and $\mathscr{P}_{NL2}$ listed in Table 5.2, unless otherwise stated.

5.5.1 Computational Simulation Results in 1D

For the 1-dimensional spatial domain, we performed the simulations on the domain $D_{1D} = (0, 10)$. Each unit length is discretised into 100 grid cells, or $\Delta x = 0.01$. At $x = 0$ we impose symmetry boundary conditions while zero-flux boundary conditions are applied at $x = 10$. Initially we assume there are cancer cells with unit density ($c_0 = 1$) occupying $1/10$ of the domain and penetrating into a half degraded matrix. The initial uPA concentration is half of the magnitude of cell density, while the initial concentration of PAI-1 is $1/20$ of cell density. There is no plasmin concentration initially. This initial condition set up is illustrated in Fig. 5.3, where the solid line represents cancer cell density, the dotted line represents matrix density, the dash-dotted line represents uPA, and the dashed line represents PAI-1. We performed the simulations up to dimensionless time $t = 300$, before the front of cancer cell density reaches the boundary. This way, we may notice the behaviour of cells without any potential numerical effects of the boundaries.

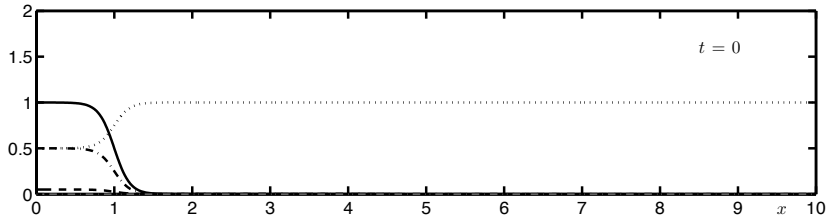

Figure 5.3: Initial condition setup for 1D numerical simulations.

Fig. 5.4 shows the progression of solutions using diffusion parameter set D_1 which has the same values of diffusion as in parameter set $\mathscr{P}$ ($D_c = 3.5 \times 10^{-4}$, $D_u = 2.5 \times 10^{-3}$, $D_p = 3.5 \times 10^{-3}$, and $D_m = 4.91 \times 10^{-3}$), taken at dimensionless times $t = 10$, $t = 100$, $t = 200$, and $t = 300$. The solutions for cancer cell density are shown on the left figures which depict the movement of cancer cell density in a travelling-wave like manner, moving forward with a little hump at its invading front. We also see on the right figure that the matrix density is degraded homogeneously. The dispersion relation for the simulations is shown in Fig. 5.5.

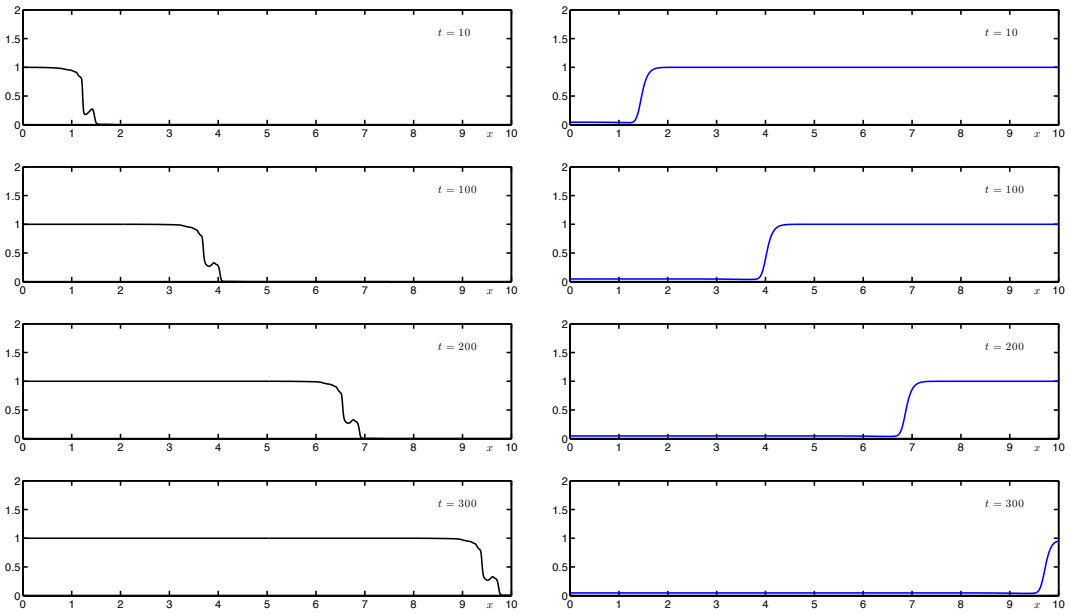

Figure 5.4: Sequence of profiles showing the spatio-temporal evolution of cancer cells c (black, left figures) invading the ECM v (blue, right figures) for model (5.12) with diffusion parameter set D_1 where $D_c = 3.5 \times 10^{-4}$, $D_u = 2.5 \times 10^{-3}$, $D_p = 3.5 \times 10^{-3}$, and $D_m = 4.91 \times 10^{-3}$, and other parameters are the same as those given in parameter set $\mathscr{P}_{NL1}$ at dimensionless times $t = 10$, $t = 100$, $t = 200$, and $t = 300$.

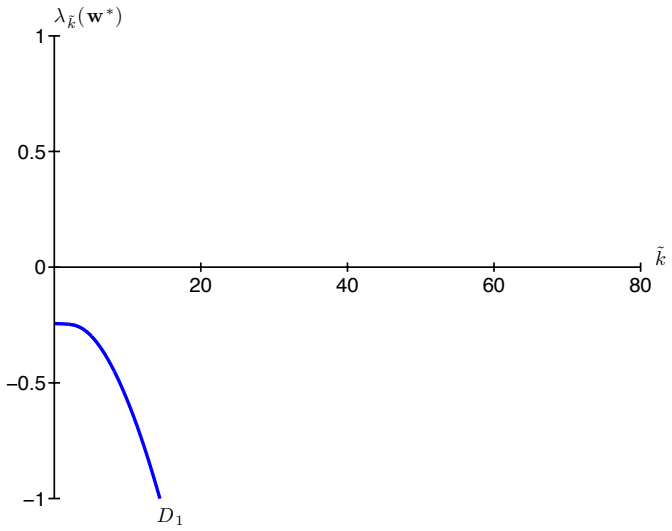

Figure 5.5: Dispersion relation for simulations in Fig. 5.4 using default diffusion coefficient values as given in parameter set $\mathscr{P}$ in Table 4.1. The nonlocal parameters are $S_{cv} = 0.1$, $S_{cc} = 0.01$, $R = 0.1$, and $\Omega(r) = 1/2R$.

Next decreasing diffusion, we use diffusion parameter set D_2 (where $D_c = 3.5 \times 10^{-5}$, $D_u = 2.5 \times 10^{-4}$, $D_p = 3.5 \times 10^{-4}$, and $D_m = 4.91 \times 10^{-4}$), and as we see in Fig. 5.6 spatial patterns start to emerge, but to a small extent. The corresponding dispersion relation is shown in Fig. 5.7.

The perturbations to the uniform wave-like solutions of cancer cell density in Fig. 5.6 only affect the area near the invading front. The cancer cell density behind the perturbed area is still dominated by a uniform solution with unit density ($c = 1$). We notice that the speed of cell invasion is slightly reduced compared to the speed of cell invasion in Fig. 5.4. As for the matrix density, it is homogeneously degraded in the uniform area of cell and slightly fluctuated in the area with perturbed solution.

Patterns become more apparent if we use smaller values of diffusion parameters. Fig. 5.8 shows the progression of solutions over time using parameter set $\mathscr{P}_{NL1}$. We see here the perturbations now dominate the solution of cancer cell density in the form of peaks close to each other and the average height of cell density is maintained at $c = 1$, although there is a small peak of cell density at the invading front. We observe

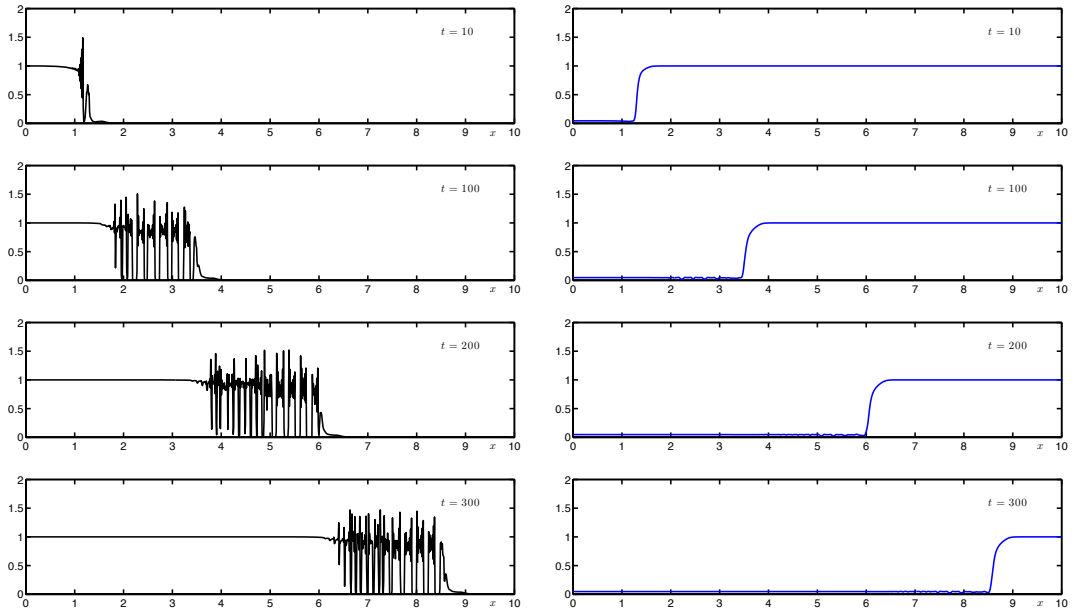

Figure 5.6: Plots showing solutions with diffusion parameter set D_2 where $D_c = 3.5 \times 10^{-5}$, $D_u = 2.5 \times 10^{-4}$, $D_p = 3.5 \times 10^{-4}$, and $D_m = 4.91 \times 10^{-4}$. Other parameters are the same as those given in parameter set $\mathscr{P}_{NL1}$.

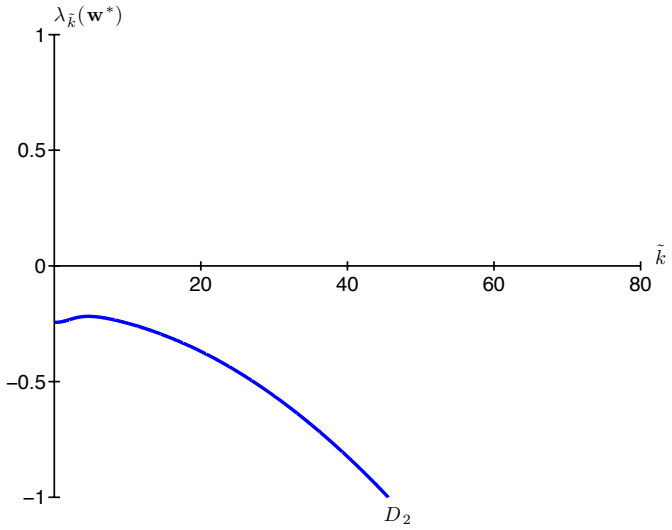

Figure 5.7: Dispersion relation for simulations in Fig. 5.6 using $D_c = 3.5 \times 10^{-5}$, $D_u = 2.5 \times 10^{-4}$, $D_p = 3.5 \times 10^{-4}$, and $D_m = 4.91 \times 10^{-4}$.

that the cancer cells invade the matrix with a constant speed in all solutions in Figs. 5.4, 5.6, and 5.8. In particular here, if we calculate the speed of invasion, it can be seen in Fig. 5.8 that at dimensionless time $t = 100$ the invading front lies at $x = 3.5$, after

another 100 time later (at $t = 200$) the invading front reaches $x = 6$ which is 2.5 units away from the cell position at $t = 100$, and at $t = 300$ the invading front takes the position at $x = 2.5 + 6$ or equal to $x = 8.5$. By taking $\Delta t = 100$ and $\Delta s = 2.5$, the constant invasion speed is about $\Delta s/\Delta t = 0.025$. Another thing that we can notice in Fig. 5.8 is that cancer cells are more dense near the area of initial position and cancer cells further away progress forward in peaks with a regular pattern and less dense. The matrix now has been degraded in a less homogeneous manner compared to the degradation with previous diffusion parameters, where here matrix degradation shows more fluctuations in its degraded density.

The regular peaks of cell density in Fig. 5.8 are thought to be associated with cell adhesion in the nonlocal term, where cell-matrix adhesion is 10 times higher than the cell-cell adhesion coefficient. If we invert the values of cell adhesion parameters, by increasing cell-cell adhesion to $S_{cc} = 0.1$ and reducing cell-matrix adhesion to $S_{cv} = 0.01$, the results are a pattern of cell density with irregular peaks, as we observe in Fig. 5.9. The cell peaks are more densely packed at some area and sparse at other areas. We see that the solution near the initial position is not affected by perturbations at all, as there is no peaks in that area. Although the average cell density is maintained at $c = 1$, some peaks are slightly higher and a few peaks are smaller than the uniform density $c = 1$. The matrix is also degraded less homogeneously, showing small fluctuations in the density of degraded matrix.

The simulations shown in Figs. 5.8 and 5.9 suggest that cell adhesion can play a role in shaping spatial patterns that occur, particularly from using parameter set $\mathscr{P}_{NL1}$. The corresponding dispersal relations for the simulations are shown in Fig. 5.10. It is of interest to see the patterns that may emerge in 2-dimensional spatial domain if we vary parameters such as cell-cell and cell-matrix adhesion as we discuss in the next subsection.

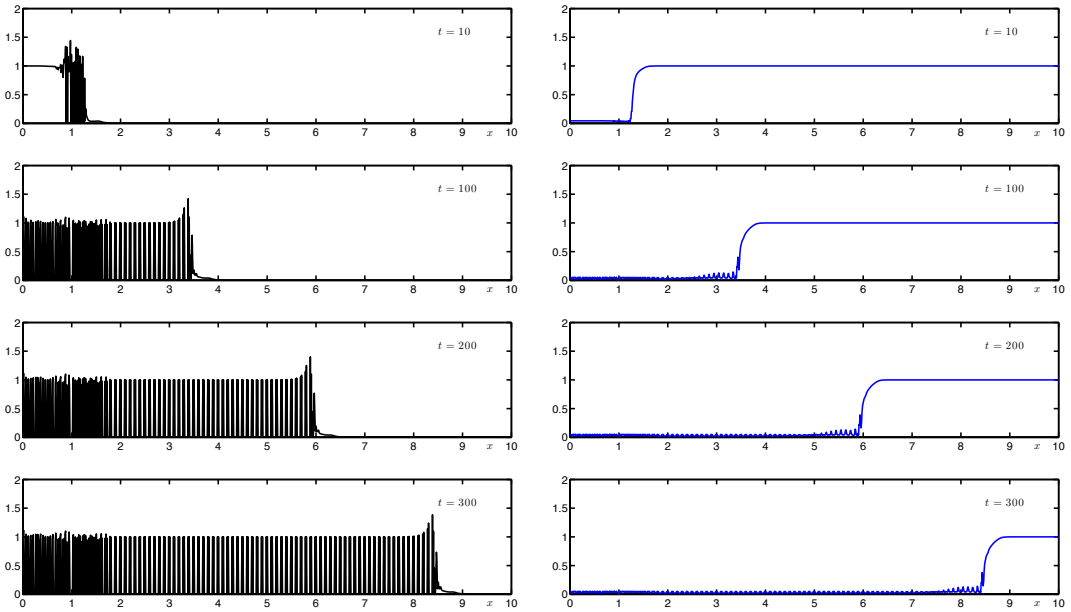

Figure 5.8: Sequence of profiles showing the spatio-temporal evolution of cancer cells c (black, left figures) invading the ECM v (blue, right figures) for model (5.12) with parameter set $\mathscr{P}_{NL1}$ at dimensionless times $t = 10$, $t = 100$, $t = 200$, and $t = 300$. Cancer cells invade the ECM with a constant speed.

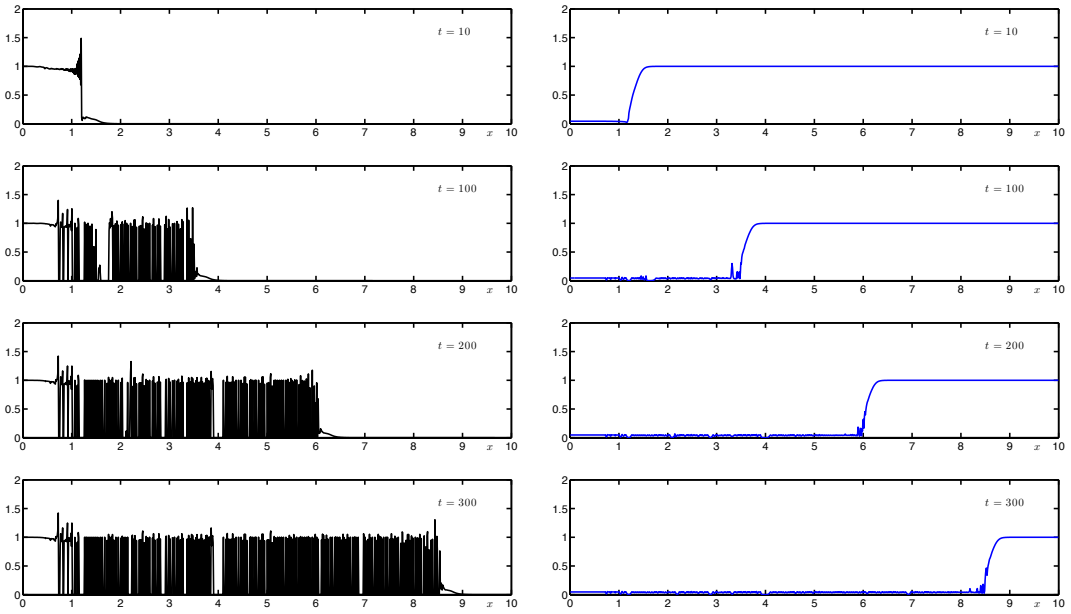

Figure 5.9: Plots showing less regular invading cancer cells (black, left figures) and degraded matrix (blue, right figures) are produced when cell-cell adhesion is higher than cell-matrix adhesion, that is $S_{cc} = 0.1$ and $S_{cv} = 0.01$ at dimensionless time $t = 100$, $t = 200$, and $t = 300$. All other parameters are as in parameter set $\mathscr{P}_{NL1}$.

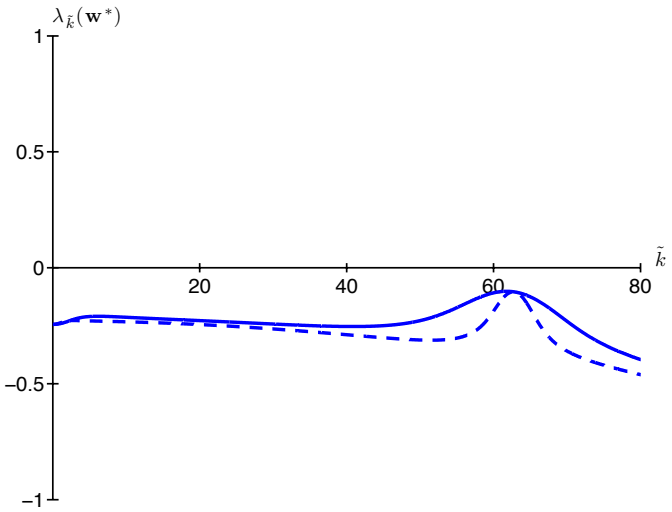

Figure 5.10: Dispersion relations for simulations in Fig. 5.8 (*solid blue line*) using $S_{cv} = 0.1$, $S_{cc} = 0.01$ and Fig. 5.9 (*dashed blue line*) using $S_{cv} = 0.01$, $S_{cc} = 0.1$, all with $D_c = 3.5 \times 10^{-6}$, $D_u = 2.5 \times 10^{-5}$, $D_p = 3.5 \times 10^{-5}$, and $D_m = 4.91 \times 10^{-5}$.

5.5.2 Computational Simulation Results in 2D

The simulations for a 2-dimensional spatial domain were performed on a rectangular domain $D_{2D} := (0, M_x) \times (0, M_y) \subset \mathbb{R}^2$ where in all simulations $M_x = 4$ and $M_y = 2$ in x and y directions, respectively, unless otherwise stated. Here mixed types of boundary conditions are imposed on each side of the rectangular domain. Periodic boundary conditions are applied at the opposite sides (at $y = 0$ and $y = M_y$) while symmetry boundary conditions are applied at the left side where the cells initially deposited (at $x = 0$), and the right side (at $x = M_x$) with zero-flux boundary conditions. The schematic for the setup of boundary conditions for the 2D domain is shown in Fig. 5.11.

Each unit size is discretised into 50 grid cells, in which $\Delta x = \Delta y = 0.02$. We ran the simulations up to a maximum dimensionless time $t = 500$ or before the solutions reach the right side boundary ($M_x = 4$) to avoid any numerical effects of the boundaries. Initially at $t = 0$ we assume there is already a uniform cell density occupying $1/4$ of the area of the domain and the extracellular matrix takes up the rest of the domain.

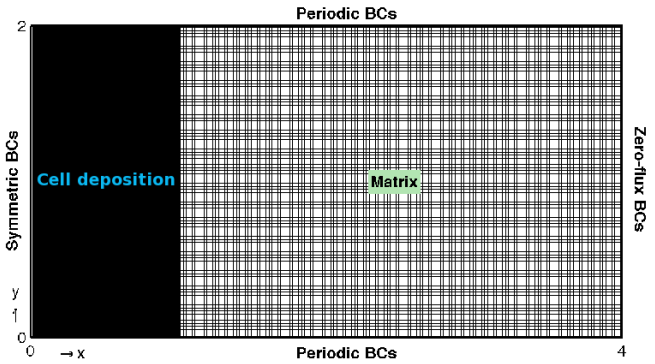

Figure 5.11: Boundary conditions setup for 2D computational simulations on a rectangular domain $D = (0,4) \times (0,2)$. Periodic boundary conditions are imposed at $y = 0$ and $y = 2$, while symmetric boundary conditions at $x = 0$ and zero-flux boundary conditions at $x = 4$.

These initial conditions are the same as the initial conditions for the 2-dimensional domain of the base model given in Section 4.5 of Chapter 4.

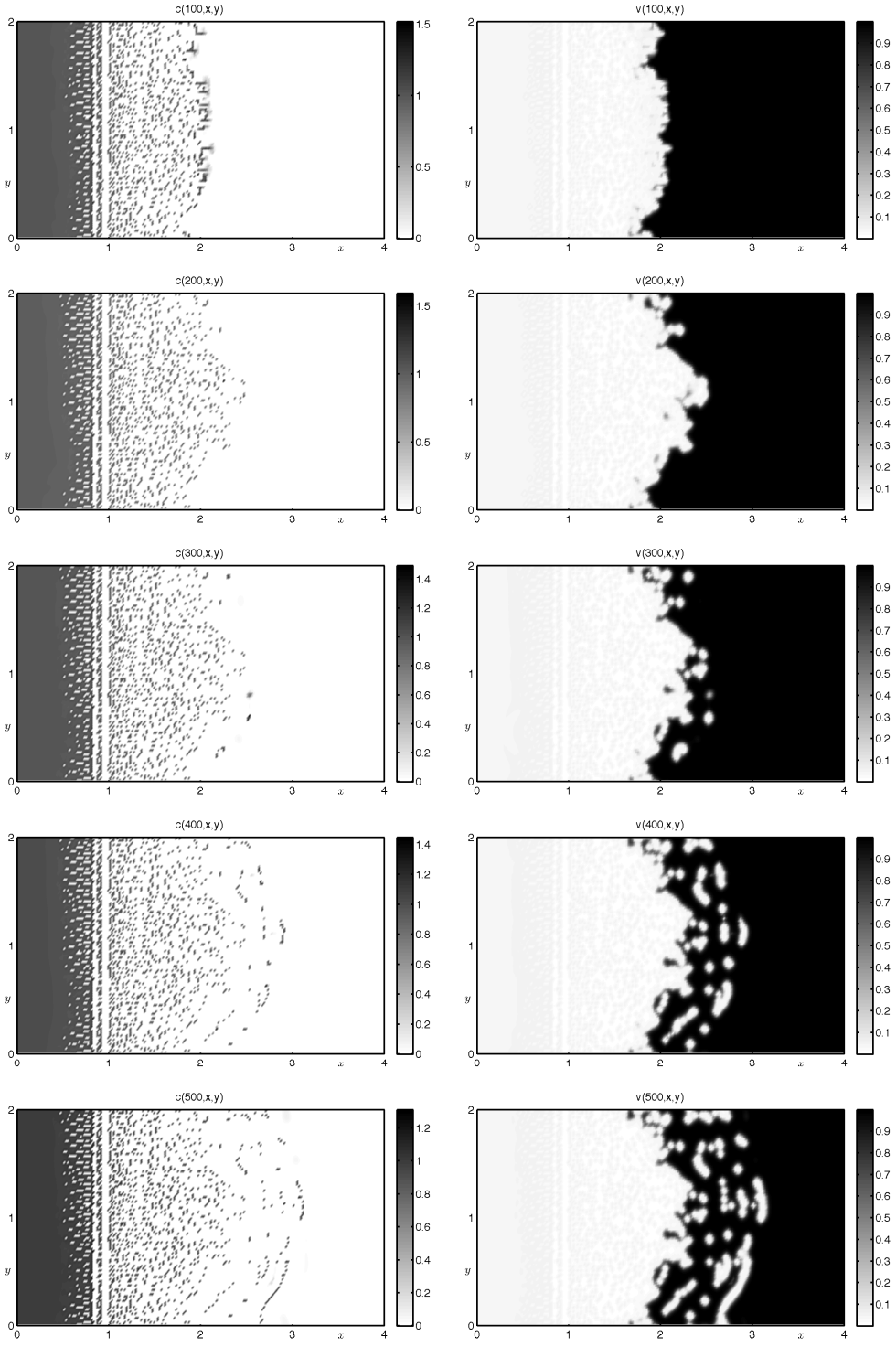

Figure 5.12: Plots showing the distribution of the cancer cell density $c(t,x,y)$ (left figures) and ECM density $v(t,x,y)$ (right figures) in a rectangular domain $\Omega = (0,4) \times (0,2)$ with parameter set $\mathscr{P}_{NL1}$ taken at dimensionless times $t = 100$, $t = 200$, $t = 300$, $t = 400$, and $t = 500$.

In Fig. 5.12 we plot solutions of cancer cell density (left figures) and the extracellular matrix (right figures) using parameter set $\mathscr{P}_{NL1}$ at dimensionless times $t = 100$, $t = 200$, $t = 300$, $t = 400$, and $t = 500$ arranged from top to bottom. In this simulation cell-matrix adhesion is set higher than cell-cell adhesion, taking $S_{cv} = 0.1$ and $S_{cc} = 0.01$. We observe here that the cell density invades the matrix in an irregular manner, with the cell density in the middle part advancing more than the cell density near the top and bottom boundaries. Until $t = 100$ the cell density shows a "collective" cell movement. The effects of stronger cell-matrix adhesion is more evident after $t = 200$ where the cell density spreads as "colonies" or "clusters". Cells are no longer tightly attached to the group, spreading across the domain with the invading front dominated by cell density at the middle part. We also observe that the distribution of cell density almost resembles the pattern in the 1-dimensional domain shown in Fig. 5.8, where the cell density near the initial position is more compact than the cell density in other areas. Stronger cell-matrix adhesion also causes erosion of the uniform cell density in the area of initial position. These results are comparable with the experimental data for the most invasive cancer cells shown in Fig. 4.14, on the right bottom figure.

In Figs. 5.13 and 5.14 we increase the cell-cell adhesion to $S_{cc} = 0.5$ but keep the cell-matrix adhesion at $S_{cv} = 0.1$. In Fig. 5.13 we plot the solutions from $t = 10$ to $t = 50$ to have a closer look at the behaviour of solutions when cell-cell adhesion is very strong and the pattern that the cells generate. At $t = 10$ the cell density immediately aggregates, destabilising the uniform density and forming a pattern of stripes of high densities. Soon afterwards the high cell densities start to reduce and at $t = 30$ deformation of the stripe pattern occurs. In Fig. 5.14 from $t = 100$ onwards the cell density is reduced to values close to uniform and moves forward invading the matrix in a way between collective and cluster motility. We also see some cell densities moving in stripes. Because cell-cell adhesion is strong, the speed of invasion here is relatively slower than in Fig. 5.12.

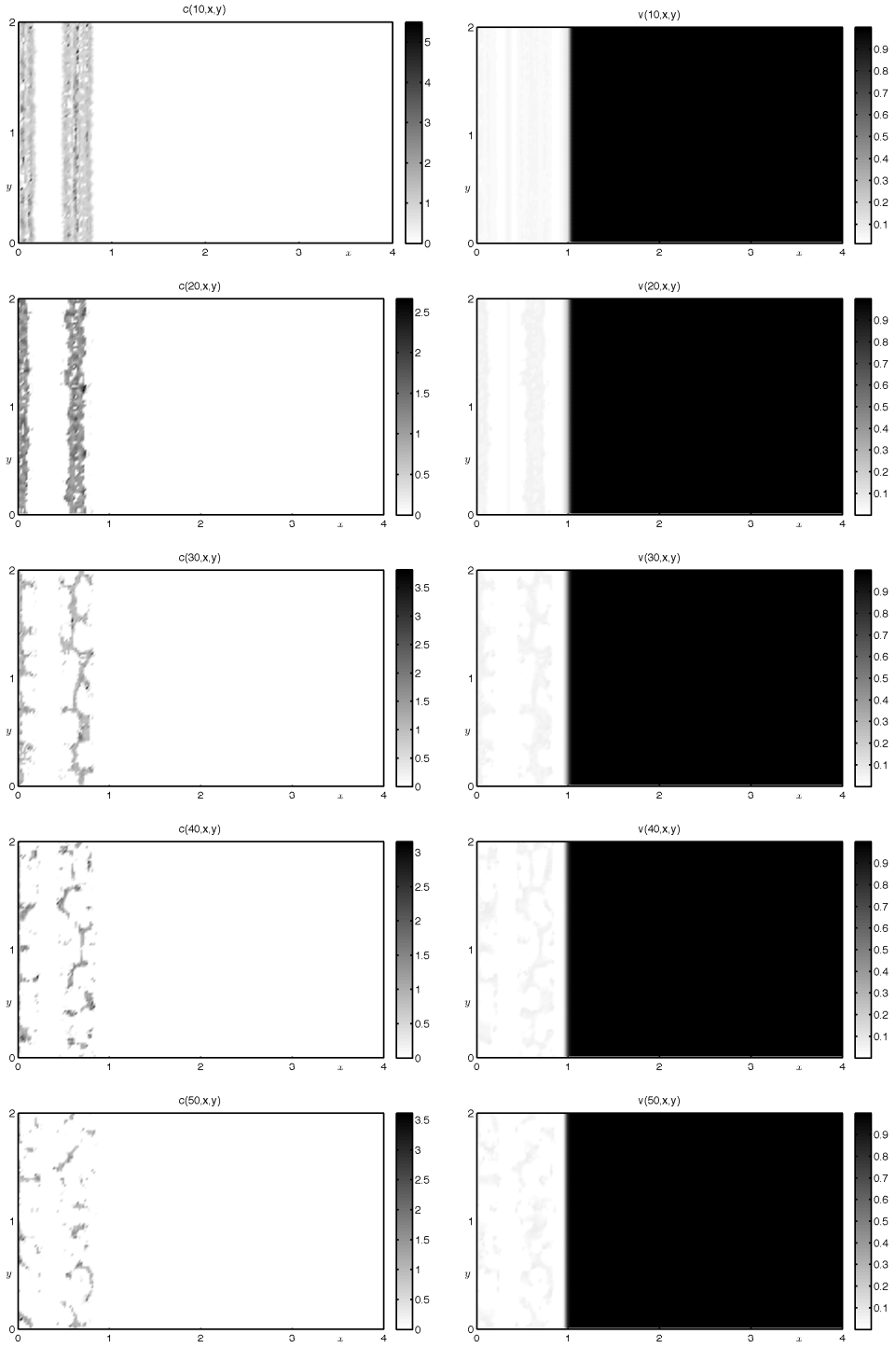

Figure 5.13: Plots showing the distribution of the cancer cell density $c(t,x,y)$ and matrix density $v(t,x,y)$ with parameter set $\mathscr{P}_{NL1}$ where we keep $S_{cv} = 0.1$ but increasing cell-cell adhesion S_{cc} to 0.5. We observe the effects of strong cell-cell adhesion.

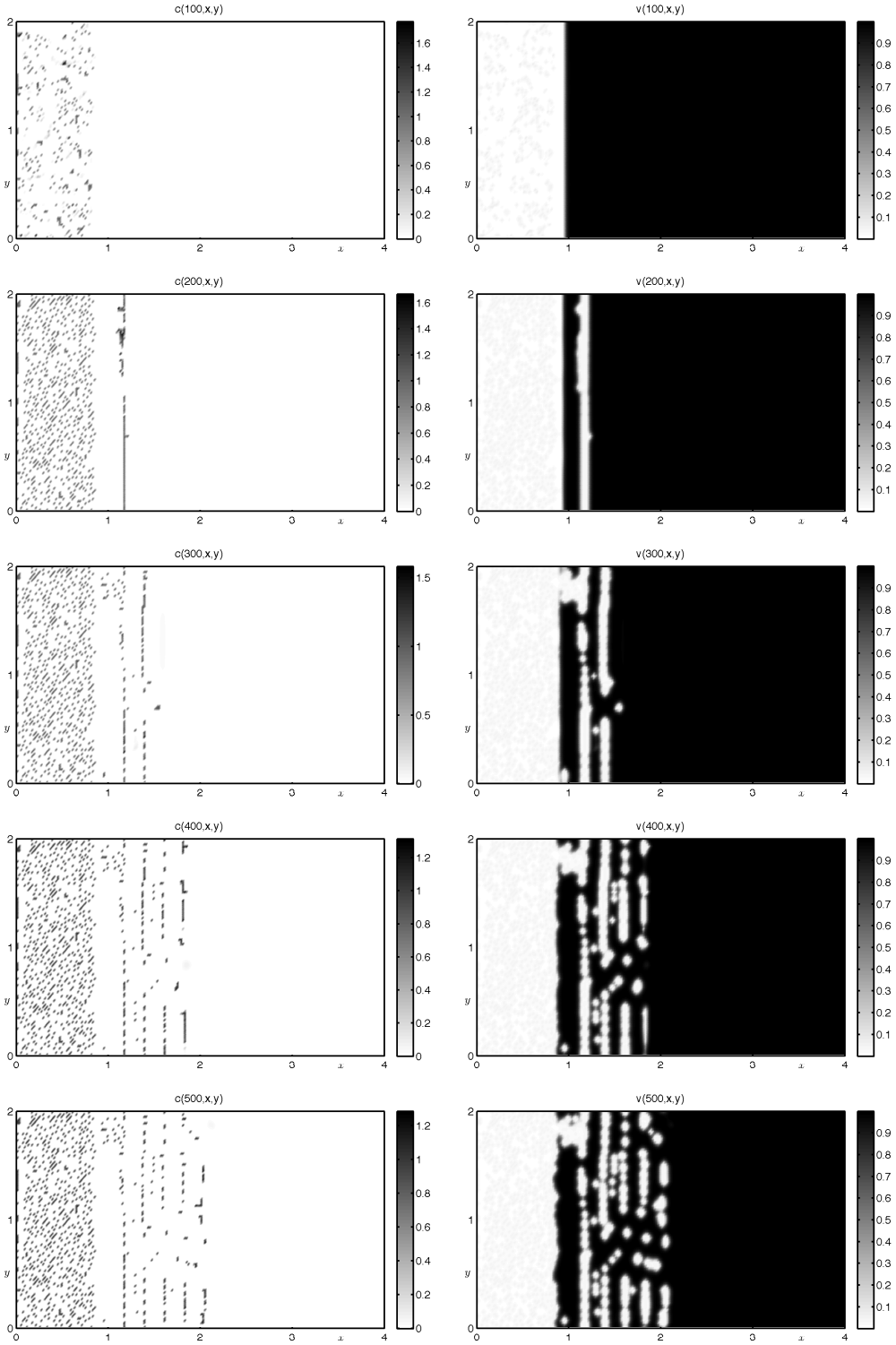

Figure 5.14: Continued from Fig. 5.13 for $t = 100$ to $t = 500$.

More interesting patterns emerge when cell-cell adhesion is increased to $S_{cc} = 0.1$ and cell-matrix adhesion is reduced to $S_{cv} = 0.01$. The solutions are shown in Fig. 5.15. Other parameter values remain the same as in parameter set $\mathscr{P}_{NL1}$. At time $t = 100$ we observe a slow movement of cell density because cells maintain strong attachment to other adjacent cells and less attachment to the extracellular matrix. Cells form high density regions along the domain boundaries where periodic boundary conditions are applied. The cell density along the boundaries moves faster than the cell density in the middle part of domain. If we compare these with the solutions in Figs. 5.12, the cell density in Fig. 5.15 progresses forward by keeping a tight connection within cells and the solutions look like the opposite of the solutions in Figs. 5.12 where cell density in the middle part refrain from moving forward fast. The strong cell-cell adhesion effects are also seen in the cell density near the initial position, where the cell density in that area is less deteriorated and it maintains its uniform steady state. In the matrix density we see less homogeneous degradation with a few spots of high matrix densities in the degraded area.

Different patterns emerge if cell-cell adhesion and cell-matrix adhesion are equally strong or equally weak. When the cell-cell adhesion and cell-matrix adhesion parameters are set to be sufficiently equally weak, such as $S_{cc} = S_{cv} = 0.01$, we see less pulling together and/or less spreading of cell density patterns as shown in Fig. 5.16. Until time $t = 100$ there seems to be a reluctance in the movement of cells, with very few advancing parts at the front observed. But at time $t = 200$ onwards we can see coherent movement, where the cell density moves forward due to cell-matrix adhesion and moves collectively due to cell-cell adhesion. The speed of invasion here is comparable with the simulations shown in Fig. 5.14. A uniform steady state cell density at the area of initial position is maintained, even until time $t = 500$.

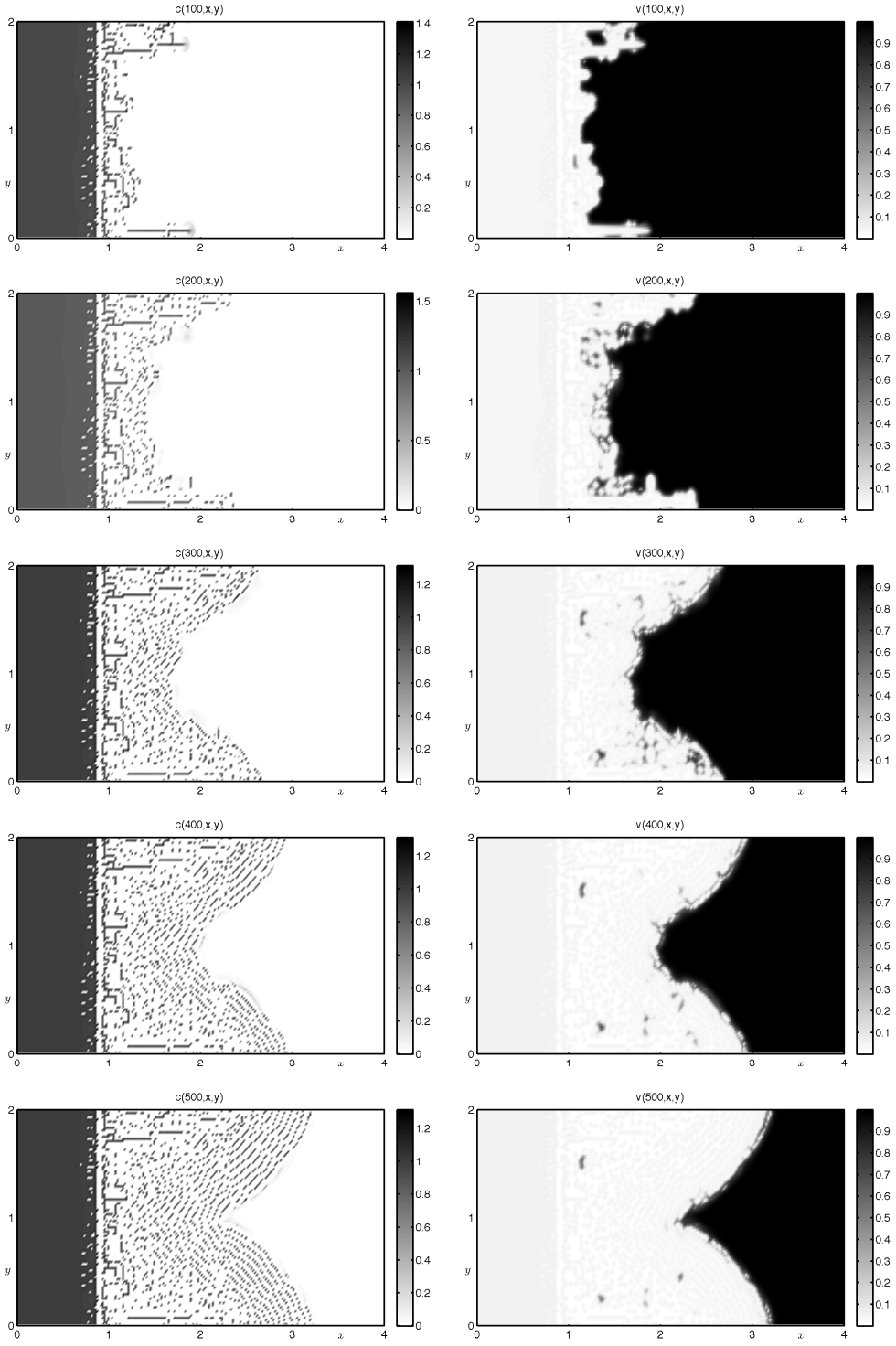

Figure 5.15: Plots showing the evolving of the cancer cell density $c(t,x,y)$ and matrix density $v(t,x,y)$ patterns with parameter set $\mathscr{P}_{NL}$, but cell-cell adhesion is increased to $S_{cc} = 0.1$ and cell-matrix adhesion is decreased to $S_{cv} = 0.01$.

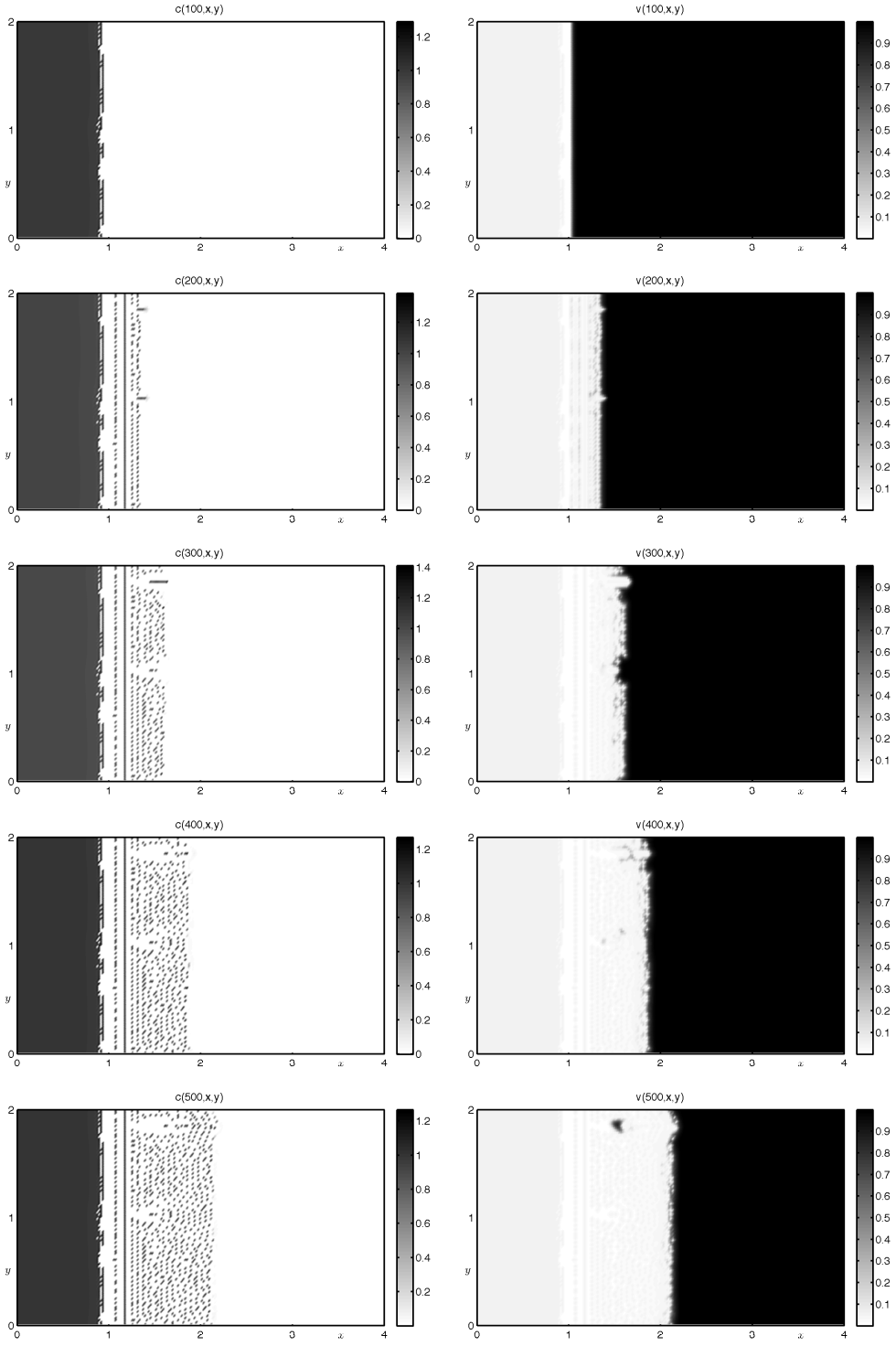

Figure 5.16: Plots showing the evolving patterns of the cancer cell density $c(t,x,y)$ and matrix density $v(t,x,y)$ with parameter set $\mathscr{P}_{NL1}$ and equally weak cell-cell and cell-matrix adhesion, $S_{cc} = S_{cv} = 0.01$.

Setting cell-cell and cell adhesion to be almost equally strong, such as $S_{cc} = S_{cv} = 0.1$ we get a completely different pattern of cell density, as seen in Fig. 5.17. Strong cell adhesion immediately destabilises the uniform steady state of cell density. Cells spread faster and form an irregular pattern. We conjecture that the irregular pattern is attributed to an intense competition between cell-cell and cell-matrix adhesion.

To classify how abnormal cancer cells look under a microscope and how quickly the tumour is likely to grow and spread, a measure called histologic grade or differentiation is used. Well-differentiated cells have tight junctions between cells as a result of strong cell-cell adhesion. They move collectively or in an epithelial manner and move at a slower rate. These cells resemble normal cells. Invasive cancer cells on the other hand are poorly differentiated because of a lack of structure and function of normal cells. They are less adherent due to lack of cell-cell adhesion and are moderately adherent to matrix for movement/invasion. They move in small clusters or colonies and spread faster. Varying parameters of cell-cell and cell-matrix adhesion has enabled us to mimic the patterns of cell spreading that might be exhibited from well-differentiated and poorly-differentiated cells.

In Fig. 5.18 we see the effects of decreasing chemotaxis and slightly increasing diffusion to the nonlocal system, by using parameter set $\mathscr{P}_{NL2}$ listed in Table 5.2. The chemotaxis due to uPA and PAI-1 is set to 10 times lower than the chemotaxis in the previous simulations, where now $\chi_u = 3.05 \times 10^{-3}$ and $\chi_p = 3.75 \times 10^{-3}$. Diffusion parameters are increased two times higher than the diffusion parameters of parameter set $\mathscr{P}_{NL1}$, except for the diffusion parameter of cancer cell density where it was chosen to be 1.3×10^{-5}. Using these parameters and setting cell-matrix adhesion higher than cell-cell adhesion results in a cell density solution that forms fingering-like pattern. We observe that the cell density advances by forming extending parts that are almost regular in shape and are expanding with the same length over time. The extending parts also form tips at the invading fronts whose size is slightly larger than the width of

the extending parts. It is also noticeable that the density of the tips is relatively high.

Intuitively, increasing diffusion parameters leads to the increase of the speed of the invasion of cell density. This is observable in Fig. 5.18 where the cell density has reached $x = 3$ at time $t = 250$ while it takes up to $t = 500$ for the cell density in the previous simulations (in Figs. 5.12 and 5.15) to reach the position. We notice here that chemotaxis plays less of a role in this simulation, because reducing the chemotactic parameters does not reduce the speed of cell invasion.

The diffusion and chemotaxis parameters in parameter set $\mathscr{P}_{NL2}$ are sensitive to the variation of cell adhesion parameters. If we reduce the cell-cell and cell-matrix adhesion parameters to $S_{cc} = 0.001$ and $S_{cv} = 0.01$, respectively, the speed of invasion also reduces where the invading fronts of cell density reach just before $x = 3$ at time $t = 500$. Also interesting here is that we observe a "mixed pattern" emerging as shown in Fig. 5.19. The cell density forms patterns that are a mixture of uniform, heterogeneous, and fingering-like patterns. Between the uniform pattern and fingering-like pattern, there is a transition pattern which is irregular in shape. Unlike the extending parts in the simulation of Fig. 5.18, there are no heads or tips that are larger than the width of the extending parts at the invading fronts.

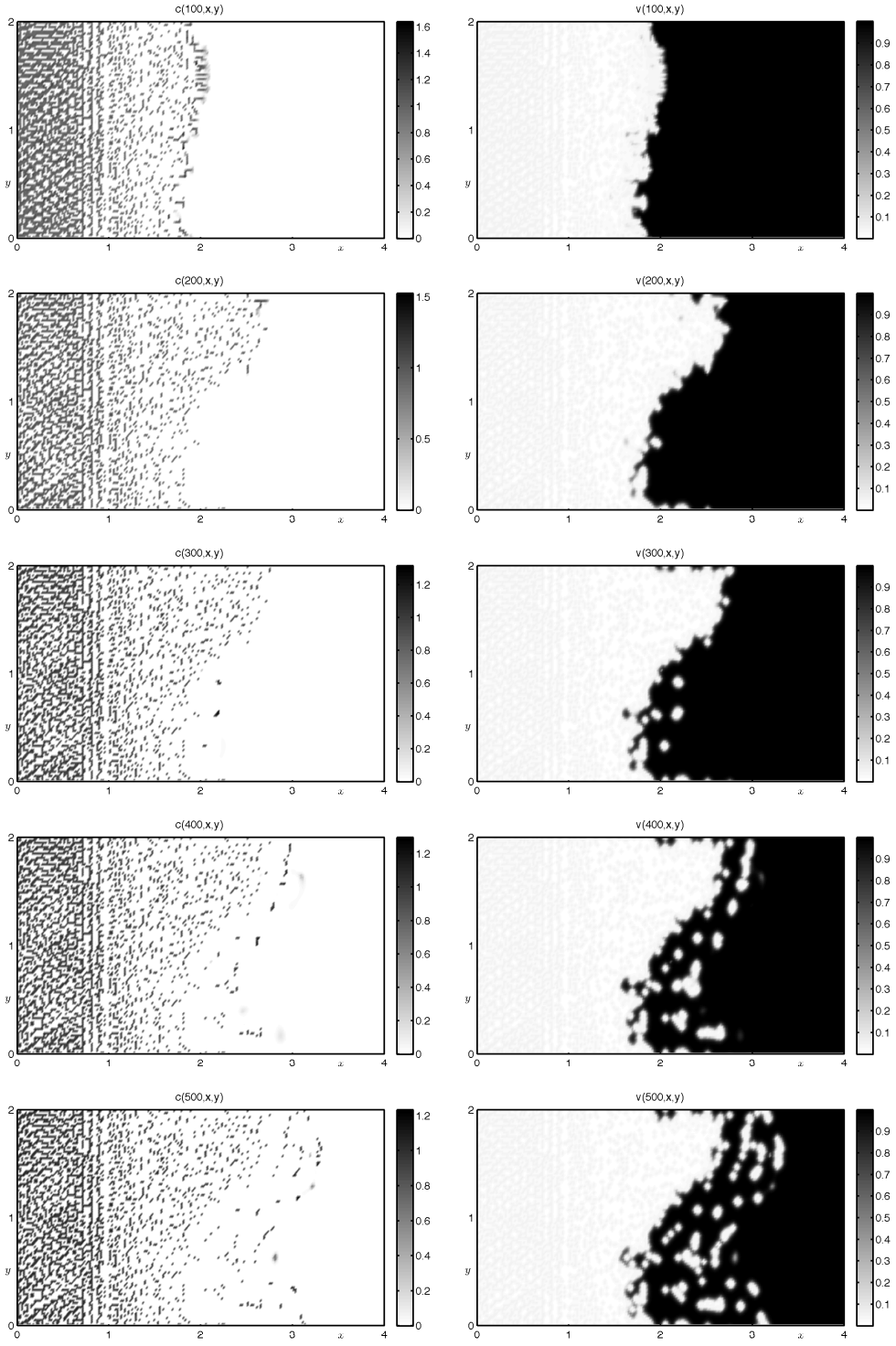

Figure 5.17: Plots showing the evolving patterns of the cancer cell density $c(t,x,y)$ and matrix density $v(t,x,y)$ with parameter set $\mathscr{P}_{NL1}$ and equally strong cell-cell and cell-matrix adhesion, $S_{cc} = S_{cv} = 0.1$.

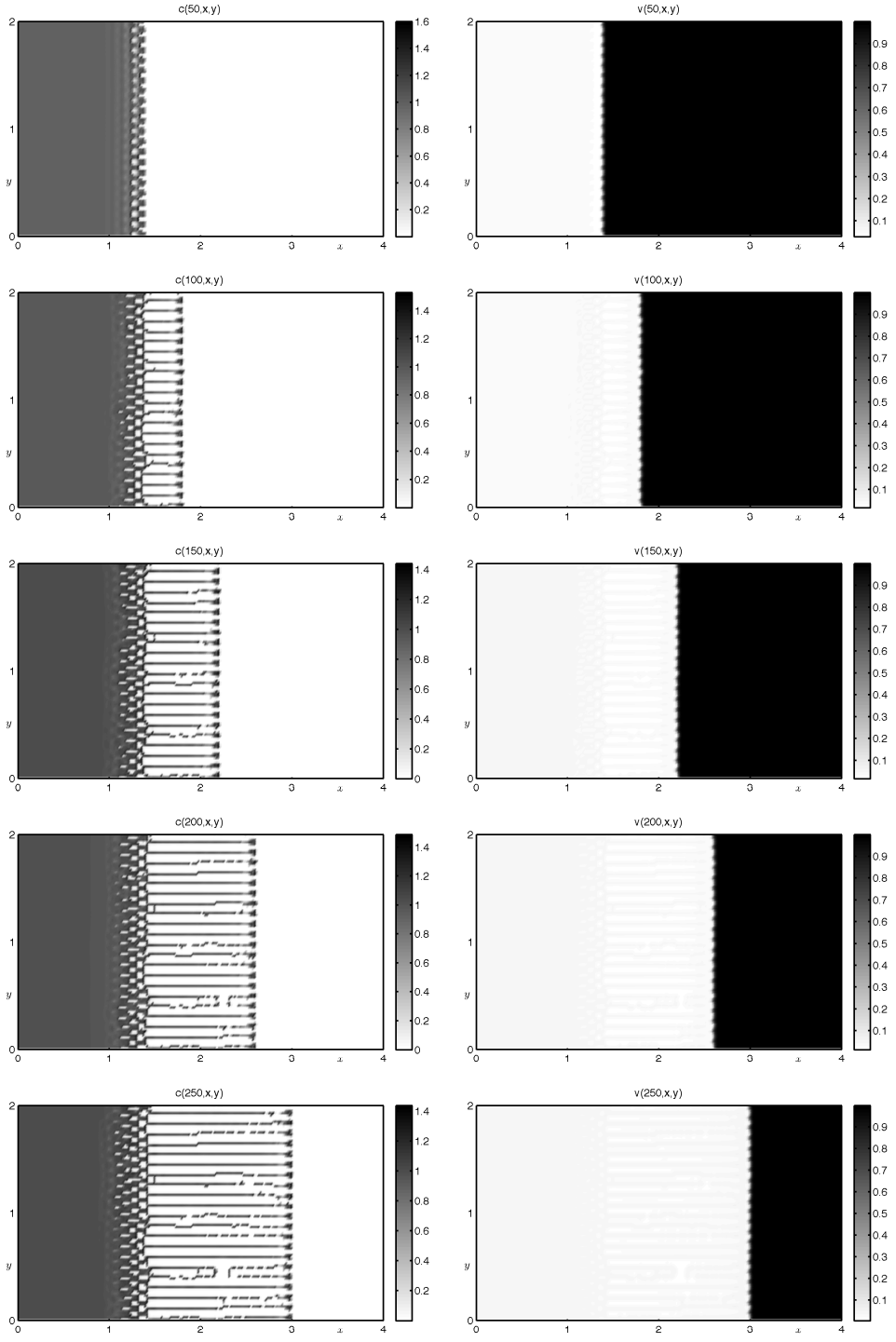

Figure 5.18: Plots showing a pattern of fingering of the cancer cell density $c(t,x,y)$ and the matrix density $v(t,x,y)$ with parameter set $\mathscr{P}_{NL2}$, where the diffusion parameters are increased and the chemotactic parameters are decreased, cell-cell adhesion $S_{cc} = 0.01$ and cell-matrix adhesion $S_{cv} = 0.1$. Plots are taken at $t = 50$, $t = 100$, $t = 150$, $t = 200$, and $t = 250$.

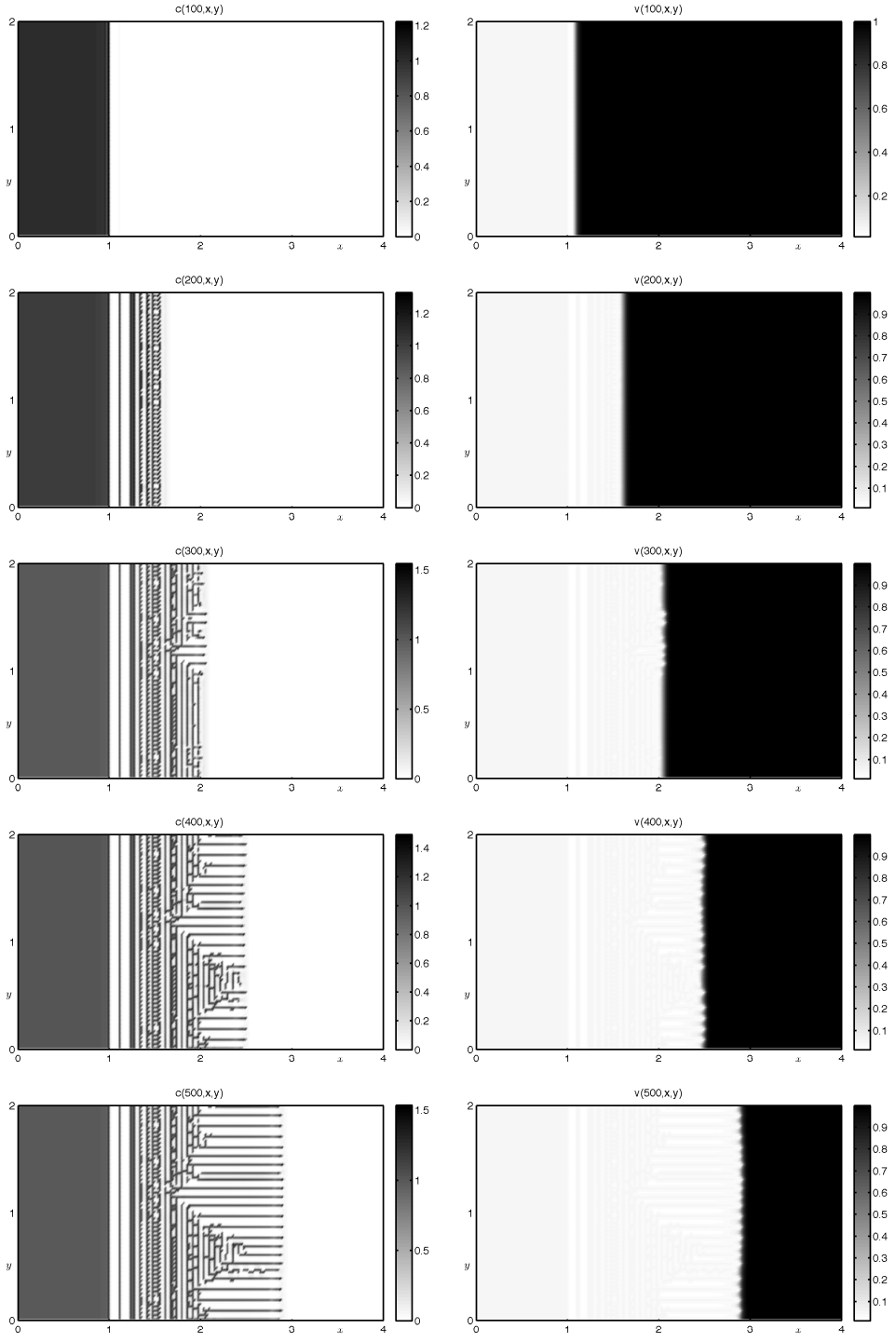

Figure 5.19: Plots showing a "mixed pattern" of the cancer cell density $c(t,x,y)$ and matrix density $v(t,x,y)$ with parameter set $\mathscr{P}_{NL2}$ and lowering cell adhesion parameters S_{cv} to 0.01 and S_{cc} to 0.001.

Invasion in a Heterogeneous Matrix

The *in vivo* structure of extracellular matrix is composed of 3 major classes of biomolecules: (1) structural proteins, such as collagen and elastin; (2) specialised proteins, such as fibrillin, fibronectin, and laminin; and (3) proteoglycans, which are composed of a protein core to which is attached long chains of repeating disaccharide units termed glycosaminoglycans (GAGs), forming extremely complex high molecular weight components of the matrix. There are also other glycoproteins including proteolytic enzymes involved in the degradation and remodelling of the extracellular matrix. These matrix macromolecule components are secreted locally and assembled into an organised meshwork. The relative amounts of the matrix molecules are varied and diverse, based on functional requirements of the particular tissue. Matrix is also under constant remodelling by simultaneous degradation and synthesis of matrix components with different turn-over rates. All of these give rise to heterogeneity in matrix density (Alberts et al., 2002).

Attempts to mathematically model the behaviour of cell movement in heterogeneous and anisotropic fibre networks using a continuum approach has been done previously, such as a model by Chauviere et al. (2007). In order to see the influence of complex matrix composition, or heterogeneous matrix, on our nonlocal model, we use two different types of heterogeneous matrix, as shown in Fig 5.20. The first type (left plot) has clusters of uneven high densities, formulated as

$$v_0 = \sum_{i=1}^{n} a_i \exp\left(-\left(\frac{(x-x_i)^2+(y-y_i)^2}{b_i}\right)\right), \tag{5.25}$$

where we choose arbitrarily $n = 21$ points (x_i, y_i) each with different values of a and b. The second type (right plot) consists of two stripes of high densities,

$$v_0 = m_0 + m_1 \cos\left(2\pi k_y \left(\frac{y-0.5}{L_y}\right)\right) \tag{5.26}$$

where for the $D_{2D} := (0,4) \times (0,2)$ domain we use $m_0 = 0.7, m_1 = 0.3, k_y = 2$, and $L_y = 2$.

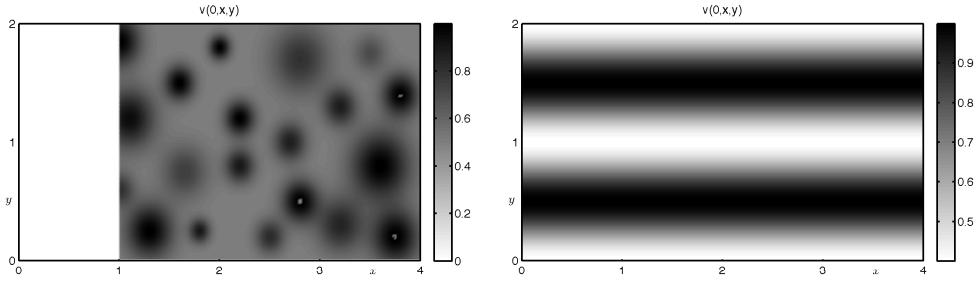

Figure 5.20: Plots showing the two types of heterogeneous matrix for simulations in Figs. 5.21 and 5.22.

To maintain the shape of the heterogeneous matrix throughout the simulations, in the following two simulations shown in Figs. 5.21 and 5.22 we reduce the value of matrix proliferation rate to $\mu_2 = 0.0001$. Due to the nature of our model, if we use the default value of $\mu_2 = 0.15$ the heterogeneous matrix composition will be deformed and the matrix density immediately returns to the uniform state, as the initial condition for matrix density in other previous simulations. The parameter values in parameter set $\mathscr{P}_{NL1}$ are used in these two simulations.

By using a heterogeneous matrix, we observe that cells tend to move or invade faster in regions of low matrix density although regions of high matrix density are eventually degraded. We also see that the pattern of degraded matrix follows the pattern of invading cells.

Since there are many regions of low matrix density, this enables cells to move faster and reach the other side of the domain in less than $t = 250$. Therefore, we deduce that the rate of invasion on heterogeneous matrix density is faster than that on homogeneous matrix density (uniform matrix density, $v = 1$).

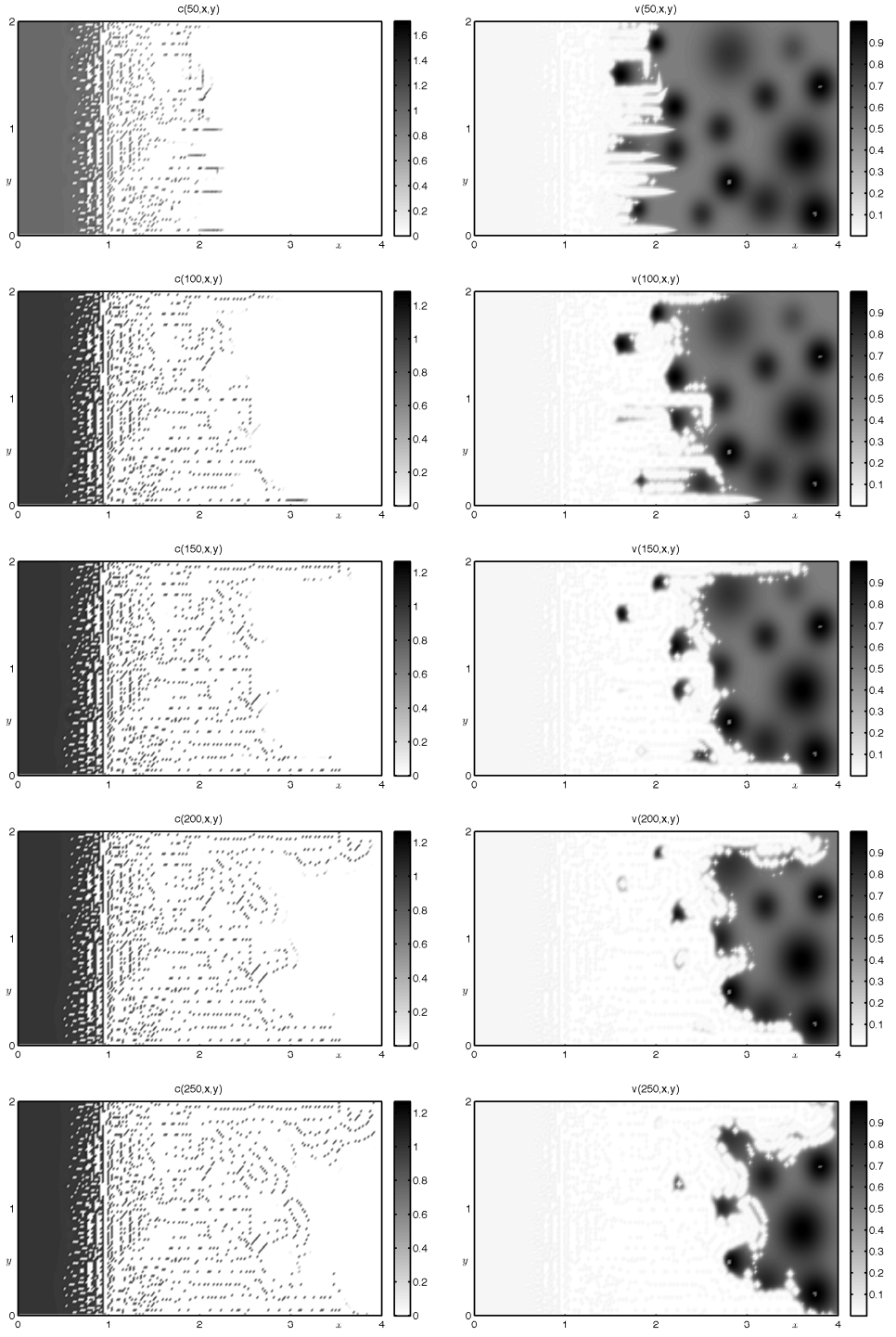

Figure 5.21: Plots showing the patterns that evolve from simulations with a heterogeneous matrix, where the initial condition of matrix is shown on the left figure of Fig. 5.20 at dimensionless times $t = 50$, $t = 100$, $t = 150$, $t = 200$, and $t = 250$ using parameter set $\mathscr{P}_{NL1}$.

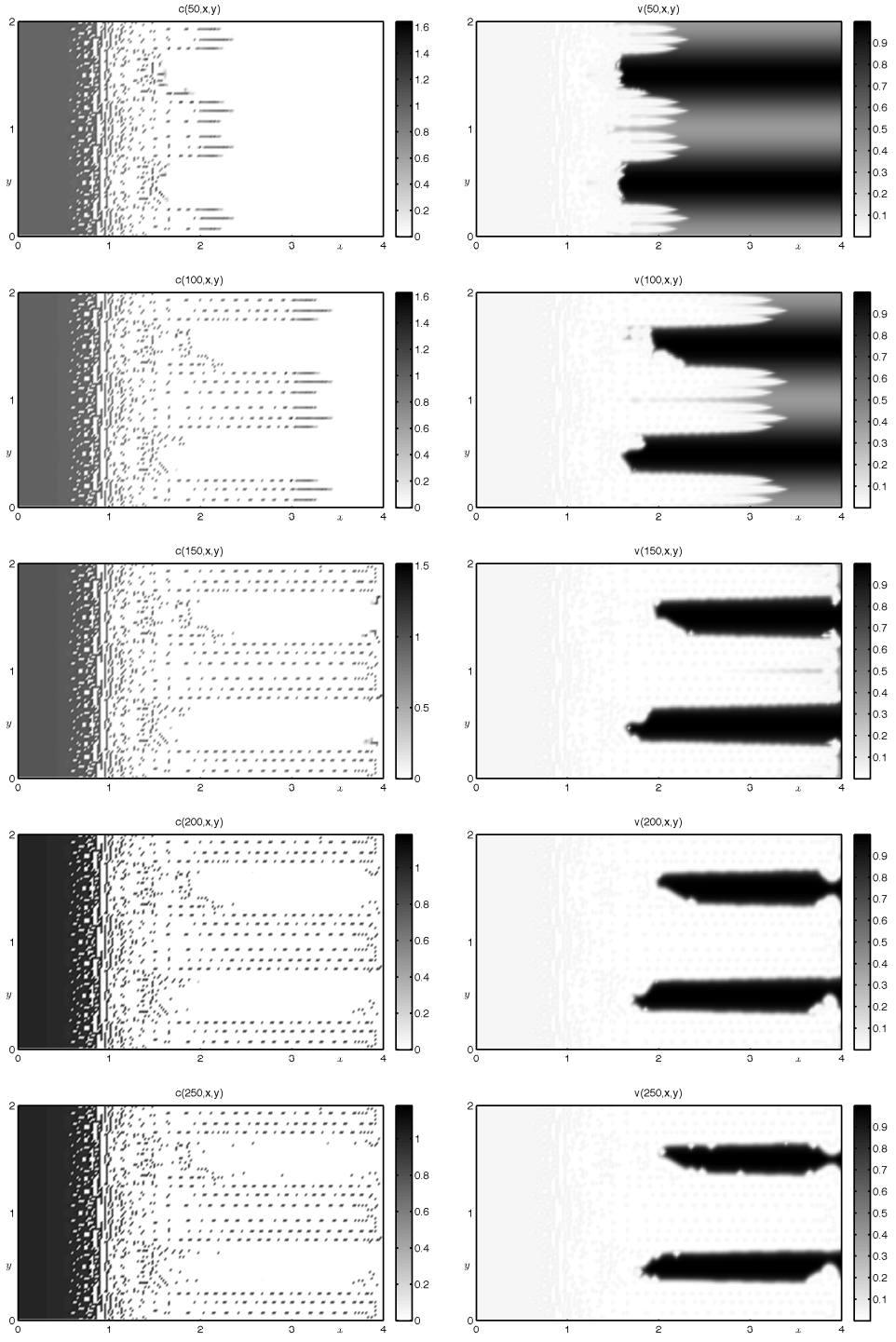

Figure 5.22: Plots showing the patterns that evolve from simulations with a heterogeneous matrix with two stripes as matrix initial condition as shown on the right figure of Fig. 5.20 at dimensionless times $t = 50$, $t = 100$, $t = 150$, $t = 200$, and $t = 250$ using parameter set $\mathscr{P}_{NL1}$.

Biphasic Dependence

There is a growing evidence that cell motility is regulated by the chemical and physical properties of extracellular matrix. The factors that govern whether cells migrate or not on extracellular matrix, and also their speed, depend on several variables related to interactions between cell surface protein integrins and matrix proteins (such as fibronectin), including integrin levels, surface density and distribution of matrix proteins, and binding affinities between integrin-matrix proteins (Palecek et al., 1997). Studies suggest that cell migration speed exhibits a biphasic dependence on the surface density of matrix protein, where the maximum speed of migration is attained at an intermediate level of physical distribution of matrix proteins, density or adhesiveness (Huttenlocher et al., 1996; Lauffenburger and Horwitz, 1996; Choquet et al., 1997; Palecek et al., 1997; Stahl and Mueller, 1997; Maheshwari et al., 1999, 200; Cox et al., 2001; Gobin and West, 2002; Hocking and Chang, 2003; Li et al., 2005; Peyton and Putnam, 2005; Khatiwala et al., 2006; Zaman et al., 2006; Silvestre et al., 2009). This implies that a significant increase in matrix protein density surrounding cells would lead to a drastic reduction of migration speed at a given level of motile force. The same effect also applies for very low matrix protein density, that causes very low anchorage for cells thus refraining from performing movement. Since the interactions between cells (or cell surface proteins) with matrix protein density result in adhesiveness or cell-matrix adhesion, it can also be stated that cell speed exhibits biphasic dependence on adhesive strength between cell and extracellular matrix.

In the nonlocal model (5.12) there are two separate variables for matrix density and cell-matrix adhesion. It is of interest to see the effects of biphasic dependence of cell speed on both matrix component density and cell-matrix adhesion to the nonlocal model, each applied independently. Plots of the biphasic manners are illustrated Fig. 5.23, where cell random motility parameter D_c is dependent on matrix density v (left plot) and on cell-matrix adhesion S_{cv} (right plot). We use a smooth step function

that models the biphasic manner, *i.e.*,

$$D_c(v) = D_c\left(\exp\left(-\frac{(v-0.5)^2}{0.05}\right)\right). \tag{5.27}$$

for D_c as a function of matrix density ranging from $[0,1]$, and

$$D_c(S_{cv}) = D_c\left(\exp\left(-\frac{(S_{cv}-0.1)^2}{0.002}\right)\right), \tag{5.28}$$

for D_c as a function of cell-matrix adhesion within a range $S_{cv} = [0, 0.2]$, where D_c is the default diffusion parameter in parameter set $\mathscr{P}_{NL1}$.

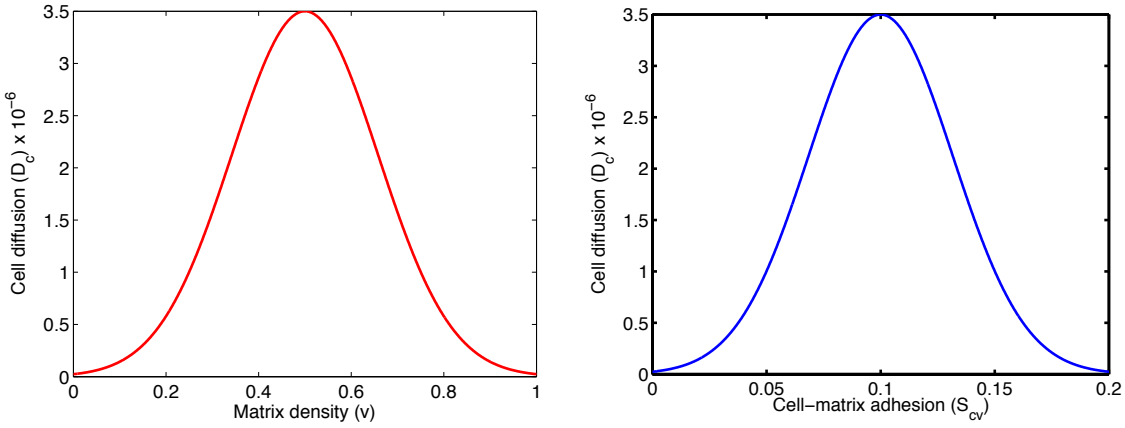

Figure 5.23: Plots illustrating the biphasic dependence of cell diffusion coefficient on matrix density (left) and on cell-matrix adhesion (right).

By using parameter set $\mathscr{P}_{NL1}$, if we apply the diffusion coefficient dependence on matrix density we get slightly slower movement for low and high matrix density compared to intermediate matrix density, as shown in Fig. 5.24 where all plots are taken at simulation time $t = 400$. The top plots show the dispersion of cells (left) on a uniformly low matrix density ($v = 0.2$) and the bottom plots for simulations using a high and uniform matrix density $(v = 1)$. Both simulations exhibit relatively slower movement of cells compared to the simulation with an intermediate uniform matrix density ($v = 0.5$) which is shown in middle figures. All simulations generate patterns that are similar to each other, although the shape of the invading fronts are slightly different.

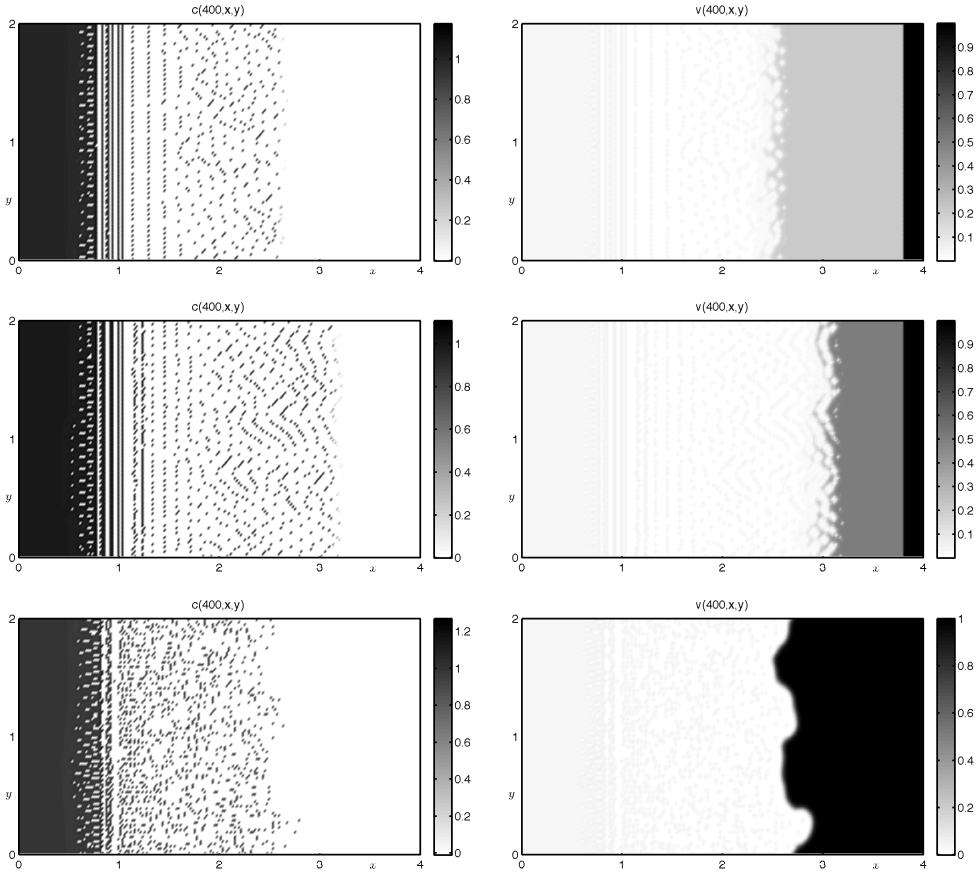

Figure 5.24: Plot showing the simulation results with biphasic dependence of the cell diffusion coefficient D_c on matrix density at time $t = 400$ using parameter set $\mathscr{P}_{NL1}$. Top figures show results of simulation with uniformly low matrix density ($v = 0.2$), middle figures for simulation with intermediate and uniform matrix density ($v = 0.5$), and bottom figures for simulation with high and uniform matrix density ($v = 1$).

A more significant difference in cell speed is seen in the simulations if the cell diffusion is a function of cell-matrix adhesion, as shown in Fig. 5.25. Based on the biphasic curve in Fig. 5.23 (right plot) where we randomly set the maximum cell-matrix adhesion 0.2, cell density attains its maximum speed at the intermediate adhesion $S_{cv} = 0.1$, shown by the middle plots of Fig. 5.25. At low cell-matrix adhesion, where we set $S_{cv} = 0.025$, the movement of cells is very slow, as shown by the top figures. It also occurs at high cell-matrix adhesion ($S_{cv} = 0.175$), shown by the bottom plots. All plots are taken at simulation time $t = 500$. Different patterns emerge here,

for biphasic dependence on cell-matrix adhesion. Simulation with low cell-matrix adhesion exhibits a pattern of cells that consists of uniform cell density (near the initial position area) and regular dispersion of cell density that moves forward invading matrix. The simulation with intermediate cell-matrix adhesion exhibits a combination of uniform cell density, connective cell density movement, and dispersion of clusters of cell density. While for high cell-matrix density we observe a pattern of cells that have dispersed throughout (destabilising uniform density) but moving very slow. There are also a few clusters of cell density forming at the invading front.

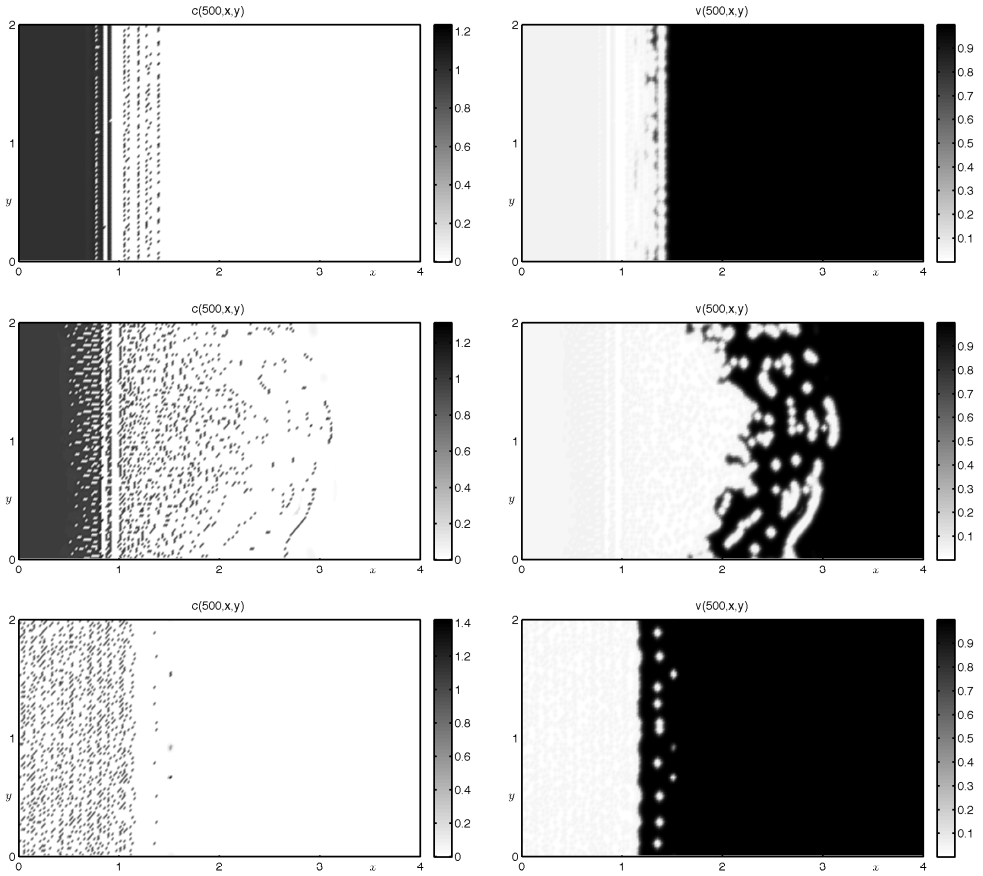

Figure 5.25: Plots showing the comparison of simulations with biphasic dependence of cell diffusion coefficient D_c on cell-matrix adhesion at time $t = 500$. Top figures show results of simulation with relatively low cell-matrix adhesion ($S_{cv} = 0.025$), middle figures for simulation with relatively intermediate cell-matrix adhesion ($S_{cv} = 0.1$), and bottom figures for simulation with relatively high cell-matrix adhesion ($S_{cv} = 0.175$).

Modified Cell Proliferation and Matrix Remodelling Terms

As it has been discussed in Chapter 4, in order to take into account the effect of space competition between cells and matrix, all motility, cell proliferation, and matrix remodelling terms are expressed with a carrying capacity effect that incorporates the limited spatial availability for competition between cells and matrix, where the equations for cancer cells and the extracellular matrix now become

$$\frac{\partial c}{\partial t} = \underbrace{D_c \nabla^2 c}_{\text{random motility}} \underbrace{-\nabla \cdot \left(\frac{c}{R} \int_{-R}^{R} (S_{cc}c + S_{cv}v)(1-c-v)\Omega(r)dr \right)}_{\text{adhesive movement}} - \underbrace{\nabla \cdot (\chi_u c(1-c-v)\nabla u)}_{\text{uPA-chemotaxis}}$$

$$- \underbrace{\nabla \cdot (\chi_p c(1-c-v)\nabla p)}_{\text{PAI-1-chemotaxis}} + \underbrace{\mu_1 c(1-c-v)}_{\text{proliferation}}, \tag{5.29a}$$

$$\frac{\partial v}{\partial t} = - \underbrace{\delta v m}_{\text{degradation}} + \underbrace{\phi_{21} p u}_{\text{uPA/PAI-1}} - \underbrace{\phi_{22} p v}_{\text{PAI-1/VN}} + \underbrace{\mu_2 v(1-c-v)}_{\text{remodelling}}, \tag{5.29b}$$

subject to the given initial and boundary conditions given previously. Here we use a slightly different form for matrix remodelling than that in (4.16b) where the remodelling term is given by $\mu_2(1-c-v)$. Here in (5.29b) we propose a form of $\mu_2 v(1-c-v)$ for matrix remodelling which takes the same form as cell proliferation.

Simulation results using the new form for cell proliferation and matrix remodelling using parameter set $\mathscr{P}_{NL1}$ exhibit cells whose uniform density pattern breaks and progresses forward very little, as shown in Fig. 5.26. We notice that at dimensionless times $t = 500$ and $t = 1000$ the cell density remains almost at the same position. Assuming it is due to diffusion coefficients that are too small for the modified proliferation and remodelling terms and hence prevent the cells from moving, we increased the diffusion coefficients in $\mathscr{P}_{NL1}$ 10 times higher, that is to $D_c = 3.5 \times 10{-}5, D_u = 2.5 \times 10^{-4}, D_p = 3.5 \times 10^{-4}$, and $D_m = 4.91 \times 10^{-4}$. Now the cell density exhibits movement as shown in Fig. 5.27. The cells invade the matrix and spread as clusters. Matrix that has been degraded shows darker area, indicating high matrix remodelling.

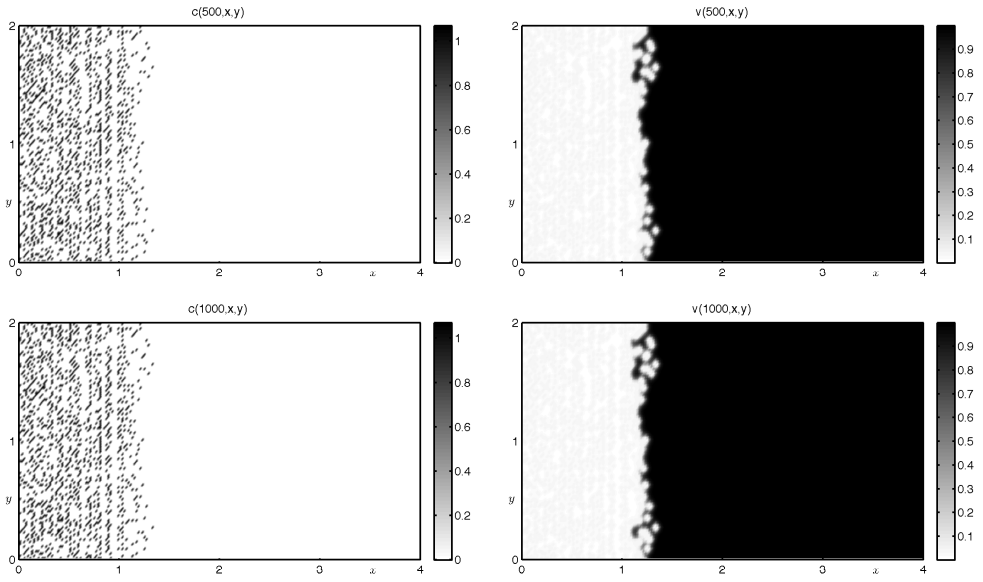

Figure 5.26: Plots showing simulation results using a modified form of cell proliferation and matrix remodelling as in (5.29) with parameter set $\mathscr{P}_{NL1}$ at dimensionless time $t = 500$ (top figures) and $t = 1000$ (bottom figures). Left figures show cancer cell density and right figures show matrix density.

That the modified cell proliferation and matrix remodelling terms slow down cancer cell invasion is also shown in simulation results in Fig. 4.13 of Chapter 4.

5.6 Discussion and Conclusions

In this chapter we have presented an extensive mathematical model of cancer cell invasion of tissue that combines the roles of proteolysis and cell adhesion. We used the urokinase-type plasminogen activator (uPA) model that was presented and analysed in Chapter 4 as a base model and extended it with adhesion properties by incorporating an adhesive movement term in the equation for cancer cell density. The adhesive movement term is nonlocal (in space) and it comprehensively accounts for adhesiveness between cell and cell or cell-cell adhesion and adhesiveness between cell and extracellular matrix or cell-matrix adhesion. This adhesive movement term (nonlocal term) replaces the haptotactic term used in the uPA model for gradient movement of cells

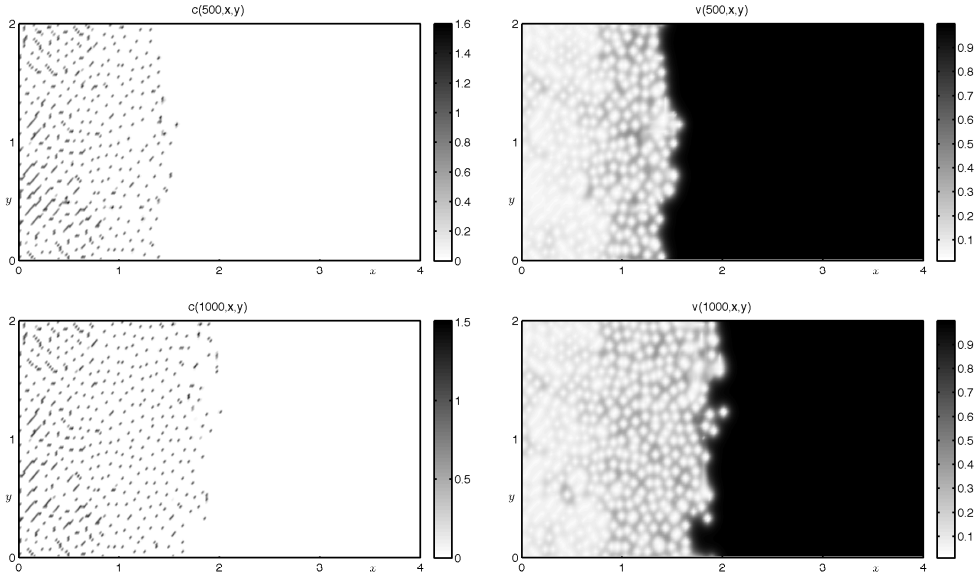

Figure 5.27: Plots showing simulation results using the modified cell proliferation and matrix remodelling terms in (5.29) with increased diffusion coefficients, where here $D_c = 3.5 \times 10{-}5, D_u = 2.5 \times 10^{-4}, D_p = 3.5 \times 10^{-4}$, and $D_m = 4.91 \times 10^{-4}$ at dimensionless times $t = 500$ (top figures) and $t = 1000$ (bottom figures). Left figures show cancer cell density and right figures show matrix density.

toward matrix components. The extended model (or nonlocal model) is biologically more realistic and it resembles local invasion of cancer cells of tissue where malignant tumour cells or cancer cells must detach from the main tumour body, degrade surrounding tissue and migrate through the tissue (Liotta, 1986).

In order to account for population pressure or increased crowding in cell and matrix density we used a volume filling mechanism in the motility terms, *i.e.*, the adhesive movement and chemotaxis terms. With the volume filling term, aggregation is limited by available space in which the movement should decrease with increasing total density of cell and matrix. Although the use of volume filling may result in no heterogeneous spatial patterns or only travelling-wave like patterns of the solutions, with linear stability analysis it is possible to determine the parameters that drive the dispersion relation to go to an unstable regime or at least close to instability. It was revealed by a linear stability analysis that decreasing diffusion parameters may lead to a finite range of positive eigenvalues, which is the requirement for generation of spatial patterns. We chose

the range of diffusion parameters between 3.5×10^{-6} for cell diffusion to 2.5×10^{-5} for uPA diffusion, which are 100 times lower than the diffusion parameters used in Chapter 4. These diffusion parameters yield a dispersion relation curve that is close to the "unstable " dispersion relation curve shown in Fig 5.2. It is the aim of our future work to carry out a nonlinear stability analysis of the nonlocal model.

We have seen in Chapter 5.5 the effects of cell adhesion in the uPA system, where varying cell adhesion parameters in the nonlocal system (5.12) exhibits various patterns of cell movement or dispersion, particularly for simulations on a 2-dimensional spatial domain. Cell adhesion also influences the speed of movement. Experimentally it has been proposed that aside from the cancer cell environment, properties of cancer cells such as cell adhesion, may influence the patterns of spread and growth (Fidler, 1978). As we have discussed in Chapter 4, the depth and pattern of invasion are two key features of cancer cell invasion. Using the nonlocal model, by tuning cell-cell and cell-matrix adhesion parameters it is possible to obtain patterns that mimic invasion behaviours in organotypic culture, such the experimental data in Fig. 4.14 and patterns in Nyström et al. (2005). There is also a degree of freedom in adjusting cell adhesion parameters to generate proper invasion speed or invasion depth. These aspects may lead to possible generation of a numerical "Invasion Index" based on a mathematical model.

As has been discussed in section 4.6 of Chapter 4, by using different sub-populations of cancer cells (cf. cancer as a progressive disease), here we present the "mutation pathway" into the nonlocal model and the equations for cell densities c_1 (less invasive) and c_2 (more invasive) are given by

$$\frac{\partial c_1}{\partial t} = \underbrace{D_{c_1}\nabla^2 c_1}_{\text{random motility}} \underbrace{-\nabla\cdot\left(\frac{c_1}{R}\int_{-R}^{R}(S_{cc_1}c_1+S_{cv_1}v)(1-c-v)\Omega(r)dr\right)}_{\text{adhesive movement}}$$

$$\underbrace{-\nabla\cdot(\chi_{u_1}c_1(1-c-v)\nabla u)}_{\text{uPA-chemotaxis}} \underbrace{-\nabla\cdot(\chi_{p_1}c_1(1-c-v)\nabla p)}_{\text{PAI-1-chemotaxis}}$$

$$+\underbrace{\mu_{11}c_1(1-c-v)}_{\text{proliferation}} - \underbrace{\lambda c_1 F(t,v)}_{\text{conversion to } c_2}\ , \tag{5.30a}$$

$$\frac{\partial c_2}{\partial t} = \underbrace{D_{c_2}\nabla^2 c_2}_{\text{random motility}} \underbrace{-\nabla\cdot\left(\frac{c_2}{R}\int_{-R}^{R}(S_{cc_2}c_2+S_{cv_2}v)(1-c-v)\Omega(r)dr\right)}_{\text{adhesive movement}}$$

$$\underbrace{-\nabla\cdot(\chi_{u_2}c_2(1-c-v)\nabla u)}_{\text{uPA-chemotaxis}} \underbrace{-\nabla\cdot(\chi_{p_2}c_2(1-c-v)\nabla p)}_{\text{PAI-1-chemotaxis}}$$

$$+\underbrace{\mu_{12}c_2(1-c-v)}_{\text{proliferation}} + \underbrace{\lambda c_1 F(t,v)}_{\text{conversion from } c_1}\ , \tag{5.30b}$$

where D_{c_1}, S_{cc_1}, S_{cv_1}, μ_{11} all have the values as in parameter set $\mathscr{P}_{NL1}$ and the parameters for more invasive cells c_2 are: $D_{c_2} = 4.5\times10^{-6}$, $S_{cc_2} = 0.005$, $S_{cv_2} = 0.2$, $\mu_{12} = 0.5$ with exception χ_{u_2} and χ_{p_2} which we set the same as the chemotactic parameters in parameter set $\mathscr{P}_{NL1}$. These parameters for more invasive cells represent higher cell motility, reduced cell-cell adhesion and increased cell-matrix attachment for more motile cells, and higher rate of proliferation. The cells are converted from less invasive into more invasive with rate $\lambda = 0.1$. The conversion function F is given by

$$F(t,v) = H(60<t<70)\cdot H(v-0.3)\,. \tag{5.31}$$

The conversion function that we choose here is slightly different that in (4.18), where in (5.31) the conversion time from less invasive cells c_1 to more invasive/malignant cells c_2 is limited to occur only between $t > 60$ and $t < 70$. The results of the computational simulations for the "mutation pathway" mechanism are shown in Fig. 5.28.

The top figure shows the progression of the less invasive cell density c_1, the middle figure with the more invasive cell density c_2, and the extracellular matrix density at the bottom. At dimensionless time $t = 500$ cells of sub-population 2 (c_2) which are more invasive spread and invade the matrix faster and disperse more (less crowded) than cells of sub-population 1 (c_1).

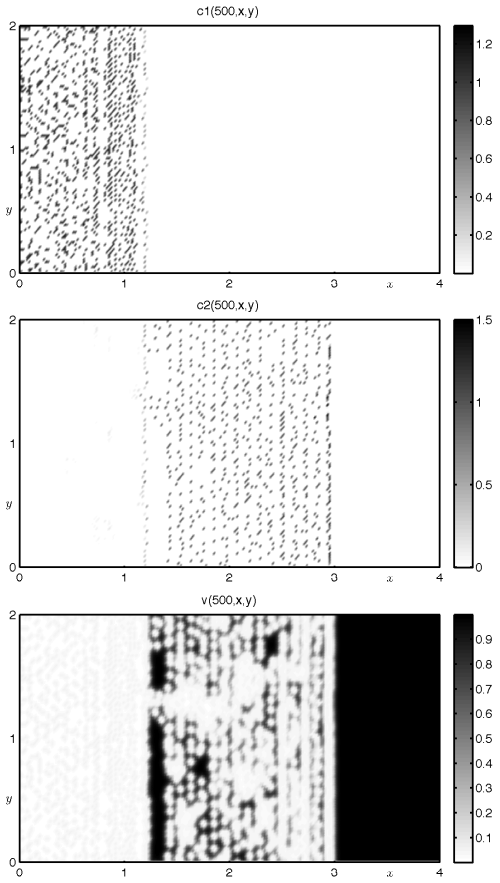

Figure 5.28: Plots showing the simulation results using different sub-populations of cancer cells as in (5.30), where cells of sub-population 2 (middle figure) are more invasive than cells of sub-population 1 (top figure). Parameters for cells of sub-population 1 are as in parameter set $\mathscr{P}_{NL1}$ and the parameters for more invasive cells are: $D_{c_2} = 4.5 \times 10^{-6}$, $S_{cc_2} = 0.005$, $S_{cv_2} = 0.2$, $\mu_{12} = 0.5$.

With the results achieved in this chapter, we believe that the nonlocal model offers a deeper understanding of the processes involved in cancer cell invasion, particularly adhesion processes that are clinically and experimentally very complex but is crucial to understand for cancer studies and improving cancer treatment strategies. Although

the present model provides a suitable level of sophistication and complexity to discuss important features of cancer cell invasion, there are still many other known processes that we do not explicitly account for, such as genetic mutations and signal transduction pathways. Incorporation of such intracellular and genetic events in a genuine multi-scale model is the next big challenge appearing on the modelling horizon.

5.6.1 Comments on the Numerical Scheme and Validation of the Simulation Results

In this final section, we would like to add some notes concerning the numerical validity of the simulations presented in this chapter. It is necessary to examine the behaviour of the numerical simulations as we use finer spatial grids to demonstrate whether the numerical simulations we have presented are the products of genuine model behaviour or whether there are numerical artefacts involved. For 1D simulations, as we have mentioned in subsection 5.5.1, all simulations were performed using a grid spacing of size $\Delta x = 0.01$. Here we look at simulations results obtained by using grid spacings of size $\Delta x = 0.005$ and $\Delta x = 0.0025$. For 2D simulations, the numerical validation is performed by using a finer grid spacing of size $\Delta x = \Delta y = 0.01$ to compare with the results in subsection 5.5.2 which used a grid spacing of size $\Delta x = \Delta y = 0.02$.

Fig. 5.29 shows the results of 1D simulation using a grid spacing of size $\Delta x = 0.005$ for comparison with the results in Fig. 5.4 where the diffusion coefficients used are $D_c = 3.5 \times 10^{-4}$, $D_u = 2.5 \times 10^{-3}$, $D_p = 3.5 \times 10^{-3}$, and $D_m = 4.91 \times 10^{-3}$. For even smaller grid spacings of size $\Delta x = 0.0025$ the results are shown in Fig. 5.30. We can see that the simulation results for finer grids with grid spacings of sizes $\Delta x = 0.005$ and $\Delta x = 0.0025$ behave the same as the results using grid spacings of size $\Delta x = 0.01$.

The little hump at the invading front is suspected to be a genuine consequence of the nonlocal expression, where $S_{cv} = 0.1$ and $S_{cc} = 0.01$. If we swap the values of S_{cv} and S_{cc}, as shown in Figs. 5.31 and 5.32, where now $S_{cv} = 0.01$ and $Scc = 0.1$, the

invading front changes shape.

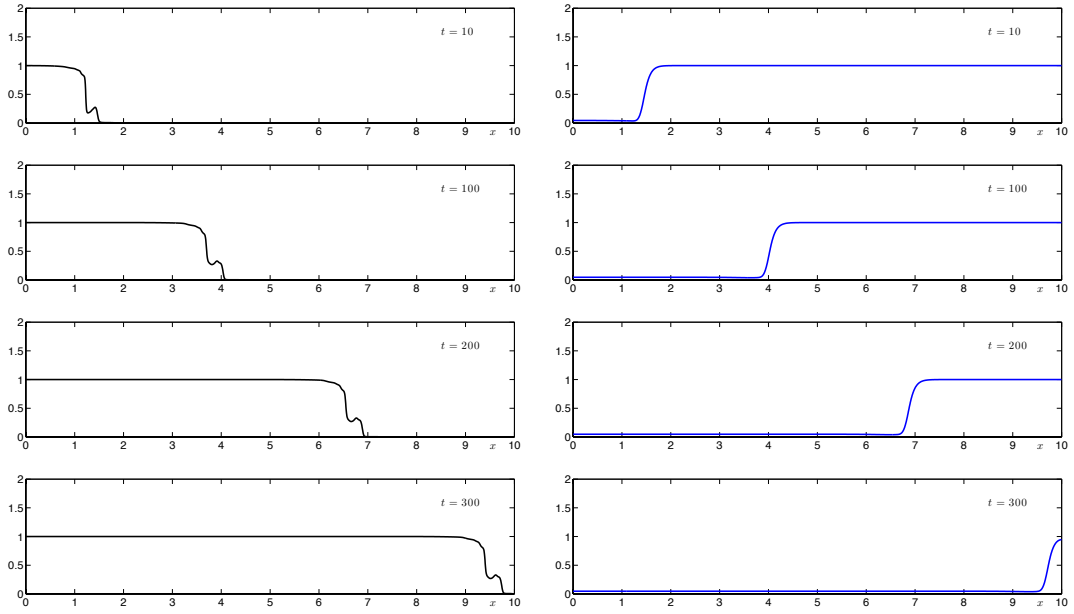

Figure 5.29: Sequence of profiles showing the spatio-temporal evolution of cancer cells c (black, left figures) invading the ECM v (blue, right figures). Here we use a grid spacing of size $\Delta x = 0.005$ and diffusion coefficients $D_c = 3.5 \times 10^{-4}$, $D_u = 2.5 \times 10^{-3}$, $D_p = 3.5 \times 10^{-3}$, and $D_m = 4.91 \times 10^{-3}$, and $S_{cv} = 0.1$ and $S_{cc} = 0.01$.

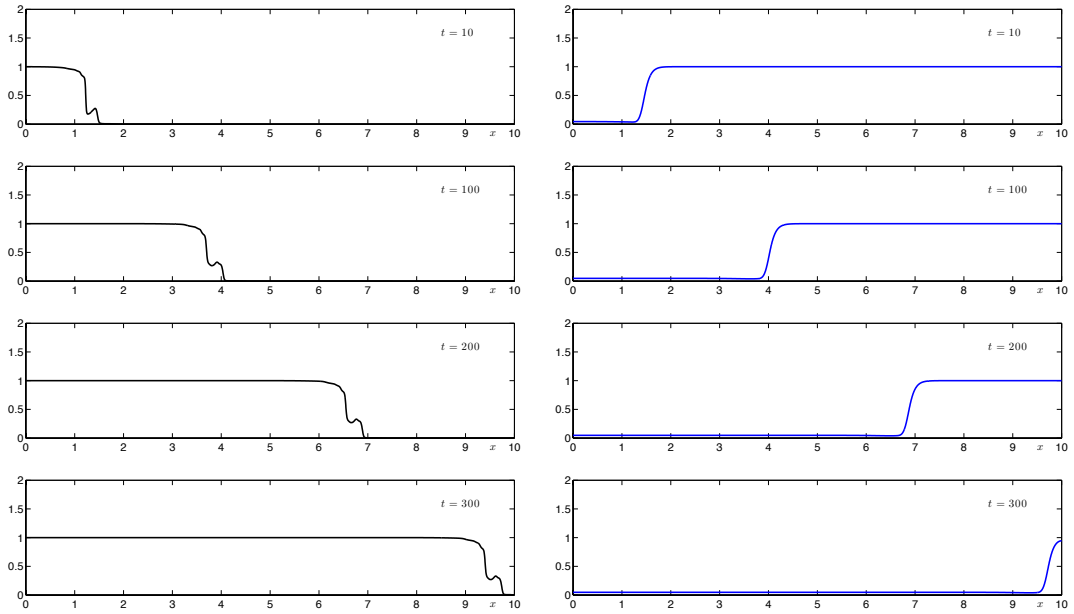

Figure 5.30: Sequence of profiles of cancer cells c (black, left figures) invade the ECM v (blue, right figures) using a grid spacing of size $\Delta x = 0.0025$ for comparison with Fig. 5.4. The other parameters remain the same as in Fig. 5.4 and/or Fig. 5.29.

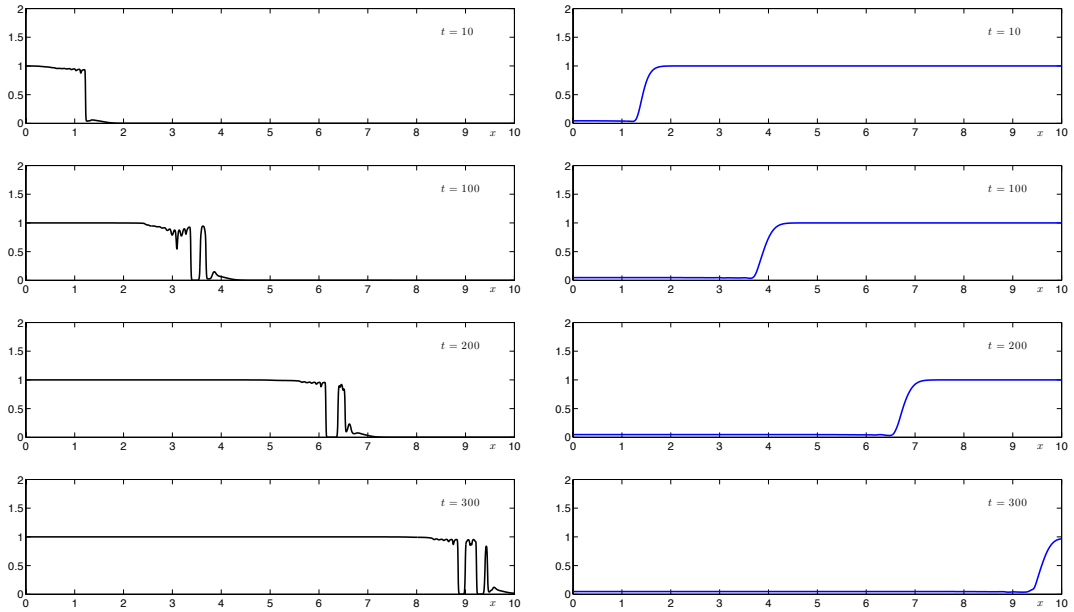

Figure 5.31: Sequence of profiles showing the spatio-temporal evolution of cancer cells c (black, left figures) invading the ECM v (blue, right figures) using $S_{cv} = 0.01$ and $S_{cc} = 0.1$ with a grid spacing of size $\Delta x = 0.005$ and diffusion coefficients $D_c = 3.5 \times 10^{-4}$, $D_u = 2.5 \times 10^{-3}$, $D_p = 3.5 \times 10^{-3}$, and $D_m = 4.91 \times 10^{-3}$.

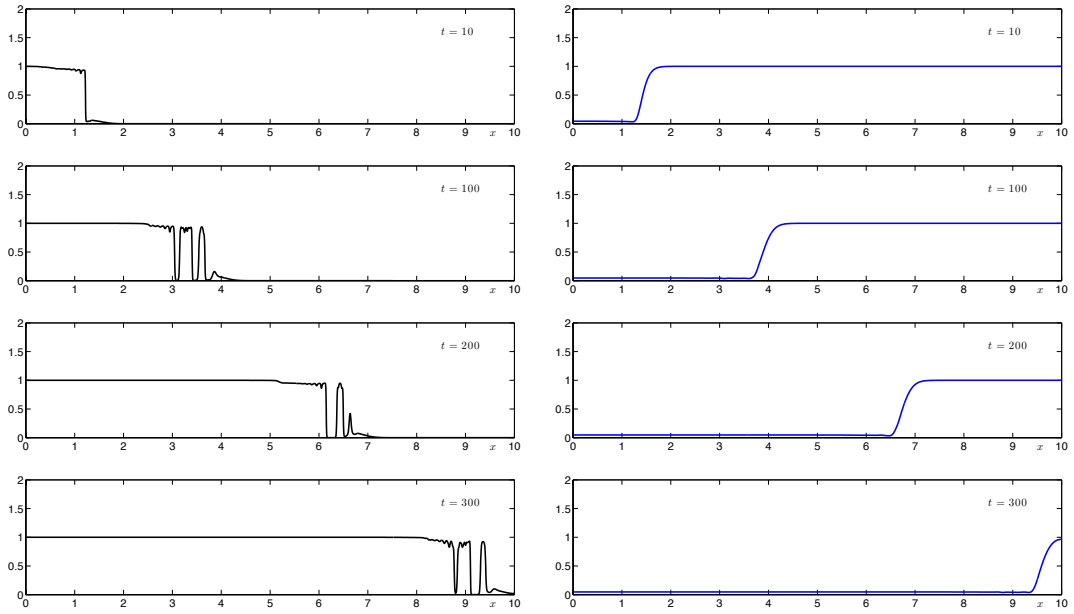

Figure 5.32: Sequence of profiles showing the spatio-temporal evolution of cancer cells c (black, left figures) invading the ECM v (blue, right figures) using $S_{cv} = 0.01$ and $S_{cc} = 0.1$ with a grid spacing of size $\Delta x = 0.0025$ and other parameters used are the same as in simulations in Fig. 5.31.

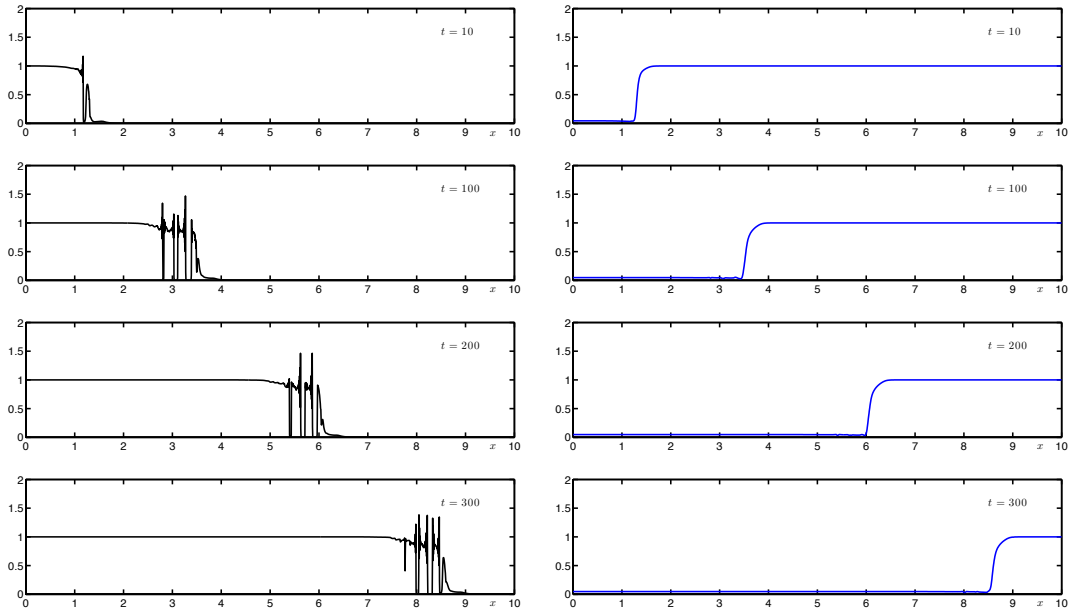

Figure 5.33: Sequence of profiles showing the spatio-temporal evolution of cancer cells c (black, left figures) invading the ECM v (blue, right figures) for comparison with Fig. 5.6 where here the grid spacing is size $\Delta x = 0.005$ and diffusion coefficients $D_c = 3.5 \times 10^{-5}$, $D_u = 2.5 \times 10^{-4}$, $D_p = 3.5 \times 10^{-4}$, and $D_m = 4.91 \times 10^{-4}$, and $S_{cv} = 0.1$ and $S_{cc} = 0.01$.

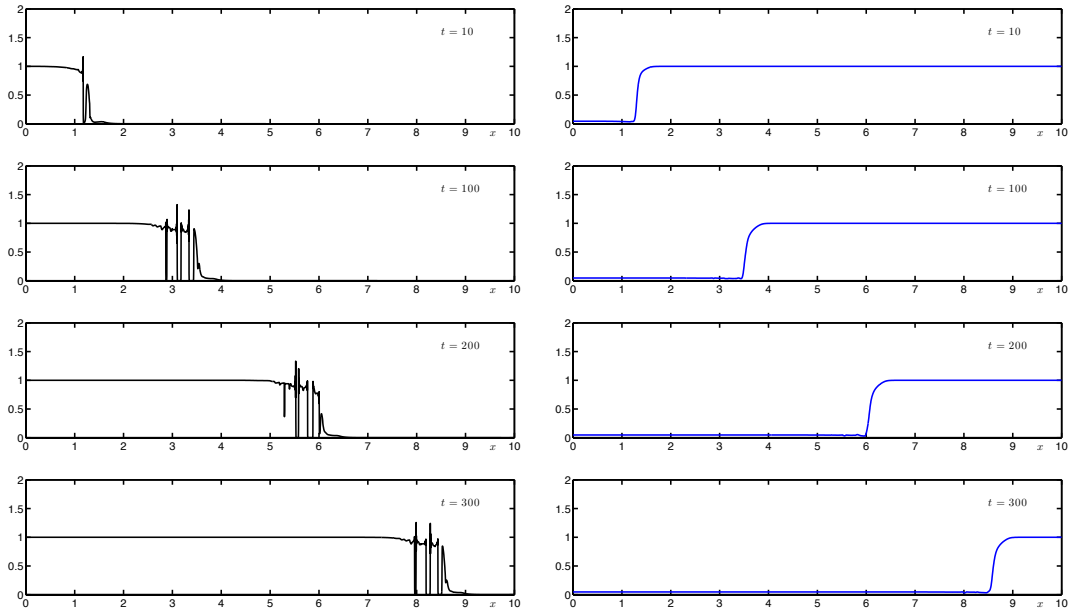

Figure 5.34: Sequence of profiles showing the spatio-temporal evolution of cancer cells c (black, left figures) invading the ECM v (blue, right figures) for comparison with Fig. 5.6 as a numerical validation with a grid spacing of size $\Delta x = 0.0025$. The other parameters remain the same as in Fig. 5.6 and/or Fig. 5.33.

The numerical simulations behave slightly differently for the simulation results with smaller diffusion coefficients $D_c = 3.5 \times 10^{-5}$, $D_u = 2.5 \times 10^{-4}$, $D_p = 3.5 \times 10^{-4}$, and $D_m = 4.91 \times 10^{-4}$ if we use finer grids with grid spacings of size $\Delta x = 0.005$ and $\Delta x = 0.0025$ as shown in Figs. 5.33 and 5.34, respectively, as compared with the results using $\Delta x = 0.01$ presented in Fig. 5.6. We observe in Figs. 5.33 and 5.34 that the heterogeneity width at the invading front reduces significantly, more than half of the width of the heterogeneity of the invading front in Fig. 5.6.

The slight change of behaviour also occurs for smaller diffusion coefficients listed in parameter set $\mathscr{P}_{NL1}$. In Figs. 5.35 and 5.36 where the grid spacing sizes used are $\Delta x = 0.005$ and $\Delta x = 0.0025$, respectively, the spikes of cancer cell density tend to become irregular as compared with the regular spikes observed in Fig. 5.8 where $\Delta x = 0.01$. The heterogeneity in the extracellular matrix is also more visible in Figs. 5.35 and 5.36, which is a consequence of the irregular cell density. We can also confirm here that the solutions converge since there are approximately about 3 grid cells within each spike for all grid sizes.

The differences of the numerical simulation results arise by using different grid spacing sizes may be due to numerical artefacts in the code, where the code may not be able to cope with the highly nonlinear equations that we use. Despite these differences, nevertheless, the results are qualitatively the same and a range of parameter values gives rise to heterogeneity in the solutions.

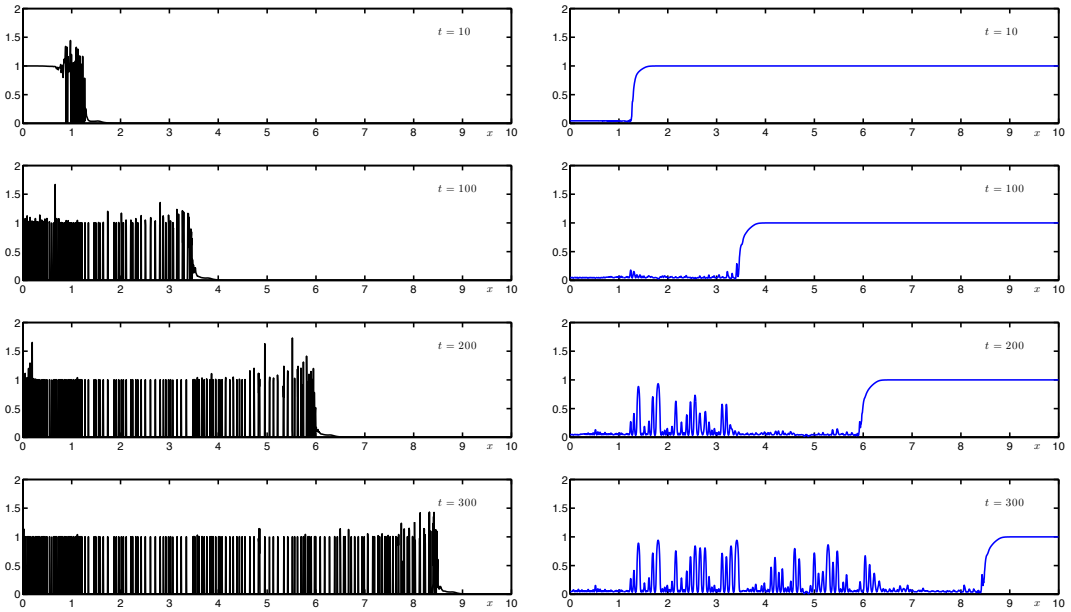

Figure 5.35: Sequence of profiles showing the spatio-temporal evolution of cancer cells c (black, left figures) invading the ECM v (blue, right figures) for comparison with Fig. 5.8 where here the grid spacing is of size $\Delta x = 0.005$ and diffusion coefficients $D_c = 3.5 \times 10^{-6}$, $D_u = 2.5 \times 10^{-5}$, $D_p = 3.5 \times 10^{-5}$, and $D_m = 4.91 \times 10^{-5}$, and $S_{cv} = 0.1$ and $S_{cc} = 0.01$.

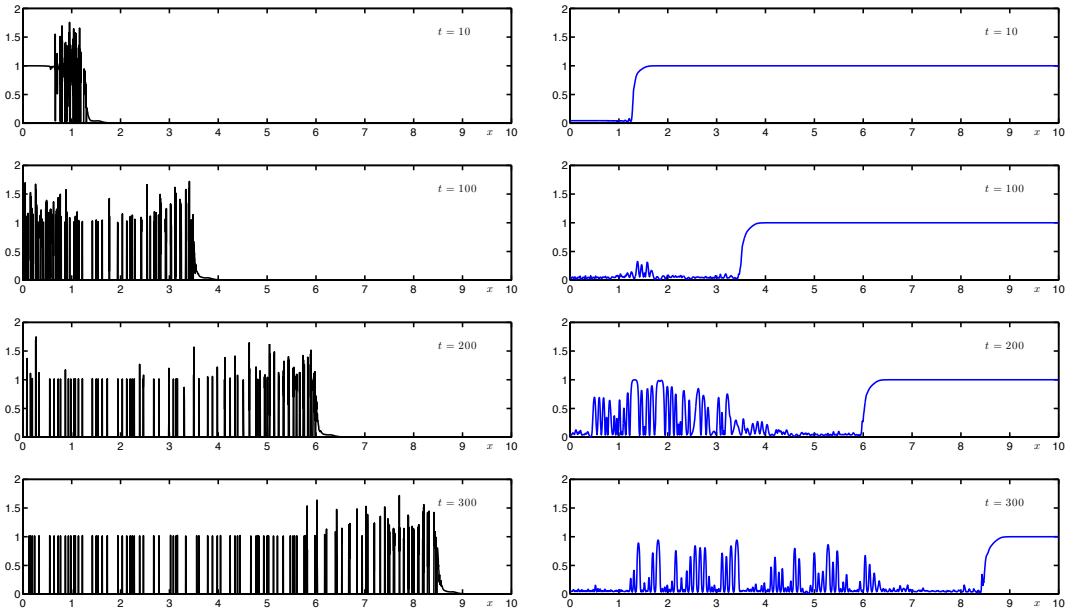

Figure 5.36: Sequence of profiles of cancer cells c (black, left figures) invading the ECM v (blue, right figures) for comparison with Fig. 5.8 as a numerical validation with a grid spacing of size $\Delta x = 0.0025$. The other parameters remain the same as in Fig. 5.6 and/or Fig. 5.33.

For our 2D simulations, changes of behaviour are observed if we use finer grids, as can be seen in Fig. 5.37 where the grid spacing size is $\Delta x = 0.02$ (top figures) and $\Delta x = 0.01$ (bottom figures). The speed of invasion is faster for simulations using a finer grid of spacing $\Delta x = 0.01$ where the breaking of symmetry also becomes less.

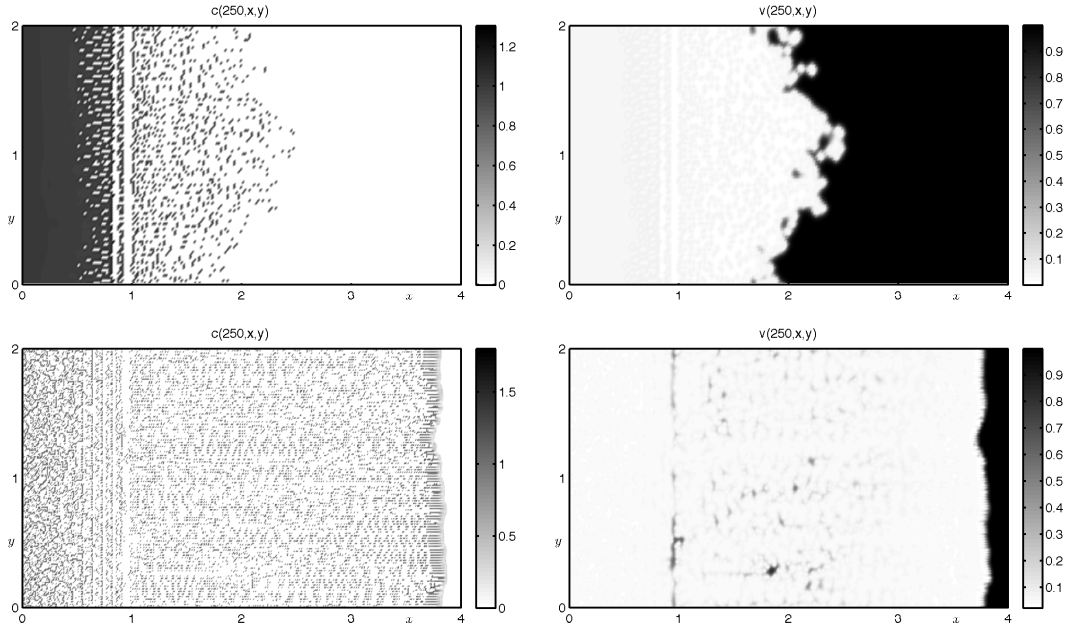

Figure 5.37: Sequence of profiles showing the spatio-temporal evolution of cancer cells c (left figure) invading the ECM v (right figure) with grid spacing size of $\Delta x = 0.02$ (top figures) and $\Delta x = 0.01$ (bottom figures) taken at $t = 250$. Parameters used are $D_c = 3.5 \times 10^{-6}, D_u = 2.5 \times 10^{-5}, D_p = 3.5 \times 10^{-5}, D_m = 4.91 \times 10^{-5}, S_{cc} = 0.01, S_{cv} = 0.1$, and $R = 0.1$.

We have investigated the potential influence of initial conditions on the solutions. We performed this by using smooth initial conditions, the same initial conditions that have been used for our 1D simulations, where now

$$\begin{aligned} c(0,\mathbf{x}) &= \left(1+\exp\left(\frac{\mathbf{x}-1.0}{0.1}\right)\right)^{-1}, \\ v(0,\mathbf{x}) &= 1-c(0,\mathbf{x}), \\ u(0,\mathbf{x}) &= \frac{1}{2}\,c(0,\mathbf{x}), \qquad \text{for} \quad \mathbf{x} \in \bar{D}_{2D}, \\ p(0,\mathbf{x}) &= \frac{1}{20}\,c(0,\mathbf{x}), \\ m(0,\mathbf{x}) &= 0, \end{aligned} \tag{5.32}$$

and the results are shown in Fig. 5.38. The top figures show the smooth initial conditions for cancer cell density (left figure) and extracellular matrix (right figure). By using the smooth initial conditions, the patterns of solutions are now different than those obtained by using step function initial conditions, compared with Fig. 5.12. There is no breaking of symmetry of cancer cell density, either with grid spacing size $\Delta x = 0.02$ (shown on the left middle figure of Fig. 5.38) or a finer grid spacing size $\Delta x = 0.01$ (shown on the left bottom figure). The speed of cancer cell invasion is the same for both grid spacings. Because of the differences in the results for validation than the results presented in Section 5.5, it is part of our future work to investigate the numerical technique used in the code.

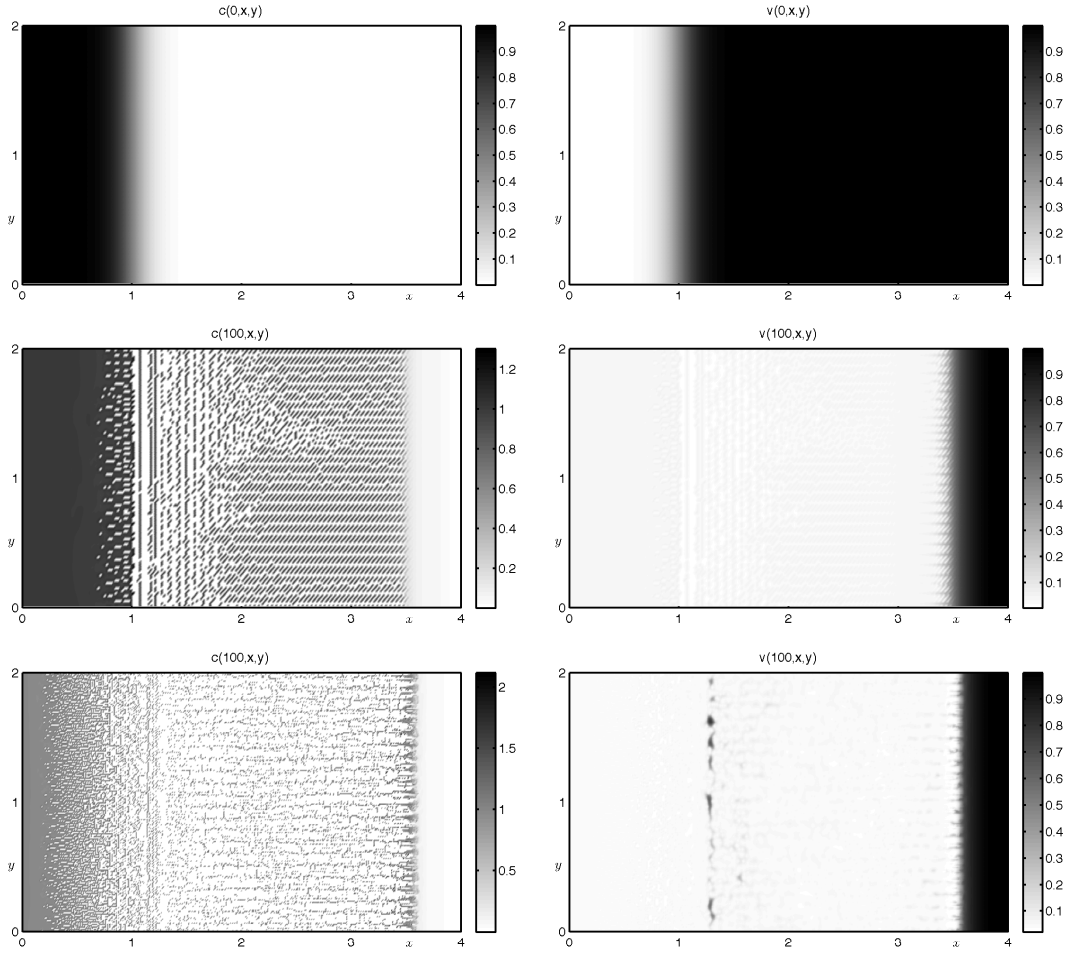

Figure 5.38: Sequence of profiles showing the spatio-temporal evolution of cancer cells c (left figure) invading the ECM v (right figure) at $t = 100$ using smooth initial conditions as in Eq. (5.32) and shown in the top figures. The results with grid spacing size $\Delta x = 0.02$ are shown in the middle figures and the results with grid spacing size $\Delta x = 0.01$ are shown in the bottom figures. Parameters used are $D_c = 3.5 \times 10^{-6}, D_u = 2.5 \times 10^{-5}, D_p = 3.5 \times 10^{-5}, D_m = 4.91 \times 10^{-5}, S_{cc} = 0.01, S_{cv} = 0.1$, and $R = 0.1$.

Finally, as we have seen in Fig. 4.4 of Chapter 4 where the uPA chemotactic term caused destabilisation of homogeneous steady state, we plot the dispersion relation in which we reduce the value of χ_u from 3.05×10^{-2} to 3.05×10^{-4}. The result is that with smaller values χ_u there is a range of $\tilde{k}$-values where $\lambda_k(\mathbf{w}^*)$ is positive as shown in Fig. 5.39, which suggests that uPA chemotaxis may play role in creating the observed heterogeneity. The 2D computational simulations result in (almost) similar heterogeneous patterns and invasion speed for both grid sizes $\Delta x = 0.02$ and $\Delta x = 0.01$,

as shown in Fig. 5.40.

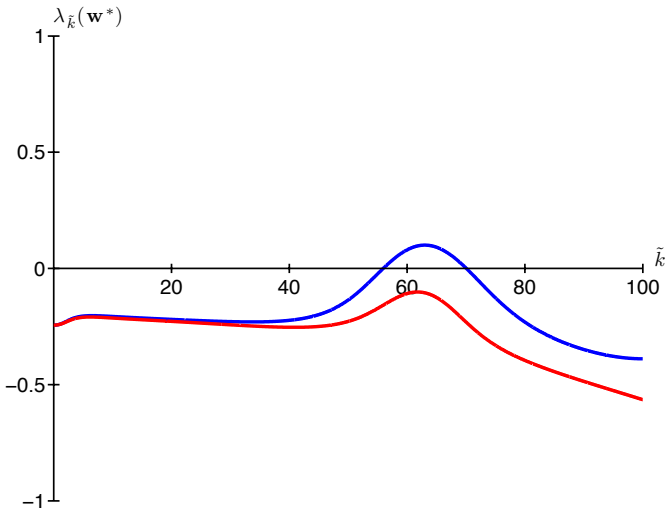

Figure 5.39: Dispersal relations with $\chi_u = 3.05 \times 10^{-4}$ (*blue line*) and $\chi_u = 3.05 \times 10^{-2}$ (*red line*).

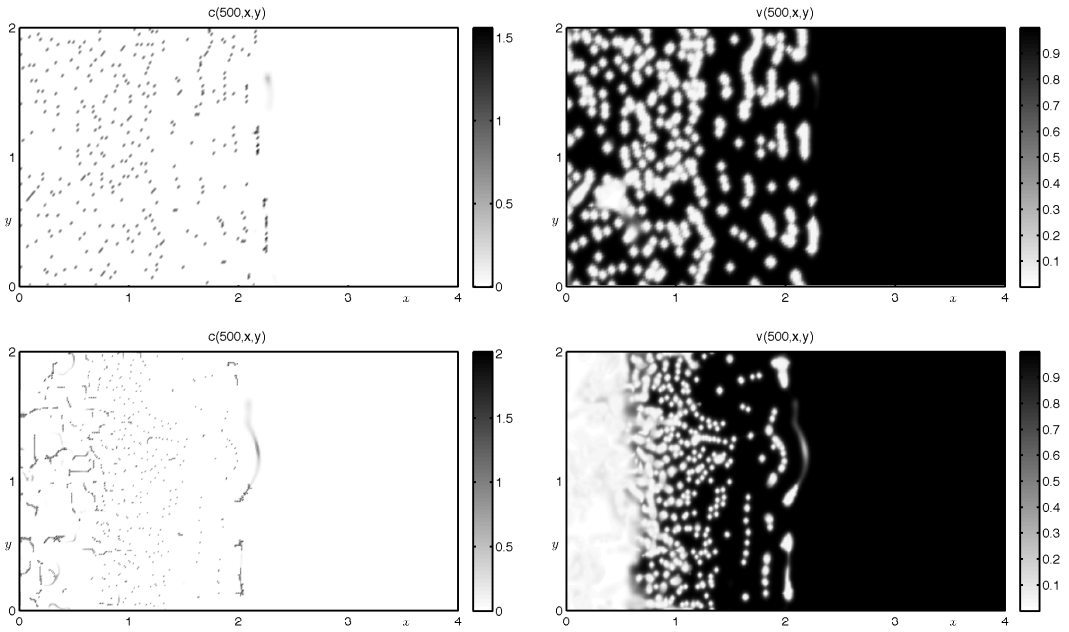

Figure 5.40: Sequence of profiles showing the spatio-temporal evolution of cancer cells c (left figure) invading the ECM v (right figure) with grid spacing size $\Delta x = 0.02$ (top figures) and $\Delta x = 0.01$ (bottom figures) at $t = 500$, where now $\chi_u = 3.05 \times 10^{-4}$ and the rest of parameters take the same values as simulations in Fig. 5.38 (here we used step function initial conditions).

Chapter 6

A Multiscale Individual Cell-based Model of Cancer Invasion

6.1 Introduction

Having seen the role of cell adhesion in cancer invasion modelling from a cell population/density approach in the previous chapters, now we change scale and look into the adhesion processes inside of the cell. In this chapter we present a multiscale, individual-based simulation environment that integrates CompuCell3D for lattice-based modelling on cellular level and Bionetsolver for intracellular modelling. CompuCell3D or CC3D provides an implementation of the lattice-based Glazier-Graner-Hogeweg or GGH model, an extension of Cellular Potts Model or CPM, and a Monte Carlo method based on metropolis algorithm for system evolution. The integration of CC3D for cellular and Bionetsolver for subcellular modelling mechanisms enables us to study cells in action due to the dynamics inside of the cells, capturing aspects of cell behaviour and interactions that is not possible using continuum approaches. We then apply this multiscale modelling technique to a model of cancer growth and invasion, based on the work of Ramis-Conde et al. (2008) where individual cell behaviours are

driven by a molecular network describing the dynamics of E-Cadherin and β-catenin. In this centre based model an alternative individual-based modelling technique has been used, namely, an off-lattice approach. In many respects, GGH methodology and the centre based model have the same overall goal, that is to mimic behaviours and interactions of individual biological cells. Although the mathematical foundations and computational implementations of the two approaches are very different, the results of the simulations we will present are compatible with each other suggesting that using cell behaviours we can formulate a natural way of describing complex multicell, multiscale models. The ability to easily reproduce results of one modelling approach using an alternative approach is essential from a model cross-validation stand point and also helps to identify modelling artefacts specific to a given computational implementation.

Modelling methodologies that explicitly represent individual cells are particularly appropriate for the modelling and simulation of cancer invasion. There are important events and physical phenomena associated with cancer invasion on the single-cell level that can only be suitably captured in simulations by accounting for individual cell properties and important aspects of cell-cell interactions, such as changes in cell-cell contact area.

In modelling the various stages of cancer progression, certain computational and mathematical methodologies are more suitable than others. For example, in the case of solid avascular tumour growth, simple continuum models are well-suited since they capture bulk properties of tissues. Instead of explicitly treating individual cells, collective properties of the tumour tissue are modelled, such as cell density and oxygen concentration. An advantage of such an approach is that systems with large number of cells, on the order of 10^6 or higher, can be handled. On the other hand, explicit representation of individual cells and their properties, such as locations, radii, morphology, surface area, volume, etc., can become computationally burdensome when trying to

model on the order of 10^4 to 10^6 cells. Nevertheless, such individual cell-based modelling approaches are capable of capturing phenomena and behaviour in multicellular systems that continuum approaches cannot capture.

The aim of the work in this chapter is to present a case study on model cross-validation. We simulate, reproduce, and compare the cancer invasion model described in Ramis-Conde et al. (2008) with the equivalent CC3D-based implementation.

6.2 The CC3D-Bionetsolver Framework for Biomedical Multiscale Individual Cell-based Simulations

CompuCell3D or CC3D is an open source simulation environment that is based on the Glazier-Graner-Hogeweg or GGH model to simulate cell behaviours, such as individual cells that can interact with each other or with a medium. The GGH model is an extension of the large-q Potts model, while the large-q Potts model itself is an extension of the *Ising model*, a simple early model of ferromagnetism based on the magnetic moments, or spins, of individual atoms and their interaction energies. The interaction between a single pair of neighbouring spins is called a *link* or a *bond*, and the spins interact via an energy function called a Hamiltonian (Glazier et al., 2007), which we describe in this section.

Systematic building of a biomedical model can be divided into following distinct stages: a) building a conceptual biomedical model; b) formal description of the model based on agreed upon modelling language, such as Systems Biology Markup Language or SBML; c) translating the formal language into a mathematical formalism, for example, SBML is translated into a set of ordinary differential equations or ODEs; and d) computational implementation of c).

"Traditional" biomedical model building skips intermediate stages and jumps from conceptual model description directly into low-level code. This is often convenient

from the perspective of the modeller but it greatly impedes model cross-validation, reuse or sharing. Problem solving environments such as CC3D, Mason, or Flame greatly reduce the amount of effort necessary to build a model which rigorously follows stages a)–d) and at the same time offers the same level of flexibility in model construction as low-level programming languages.

A CC3D model contains a description of objects (*e.g.*, cells, ECM, diffusible fields), interactions (*e.g.*, cell-cell adhesion, morphogen-dependent cell growth), initial conditions (*e.g.*, initial configuration of cells based on time-lapse microscopy image), and a description of the time evolution of cell properties (*e.g.*, β-catenin concentration dynamics driving adhesive cell properties or rule-based cell type differentiation).

CC3D models are described using a combination of CompuCell3D Markup Language (CC3DML) and Python scripting. Such a combined approach allows one to build complex biomedical models and does not require recompilation when running them. In typical CC3D simulations "static" aspects of the model such as lattice size, simulation runtime, list of cell types, initial conditions or cadherin affinities are usually described using CC3DML. We can replace CC3DML with the equivalent Python syntax. The "dynamic" part of the CC3D model is described using Python scripting. Since Python is a full featured programming language, modellers have freedom to express complex cell type differentiation rules, coupling of cell properties to concentration of diffusive chemicals cell-cell signalling or parameterising cell adhesive properties in terms of the underlying molecular or gene regulatory networks.

Several models of tumour growth and angiogenesis have already been simulated using the CC3D environment, see for example articles by Poplawski et al. (2006, 2008, 2009); Shirinifard et al. (2009); Swat et al. (2009).

6.2.1 GGH Methodology

The GGH model uses an effective-energy formalism. It facilitates multiscale simulations by defining spatially extended generalised cells, which can represent clusters of cells, single cells, subcompartments of single cells or small subdomains of non-cellular materials. All GGH models include a list of *objects*, their *interaction descriptions*, their *dynamics*, and appropriate *initial conditions*. Objects in a GGH model can be *generalised cells* or *fields*. Generalised cells are spatially-extended objects which reside on a single cell lattice and in the current model represents cancer cells (Balter et al., 2007; Glazier et al., 2007). Generalised cells carry a set of state descriptors, *e.g.*, the cell's target volumes and volumes at which mitosis occurs.

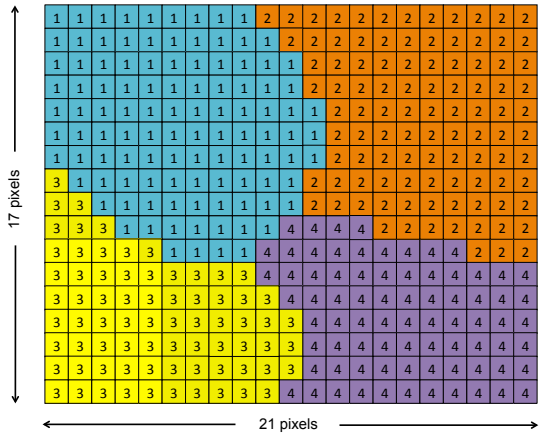

Figure 6.1: Schematic diagram showing an example of a 2-dimensional GGH cell-lattice configuration. The size of lattice is 21×17 pixels. Each colour domain represents the type of generalised cells $\tau(\sigma(\mathbf{i}))$. Each generalised cell is composed of a set of pixels $\mathbf{i}$ with unit index $\sigma(\mathbf{i})$, here 1, 2, 3, and 4.

In a GGH model, a generalised cell is represented by a collection of lattice sites with the same index. A lattice site or a *pixel* is denoted by a vector of integers $\mathbf{i}$. A unique index for each generalised cell $\sigma(\mathbf{i}) \in [1,...,N]$ is defined at each lattice site or pixel, where N is the maximum number of generalised cells, and cell type for each cell is denoted by $\tau(\sigma(\mathbf{i}))$. Each generalised cell has a unique cell index and contains many pixels. Many generalised cells may share the same cell type. As an example, in

Fig. 6.1, in a 2-dimensional lattice of size 21×17 pixels there are 4 types of generalised cells $\tau(\sigma(\mathbf{i}))$, each has index value $\sigma(\mathbf{i})$: 1 (blue cell), 2 (orange cell), 3 (yellow cell), and 4 (purple cell).

Fields are continuously-variable concentrations, each of which resides on its own lattice. Fields can represent diffusible chemicals, non-diffusing extracellular matrix, etc. Fields such as chemical attractant are used in our simulations for cancer cell detachment from a layer of cells and a spheroid tumour, which is explained in detail in Chapter 6.4.

The initial condition specifies the initial configurations of the cell lattice, fields, a list of cells and their internal states related to auxiliary equations and any other information required to completely describe the simulation.

Interaction descriptions and *dynamics* define how the various *objects* behave both biologically and physically. For generalised cells, these behaviours and interactions are embodied primarily in the *effective energy* which describes the behaviours and interactions of a generalised cell, such as its shape, motility, adhesion, and also its response to extracellular signals (Glazier et al., 2007). The effective energy mixes true energies such as cell-cell adhesion with terms that mimic energies, *e.g.*, the response of a cell to a chemotactic gradient of a field. The effective energy, also called the Hamiltonian $\mathscr{H}$, is the core of the GGH model. Adhesion is one the most important effective energy terms, due to its critical feature in biology.

To represent variations in energy due to adhesion between cells of different types, a *boundary energy*, that depends on $J(\tau(\sigma(\mathbf{i})), \tau(\sigma(\mathbf{j})))$ between two cells (σ, σ') of given cell types $(\tau(\sigma), \tau(\sigma'))$ at a link (the interface between two neighboring pixels), is defined as (Glazier et al., 2007)

$$\mathscr{H}_{\text{boundary}} = \sum_{(\mathbf{i},\mathbf{j})\,\text{neighbours}} J(\tau(\sigma(\mathbf{i})), \tau(\sigma(\mathbf{j})))(1 - \delta(\sigma(\mathbf{i}), \sigma(\mathbf{j}))), \tag{6.1}$$

where the sum is over all neighbouring pairs of lattice sites $\mathbf{i}$ and $\mathbf{j}$ (note that the neighbour range may be greater than one), the boundary energy coefficients are symmetric,

$$J(\tau,\tau') = J(\tau',\tau)\,, \tag{6.2}$$

and

$$\delta(x,y) = \begin{cases} 1 & \text{if} \quad x = y \\ 0 & \text{if} \quad x \neq y\,. \end{cases}$$

In addition to boundary energy, most simulations include multiple constraints on cell behaviour. The use of constraints to describe behaviours comes from the physics of classical mechanics. In the GGH context (based on Monte-Carlo dynamics) a *constraint energy* can be written in a general elastic form (Glazier et al., 2007)

$$\mathscr{H}_{\text{constraint}} = \lambda\,(\text{value} - \text{target value})^2\,. \tag{6.3}$$

This constraint is zero if "value = target value" and grows as "value" diverges from "target value". λ is the spring constant (a positive real number), which determines the constraint strength. Smaller values of λ allow the pattern to deviate more from the equilibrium condition (*i.e.*, the condition satisfying the constraint).

For cell volume, most GGH simulations employ a volume constraint that restricts volume variations of generalised cells from their target volumes (Glazier et al., 2007),

$$\mathscr{H}_{\text{volume}} = \sum_{\sigma} \lambda_{\text{volume}}(\tau(\sigma))(v(\sigma) - V_t(\sigma))^2 \tag{6.4}$$

where for cell σ, $\lambda_{\text{volume}}(\tau(\sigma))$ denotes the inverse compressibility of the cell, $v(\sigma)$ is the number of pixels in the cell (cell volume), and $V_t(\sigma)$ is the cell's target volume. One useful result from the constraint formalism is that it defines $P \equiv -2\lambda\,(v(\sigma) - V_t(\sigma))$ as the pressure inside the cell. If $v < V_t$ the cell has a positive internal pressure while if $v > V_t$ the cell has a negative pressure.

Because cells have nearly fixed amounts of cell membrane, a surface area constraint can be defined

$$\mathscr{H}_{\text{surface}} = \sum_{\sigma} \lambda_{\text{surface}}(\tau(\sigma))(s(\sigma) - S_t(\sigma))^2 \tag{6.5}$$

where $s(\sigma)$ is the surface area of cell σ, $S_t(\sigma)$ is cell's target surface area, and $\lambda_{\text{surface}}(\tau(\sigma))$ is cell's inverse membrane compressibility.

Now, the effective energy or the full Hamiltonian (Glazier et al., 2007) for our simulations is formulated as the sum of the boundary energy (6.1), the volume constraint (6.4), and the surface area constraint (6.5):

$$\begin{aligned}\mathscr{H}_{GGH} &= \sum_{(\mathbf{i},\mathbf{j})\,\text{neighbours}} J(\tau(\sigma(\mathbf{i})),\tau(\sigma(\mathbf{j})))(1-\delta(\sigma(\mathbf{i}),\sigma(\mathbf{j})))\\ &+ \sum_{\sigma} \lambda_{\text{volume}}(\tau)(\sigma)(v(\sigma)-V_t(\tau(\sigma)))^2\\ &+ \sum_{\sigma} \lambda_{\text{surface}}(\tau(\sigma))(s(\sigma)-S_t(\sigma))^2\,. \qquad (6.6)\end{aligned}$$

6.2.2 Bionetsolver Programming Library

Bionetsolver is a C++ library with a high-level Python API that permits easy definition of sophisticated models coupling reaction-kinetic models described in the SBML with GGH objects for execution in CC3D. Bionetsolver makes use of the SBML ODE Solver Library (SOSlib) to implement reaction-kinetic network dynamics which can regulate the cell dynamics generated by the GGH core. For further reference on SOSlib the reader may refer to the paper by Machné et al. (2006). SOSlib provides functionality both for reading SBML models and solving them as a system of ODEs. In addition to this functionality, there are three classes – BionetworkSBML, BionetworkTemplateLibrary and Bionetwork – that provide some additional convenience in storing and manipulating SBML models as well as creating ODE integrators and time-stepping the integrators. The Python API of Bionetsolver provides a set of 7 core functions that can be called from within a CC3D Steppable. These 7 functions are used for the initialisation and manipulation of Bionetsolver objects from within the steppable. In this way, the entire specification of a multiscale (cell-subcell-level) simulation can be written in

Python and executed in the CC3D player.

The Bionetsolver API is imported and initialised in a typical CC3D steppable file, at which point the API is made available within the steppable. SBML models are loaded with a `loadSBMLModel` function and each SBML model can be added to one or more template libraries using the function `addSBMLModelToTemplateLibrary`. When `loadSBMLModel` is called, a string argument is required that signifies a name for the SBML model. Similarly, when `addSBMLModelToTemplateLibrary` is called, the user provides the SBML model name (specified when `loadSBMLModel` was called) as well as a string argument that signifies the name of the template library. A single SBML model may be added to several template libraries and each template library may contain one or more SBML models.

In addition, a `setBionetworkInitialCondition` function can be used to specify initial conditions for parameters and state variables in any SBML model within a template library. As arguments to this function, the user provides a template library name, a variable or parameter name and the corresponding initial numerical value of the variable or property. A set of SBML models stored within a template library can be associated with a CC3D cell type by providing the cell type name as the name of the template library. When the function `initializeBionetworks` is called, a separate bionetwork object is created for each cell of the given cell type and the previously specified initial conditions (specified using `setBionetworkInitialCondition`) are set for each of the bionetworks. Any parameters or state variables for which `setBionetworkInitialCondition` was not called are simply initialised, by default, to values specified in the original SBML models.

All of the functions mentioned above are initialisation functions and are called within the start function of the CC3D steppable. In addition, there are three more functions that are called within the step function of the CC3D steppable. These are (1)

`timestepBionetworks`, for time-stepping the ODE integrators, (2) `getBionetworkValue`, for retrieving SBML property and state variable values from the integrators, and (3) `setBionetworkValue`, for setting SBML property values of the integrators. CC3D cell-level properties can be retrieved using procedures described in the CC3D documentation and the CC3D demo simulations. Finally, SBML property values can be set as a function of CC3D cell properties and, likewise, CC3D cell properties can be set as a function of SBML state variable values. This is how mechanistic coupling can be established between SBML (subcellular) and CC3D (cell-level) properties and dynamics.

6.2.3 Comparison of Cell Center-model and GGH-model for Multicellular Simulation

Here we briefly discuss fundamental differences and some similarities between the centre based model of Ramis-Conde et al. (2008) and our model based on the GGH model. As indicated, CC3D is a software application that implements the GGH model, allowing lattice-based simulation of multicellular systems. Each biological cell is represented as a set of contiguous sites on a lattice and the system evolves in time through an energy minimization procedure. On the other hand, the centre based model represents each biological cell in terms of the location of its centre of mass and its radius. This fundamental distinction between the two methodologies is illustrated in Fig. 6.2.

The cells of the centre model behave as elastic spheres and equations describing their behaviour and interactions are derived on the basis of classical mechanical concepts. It approximates cell-cell contact areas using the radii of neighbouring cells and the distance between their centres. In the GGH model, the concept of cell neighbour has an explicit representation, where two cells share one or more lattice edges (for 2D simulations) or faces (3D simulations). These are the differences between the two models. Each model has relative strengths and weaknesses with respect to

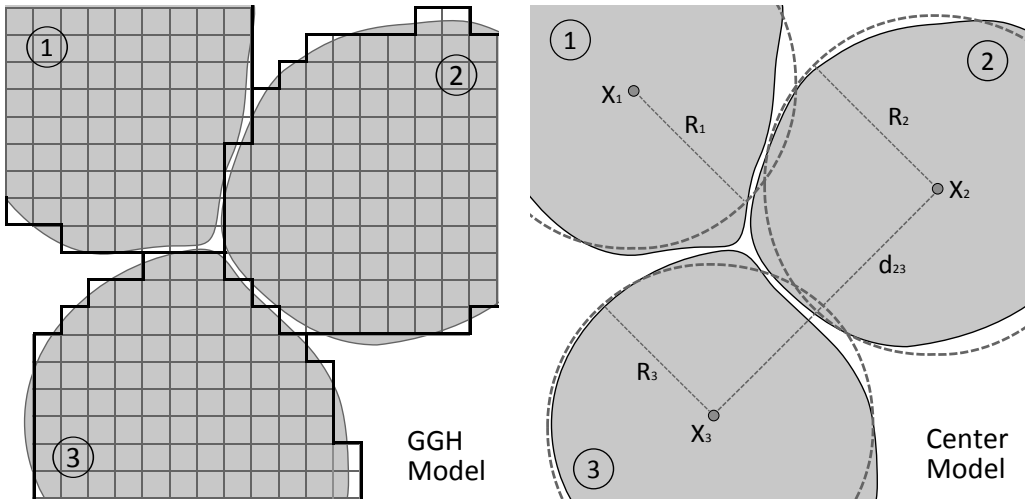

Figure 6.2: Illustration of lattice-based representation of cells in the GGH model (left figure) and lattice-free representation in the centre based model (right figure).

different biophysical processes and phenomena. In terms of biological and biophysical concepts captured by the two approaches, the GGH and centre models also bear many similarities. Both methodologies use continuum, reaction-diffusion equations to model extracellular chemical fields and they both incorporate cell-cell adhesion and mechanical constraints on cell shape. In each case, extracellular chemical fields can both modify and be modified by cell behaviours or properties such as cell growth rates, secretion, absorption and chemotaxis.

6.3 An Application to Multiscale Modelling of Cancer Growth and Invasion

Recently Ramis-Conde et al. (2008) developed a multiscale model of cancer growth and invasion incorporating important aspects of E-cadherin-β-catenin signaling and its coupling to cell-level properties of intercellular contact and adhesion. This model requires explicit representation (on a cell to cell basis) of localised and spatially heterogeneous changes in cell-cell adhesion strength and contact areas. It is at this level

of "granularity" that invasive cancer cells sense and respond to their environment. In terms of biological processes, the model of Ramis-Conde et al. (2008) captures cell-contact-dependent recruitment of E-cadherin and β-catenin to the cell membrane and reincorporation of both back into the cytoplasm. Computationally, the simulations incorporated: (1) time-varying changes in cell-cell adhesion as a function of a system of ordinary differential equations (ODEs) for the intracellular reaction kinetic model of E-cadherin-β-catenin signalling, and (2) changes in rate parameter values in the reaction kinetic model as a function of changing contact areas between neighbouring cells.

6.3.1 Biological Background

To maintain tissue structures and organisation, cells adhere to each other and to the extracellular matrix through families of cell surface glycoproteins called cell adhesion molecules (CAMs). One group of CAMs that is responsible for cell to cell adhesion is called the cadherins, transmembrane glycoproteins that are dependent on calcium (Ca^{2+}) ions to function. Classical cadherins are named based on the types of the main tissues where they are found, *e.g.*, E-cadherins are found in epithelial tissues, N-cadherins are expressed predominantly in the nervous system, and P-cadherins are present on cells in the placenta and epidermis, etc. Of all the types of cadherins, E-cadherins are the most well-studied cell-cell adhesion proteins. After their translation from mRNA, E-cadherins are transported to the cell membrane where they anchor and function as transmembrane proteins with distinct cytoplasmic and extracellular domains. The extracellular domain is responsible for cadherin's ability to link adjacent cells by interacting with the extracellular domain of neighbouring cells in a calcium dependent manner. The cytoplasmic domain is connected indirectly with actin filaments mediated by a group of intracellular anchor proteins called catenins, *e.g.*, p120-catenin, α-catenin, γ-catenin, and β-catenin (Jiang, 1996; Alberts et al., 2002). These catenins

offer mechanical linkage between E-cadherin and cytoskeleton, hence the function of E-cadherins is highly dependent on the functional activity of catenins (Garrod, 1993; Tsutsui et al., 1996).

In vitro and *in vivo* analyses showed that newly synthesised E-cadherin may bind to β-catenins before being translocated to the cell membrane. α-catenin then binds to E-cadherin-β-catenin complexes at the cell membrane (Jiang, 1996). When a cell adheres to another cell, a high expression of E-cadherin-catenin complexes appears in the area of adhesion. In cancer, if cells proliferate while maintaining tight cell-cell adhesion, their expansive growth will be similar to that of a benign tumour, and hence the tumour can be contained. Disruption of the E-cadherin-catenin complexes is associated with invasive and metastatic behaviour of tumour cells, particularly those of epithelial origin. This mechanism leads to the formation of mesenchymal cells from epithelial cell lines, or epithelial-mesenchymal transition (EMT), which are dominant in many types of carcinomas (Thiery, 2002) and life threatening for cancer patients. Due to this, the E-cadherin-catenin complex is considered as a tumour invasion suppressor.

6.3.2 Kinetics of E-cadherin and β-catenin

In Ramis-Conde et al. (2008), the kinetic interactions between E-cadherin and β-catenin in a cell are conceptually modelled as follows. After being synthesised, E-cadherin is released to the cytoplasm as free E-cadherin (the concentration is denoted by $[E_c]$). Free β-catenin (concentration $[\beta]$) is assumed to be distributed in the cytoplasm and near the cell membrane. When there is signalling for cell-cell contact, free E-cadherin in the cytoplasm ($[E_c]$) is transported to the cell membrane (concentration $[E_m]$) where its cytoplasmic domain binds to free β-catenin to form E-cadherin-β-catenin complex (concentration $[E/\beta]$) and the extracellular domain binds to the

E-cadherin-β-catenin complex of adjacent cells. If cell detachment occurs, the E-cadherin-β-catenin complex dissociates, releasing free β-catenin and sequestering E-cadherin into the cytoplasm by endocytosis. The free β-catenin is then degraded and downregulated after binding with proteasome. These intracellular interactions are summarised in a schematic diagram shown in Fig. 6.3 and can be described by the chemical reactions

$$[\mathrm{E}_c] \xrightarrow[\{\text{contact}\}]{c_i(t)} [\mathrm{E}_m] \,, \tag{6.7}$$

$$[\beta] + [\mathrm{E}_m] \xrightarrow[\nu]{} [\mathrm{E}/\beta] \,, \tag{6.8}$$

$$[\mathrm{E}/\beta] \xrightarrow[\{\text{detachment}\}]{d_i(t)} [\mathrm{E}_c] + [\beta] \,, \tag{6.9}$$

where ν is the rate of binding of E-cadherin and β-catenin. Applying mass conservation for the total concentration of E-cadherin E_T gives

$$\mathrm{E}_T = [\mathrm{E}_c] + [\mathrm{E}_m] + [\mathrm{E}/\beta] \,, \tag{6.10}$$

where $\mathrm{E}_T$is constant.

Free β-catenin from a ruptured E-cadherin-β-catenin complex due to cell detachment then forms a complex with a proteasome (concentration [P]). This complex (concentration denoted by [C]) is eventually degraded by the proteasome system as follows:

$$[\beta] + [\mathrm{P}] \underset{k^-}{\overset{k^+}{\rightleftharpoons}} [\mathrm{C}] \xrightarrow[k_2]{} [\mathrm{P}] + \omega \,, \tag{6.11}$$

where ω is the final product of the degradation process, k^+ and k^- are the rates of association and disassociation of the β-catenin-proteasome complex, respectively, and k_2 is the β-catenin degradation rate in the proteasome system. The total concentration of proteasome consists of the concentration of proteasome and its complex and is considered to be constant $[\mathrm{P}_T]$, hence

$$\mathrm{P}_T = [\mathrm{C}] + [\mathrm{P}] \,. \tag{6.12}$$

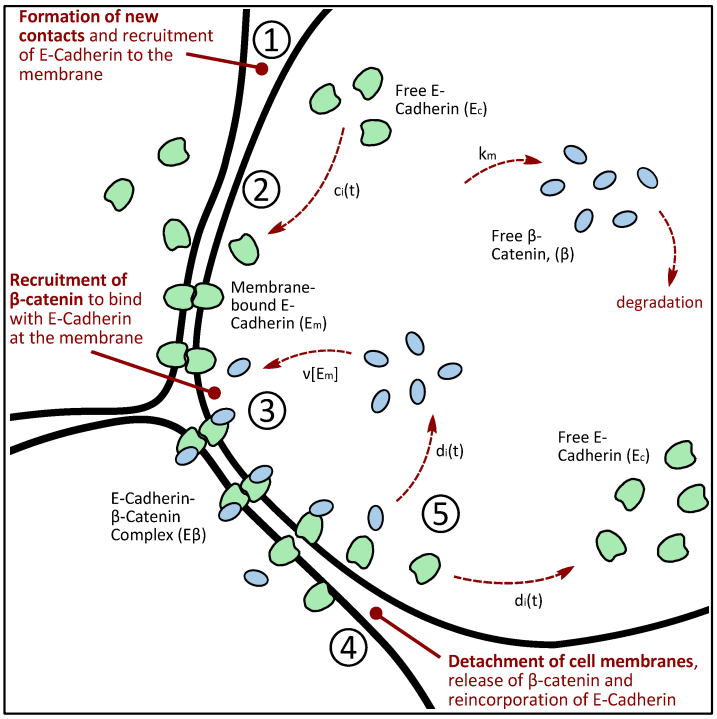

Figure 6.3: A schematic diagram of the E-cadherin interactions with β-catenin.

Invoking the law of mass action we write the system of ODEs for the concentration of E-cadherin in the cytoplasm [E_c], the concentration of the E-cadherin-β-catenin complex [E/β], the concentration of free β-catenin [β], and the concentration of the β-catenin-proteasome complex [C] for each individual cell i as

$$\frac{d[E_c]}{dt} = -c_i(t)[E_c] + d_i(t)[E/\beta], \tag{6.13a}$$

$$\frac{d[E/\beta]}{dt} = \mathscr{A}_1 - d_i(t)[E/\beta], \tag{6.13b}$$

$$\frac{d[\beta]}{dt} = \mathscr{A}_2 + d_i(t)[E/\beta] - k^+[\beta](P_T - [C]) + k^-[C] + k_m, \tag{6.13c}$$

$$\frac{d[C]}{dt} = k^+[\beta](P_T - [C]) - k^-[C] - k_2[C], \tag{6.13d}$$

where, depending on signalling,

$$\mathscr{A}_1 = \begin{cases} \nu\left(\mathrm{E}_T - [\mathrm{E}_c] - [\mathrm{E}/\beta]\right)[\beta], & \text{for attachment}, \\ \\ -\alpha[\mathrm{E}/\beta], & \text{for detachment}, \end{cases} \tag{6.14}$$

and

$$\mathscr{A}_2 = \begin{cases} -\nu\left(\mathrm{E}_T - [\mathrm{E}_c] - [\mathrm{E}/\beta]\right)[\beta], & \text{for attachment}, \\ \\ \alpha[\mathrm{E}/\beta], & \text{for detachment}, \end{cases} \tag{6.15}$$

The parameter k_m is the rate of production of β-catenin, $c_i(t)$ is a time-dependent function that measures the amount of cadherins stimulated to form bonds for cell-cell contact, $d_i(t)$ is a function that measures the amount of cadherins resulting from broken bonds during cell detachment, and α is the rate of dissociation of E-cadherin-β-catenin complex once the migration decision has been made. These functions ($c_i(t)$ and $d_i(t)$) depend on the area of contact between adjacent cells that changes over time, and are defined as

$$c_i(t) = \sum_{\text{new contacts}} a_{c,j}(t)\rho_c\,, \tag{6.16}$$

and

$$d_i(t) = \sum_{\text{new detachments}} a_{d,j}(t)\rho_d\,, \tag{6.17}$$

where ρ_c and ρ_d are the rates of E-cadherin translocation between the cell membrane and the cytoplasm. When there is signalling for cell-cell contact ρ_c measures how fast the E-cadherin is transported from the cytoplasm to the cell membrane and ρ_d measures the reverse action (from the membrane to the cytoplasm) for cell detachment. In Ramis-Conde et al. (2008), $a_{c,j}(t)$ and $a_{d,j}(t)$ are time-dependent functions, to determine enhancement of the area of contact (when E-cadherin is transported from the cytoplasm to the membrane) and loss of area of contact (when E-cadherin is brought back from the membrane to the cytoplasm), respectively. These functions are defined

as

$$a_{c,j}(t) = \begin{cases} \dfrac{\partial}{\partial t}\hat{a}(t)_j, & \text{if} \quad \dfrac{\partial}{\partial t}\hat{a}(t)_j > 0, \\ \\ 0, & \text{otherwise}, \end{cases}$$

and

$$a_{d,j}(t) = \begin{cases} \| \dfrac{\partial}{\partial t}\hat{a}(t)_j \|, & \text{if} \quad \dfrac{\partial}{\partial t}\hat{a}(t)_j < 0, \\ \\ 0, & \text{otherwise}, \end{cases}$$

where $\hat{a}(t)_j$ is the approximated contact area between cells i and j at time t divided by the surface area of cell i.

Studies suggested that the loss of E-cadherin expression freed cells from tight cell-cell association and provided them with malignant properties (Shimoyama et al., 1992). Therefore we may propose that the condition for attachment is assumed valid as long as the concentration of free β-catenin $[\beta]$ is below a threshold c_T. For detachment to occur, the amount of free β-catenin in the cytoplasm must be large enough, with an additional increase from broken E-cadherin-β-catenin complex, or $[\beta] > c_T$. This claim is based on several studies that have found upregulation of β-catenin in the cytoplasm (or termed nuclear β-catenin) at the invasive front of colorectal carcinomas (Brabletz et al., 2001; Suzuki et al., 2008), invasive breast cancer (Uchino et al., 2010), fibrosarcoma, clear cell sarcoma and carcinosarcoma (Ng et al., 2005). Nuclear accumulation of β-catenin initiates the loss of epithelial differentiation and gain of mesenchyme-like capabilities of the tumour cells at the invasive front. In the central areas of the primary tumours, nuclear β-catenin was found to be localised at the cell membrane. Nuclear accumulation of β-catenin has been the most powerful predictor of liver metastasis in colorectal cancer. This may be an important marker for adjuvant therapy or other treatment modalities.

In order to obtain a nondimensional system of equations, we nondimensionalise

Eqs. 6.13a-6.13d in the usual way by setting the following dimensionless variables:

$$\mathrm{E}_c{}^* = \frac{\mathrm{E}_c}{E}, \qquad \mathrm{E}/\beta^* = \frac{\mathrm{E}/\beta}{E}, \qquad \beta^* = \frac{\beta}{E}, \qquad \mathrm{C}^* = \frac{\mathrm{C}}{E}, \qquad t^* = \frac{t}{T}$$

where E is a reference concentration of E-cadherin and T is an appropriate reference time, from which we obtain dimensionless parameters:

$$c_i^*(t) = c_i(t)T, \qquad d_i^*(t) = d_i(t)T, \qquad k^{-*} = k^-T, \qquad k_2^* = k_2T,$$
$$k^{+*} = k^+TE, \qquad \nu^* = \nu TE, \qquad \alpha^* = \alpha T, \qquad k_m^* = k_m\frac{T}{E}$$

Inserting the dimensionless variables and parameters into the system (6.13) and after dropping the asterix signs for notational convenience, we obtain the dimensionless system of equations

$$\frac{d[\mathrm{E}_c]}{dt} = -c_i(t)[\mathrm{E}_c] + d_i(t)[\mathrm{E}/\beta], \tag{6.18a}$$

$$\frac{d[\mathrm{E}/\beta]}{dt} = \mathscr{A}_1 - d_i(t)[\mathrm{E}/\beta], \tag{6.18b}$$

$$\frac{d[\beta]}{dt} = \mathscr{A}_2 + d_i(t)[\mathrm{E}/\beta] - k^+[\beta](\mathrm{P}_T - [\mathrm{C}]) + k^-[\mathrm{C}] + k_m, \tag{6.18c}$$

$$\frac{d[\mathrm{C}]}{dt} = k^+[\beta](P_T - [\mathrm{C}]) - k^-[\mathrm{C}] - k_2[\mathrm{C}]. \tag{6.18d}$$

The dimensionless parameter values used in the simulations of this chapter can be found in Table 6.1. The dimensionless values are based on the parameters used in Ramis-Conde et al. (2008).

Using the parameter values given in Table 6.1, we solve the underlying ODEs given above to see the dynamics of the concentrations of β-catenin, E-cadherin-β-catenin complex, and β-catenin-proteasome complex at attachment and when there is signalling for detachment, as shown in Fig. 6.4.

Table 6.1: Dimensionless intracellular parameter values for the cell detachment simulations

Parameter	Definition	Value	Reference
ν	E-cadherin-β-catenin binding rate	100	Ramis-Conde et al. (2008)
k^+	β-catenin-proteasome downregulated binding rate	1.5	Estimated
k^-	β-catenin-proteasome dissociation rate	19	Ramis-Conde et al. (2008)
k_2	β-catenin degradation rate in proteasome	1	Ramis-Conde et al. (2008)*
k_m	β-catenin production rate	14	Ramis-Conde et al. (2008)*
α	E-cadherin-β-catenin dissociation rate	2	Ramis-Conde et al. (2008)
c_T	β-catenin threshold value	50	Ramis-Conde et al. (2008)
ρ_c	E-cadherin cytoplasm-surface translocation rate	200	Ramis-Conde et al. (2008)
ρ_d	E-cadherin surface-cytoplasm translocation rate	200	Ramis-Conde et al. (2008)
P_T	Proteasome total concentration	21	Ramis-Conde et al. (2008)*
E_T	E-cadherin total concentration	100	Ramis-Conde et al. (2008)

* appears in the paper's correction.

6.3.3 Implementation of CC3D in the Model

Cellular behaviours, such as motion, interactions, mechanics, etc., are described as energy terms in the overall system Hamiltonian. In our simulations we use three major terms to describe cell-cell adhesiveness, cell volume elastic constraint, and cell surface elastic constraint. The simulation itself consists of a series of random attempts of cells to extend their boundaries by copying the value of a pixel $\sigma(\mathbf{i})$ to neighbouring site, see Fig. 6.5. Since each cell in the GGH model is represented as a collection of pixels $\mathbf{i}$, at each step we randomly select a pixel $\mathbf{i}$ as a target pixel and randomly select one of its fourth-order neighbouring pixel $\mathbf{i}'$ as a source pixel. Then we attempt to change its index from $\sigma(\mathbf{i})$ to the index $\sigma' = \sigma(\mathbf{i}')$. If they belong to the same generalised cell, $\sigma(\mathbf{i}) = \sigma(\mathbf{i}')$, we do not need to copy the index. A successful index copy increases the

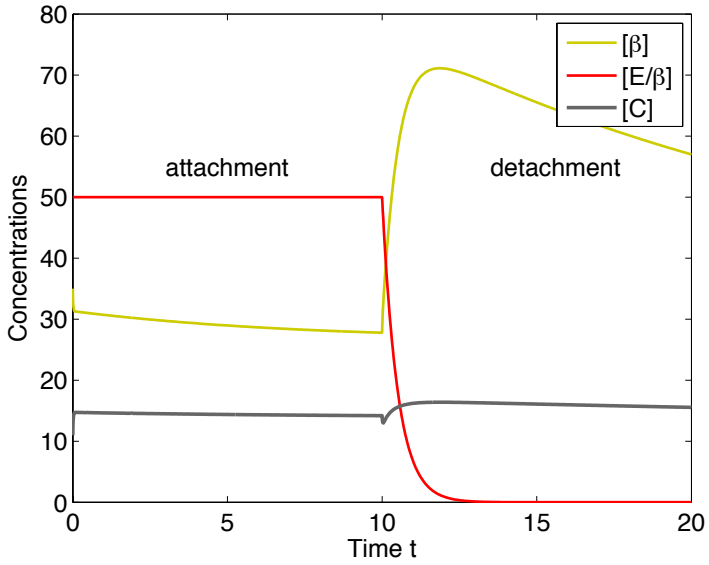

Figure 6.4: Dynamics of β-catenin, E-cadherin-β-catenin complex, and β-catenin-proteasome complex at attachment and detachment conditions based on the underlying ODEs using parameters in Table 6.1.

volume of the source cell and decreases the volume of the target cell by one pixel. At each pixel copy attempt we calculate the change in the system energy ΔE and accept pixel reassignment with probability $P(\Delta E)$

$$P(\Delta E) = \begin{cases} 1\,, & \text{for } \Delta E \leq 0\,, \\ \\ \exp(-\frac{\Delta E}{T_m})\,, & \text{for } \Delta E > 0\,, \end{cases} \tag{6.19}$$

where T_m is a parameter representing the effective cell motility.

Energy dependent pixel copy probability and Hamiltonian terms constitute the essence of the GGH models. Although ΔE denotes change of the overall system energy, in practice contributions to ΔE are almost always "local" *i.e.*, in our calculations we only have to examine a small neighbourhood of pixels involved in the pixel-copy. The simulation is subdivided in the so-called Monte Carlo Steps (MCS) which correspond to a unit of physical time. By convention, each MCS consists of one index-copy attempt for each pixel in the cell lattice. The conversion between MCS and physical time depends on model parameters. In a simple case for example, in Bionetsolver we

set `timestepBionetwork` to 0.03 and if Bionetsolver gets called every MCS then 1 MCS corresponds to 0.03 hours. In this chapter we do not specifically set a relationship between MCS and the physical time because in the computational simulations we also incorporate cell mitosis or cell division which in the process itself also requires another time convention. In the mitosis process we do not apply any intracellular pathway, but instead we use a built-in mitosis function provided by CompuCell3D. The physical distance is recovered by converting pixels into unit of length. This conversion is more straightforward than time conversion and in our simulations we set 1 pixel corresponds to 2 μm.

Unlike models where cellular behaviours are put by hand by specifying various parameters of the Hamiltonian, in our model the most critical parameters (*i.e.*, concentrations of E-cadherins, β-catenins, and E-cadherin-β-catenin complexes) are linked to the molecular pathways running inside each individual cell. This approach allows us to represent more faithfully the multiscale nature of tumour invasion. Biological cells (or tumour cells) change their phenotypic properties due to the dynamic events explained in the previous subsection which occur inside the cell, in the nucleus or cytoplasm, and on the cell membrane. We try to mimic the biology as closely as possible by linking phenomena occurring at the intracellular scales (E-cadherin/β-catenin dynamics) to processes which operate at the cell/multicell level (cellular adhesion).

To build the CC3D-Bionetsolver implementation, we provide four files and do the following. The pathway of E-cadherin and β-catenin interactions is written in an SBML file using JarnacLite (`http://www.sys-bio.org/sbwWiki/sbw/jarnaclite`). The setup of Potts dimension, related CC3D plugins, and initial configuration are listed in an XML file. In addition to plugins, there are also modules called steppables which run either repeatedly after a defined intervals of Monte Carlo Steps or once at the beginning or the end of the simulation. Steppables typically define initial conditions,

alter cell states, update fields or output intermediate results. The Bionetsolver functions are called from within CC3D steppables. The CC3D steppables and Bionetsolver functions are written in a Python file. The main file that is called from the CC3D player to run the simulation is written in Python and it lists the core CC3D simulation objects and required steppables.

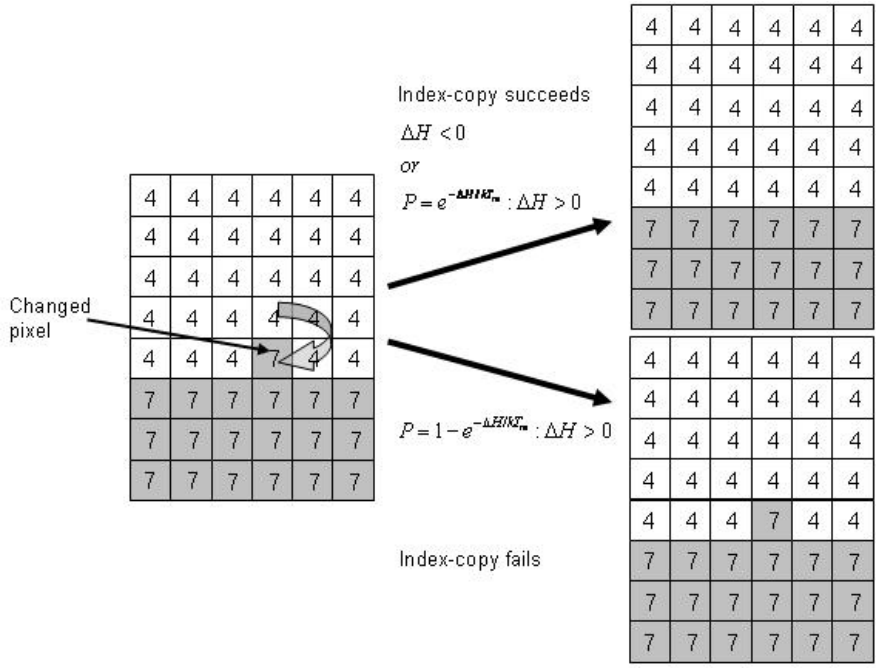

Figure 6.5: Schematic diagram showing the GGH representation of an index-copy attempt for two cells on a 2-dimensional square lattice. The "white" pixel (source) attempts to replace the "grey" pixel (target). The probability of accepting the index copy is given by equation (6.19).

For the boundary energy ($\mathscr{H}_{\text{boundary}}$) of the Hamiltonian (6.6) we use the `ContactLocalProduct` plugin that calculates the boundary energy based on the levels of E-cadherin expression per cell. We set two types of cells, namely "LowBetaCat" for cells having concentration of β-catenin below the threshold c_T and "HighBetaCat" for cells with β-catenin higher than c_T. The values of contact/boundary energy between the two types of cells, between the cells and the medium are specified in the `ContactLocalProduct` plugin. The medium is the non-cell area. The

`VolumeLocalFlex` and `SurfaceLocalFlex` plugins are used for the volume constraint ($\mathscr{H}_{\text{volume}}$) and the surface constraint $\mathscr{H}_{\text{surface}}$), respectively. We use these plugins in the XML file to allow the target volume and the target surface to vary individually for each cell during the simulation without having to explicitly specify the values of λ_{volume}, V_t, λ_{surface}, and S_t. For initialisation, in the steppable file we assign their dimensionless parameter values as listed in Table 6.2.

Table 6.2: CC3D parameter values

Parameter	Definition	Dimensionless Value
λ_{volume}	Cell's inverse compressibility	0.5
V_t	Cell's target volume	1.2×cell volume
λ_{surface}	Cell's inverse membrane compressibility	1.5
S_t	Cell's target surface area	400

The integration of CC3D and Bionetsolver in the model is illustrated in the flow chart, see Fig. 6.6. The simulations are started by adjusting cell shape and for simulations that require cell division we invoke the cell mitosis function, which is a built-in function of CC3D. After a certain time (denoted by $T1$), we start the Bionetsolver for the numerical integration of the differential equations. To change the concentration of β-catenin at time $T2$, we switch the values of k_2 and k^+, where if the concentration of β-catenin inside each cell ($[\beta]$) is higher than the concentration of β-catenin threshold (c_T) the cell then detaches from the main tumour mass.

6.4 Computational Simulation Results

We modelled three different scenarios as follows: (1) detachment waves of β-catenin on a thin layer of epithelial cells, described in subsection 6.4.1; (2) tumour growth and

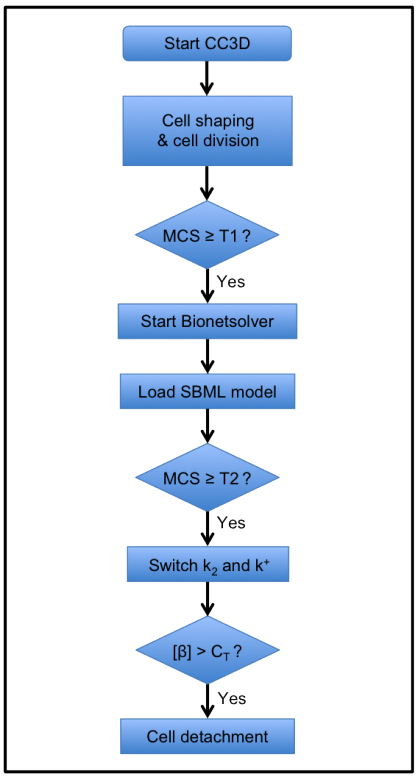

Figure 6.6: Flow chart of the integration of CC3D and Bionetsolver in the model.

detachment of cells from a layer of epithelial cells; and (3) tumour growth and detachment of cells in a multicellular tumour spheroid, both described in subsection 6.4.2.

6.4.1 Detachment Waves of Epithelial Layer Simulations

To simulate detachment waves of β-catenin on a thin layer of epithelial cells, we performed the simulation on a domain or a lattice of $264 \times 224 \times 60$ pixels in x, y, and z directions, respectively, with the z-axis being perpendicular to the page. In the lattice we placed a sheet of cells with an arrangement of 30 cells along the x-axis (horizontal), 25 cells along the y-axis (vertical), and 1 cell in the z-axis. Initially each cell occupies a cube of dimension $7 \times 7 \times 7$ pixels and we insert a gap of 1 pixel between each cell, as can be seen in the top left plot of Fig. 6.7. The initial target volume for cells is set to 1.2 times the cell volume, making the average volume of each cell about 410 pixels. We set 1 pixel equivalent to 2 μm. Therefore one tumour cell has a volume

of about 3280 μm^3, and the sheet represents a thin layer of tissue with a volume of $0.48 \times 0.408 \times 0.014$ mm^3 $= 2.74 \times 10^{-3}$ mm^3.

From time 0 MCS (Monte Carlo Steps) to 20 MCS we let the cells grow, where cell volume increases, followed by increasing cell surface area, and eventually the cells become more spherical. During this period of the simulations, cell-cell contact areas undergo an equilibrating transient that does not reflect natural phenomena. Thus, we did not start the numerical integration of the differential equations (corresponding to the subcellular biochemical networks) until 20 MCS. Keeping in mind that the subcellular model is sensitive to changes in intercellular contact areas, if numerical integration occurred during the initial cell shape changes, unrealistic subcellular dynamics could occur as an artefact of these changes. Starting the integration at 20 MCS helped avoid this. This is done to all simulations. All parameter values used in the computational simulations are listed in Tables 6.1 and 6.2, unless stated otherwise. In the intracellular model, summarised in Eqs. 6.18a-6.18d, disruption of cell-cell adhesion occurs when there is an increase in the concentration of free β-catenin in the cytoplasm, that is the β-catenin concentration exceeds a specified threshold value as a result of disassociation of the E-cadherin-β-catenin complex at the cell membrane. The threshold we specified for our simulations is 50.0. As explained previously, for cell detachment to occur nuclear β-catenin must exceed this threshold value and the terms $\mathscr{A}_1$ and $\mathscr{A}_2$ in Eqs. 6.14 and 6.15 change accordingly. This essentially amounts to setting ν equal to 0 in Eqs. 6.14 and 6.15, and replacing $\mathscr{A}_1$ by $-\alpha[\mathrm{E}/\beta]$ and $\mathscr{A}_2$ by $\alpha[\mathrm{E}/\beta]$ in Eqs. 6.18b and 6.18c, respectively. In the SBML implementation of our subcellular model, we actually do not implement two separate sets of equations for attachment and detachment. Instead, the equations, as implemented in the SBML model, are equivalent to Eqs. 6.18a-6.18d with $\mathscr{A}_1$ and $\mathscr{A}_2$ as for attachment condition, but with all instances of components of $\mathscr{A}_1$ and $\mathscr{A}_2$ are swapped. In our CC3D-Bionetsolver implementation (*i.e.*, our Python script), the increase of β-catenin concentration above the threshold

is deliberately done by decreasing the value of k^+ at a specified time, that is from $k^+ = 1.5$ to $k^+ = 1.0$ at $= 70$ MCS. This parameter influences the association rate of β-catenin with the proteasome. When $k^+ = 1.5$, the β-catenin-proteasome complex formation is sufficiently rapid to keep the β-catenin concentration of all cells well below the threshold of $c_T = 50.0$. However, when k^+ is decreased to a value of 1.0, β-catenin accumulates in the cytoplasm as a result of decreased proteasomal degradation.

We check the β-catenin concentration for every cell at each MCS. If the β-catenin concentration for a cell of type "LowBetaCat" increases above a threshold value of 50.0, the cell type is changed to "HighBetaCat", ν is set to 0.0 instead of 100.0 and α is set to 2.0 instead of 0.0. Similarly, when the β-catenin concentration of a "HighBetaCat" cell decreases below the threshold, the value of ν for that cell is set to 100.0 and α is set to 0.0.

In the case of an EMT event (*i.e.*, a cell type change from "LowBetaCat" to "HighBetaCat"), changing the values of ν and α as described is equivalent to swapping the components of the terms $\mathscr{A}_1$ and $\mathscr{A}_2$, between attachment and detachment. Physically, this corresponds to (1) a cessation of E-cadherin-β-catenin complex formation in the membrane ($\nu = 0.0$) and (2) an accelerated dissociation of E-cadherin-β-catenin complex (*i.e.*, the dissociation rate parameter $d_i(t)$, is increased by $\alpha = 2.0$) to form cytoplasmic (free) E-cadherin and free β-catenin. Together, the effects of these two changes are: (1) an increased concentration of β-catenin in the cytoplasm; and (2) a significantly reduced adhesion strength between the transformed cell and its neighbouring cells (due to the loss of the E-cadherin-β-catenin complex in the membrane).

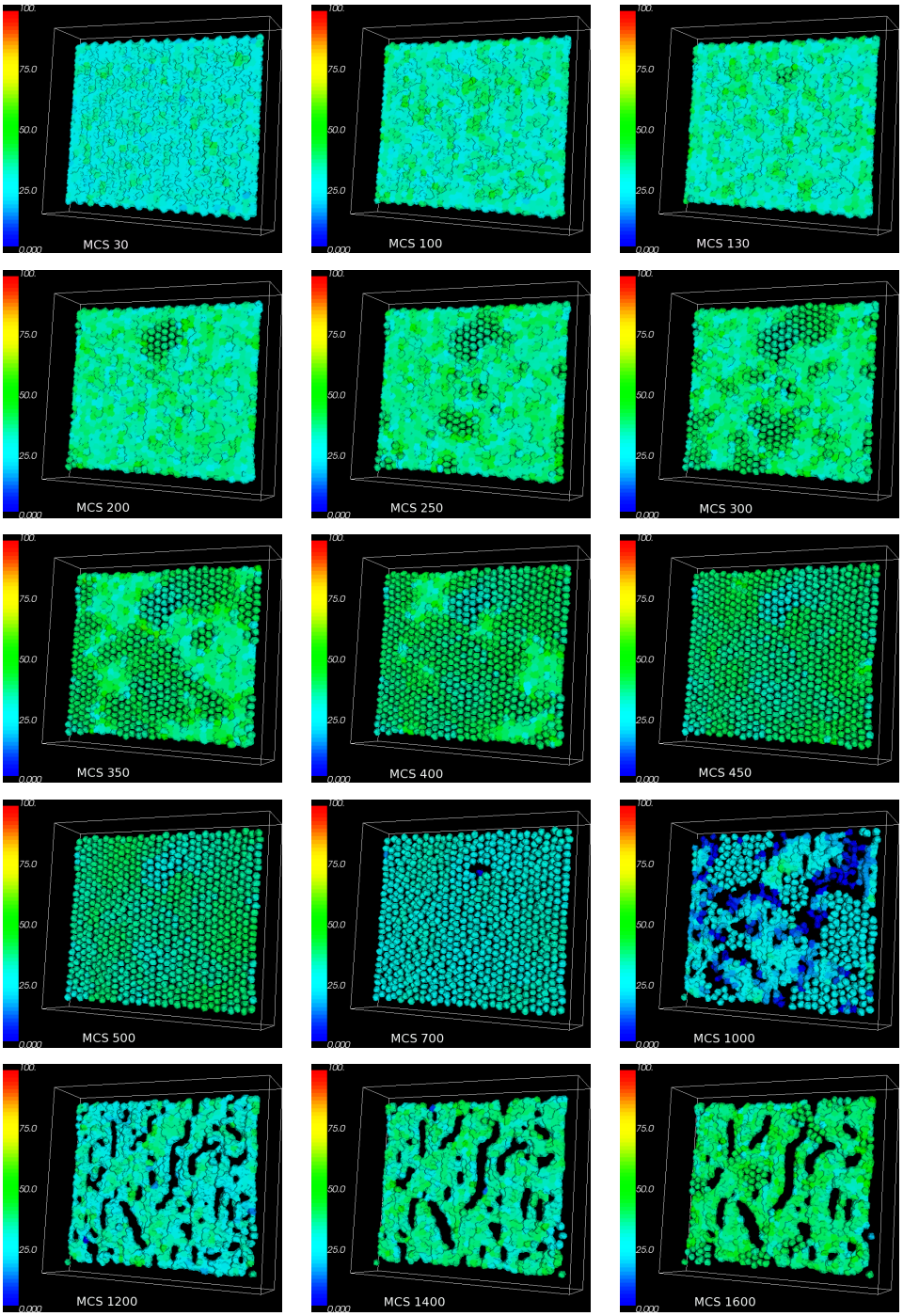

Figure 6.7: Plots showing a sequence of the disruption of a layer of epithelial cells due to an increase in the β-catenin concentration inside the cells. After all cells have been detached from the layer of cells or from each other showing EMT, low concentration of β-catenin causes cells that are close to each other to perform re-attachment and regain MET while some cells that are not close remain as mesenchymal cells. Colours of the cells represent concentration of β-catenin, shown by the bar on the left.

In Fig. 6.7 an increase of β-catenin concentration above threshold is triggered by several cells. When one cell is induced with a high β-catenin concentration above the threshold c_T, the cell becomes vulnerable to the loss of cell-cell attachment leading to EMT. The event propagates away, affecting neighbouring cells and subsequently the cells in the neighbourhood of the affected neighbouring cells and so on, where the concentration of β-catenin of the neighbouring cells also exceeds the threshold and the neighbouring cells also become vulnerable to EMT. We observe a small group of cells at 130 MCS start to detach and at 200 MCS the detachment waves have spread affecting more adjacent cells. As time evolves, some cells at other positions also show detachment waves independently. Eventually at around 500 MCS all cells in the layer have been affected and are detached from each other, which is the hallmark of EMT events. There is an alteration of the configuration of the epithelial layer of cells, where the cells are displaced from their original position, remaining detached near the initial configuration of the epithelial layer since we do not apply any chemoattractant in this simulation. By letting the simulation run for a longer time, that is up to 5000 MCS, we observe that the concentration of β-catenin of all the detached cells decreases and some cells even have near zero concentration of β-catenin. The colour of cells in all figures indicates the concentration of β-catenin. Low concentration of β-catenin causes cells that are close to each other to perform re-attachment and this subsequently causes an increase of β-catenin concentration. The cells recover the formation of epithelial cell lines, or a mesenchymal-epithelial transition (MET), with irregular configuration of the cell layer. The results we report here are consistent with those of Ramis-Conde et al. (2008). We also observe from the simulation results that after the first EMT event there are a few of cells that are dragged relatively far away from the other cells. As a consequence of the big gaps between them, these cells cannot re-attach with the other cells and remain as “mesenchymal” cells.

In order to see how the concentration of the proteins inside each individual cell vary

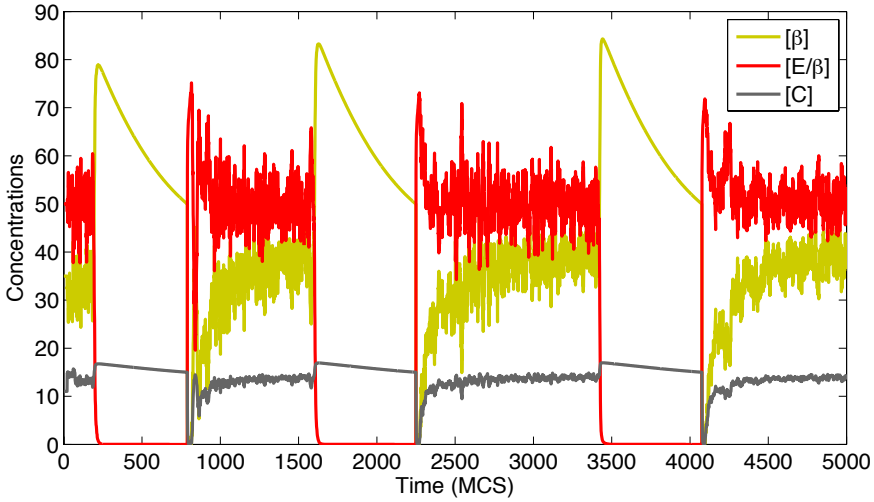

Figure 6.8: Plots of β-catenin, E-cadherin-β-catenin complex, and proteasome-β-catenin concentrations for a scenario of a cell that underwent an epithelial-mesenchymal transition (EMT), and then regained mesenchymal-epithelial transition (MET) by reattaching with adjacent cells. The cycle of detachment and re-attachment continues for about 3 times until 5000 MCS.

over time, in our CC3D-Bionetsolver codes we recorded and saved data of all concentrations at every MCS. In Fig. 6.8 we plot the typical concentrations of β-catenin, E-cadherin-β-catenin complex, and β-catenin-proteasome complex for cells that undergo EMT and gain MET from the simulation shown in Fig. 6.7. Because of the stochastic nature of the GGH model, the concentrations vary in response to fluctuations in contact area between cells. We can verify that when the concentration of β-catenin increases significantly (due to loss of contact area between cells) and immediately decreases afterwards, the transition curve becomes smooth showing no fluctuations. After the cell regain contacts with other cells, the curve fluctuates again. By running the simulation up to 5000 MCS, from Fig. 6.8 we can see that there are three cycles of detachment and attachment as can be seen from the repeated cycles of the high and low concentration of β-catenin (yellowish-green line).

As for cells that cannot re-attach after the first detachment because they have been displaced relatively far away from other cells and remain mesenchymal (cannot recover MET), the concentrations of the subcellular proteins immediately reach their

own steady states, as shown by plots of data in Fig. 6.9.

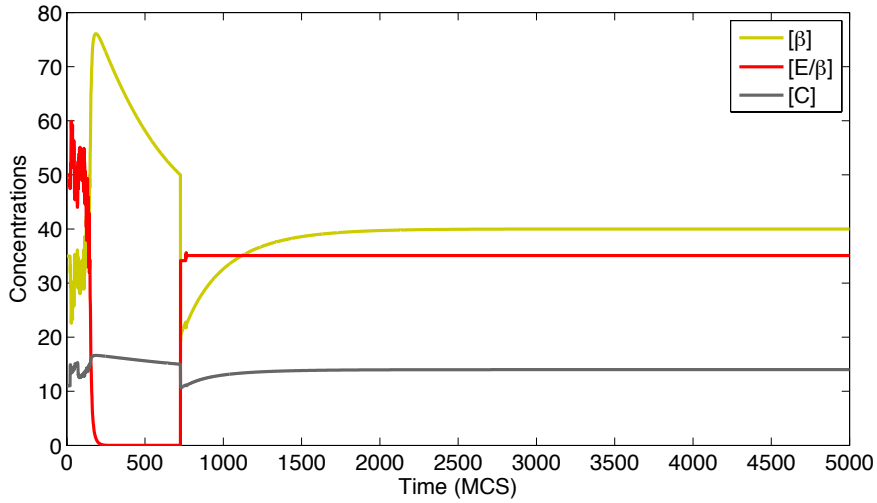

Figure 6.9: Plots of β-catenin, E-cadherin-β-catenin complex, and proteasome-β-catenin concentrations for a scenario of a cell that underwent an epithelial-mesenchymal transition.

6.4.2 Tumour Growth and Invasion

For simulations involving tumour growth, the GGH target volume is incremented each MCS during growth phases, at a constant rate of 0.02 times the current cell volume and the GGH target surface area is also incremented at a constant rate of 0.02 times the current cell surface area. This results in a doubling of cell number approximately every 40 MCS. Cell division was set to occur when the volume of a cell exceeded 2 times its initial volume. This rate of growth was not necessarily intended to reflect *in vivo* rates of tumour cell growth. Rather, the purpose in our simulations is simply to let the tumour grow to a specified size so that we can then initiate EMT events and observe the subsequent dynamics of cell detachment and migration.

Tumour from a Layer of Cells

To simulate the growth of a tumour from a layer of cells, a common occurrence for tumours of epithelial tissue origin, we use a bigger 3-dimensional lattice or a cubic

lattice of size $120 \times 120 \times 120$ pixels in the x, y, and z directions. Initially we placed one layer of cells, which consists of 10×10 cells, at one face/side of the cube, or at $x = 120$ as shown by the configuration of the top left plot in Fig. 6.10. All cells are cubic in shape with size $7 \times 7 \times 7$ pixels with a 1 pixel gap between each of them. Here we apply a gradient of some chemoattractant linearly in the direction of the x-axis to generate cell migration into the tissue space.

From a single thin layer, the tumour grows and becomes a bulky layer as a result of cell division. In the implementation of CC3D-Bionetsolver it is possible to let the tumour grow infinitely, but in this type of simulation we limit the cell division until the number of cells in the tumour mass reaches a maximum of 500 cells. After 200 MCS we initiate an increase of free β-catenin concentration by reducing the value of k^+ from 1.5 to 1.0. Some random cells at the outer layer show a high concentration of free β-catenin at 500 MCS and these cells eventually break away from the primary tumour mass and migrate toward the region of high concentration of the chemoattractant, which we apply at $x = 0$. As the EMT events propagate, over time as some cells at the outer layer have detached, the cells that were underneath the detached cells fill in the gap left by the detached cells. Subsequently these cells have reduced attachment with neighbouring cells which causes an increase in the concentration of β-catenin above the threshold, and eventually these cells detach.

To see the distribution of free β-catenin inside the cells that remain and are still attached to the primary tumour mass, we plot a cross sectional view of the tumour mass along the yz plane, as shown in Fig. 6.11. Cells of blueish colour that are bound to other cells inside the tumour have a concentration of free β-catenin lower than the threshold c_T. Cells that have fewer binding sites, which lie at the outer layer, show a higher concentration of free β-catenin above c_T (shown in Fig. 6.11 by colours ranging from yellowish green to dark orange). These results are qualitatively in good agreement with the simulation results of Ramis-Conde et al. (2008) and the experimental data of

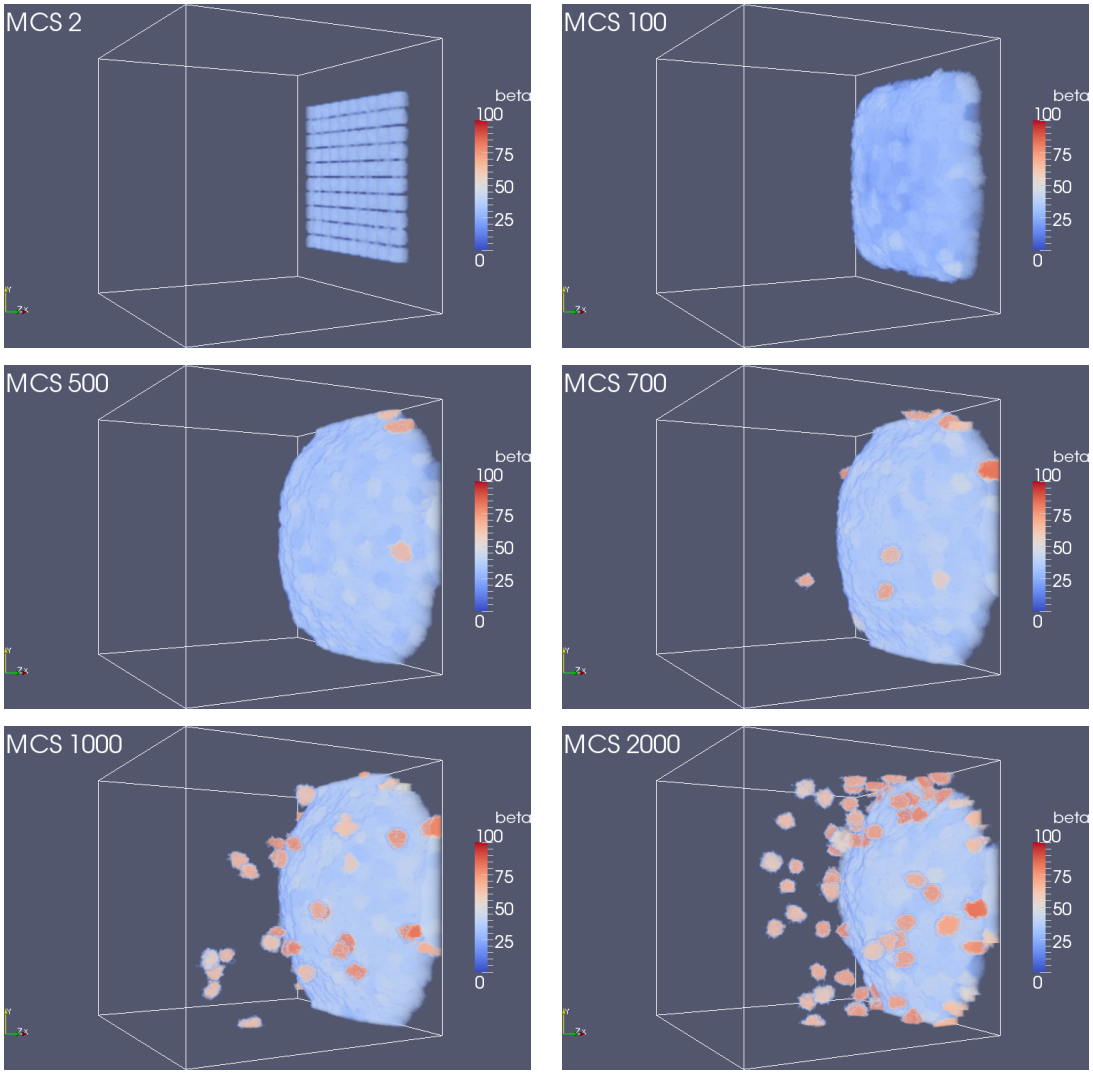

Figure 6.10: Plots showing tumour growth and local invasion (detachment) from a layer of cells. After the tumour reaches a certain size (by limiting the number of maximum cells in the tumour mass), the cells at the outer layer lose cell-cell attachment due to the disruption of E-cadherin-β-catenin complex. The EMT events then take place. A gradient of chemoattractant that is applied linearly in the direction of the x-axis causes the detached cells to perform chemotactic migration into the tissue space. Colours in the cells represent the concentration of β-catenin.

Brabletz et al. (2001). We may assume that the concentration of nuclear β-catenin is represented by the concentration of free β-catenin inside the cytoplasm, because our current mathematical model does not specify or distinguish between the two types of β-catenin.

To study the dependency of the multiscale dynamics on the β-catenin degradation

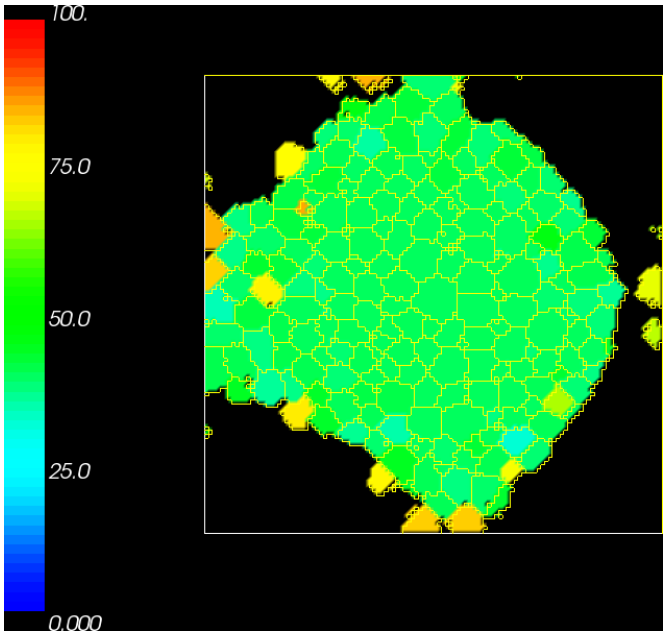

Figure 6.11: Plot of a cross sectional view showing the spatial distribution of β-catenin concentration inside cells from the simulation of tumour growth from a layer of cells. Cells in the centre of the tumour mass have a large number of binding neighbours, hence the concentration of β-catenin is lower than the cells at the outer layer of tumour mass that have fewer binding neighbours and a high concentration of free β-catenin.

rate k_2, Ramis-Conde et al. (2008) performed simulations by varying k_2 that resemble different degradation of rates of invasion assays which have been used *in vitro* as a measure of invasive potential. If k_2 is small enough, this leads to a high concentration of free β-catenin. If it reaches a value above the threshold, then the cells are susceptible to the loss of cell-cell detachment and become invasive by breaking away from the primary tumour mass. In other words, a sufficiently small k_2 can be a marker for malignant or invasive tumour cells. Ramis-Conde et al. (2008) varied the β-catenin degradation rate from $k_2 = 10\ \text{min}^{-1}$ which represents an invasion assay with a fast degradation rate, $k_2 = 1\ \text{min}^{-1}$ for an invasion assay with a medium degradation rate, and $k_2 = 0\ \text{min}^{-1}$ to represent no degradation. Our CC3D-Bionetsolver implementation is sensitive to the variations of k_2 and we only varied from $k_2 = 0.95$ for the very low degradation rate, $k_2 = 1$ for medium degradation rate, and $k_2 = 1.05$ for invasion assay with fast degradation rate. The computational simulation results are shown in

Fig. 6.12, where the number of cells that have reached a certain distance is plotted over time. In the simulation, we remove the cells from the domain that have reached a certain distance from the tumour. We chose a distance of 70 pixels away from the initial position of cells (the position of the single layer of cells at the start of simulations) as the position where a cell is counted. In Fig. 6.12 we have plotted the number of cells removed from the domain over time, up to the maximum permitted number of 500 which we imposed as an upper threshold. The simulation results with $k_2 = 0.95$ show a curve that quickly increases exponentially in a small time (purple line), while the simulation results with $k_2 = 1.0$ show a linear increase of the number of cells that has been removed over time (blue line), and finally with the fast degradation rate of invasion assay $k_2 = 1.05$ there is only a very small number of cells that have been removed beyond the distance of 70 pixels (green line).

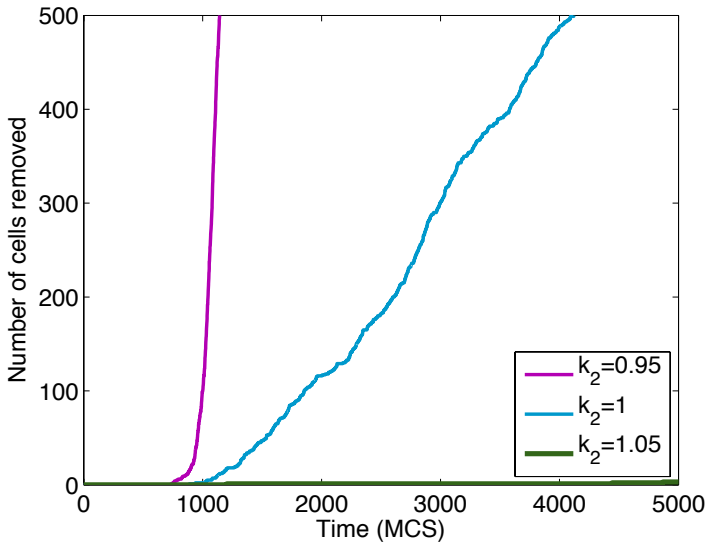

Figure 6.12: Number of cells removed from simulations of tumour growth from a layer of cells by varying k_2.

Multicellular Spheroid Growth

It is also of interest to see how our CC3D-Bionetsolver can mimic the growth and invasion of multicellular spheroids which are spherical aggregations of (malignant)

cells that can be grown *in vitro*. Multicellular spheroids are particularly used in cancer research for studying multicellular resistance or chemo- or radiotherapy assays (Oudar, 2000). They can be used to study cell-cell and cell-matrix adhesion *in vitro* and also the influence of the environment on many cellular functions such as differentiation, cell death, apoptosis, gene expression and regulation of proliferation.

As in the simulations for tumour growth from a layer of cells, here we also use a cubic lattice with size $240 \times 240 \times 240$ pixels in the x, y, and z directions. Once again the initial cell has a cubic shape with size $7 \times 7 \times 7$ pixels. The simulations are started with one cell placed at the centre of the cubic lattice. As the cells divide, to maintain tumour compactness and prevent any undesirable effects before we trigger detachment, we set the threshold value of β-catenin concentration, c_T, high enough, *i.e.*, $c_T = 70$. We let the tumour grow and become spherical in shape, as shown by the top right plot in Fig. 6.13. At time 400 MCS, the value of k^+ is decreased from 1.5 to 1.0 and we observe at time 500 MCS, cells at the surface of the tumour spheroid start to show a high concentration of free β-catenin. In this type of simulation we apply a radially symmetric concentration field of chemoattractant. After having lost cell-cell adhesion with neighbouring cells due to the high concentration of free β-catenin above the threshold, the detached cells migrate radially outwards in response to the applied chemoattractant field.

An interesting result from these simulations is that it gives an indication of the size of the tumour at which invasion begins. In Fig. 6.14 we plot the graphs of cell position over time for simulations with different values of k_2. All plots in Fig. 6.14 were taken from the cell of ID1, which is the cell that we set at initial configuration, at time 0 MCS. The red line represents the case with $k_2 = 0.95$, the blue line represents the case with $k_2 = 1.0$, and the black line is for the case with $k_2 = 1.02$. At each k_2 value, the cell detaches from the primary tumour mass at a different "invasion time". The most invasive cell is the one that detaches the earliest, that is with $k_2 = 0.95$. The least

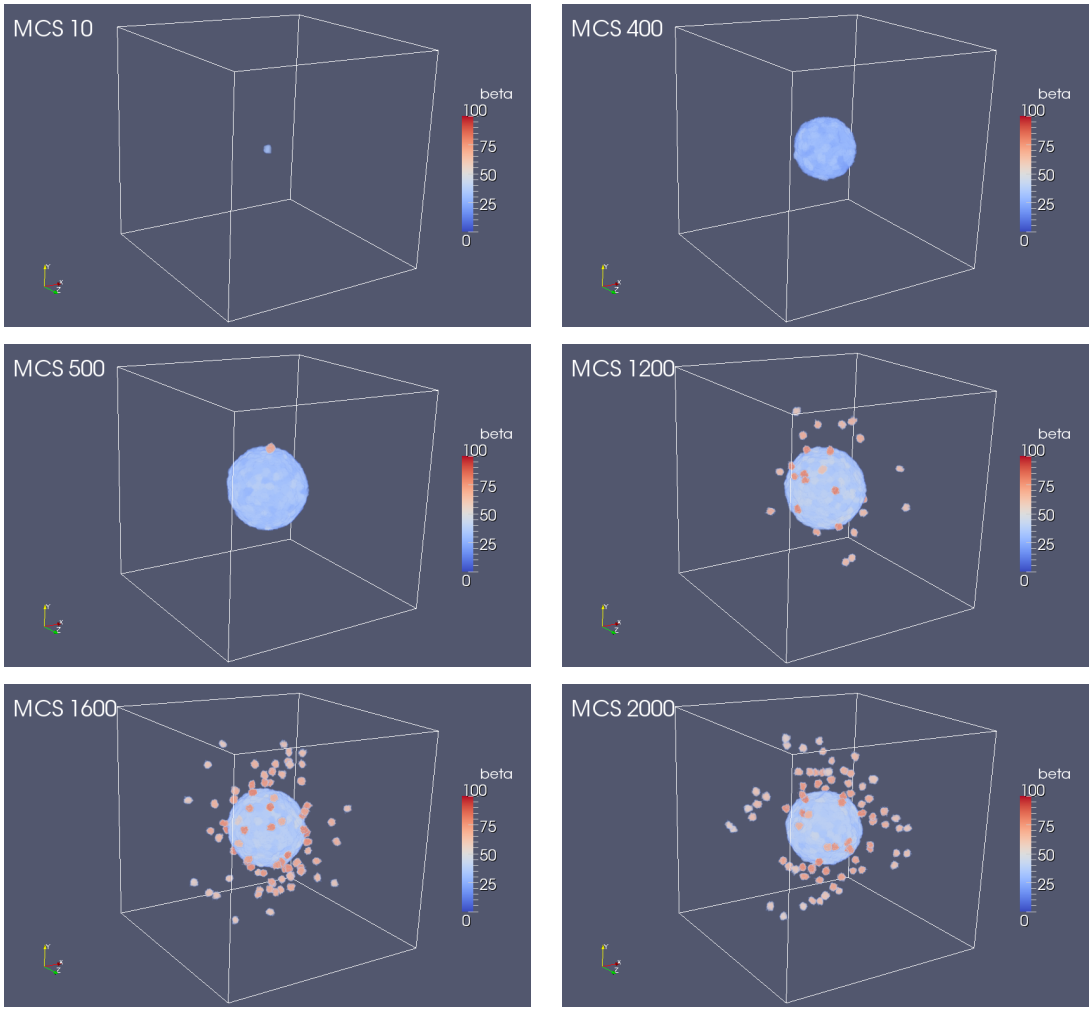

Figure 6.13: Plots showing the computational simulation results of multicellular tumour spheroid growth. The tumour grows from a single cell placed in the middle of cubic lattice. At a certain stage in its growth, cells may detach and invade into the external tissue driven by chemotactic migration which has overcome the cell-cell adhesion. The colours of the cells indicate the concentration of β-catenin.

invasive cell, with $k_2 = 1.05$, detaches the latest. The reason we chose cell of ID1 is because the cell started at the centre of the domain and as the simulation goes it moves along the way to the boundary of the tumour mass before it detaches itself from the tumour mass whereas other cells that came out of cell division started their position not at the centre of the domain. Hence tracking the position of cell of ID1 is the best choice for determining tumour radius or diameter.

After having been detached, the cells migrate radially away from the tumour mass

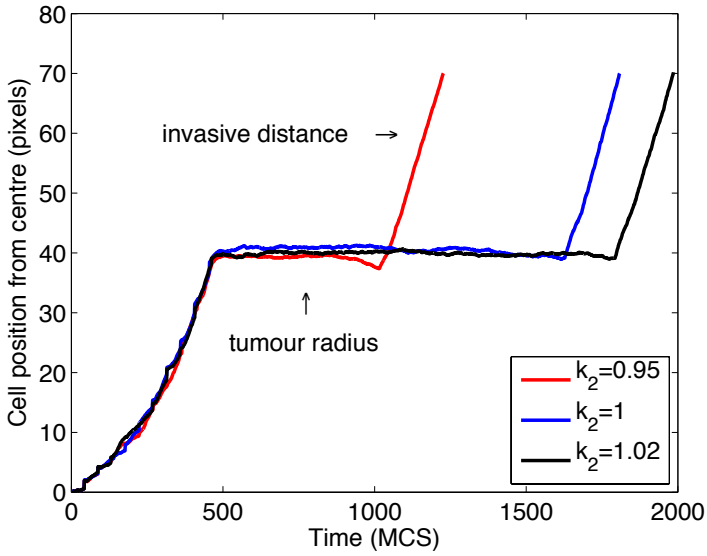

Figure 6.14: Position of cell ID1 from the centre of cubic lattice of size $240 \times 240 \times 240$ pixels from simulations of multicellular spheroid when parameter k_2 is varied from $k_2 = 0.95$, $k_2 = 1$, and to $k_2 = 1.02$. Tumour radius is determined from a position of cell which is on a horizontal curve for a period of time, here at pixel 40. Invasive distance is the position of cell within a circle around the multicellular spheroid.

following the gradients of the applied chemoattractant. The distance between the furthest cell and the radius of the multicellular spheroid is defined as the "invasive distance", as shown in Fig. 6.14. This invasive distance has been demonstrated in a study of the growth and invasion of a glioblastoma multiforme (GBM) in 3-dimensional collagen I matrices by Kaufman et al. (2005).

Plots of data for the number of cells that have reached a distance 70 pixels from the centre of lattice show almost similar patterns as the data for simulations with layer of cells, as shown in Fig. 6.15. For data of invasion assay with rate of degradation of β-catenin low ($k_2 = 0.95$) the curve shows exponential increase of the number of cells that have reached distance 70 pixels or have been removed from the simulations (purple line). For simulation with $k_2 = 1.0$ and $k_2 = 1.02$ the rates of cells that have been removed are fewer than simulation with $k_2 = 0.95$, suggesting less invasive tumours.

Our simulation results have verified *in vitro* and *in vivo* experiments, that the level of invasiveness of tumour cells can be assessed from the extent of the loss of cell-cell

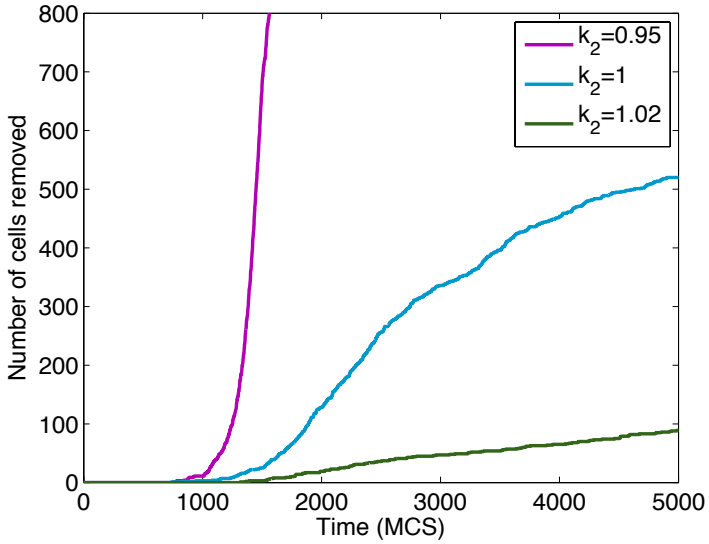

Figure 6.15: Plots showing the number of cells removed from multicellular spheroid simulations using different values of k_2.

adhesion. We can see in our simulations that high level of invasiveness is achieved by down-regulation of cell-cell adhesion, that is by decreasing the values of k_2. We use $k_2 = 0.95$ to simulate more invasive scenario and $k_2 = 1.0$ for less invasive scenario as shown by the bottom right and bottom left figures in Fig. 6.16, respectively. This then must be followed by up-regulation of cell-matrix adhesion, another component that is required for successful invasion. This "discrete analogy" can be related to the results in the previous chapter. We have learnt in Chapter 5 the inverse relation between cell-cell and cell-matrix adhesion, that is in order to invade and migrate through the surrounding tissue, cell-cell adhesion should be sufficiently low and cell-matrix adhesion should be sufficiently high.

In their experiments, Kaufman et al. (2005) showed the effects of increasing collagen concentration on the level of invasiveness of GBM cells, which is similar to increasing cell-matrix adhesion. GBM that has been implanted in a high collagen concentration shows growth pattern of malignant tumour with invasive cells that gradually accumulate from the centre of multicellular spheroid invading outwardly everywhere, as shown in top right figure of Fig 6.16. While GBM that has been implanted in a

low collagen concentration shows relatively few invasive cells that tend to be invading along distinct branches, as shown by the top left figure.

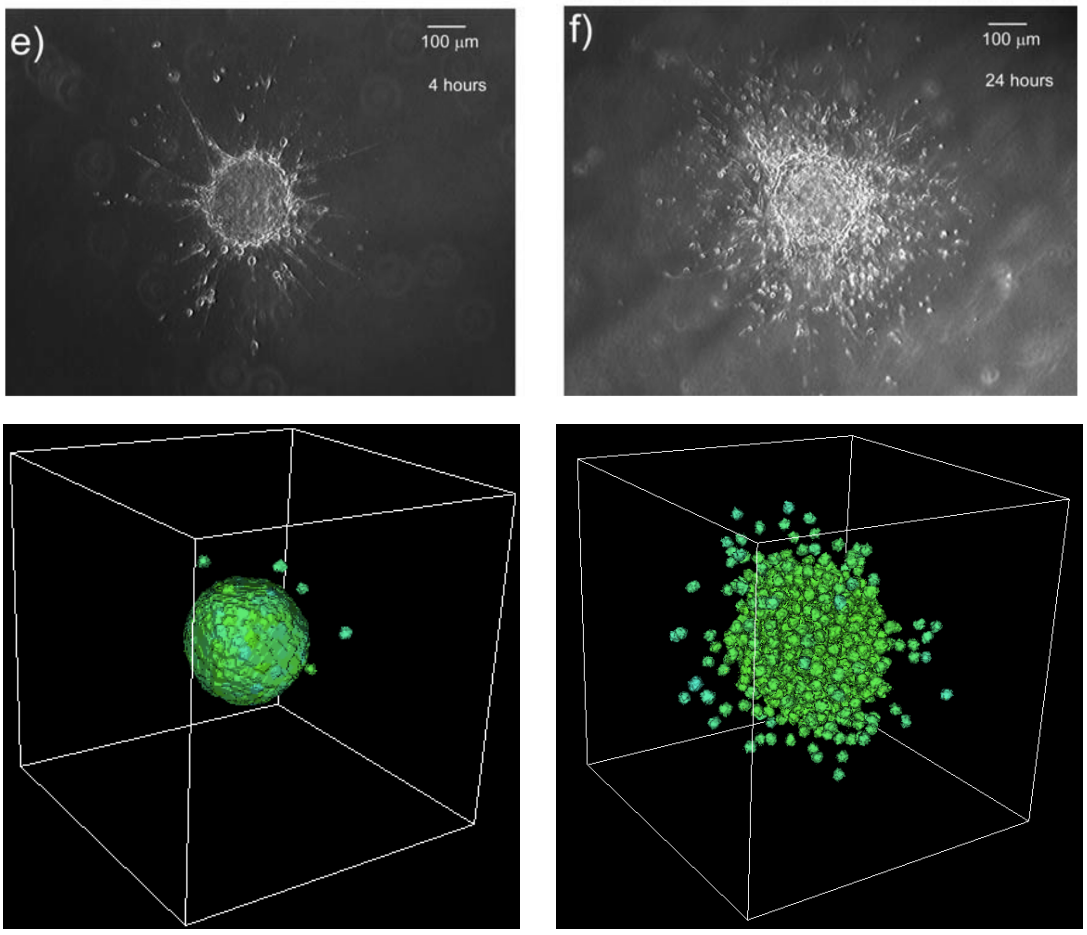

Figure 6.16: Plots showing the growth patterns of experimental data of multicellular spheroids grown in low collagen concentration (top left figure) for less invasive pattern and in high collagen concentration (top right figure) for more invasive pattern (Kaufman et al., 2005) and our computational simulation results (bottom right figure with $k_2 = 0.95$ and bottom left figure with $k_2 = 1.0$). The simulation results were taken at 900 MCS. Top right and left figures are reprinted from Biophysical Journal, 89/1, L. Kaufman, C. Brangwynne, K. Kasza, E. Filippidi, V. Gordon, T. Deisboeck, and D. Weitz, Glioma expansion in collagen I matrices: analyzing collagen concentration-dependent growth and motility patterns, 635–650, Copyright (2005), with permission from Elsevier [OR APPLICABLE SOCIETY COPYRIGHT OWNER].

Although we cannot directly compare our simulation results (bottom right and left

figures) with the experimental results of Kaufman et al. (2005) (top right and left figures), the patterns of invasion from decreasing cell-cell adhesion (our simulation results) show similarities with the patterns of invasion from increasing cell-matrix adhesion (experimental results). We note that GBM is a sarcoma and likely not use E-cadherin/β-catenin signalling as it is not originated from epithelial tissues. Instead, sarcomas along with other types of brain tumours, express N-cadherin that also mediate calcium-dependent intercellular adhesion. Nevertheless, another paper by Ramis-Conde et al. (2009) developed another multiscale model of transendothelial migration (TEM) involving N-cadherin in which the pathway that they developed is not far different than the pathway using E-cadherin, based on their literature study. Hence, there may be possibility that the kinetics of intracellular proteins of GBM similar to the kinetics we have described here.

6.5 Discussion and Conclusions

In this chapter we have developed a multiscale model of cancer growth and invasion using CC3D and Bionetsolver to study the role of intracellular dynamics of E-cadherin and β-catenin based on a mathematical model by Ramis-Conde et al. (2008). We used CC3D, a lattice-based simulation environment, for modelling on the cellular level and Bionetsolver, a programming library, for modelling on the subcellular (or intracellular) level. The integration of CC3D and Bionetsolver modelling mechanisms enables us to study cell behaviours that are driven by the dynamics inside of the cells. It allows us to tune the level of details in intracellular level, without switching simulation framework, and examine the effects of changing the level of details on a cellular level.

In the multiscale model presented here, we examined the invasive behaviours of cancer cells by modifying key parameters that are responsible for cell adhesion. Experimental studies have suggested that nuclear β-catenin upregulation may characterise invasive cell populations in many types of cancer (Brabletz et al., 2001; Ng et al.,

2005; Suzuki et al., 2008; Uchino et al., 2010). In our model it is possible to tune parameters that regulate the concentration of free β-catenin (also by implication nuclear β-catenin) to study cancer invasiveness *in silico*. Two key parameters that were considered by Ramis-Conde et al. (2008), as shown in the pathway (6.11), were the parameter k^+ which influences the association rate of β-catenin with the proteasome and the parameter k_2 which is the rate of β-catenin degradation.

A sufficiently high value for k^+ can maintain cell-cell adhesion and also tumour compactness because it keeps the β-catenin concentration of all cells below a threshold value. However, when k^+ is decreased to a sufficiently low value, free β-catenin accumulates in the cytoplasm as a result of a decreased β-catenin-proteasome complex. This leads to EMT events, where loss of cell-cell adhesion leads to cells managing to break off from the primary tumour body to migrate through and invade the surrounding tissue.

Varying parameter k_2, which is the rate of β-catenin degradation, gives characteristics of studying invasive potential on invasion assay. Sufficiently low k_2 results in cells that are more invasive than the cells with sufficiently high k_2. Our simulation results from varying k_2 are qualitatively comparable with experimental data for the study of multicellular tumour spheroids (Kaufman et al., 2005).

While we were able to qualitatively reproduce results from Ramis-Conde et al. (2008), there were noticeable discrepancies that are likely due to fundamental differences in the two simulation methodologies. In the implementation of the GGH model into CC3D-Bionetsolver, the detachment waves of β-catenin in epithelial layers cannot be controlled to appear from a single cell in a layer and propagate radially outward in a regular manner, as shown in Figures 5 and 6 of the paper by Ramis-Conde et al. (2008). Instead, by reducing k^+ from 1.5 to 1.0 in our GGH model, the detachment waves in an epithelial layer of cells are triggered by many cells which then propagate outward irregularly. See Fig. 6.17 for comparison.

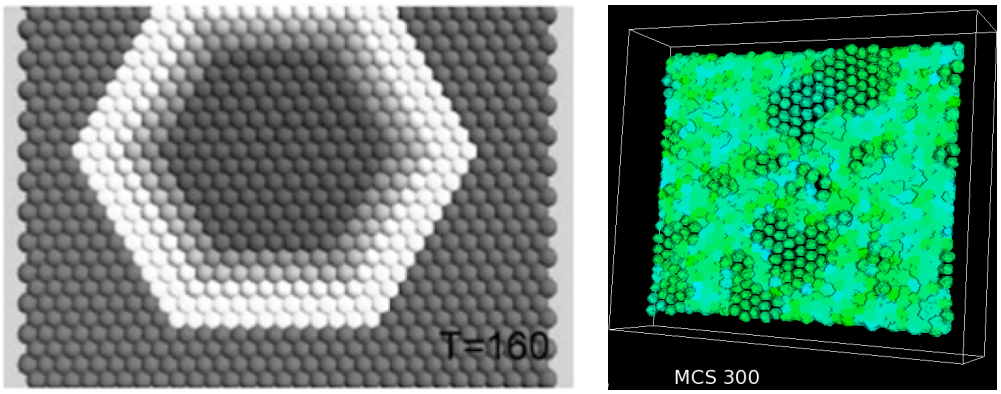

Figure 6.17: Comparison showing the difference in β-catenin detachment wave simulations between centre based model of Ramis-Conde et al. (2008) (left figure) and our CC3D-Bionetsolver results (right figure). Left figure is reprinted from Biophysical Journal, 95, I. Ramis-Conde, D. Drasdo, A.R.A. Anderson, and M.A.J. Chaplain, Modeling the influence of the E-cadherin-β-catenin pathway in cancer cell invasion: a multiscale approach, 155–165, Copyright (2008), with permission from Elsevier [OR APPLICABLE SOCIETY COPYRIGHT OWNER].

Another discrepancy, is that the stochastic nature of the GGH model produces fluctuations of the concentrations of intracellular variables in response to fluctuations in contact area between cells. This can be seen from the plots shown in Figs. 6.8 and 6.9. It should be noted that the issue of differences between simulation methodologies is distinct from the question of how well the simulation results collectively reflect or correspond to actual experimental observations. Nevertheless, there are primary contributions that we have made from our multiscale implementation study, which include the following: (1) It brings to light fundamental differences that exist between two major individual cell-based modelling methodologies, the centre-based model and the GGH model, within the context of cancer biology, and (2) it provides an introduction to CC3D-Bionetsolver, a recently developed multiscale framework for multicellular simulation.

Having seen that the CC3D-Bionetsolver can be used for multiscale modelling of cancer cell invasion to study the effects and roles of cell adhesion (including cell-cell and cell-matrix adhesion), it is our aim in the near future to augment the multiscale

model of cancer invasion by incorporating intracellular pathways that describe interactions between the cells and the matrix.

Chapter 7

Intracellular Modelling of Cell-matrix Adhesion

7.1 Introduction

Adhesive interactions between cancer cells and their surroundings, *i.e.*, the extracellular matrix, are vital for metastatic spread. The adhesive interactions are required for migration through the basement membrane and extracellular matrix surrounding the tumour after detachment from the primary tumour mass, and for penetration of the circulating tumour cells into the tissue of the target organ at the secondary site.

In the interactions between cell and matrix, termed cell-matrix adhesion, the intracellular compartment of the cell is connected with the extracellular environment through cell surface receptors. Inside the cell, cell surface receptors are indirectly linked to the actin cytoskeletal network that is dynamically remodelled. Outside the cell, cell surface receptors bind with extracellular matrix components such as fibronectin. The reorganisation of the actin cytoskeleton combined with binding of cell surface receptors to matrix components provides a mechanical linkage between cell and matrix, to produce the force or traction necessary for cell adhesion, spreading and migration.

Cancer cells migrate in various ways, according to cell type and degree of differentiation. The molecular mechanisms underlying the migration of cancer cells through the tissues are similar to the mechanisms used by normal, non-neoplastic cells for migration during physiological processes, such as wound healing, embryonic morphogenesis, immune cell trafficking, etc. The principles of cell migration were initially investigated in non-neoplastic fibroblasts, keratinocytes and myoblasts, but additional studies on tumour cells show that the same basic strategies are retained (Friedl and Wolf, 2003).

Cell migration is an integrated process that requires the continuous, coordinated formation and disassembly of adhesions. Migration can be viewed as a cyclical process. Based on studies, it is commonly agreed that the basic migratory cycle includes the following processes (Palecek et al., 1998; Machesky and Hall, 1997; Nishizaka et al., 2000; Webb et al., 2002; Ananthakrishnan and Ehrlicher, 2007):

- Extension of a protrusion. Polymerisation of the actin cytoskeletal network drives the initial extension of the plasma membrane at the cell front;
- Formation of stable contacts near the leading edge of the protrusion. The interaction of the cell surface receptors with the extracellular matrix stabilises the adhesions by recruiting signalling and cytoskeletal proteins;
- Cytoskeletal contraction, that generates a tractional force;
- Translocation of the cell body forward. The small, nascent adhesions may transmit strong forces, and serve as traction points for the propulsive forces that move the cell body forward; and
- Release of adhesions and retraction at the cell rear. This completes the migratory cycle allowing net translocation of the cell in the direction of movement.

The major groups of cell surface receptors for mediating cell-matrix adhesion are known as integrins, named for their role in integrating the intracellular cytoskeleton

with the extracellular matrix (Ojaniemi and Vuori, 1997). Integrins provide a bi-directional signalling for mechanochemical information across the cell membrane, that is, two-way signalling occurs from outside-to-inside and from inside-to-outside. This signalling functioning provides a major mechanism for connecting the intracellular compartment (which is the cytoskeleton) and the extracellular compartment (extracellular matrix components or glycoproteins, such as fibronectin).

Over the last twenty years there have been attempts to mathematically model the interaction between cells and surfaces representing the extracellular matrix, such as by Hammer and Lauffenburger (1987) who modelled cell adhesion to surfaces mediated by specific binding between molecules on the cell surface and complementary ligand molecules on the receiving surface. The binding depends on various quantities such as receptor number, binding affinity between receptor and ligand, bond formation rate, receptor diffusivity, distractive fluid forces, and contact area. Palecek et al. (1999) modelled the interactions between integrins, the cytoskeleton, and the matrix for cell retraction and dissociation mechanisms at the cell rear. DiMilla et al. (1991) modelled the dependence of cell speed on adhesion-receptor/ligand binding and cell mechanical properties. Their model incorporated cytoskeletal force generation, cell polarization, and dynamic adhesion for cell movement.

In this chapter we model a cell-matrix adhesion pathway describing interactions between fibronectin, integrins and actin reorganisation. Binding of fibronectin with integrins triggers a clustering of protein complexes, which then activates and phosphorylates regulatory proteins that are involved in actin reorganisation causing actin polymerisation and stress fibre assembly. Rearrangement of actin filaments with integrin/fibronectin complexes near adhesion sites and interaction with fibrillar fibronectin produces the force necessary for cell migration, accounting for cell-matrix adhesion.

7.2 Structural Components of Cell-matrix Adhesion

To model the mechanisms of cell adhesion to extracellular matrix, we consider three major components that are needed to generate traction used by cells to perform migration through the matrix. These components are the cell surface receptors integrins, the matrix glycoprotein fibronectin, and the actin cytoskeleton.

Integrins comprise a large family of transmembrane glycoproteins that mainly function to mediate cell-matrix adhesion. Integrins are composed of two subunits, α and β, and each $\alpha\beta$ combination has its own binding specificity and signalling properties (Giancotti and Ruoslahti, 1999). To date, there are 18α and 8β subunits which combine with each other to form a family of 24 distinct heterodimeric integrins that have been identified in humans (Hynes, 2002; Takada et al., 2007). Heterodimeric integrins are expressed on the cell membrane to link the actin cytoskeleton to the extracellular matrix. Three different β_1 integrins, which are $\alpha_4\beta_1$, $\alpha_5\beta_1$, and $\alpha_8\beta_1$, have been found which bind to fibronectin. Another large subfamily of integrins is composed of heterodimers sharing the α_V subunit, also receptors for fibronectin, $\alpha_V\beta_1$, $\alpha_V\beta_3$, $\alpha_V\beta_5$, $\alpha_V\beta_6$, and $\alpha_V\beta_8$ (Koistinen and Heino, 2002).

The cytoplasmic tails of integrins are generally short with roughly 50 amino acids in length, except for integrin β_4 that has ~ 1000 amino acids. The cytoplasmic tails are also devoid of enzymatic features. Hence, integrin cytoplasmic domains form multimolecular complexes with proteins involved in cell signalling and adapter proteins that connect the integrin to the actin cytoskeletal system, cytoplasmic kinases, and transmembrane growth factor receptors (Giancotti and Ruoslahti, 1999; Berrier and Yamada, 2007). The cytoskeleton organisation is performed after accumulation of cytoskeletal proteins like tensin, α-actinin, talin, vinculin, and focal adhesion kinase (FAK).

Migrating cells bind to fibronectin by means of discrete integrin clusterings at the leading or protruding edge. Integrin clustering can be a result of integrin binding

with fibronectin which then promotes the localisation of adaptor proteins linking to the cytoskeleton (Giancotti and Ruoslahti, 1999; Berrier and Yamada, 2007) or the clustering of integrins can cause binding of the leading edge of the cell with fibronectin. A study on integrin clusterings in motile fibroblasts by Regen and Horwitz (1992) showed that integrin clusterings grow at the leading edge and shrink at the cell rear over time, in the sense that they fluctuate in size, density, and shape over a period of minutes. As cells move, integrin clusterings that bind with fibronectin (often referred to as focal contacts or focal adhesion sites) appear at the leading edge and diminish in number toward the cell centre, while at the cell rear there is only a small number of clusterings that abruptly break as the cell body advances forward. Experiments carried out by Cluzel et al. (2005) demonstrated that integrin activation is a prerequisite for clustering events. They observed that integrin clusterings in the periphery of the cell occur within minutes, starts about after 3 minutes.

Integrin binding with matrix can also affect integrin activation, where integrin binding to fibronectin changes the conformational state of integrin, from inactive to active (García et al., 1998; García and Boettiger, 1999; Berrier and Yamada, 2007). Integrin activation is a prerequisite for clustering, hence activated integrins preferentially localise to the leading edge, where new adhesions form. In our model, we assume that integrin activation is triggered by binding of integrin to fibronectin, which then leads to clustering of integrin/fibronectin complexes.

The clustering of integrin/fibronectin complexes at the focal adhesion sites regulates downstream signalling pathways that induce an accumulation of signalling and adaptor proteins near the cytoplasmic domains of integrins. There are more than 50 cytoplasmic proteins present in the cell-matrix adhesion structure. The downstream signals coordinate reorganisation of the cytoskeleton as a result of actin polymerisation. The cytoskeleton is a highly dynamic part of a cell. It consists of numerous cytoskeletal actin filaments (F-actin) that constantly grow at their barbed end through

polymerisation of monomeric actin (G-actin) and shrink at the pointed end through actin depolymerisation. This process is referred to as "treadmilling", which is a steady state flux of filaments (Pollard and Mooseker, 1981; Wehrle-Haller and Imhof, 2003). The reorganisation of the actin cytoskeleton is the primary mechanism of cell motility and is essential for most types of cell migration. During cell migration, the actin cytoskeleton is dynamically remodelled, and this reorganisation produces the force necessary for cell migration. The reorganisation of actin filaments into larger stress fibres, in turn, causes more integrin clusterings, thus enhancing the matrix binding and organisation by integrins in a positive feedback system (Giancotti and Ruoslahti, 1999). Evidence accumulated from a variety of cell types has shown that the actin filaments assembled near the leading edge are also transported rearward or in a direction opposite to the movement of the cell. This phenomenon is known as retrograde flow. There is a balance between the actin cytoskeleton assembly and the retrograde flow that govern and control cell movement (Abraham et al., 1999; Mallavarapu and Mitchison, 1999; Wiseman et al., 2004; Guo and Wang, 2007).

The structure and composition of the extracellular matrix is also very important for cancer cell invasion. One of the key components of the extracellular matrix which plays a major role in cell-matrix adhesion is fibronectin. Two forms of fibronectin exist. One form, plasma or soluble fibronectin, is a major plasma protein and found at concentration of 300μg/ml in human blood. An early study by Tamkun and Hynes (1983) showed that hepatocytes of rats and hamster synthesised and secreted fibronectin as a soluble dimeric protein. In humans, soluble fibronectin is synthesised predominantly in the liver by hepatocytes in dimeric form. Another form, known as cellular fibronectin, is found at the surfaces of many different cell types, where it forms insoluble fibrillar matrices (Pankov and Yamada, 2002). A major fraction of the cellular fibronectin in the extracellular matrix has been found to be derived from plasma fibronectin (Moretti

et al., 2007). The assembly of fibronectin matrix or insoluble fibrillar matrix is a cell-mediated process. It is thought that the binding of integrin to fibronectin promotes fibrillar matrix formation through interactions with other cell-association fibronectin dimers. As fibrillar matrices form on the outside of the cell, cytoplasmic domains of integrins organise cytoplasmic proteins (signalling and adaptor proteins) into functional complexes linking to the cytoskeleton. The whole process of binding of cytoskeleton to integrins and fibronectin is essential for fibrillar matrices formation and propagation (Wierzbicka-Patynowski and Schwarzbauer, 2003). The insoluble fibrillar matrices, along with other components of extracellular matrix, provide structural support for cellular functions such as cell adhesion, migration, and tissue organisation. For migrating cells, binding onto a rigid surface helps generate tractional forces necessary for moving the cell body forward. Since the assembly of fibronectin into a fibrillar matrix is a complex process, we assume, for our model, that the fibrillar matrices are formed by binding of the clustering of integrin/fibronectin complex bound with soluble fibronectin. The more fibronectin or fibrillar matrices formed, the more rigid the extracellular matrix becomes. The rigidity of extracellular matrix causes the strengthening of the integrin-cytoskeleton linkages (Choquet et al., 1997). Hence it generates positive feedback for cytoskeleton organisation inside of the cell. The adhesion forces are the final step produced from the kinetics and mechanics of the structural components of cell-matrix adhesion.

7.3 Mathematical Model Derivation

Based on the kinetics of the major components of cell-matrix adhesion summarised in section 7.2, we assume the following steps for our cell-matrix adhesion pathway:

1. Binding of integrin [R] to plasma or soluble fibronectin [F_p] to form an integrin/fibronectin complex [FR], with reversible reactions:

$$R + F_p \underset{k_2}{\overset{k_1}{\rightleftharpoons}} FR$$

2. The clustering of integrin/fibronectin complex results from the binding of integrin with fibronectin at the cell membrane. Here we adopt a simple clustering reaction as in Fussenegger et al. (2000), which is assumed to be irreversible, with rate k_3:

$$FR \xrightarrow{k_3} \widetilde{FR}$$

3. Clustering triggers recruitment and localisation of cytoplasmic proteins, hence activation and phosphorylation of regulating proteins. This then activates actin polymerisation and actin reorganisation A_p at the leading edge that pushes the membrane forward in finger-like structures (filopodia) and can also be in sheet-like structures (lamellipodia), with rate k_4:

$$\widetilde{FR} \xrightarrow{k_4} A_p$$

   To account for processes that reduce actin filaments at the leading edge such as treadmilling and retrograde flow, we assume a natural decay with constant rate m.

4. Rearrangement of actin filaments with clusters of the integrin/fibronectin complex near focal contact sites:

$$A_p + \widetilde{FR} \underset{k_6}{\overset{k_5}{\rightleftharpoons}} A_p.\widetilde{FR}$$

5. Meanwhile, surrounding the cell in the extracellular domain, the formation of the fibrillar fibronectin network occurs with a rate k_7:

$$\widetilde{FR} + F_p \xrightarrow{k_7} F_\times$$

The formation of the fibrillar fibronectin network increases matrix rigidity, which in turn, gives a positive feedback with rate k_8 to the strengthening of the integrin/fibronectin-cytoskeleton linkage $A_p.\widetilde{FR}$.

6. Binding of the integrin/fibronectin-cytoskeleton linkage $A_p.\widetilde{FR}$ to the fibrillar network yields an adhesion force, measured by its strength, required for cell movement:

$$F_\times + A_p.\widetilde{FR} \underset{k_{10}}{\overset{k_9}{\rightleftharpoons}} F_\times.A_p.\widetilde{FR}$$

The complex $F_\times.A_p.\widetilde{FR}$ ruptures during cell detachment at the cell rear. Hence the reaction is reversible.

7. An increasing force adds a positive feedback to the clustering of complex with rate k_{11}.

These intracellular interactions are summarised in a schematic diagram shown in Fig. 7.1.

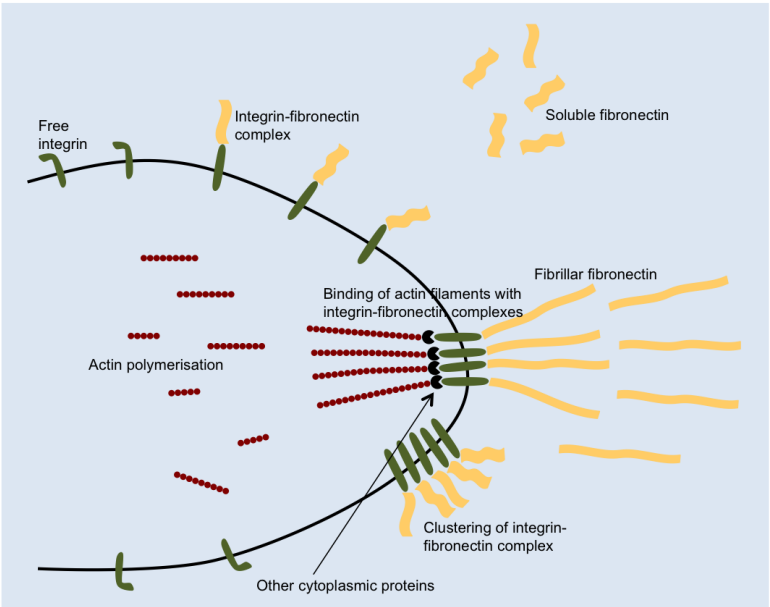

Figure 7.1: A schematic diagram of the kinetics for cell-matrix adhesion process involving integrin, fibronectin, and actin.

By letting

$$
\begin{aligned}
[\mathrm{R}] &= x_1 \\
[\mathrm{F_p}] &= x_2 \\
[\mathrm{FR}] &= x_3 \\
[\widetilde{\mathrm{FR}}] &= x_4 \\
[\mathrm{A_p}] &= x_5 \\
[\mathrm{A_p}.\widetilde{\mathrm{FR}}] &= x_6 \\
[\mathrm{F_\times}] &= x_7 \\
[\mathrm{F_\times}.\mathrm{A_p}.\widetilde{\mathrm{FR}}] &= x_8
\end{aligned}
$$

and applying the law of mass action, we obtain the system of ODEs:

$$\frac{dx_1}{dt} = k_2x_3 - k_1x_1x_2\,, \tag{7.1a}$$

$$\frac{dx_2}{dt} = k_2x_3 - k_1x_1x_2 - k_7x_2x_4\,, \tag{7.1b}$$

$$\frac{dx_3}{dt} = k_1x_1x_2 - k_2x_3 - k_3x_3\,, \tag{7.1c}$$

$$\frac{dx_4}{dt} = k_3x_3 - k_4x_4 + k_6x_6 - k_5x_4x_5 - k_7x_2x_4 + k_{11}x_8\,, \tag{7.1d}$$

$$\frac{dx_5}{dt} = k_4x_4 + k_6x_6 - k_5x_4x_5 - mx_5\,, \tag{7.1e}$$

$$\frac{dx_6}{dt} = k_5x_4x_5 + k_8x_7 - k_6x_6 - k_9x_6x_7 + k_{10}x_8\,, \tag{7.1f}$$

$$\frac{dx_7}{dt} = k_7x_2x_4 - k_8x_7 + k_{10}x_8 - k_9x_6x_7\,, \tag{7.1g}$$

$$\frac{dx_8}{dt} = k_9x_6x_7 - k_{10}x_8 - k_{11}x_8\,. \tag{7.1h}$$

We introduce dimensionless variables

$$x_1^* = \frac{x_1}{x_R}\,, \qquad x_2^* = \frac{x_2}{x_F}\,, \qquad x_5^* = \frac{x_5}{x_R}\,,$$

where x_R is the reference concentration of integrin and x_F is the reference density of plasma fibronectin. To set the reference for density of integrin/fibronectin complex, we follow García and Boettiger (1999), that under conditions of excess ligand (of fibronectin) the steady state density/concentration of integrin/fibronectin complex is proportional to

$$x_{FR} = K_a x_R x_F\,,$$

where $K_a = \dfrac{k_1}{k_2}$ is the equilibrium affinity constant for binding of integrins with fibronectin. We use it for the other dimensionless variables:

$$x_3^* = \frac{x_3}{x_{FR}}\,, \quad x_4^* = \frac{x_4}{x_{FR}}\,, \quad x_6^* = \frac{x_6}{x_{FR}}\,, \quad x_7^* = \frac{x_7}{x_{FR}}\,, \quad \text{and} \quad x_8^* = \frac{x_8}{x_{FR}}\,.$$

We nondimensionalise time as

$$t^* = \frac{t}{T}$$

where T is an appropriate reference time and we obtain the nondimensional parameters:

$$k_1^* = x_{FR}k_1T\,, \qquad k_2^* = k_2T\,, \qquad k_3^* = k_3T\,, \qquad k_4^* = k_4T\,, \qquad k_5^* = x_{FR}k_5T\,, \qquad k_6^* = k_6T$$

$$k_7^* = x_{FR}k_7T\,, \qquad k_8^* = k_8T \qquad k_9^* = x_{FR}k_9T\,, \qquad k_{10}^* = k_{10}T\,, \qquad k_{11}^* = k_{11}T\,, \qquad m^* = mT\,.$$

Inserting the dimensionless variables and parameters above into the system of equations (7.1) and after dropping the stars for notational convenience, the nondimensional model for cell-matrix adhesion is

$$\frac{dx_1}{dt} = \alpha k_2 x_3 - \frac{1}{\beta} k_1 x_1 x_2 \,, \tag{7.2a}$$

$$\frac{dx_2}{dt} = \beta k_2 x_3 - \frac{1}{\alpha} k_1 x_1 x_2 - k_7 x_2 x_4 \,, \tag{7.2b}$$

$$\frac{dx_3}{dt} = \frac{1}{\alpha\beta} k_1 x_1 x_2 - k_2 x_3 - k_3 x_3 \,, \tag{7.2c}$$

$$\frac{dx_4}{dt} = k_3 x_3 - k_4 x_4 + k_6 x_6 - \frac{1}{\alpha} k_5 x_4 x_5 - \frac{1}{\beta} k_7 x_2 x_4 + k_{11} x_8 \,, \tag{7.2d}$$

$$\frac{dx_5}{dt} = \alpha k_4 x_4 + \alpha k_6 x_6 - k_5 x_4 x_5 - m x_5 \,, \tag{7.2e}$$

$$\frac{dx_6}{dt} = \frac{1}{\alpha} k_5 x_4 x_5 + k_8 x_7 - k_6 x_6 - k_9 x_6 x_7 + k_{10} x_8 \,, \tag{7.2f}$$

$$\frac{dx_7}{dt} = \frac{1}{\beta} k_7 x_2 x_4 - k_8 x_7 + k_{10} x_8 - k_9 x_6 x_7 \,, \tag{7.2g}$$

$$\frac{dx_8}{dt} = k_9 x_6 x_7 - k_{10} x_8 - k_{11} x_8 \,, \tag{7.2h}$$

where

$$\alpha = \frac{k_1 x_F}{k_2} \qquad \text{and} \qquad \beta = \frac{k_1 x_R}{k_2} \,.$$

For migrating cells, adhesion of cells to matrix occurs instantaneously in order to prevent the formation of mature focal adhesions which are bigger in size and hold cells from moving.

7.4 Computational Simulation Results

In this section we present the results of computational simulations from the system (7.2). To obtain dimensionless parameter values, we use parameters listed in Table 7.1 for reference.

Table 7.1: Parameter values for the intracellular simulations

Parameter	Definition	Range/Value	Reference
x_R	Receptor density	$10^8 - 10^{12}\text{cm}^{-2}$	Palecek et al. (1999)
x_F	Ligand density	$10^6 - 10^{13}\text{cm}^{-2}$	Palecek et al. (1999)
$\frac{k_1}{k_2}$	Receptor-ligand equilibrium constant	$10^{-8} - 10^{-6}\text{M}^{-1}$	Palecek et al. (1999)
k_2	Reverse receptor-ligand reaction rate	$5 \times 10^{-4}\text{s}^{-1}$	Chen et al. (1999)
k_3	Rate of integrin clustering	$6.3 \times 10^{-3}\text{s}^{-1}$	Wehrle-Haller (2007)
$\frac{k_5}{k_6}$	Receptor-cytoskeleton equilibrium constant	$10^{-8} - 10^{-6}\text{M}^{-1}$	Palecek et al. (1999)
k_7	Rate of fibrillar matrix formation	$0.01141\ \text{min}^{-1}$	Monaghan et al. (2004)
T	Time integrin clusterings start at focal contacts	1 hour	Kawakami et al. (2001)

For parameter values that could not be found in the literature, we use estimated values. Dimensionless parameter values used in the simulations are summarised as follows:

$$k_1 = 1.8, \quad k_2 = 1.8, \quad k_3 = 20, \quad k_4 = 1.1, \quad k_5 = 0.36$$
$$k_6 = 0.36, \quad k_7 = 2.7, \quad k_8 = 0.01, \quad k_9 = 5, \quad k_{10} = 0.001,$$
$$k_{11} = 0.001 \quad \alpha = 1.0 \quad \beta = 0.1, \quad m = 0.005.$$

Initially we assume that there is a 0.6 fraction of free integrins on the cell membrane, a 0.45 fraction of soluble fibronectin and a small amount (0.03 fraction) of fibronectin matrix outside the surface of the cell. As a cell must have a cytoskeleton to support its shape, we assume there is a 0.3 fraction of actin filaments near the leading edge. The rest of the variables are initially zero.

The first result from the cell-matrix adhesion pathway that we show here is the adhesion force or adhesion strength produced from complex interactions between the cell surface receptor integrins as mediators, the cytoskeletal network inside of the cells and fibronectin with the fibrillar network outside of the cell. Using the dimensionless parameters given above, the computational simulations show that the generated adhesion strength shows an initial exponential increase, until it reaches a steady state or a constant strength, as shown on the right plot of Fig. 7.2. This result qualitatively agrees with the experimental data by Gallant et al. (2005) that measured fibroblast adhesion strengthening on fibronectin, as in the left plot of Fig. 7.2.

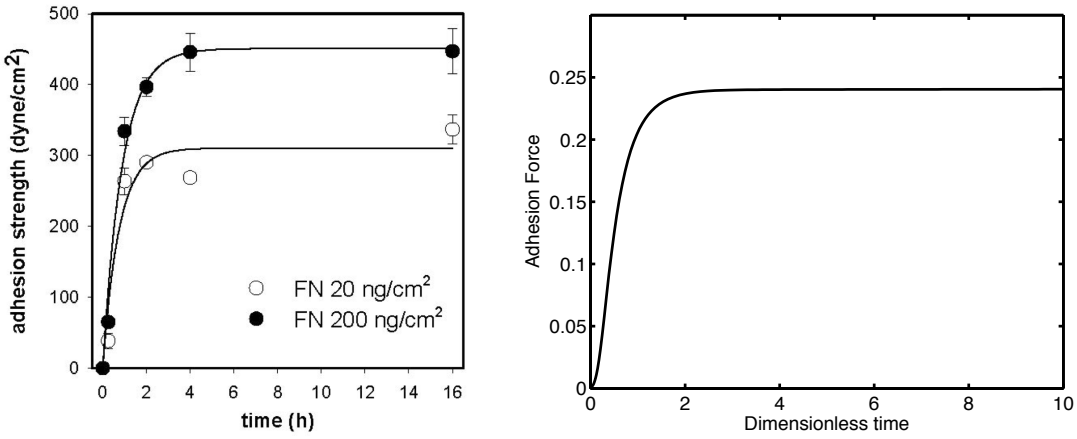

Figure 7.2: Plots showing a comparison between experimental data showing increase and steady state of adhesion force by Gallant et al. (2005) and our simulation result of generated force (right figure) from cell-matrix adhesion model (7.2) equation (7.2h).

Both experimental data and our simulation result show that the adhesion force or strength increases rapidly at early times and reaches a steady state value by 4 hours for experimental data and around dimensionless time 3 for our simulation. Experiments by Gallant et al. (2005) show the dependency of adhesion strength on fibronectin density, where a lower density of fibronectin yields a smaller constant adhesion strength (open circles) and a higher fibronectin density gives a bigger constant adhesion strength

(closed circles). For our cell-matrix adhesion model, the adhesion strength shows dependency both on integrin and soluble fibronectin densities. In Fig. 7.3 we plot adhesion strengths over time by varying the initial value of integrin $x_1(0)$ and soluble fibronectin $x_2(0)$ concentrations as shown on the left figure (for varying/increasing $x_1(0)$) and right figure (for varying/increasing $x_2(0)$). The initial value of concentrations is increased from $x_1(0) = 0.1$ (bottom curves), $x_1(0) = 0.3$, $x_1(0) = 0.6$, and $x_1(0) = 0.9$ (top curves) for both $x_1(0)$ and $x_2(0)$. Taking both $x_1(0) = 0.9$ and $x_2(0) = 0.9$, the time taken for the adhesion strength to reach a constant value is fast, around 2 dimensionless time units, and the constant adhesion strengths are also the same, about 0.25 for both initial densities of integrin and fibronectin 0.9. With the lowest initial densities $x_1(0) = 0.1$ and $x_2(0) = 0.1$, the time taken for the adhesion strength to reach a constant value is longer, around 6 dimensionless time units and the constant values of adhesion strengths are different for each integrin and fibronectin, where with $x_1(0) = 0.1$ the constant adhesion strength is around 0.16 and with $x_2(0) = 0.1$ the constant adhesion strength is around 0.195.

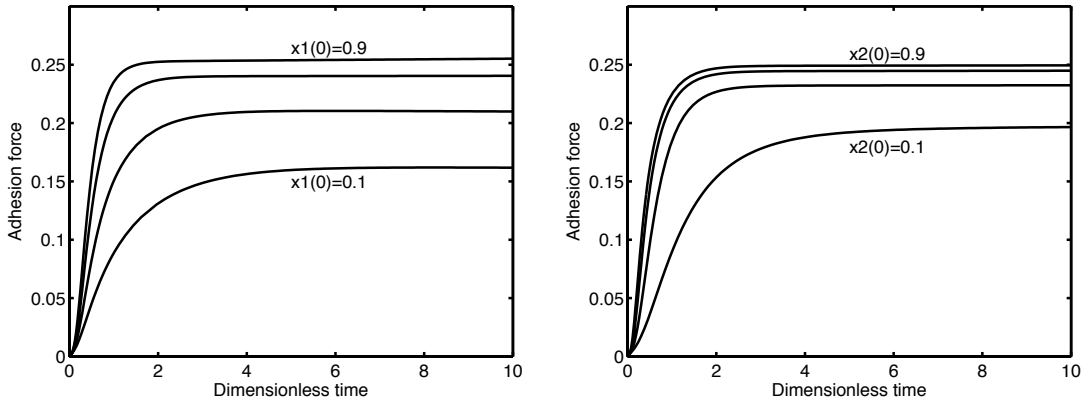

Figure 7.3: Plots showing increasing constant adhesion strength values by increasing initial concentration of integrins $x_1(0)$ (left figure) and initial concentration of soluble fibronectin $x_2(0)$ (right figure) from 0.1, 0.3, 0.6, and 0.9.

Butler et al. (2006) developed an *in vitro* assay to visualise and quantify actin polymerisation from purified $\alpha_v\beta_3$ integrin complexes that cluster at the protruding parts of the cells as shown on the left plot of Fig. 7.4. The experimental data show the

rates of actin assembly/polymerisation from different cells stimulated and unstimulated with Arg-Gly-Asp-ligand-induced β_3 tyrosine phosphorylation, where the black curve shows the rate of actin polymerisation by cells of wild type stimulated with Arg-Gly-Asp-ligand-induced β_3 tyrosine phosphorylation, the blue curve from unstimulated cells, the red curve for stimulated and expressing Y747-759F β_3 cells, and the orange curves for unstimulated expressing Y747-759F β_3 cells. The rate of actin polymerisation from experimental data shows a tendency of a rapid increase at early times until it reaches a constant value, the same pattern as the experimental data for adhesion strength. Our computational simulation result for x_5 from the model (7.2) which accounts for actin polymerisation followed by actin reorganisation near the leading edge as well as actin depolymerisation and retrograde flow for balance, also shows the same exponential increase until reaching a constant rate, as shown by the right plot of Fig. 7.4.

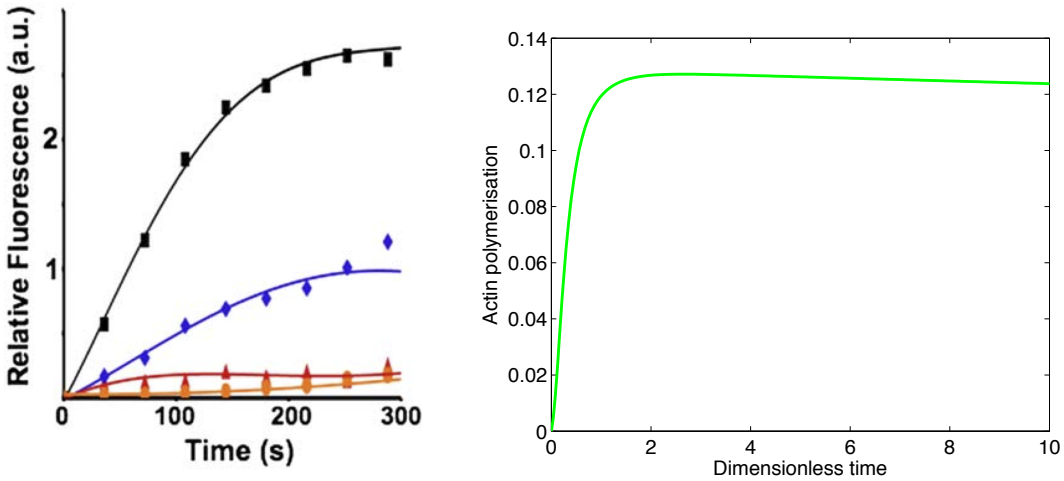

Figure 7.4: Plots showing different rates of actin polymerisation from experimental data by Butler et al. (2006) (left figure) and simulation result of actin polymerisation from cell-matrix adhesion model of equation (7.2e) (right figure). Left figure is reprinted from Current Biology, 16/3, B. Butler, C. Gao, A.T. Mersich, S.D. Blystone, Purified integrin adhesion complexes exhibit actin-polymerization activity, 242–251, Copyright (2006), with permission from Elsevier [OR APPLICABLE SOCIETY COPYRIGHT OWNER].

Other processes that are of experimental interest are the rate of change of soluble fibronectin and the rate of change of formation of insoluble cellular fibronectin or fibrillar fibronectin network (matrix) outside of the cell. We compare our simulation results for both kinetics with the experimental data of Sechler et al. (1996), as shown in Fig. 7.5. The left plot, which is the experimental data, shows the fast formation of insoluble fibronectin (open circles) from a certain type of soluble fibronectin (closed circles) (FNΔIII_{1-7}) that rapidly decreases. Both concentrations of soluble and insoluble fibronectin eventually reach contant values. The simulation results, shown by the right plot, from equations (7.2b) for soluble fibronectin concentration and (7.2g) for insoluble fibronectin concentration exhibit the same rate of reactions, which are an exponential decrease for soluble fibronectin and an exponential increase for insoluble fibronectin. The concentrations of both reach a constant steady state.

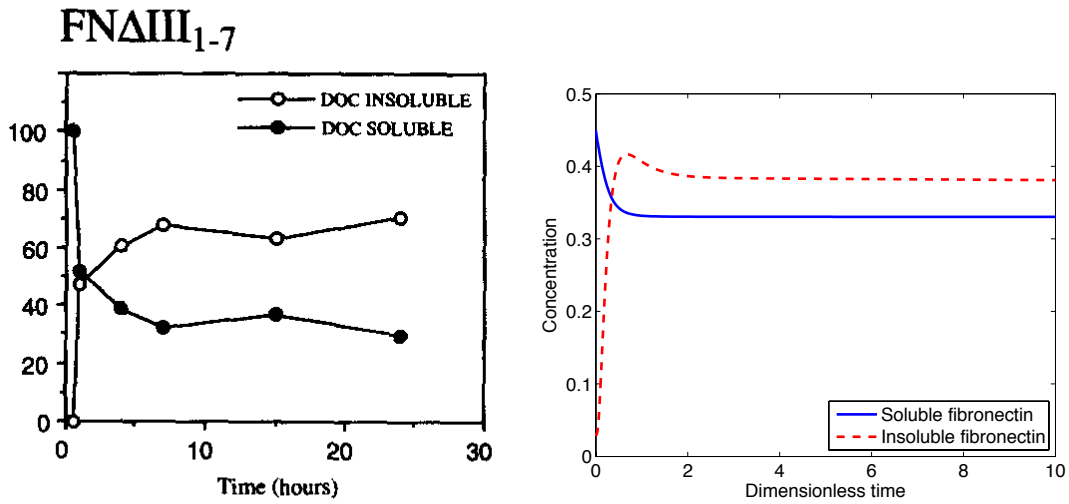

Figure 7.5: Plots showing the computational results of our model for kinetics of soluble fibronectin and the formation of insoluble fibronectin matrix (right figure) are comparable with experimental data by Sechler et al. (1996) (left figure).

7.5 Conclusions and Discussion

In this chapter we have presented a model of the key biochemical processes involved in cell-matrix adhesion that accounts for reactions between integrins, soluble fibronectin, the integrin/fibronectin complex, clustering of the integrin/fibronectin complex, actin polymerisation and reorganisation, the cytoskeletal complex, insoluble fibronectin (fibrillar network), and adhesion strength from the combination of the clustering integrin/fibronectin complex with the cytoskeletal network and attachment to insoluble fibronectin outside the cell, using a system of ordinary differential equations (7.2). We formulated the mathematical model from a proposed cell-matrix adhesion pathway that was derived based on the key events as reported in the literature.

Despite some parameters used in the simulations are only estimated values because not all parameters are available experimentally or in literature, our model shows good qualitative agreement with the experimental data, such as for adhesion strength plots shown in Figs. 7.2 and 7.3 and for kinetics of soluble fibronectin and formation of matrix fibronectin as shown in Fig. 7.5.

For migrating cells, the adhesion force generated from interactions of proteins locally is used for one cycle of movement which includes extending protrusions and moving their body forward. One cycle of cell movement takes around 30 minutes to 1 hour to occur, depending on many other variables such as a sufficient rigidity of surface/matrix for the smooth movement, an available gradient of chemoattractant, etc. The dynamics of key cell-adhesion components such as integrins, the cytoskeletal network and fibronectin, are also instantaneous. After one cycle of movement is completed, the whole pathway is restarted from the beginning to perform another cycle of movement. In order to prove this conjecture and to see whether our cell-matrix adhesion pathway works adequately, it is our aim for future work to apply the intracellular cell-matrix adhesion model into a multiscale cellular model together with the cell-cell adhesion model we have presented in Chapter 6.

Chapter 8

Conclusions and Future Work

In this thesis we have presented mathematical models of cancer cell invasion of tissue looking at the role of cell adhesion using two different mathematical approaches: (i) a continuum approach and (ii) a multiscale individual cell-based approach, or from a biological perspective the approaches refer to the tissue level and a combination between the subcellular and the cellular levels, respectively. With the continuum approach, we focused on a model of the urokinase plasminogen activation (uPA) system and the role of cell adhesion in cancer invasion, while with the individual cell-based approach we took a closer look at adhesion at a subcellular level and investigated the dynamics and interactions of proteins that control the complex phenomena.

For the uPA system model that is presented in Chapter 4 we performed a linear stability analysis and computational simulations of the model which was first proposed earlier by Chaplain and Lolas (2005). Our main contribution and finding is the observation of a very rich ("dynamic") spatio-temporal heterogeneity of the solutions. The linear stability analysis and computational simulations suggest that this may be due to a taxis-driven instability of the spatially homogeneous, positive steady state of the model. We showed that by varying key parameters of the model, the qualitative character of the solution, either of travelling-wave-like form or heterogeneous dynamics, can be changed. The prevalent character of the solution for a given parameter set can

be predicted by examining dispersion relations derived from a linear stability analysis of the system. We acknowledged that the model should be extended to a more comprehensive mechanism of invasion by including cell adhesion in the model. Cell adhesion has been shown experimentally, *in vivo* and *in vitro*, to be critical in cancer progression, from local invasion where the cancer originates to the dissemination of cancer to distant anatomical sites or metastasis

In Chapter 5 the original uPA system model, which consists of 5 PDEs, is developed and extended by including nonlocal terms to model the cell-cell and cell-matrix interactions, based on the work of Armstrong et al. (2006) and resulting in a system of integro-differential equations (Gerisch and Chaplain, 2008; Sherratt et al., 2009; Painter et al., 2010). We used the uPA model presented in Chapter 4 as a base model and extended it with adhesion properties by incorporating an adhesive movement term in the equation for cancer cell density. The adhesive movement term is nonlocal (in space), it comprehensively accounts for adhesion between cell and cell, or cell-cell adhesion, and adhesion between cell and extracellular matrix, or cell-matrix adhesion. This new adhesive movement term, or nonlocal term, replaces the original haptotactic term used in the uPA model for the directed movement of cells in response to gradients of matrix components. The extended model, or nonlocal model, is biologically more realistic and allows us to more accurately model local invasion by cancer cells of tissue where malignant tumour cells or cancer cells must detach from the main tumour body, degrade surrounding tissue and migrate through the tissue.

Using a multiscale individual cell-based approach, we also studied the role of the intracellular dynamics of E-cadherin and β-catenin based on a mathematical model developed by Ramis-Conde et al. (2008), presented in Chapter 6. We used CC3D, a lattice-based simulation environment, for modelling on the cellular level and Bionetsolver, an ODE programming library, for modelling on the subcellular (or intracellular)

level. The integration of CC3D and Bionetsolver led to a multiscale model which enabled us to study cell behaviours that are driven by the dynamics of key proteins inside the cells. We examined invasive behaviours of cancer cells by modifying key parameters that are responsible for cell adhesion, *i.e.*, E-cadherin and β-catenin. The novelty of this work is the integration of Bionetsolver with CC3D, leading to a multiscale framework for multicellular simulation. Our CC3D-Bionetsolver framework, which is a lattice-based modelling approach, proposes a different methodology than that used by Ramis-Conde et al. (2008), which is off-lattice modelling. In many respects, the two methodologies have the same overall goal, that is to mimic behaviours and interactions of biological cells. Although the mathematical foundations and computational implementations of the two are very different, the results of the computational simulations of both modelling approaches are compatible with each other, suggesting that we can formulate in a natural way complex multicell, multiscale systems. The ability to easily reproduce results of one modelling approach using an alternative approach is essential from a model cross-validation stand point and also helps to identify modelling artefacts specific to a given computational implementation. The primary aim of this study was to demonstrate cross-validation of a published model using the open-source simulation environment, CompuCell3D-Bionetsolver.

Finally in Chapter 7 we presented an intracellular pathway for the interactions between cell and matrix. We developed a model of cell-matrix adhesion that accounts for reactions between the cell surface receptor integrins, the matrix glycoprotein fibronectin, and the actin cytoskeleton. Each represents components for an intermediate compartment, the extracellular compartment, and the intracellular compartment, respectively. The model consists of a system of ODEs for integrins, soluble fibronectin, integrin/fibronectin complex, clustering of integrin/fibronectin complex, actin polymerisation and reorganisation, cytoskeletal complex, insoluble fibronectin (fibrillar network), and adhesion strength from combination of clustering integrin/fibronectin

complex with cytoskeletal network and attachment with insoluble fibronectin outside of the cell.

In vivo and *in vitro* experiments or "biological modelling" have demonstrated the significant role cell adhesion plays in cancer invasion. Using mathematical modelling we have also been able to show the importance of cell adhesion and a broad range of invasion patterns that resulted from our computational simulations. Varying the cell adhesion properties can affect the spatio-temporal behaviour of cancer cell invasion. Since the quality of any modelling process needs to be validated, we have shown that the results of our computational simulations are in qualitative good agreement with experimental data, both from the continuum and the individual cell-based approach. It will be part of our future work to get modelling and simulation results that are comparable not only qualitatively but also quantitatively with experimental data.

Similarities of the challenges in modelling from the two approaches include: (i) the choice of assumptions that we have to make to provide as simple model as possible but also to cover broad aspects relevant in biology; (ii) including as many experimentally determined parameters as possible; and (iii) running the simulations in an efficient and fast way. For the latter, running the simulations of continuum models in 2-dimensional space takes as much time as running multiscale individual cell-based models. The main difference lies in the size of the system we want to model. With a continuum approach it is appropriate to model systems with large number of cells, of the order of 10^6 or higher. On the other hand, computation becomes very expensive for modelling systems with numbers of cells larger than 10^3 for multiscale individual cell-based models.

The ability to model different phenotypes of varying degrees of malignancy as well as cell-cell and cell-matrix adhesion at a continuum level and an individual cell level, offers a fruitful future for a deeper understanding of the processes involved in cancer cell invasion and of their relative importance to each other. Therefore for the continuum model, we aim at performing nonlinear stability analysis for future work. Because of

the nonlinearity of the system, the precise patterns that evolve are governed by the full nonlinear system. Therefore a nonlinear stability analysis perhaps could give us more insight into the developed model. As for our individual cell-based model, our next work is to incorporate the cell-matrix adhesion pathway into the multiscale model together with the cell-cell adhesion pathway that has already been developed.

Bibliography

V.C. Abraham, V. Krishnamurthi, D.L. Taylor, and F. Lanni. The actin-based nanomachine at the leading edge of migrating cells. *Biophysical Journal*, 77(3):1721–1732, 1999. doi:10.1016/S0006-3495(99)77018-9.

J.A. Adam and N. Bellomo. *A survey of models for tumour-immune system dynamics*. Birkhäuser, Boston, 1996.

N. Ahmed, C. Riley, G. Rice, and M. Quinn. Role of integrin receptors for fibronectin, collagen and laminin in the regulation of ovarian carcinoma functions in response to a matrix microenvironment. *Clinical and Experimental Metastasis*, 22(2):391–402, 2005. doi:10.1007/s10585-005-1262-y.

M. Aida, T. Tsujikawa, M. Efendiev, A. Yagi, and M. Mimura. Lower estimates of the attractor dimension for a chemotaxis growth system. *Journal of the London Mathematical Society*, 74(02):453–474, 2006. doi:10.1112/S0024610706023015.

E. Van Aken, O. De Wever, A.S.C. da Rocha, and M. Mareel. Defective e-cadherin/catenin complexes in human cancer. *Virchows Arch*, 439(6):725–751, 2001. doi:10.1007/s004280100516.

T. Alarcón, H.M. Byrne, and P.K. Maini. A cellular automaton model for tumour growth in inhomogeneous environment. *Journal of Theoretical Biology*, 225(2): 257–274, 2003. doi:10.1016/S0022-5193(03)00244-3.

T. Alarcón, H.M. Byrne, and P.K. Maini. Towards whole-organ modelling of tumour growth. *Progress in Biophysics and Molecular Biology*, 85(2–3):451–472, 2004. doi:10.1016/j.pbiomolbio.2004.02.004.

T. Alarcón, H.M. Byrne, and P.K. Maini. A multiple scale model for tumor growth. *Multiscale Modeling and Simulation*, 3(2):440–475, 2005. doi:10.1137/040603760.

B. Alberts, A. Johnson, J. Lewis, M. Raff, K. Roberts, and P. Walter. *Molecular biology of the cell*. Garland Science, New York, 2002.

W. Alpízar-Alpízar, B.S. Nielsen, R. Sierra, M. Illemann, J.A. Ramírez, A. Arias, S. Durán, A. Skarstein, K. Ovrebo, L.R. Lund, and O.D. Laerum. Urokinase plasminogen activator receptor is expressed in invasive cells in gastric carcinomas from high- and low-risk countries. *International Journal of Cancer*, 126(2):405–415, 2010. doi:10.1002/ijc.24755.

R. Ananthakrishnan and A. Ehrlicher. The force behind cell movement. *International Journal of Biological Sciences*, 3(5):303–317, 2007.

A.R.A. Anderson. A hybrid discrete-continuum technique for individual-based migration models. In W. Alt, M.A.J. Chaplain, and J. Lenz, editors, *Polymer and Cell Dynamics - Multiscale Modeling and Numerical Simulations*, Mathematics and Biosciences in Interaction, chapter III.7, pages 251–259. Birkhäuser Verlag, Basel, Switzerland, 2003.

A.R.A. Anderson. A hybrid mathematical model of solid tumour invasion: the importance of cell adhesion. *IMA Journal of Mathematics Applied in Medicine and Biology*, 22(2):163–186, 2005. doi:10.1093/imammb/dqi005.

A.R.A. Anderson. A hybrid multiscale model of solid tumour growth and invasion: evolution and the microenvironment. In A.R.A. Anderson, M.A.J. Chaplain, and

K.A. Rejniak, editors, *Single-cell Based Models in Biology and Medicine*, Mathematics and Biosciences in Interaction, chapter I.1, pages 3–28. Birkhäuser Verlag, Basel, Switzerland, 2007.

A.R.A. Anderson, M.A.J. Chaplain, E.L. Newman, R.J.C Steele, and A.M. Thompson. Mathematical modelling of tumour invasion and metastasis. *Journal of Theoretical Medicine*, 2(2):129–154, 2000. doi:10.1080/10273660008833042.

A.R.A. Anderson, A.M. Weaver, P.T. Cummings, and V. Quaranta. Tumor morphology and phenotypic evolution driven by selective pressure from the microenvironment. *Cell*, 127(5):905–915, 2006. doi:10.1016/j.cell.2006.09.042.

A.R.A. Anderson, M.A.J. Chaplain, and K.A. Rejniak. *Single-cell-based models in biology and medicine*. Birkhäuser, Boston, 2007.

A.R.A. Anderson, K.A. Rejniak, P. Gerlee, and V. Quaranta. Microenvironment driven invasion: a multiscale multimodel investigation. *Journal of Mathematical Biology*, 58(4–5):579–624, 2009. doi:10.1007/s00285-008-0210-2.

P.A. Andreasen, L. Kjøller, L. Christensen, and M.J. Duffy. The urokinase-type plasminogen activator system in cancer metastasis: a review. *International Journal of Cancer*, 72(1):1–22, 1997. doi:10.1002/(SICI)1097-0215(19970703)72:1<1::AID-IJC1>3.0.CO;2-Z.

P.A. Andreasen, R. Egelund, and H.H. Petersen. The plasminogen activation system in tumor growth, invasion, and metastasis. *Cellular and Molecular Life Sciences*, 57 (1):25–40, 2000. doi:10.1007/s000180050497.

R.P. Araujo and D.L.S. McElwain. A history of the study of solid tumour growth: the contribution of mathematical modelling. *Bulletin of Mathematical Biology*, 66(5): 1039–1091, 2004. doi:10.1016/j.bulm.2003.11.002.

N.J. Armstrong, K.J. Painter, and J.A. Sherratt. A continuum approach to modelling cell-cell adhesion. *Journal of Theoretical Biology*, 243(1):98–113, 2006. doi:10.1016/j.jtbi.2006.05.030.

C. Athale, Y. Mansury, and T.S. Deisboeck. Simulating the impact of a molecular 'decision-process' on cellular phenotype and multicellular patterns in brain tumors. *Journal of Theoretical Biology*, 233(4):469–481, 2005. doi:10.1016/j.jtbi.2004.10.019.

C.A. Athale and T.S. Deisboeck. The effects of egf-receptor density on multiscale tumor growth patterns. *Journal of Theoretical Biology*, 238(4):771–779, 2006. doi:10.1016/j.jtbi.2005.06.029.

B.P. Ayati, G.F. Webb, and A.R.A. Anderson. Computational methods and results for structured multiscale models of tumor invasion. *Multiscale Modeling and Simulation*, 5(1):1–20, 2006. doi:10.1137/050629215.

A. Balter, R.M.H. Merks, N.J. Poplawski, M. Swat, and J.A. Glazier. The glazier-graner-hogeweg model: Extensions, future directions, and opportunities for further study. In A.R.A. Anderson, M.A.J. Chaplain, and K.A. Rejniak, editors, *Single-Cell-Based Models in Biology and Medicine*, Mathematics and Biosciences in Interaction, chapter II, pages 151–167. Birkhäuser Verlag, Basel, Switzerland, 2007.

E.L. Bearer, J.S. Lowengrub, H.B. Frieboes, Y.L. Chuang, F. Jin, S.M. Wise, M. Ferrari, D.B. Agus, and V. Cristini. Multiparameter computational modeling of tumor invasion. *Cancer Research*, 69(10):4493–4501, 2009. doi:10.1158/0008-5472.CAN-08-3834.

G.I. Bell and D.C. Torney. On the adhesion of vesicles by cell adhesion molecules. *Biophysical Journal*, 48(6):939–947, 1985. doi:10.1016/S0006-3495(85)83857-1.

G.I. Bell, M. Dembo, and P. Bongrand. Cell adhesion. competition between nonspecific repulsion and specific bonding. *Biophysical Journal*, 45(6):1051–1064, 1984. doi:10.1016/S0006-3495(84)84252-6.

N. Bellomo, E. De Angelis, and L. Preziosi. Multiscale modeling and mathematical problems related to tumour evolution and medical therapy. *Journal of Theoretical Medicine*, 5(2):111–136, 2003. doi:10.1080/1027336042000288633.

N. Bellomo, M.A.J. Chaplain, and E. De Angelis. *Selected Topics in Cancer Modeling: Genesis, Evolution, Immune Competition, and Therapy (Modeling and Simulation in Science, Engineering and Technology*. Birkhäuser, Boston, 2008.

A.L. Berrier and K.M. Yamada. Cell-matrix adhesion. *Journal of Cellular Physiology*, 213(3):565–573, 2007. doi:10.1002/jcp.21237.

R. Betteridge, M.R. Owen, H.M. Byrne, A. Alarcon, and P.K. Maini. The impact of cell crowding and active cell movement on vascular tumour growth. *Networks and Heterogeneous Media*, 1(4):515–535, 2006.

T. Brabletz, A. Jung, S. Reu, M. Porzner, F. Hlubek, L.A. Kunz-Schughart, R. Knuechel, and T. Kirchner. Variable β-catenin expression in colorectal indicates tumor progression driven by the tumor environment. *Proceedings of the National Academy of Sciences USA (PNAS)*, 98(18):10356–10361, 2001. doi:10.1073/pnas.171610498.

A. Breslow. Thickness, cross-sectional areas and depth of invasion in the prognosis of cutaneous melanoma. *Annals of Surgery*, 172(5):902–908, 1970. doi:10.1097/00000658-197011000-00017.

E.C. Brockbank, J. Bridges, C.J. Marshall, and E. Sahai. Integrin $\beta 1$ is required for the invasive behaviour but not proliferation of squamous cell carcinoma cells *in vivo*. *British Journal of Cancer*, 92(1):102–112, 2005. doi:10.1038/sj.bjc.6602255.

S.A. Brooks, H.J. Lomax-Browne, T.M. Carter, C.E. Kinch, and D.M.S. Hall. Molecular interactions in cancer cell metastasis. *Acta histochemica*, 112(1):3–25, 2010. doi:10.1016/j.acthis.2008.11.022.

E.B. Brown, Y. Boucher, S. Nasser, and R.K. Jain. Measurement of macromolecular diffusion coefficients in human tumors. *Microvascular Research*, 67(3):231–236, 2004. doi:10.1016/j.mvr.2004.02.001.

A.C. Burton. Rate of growth of solid tumours as a problem of diffusion. *Growth*, 30: 157–176, 1966.

B. Butler, C. Gao, A.T. Mersich, and S.D. Blystone. Purified integrin adhesion complexes exhibit actin-polymerization activity. *Current Biology*, 16(3):242–251, 2006. doi:10.1016/j.cub.2005.12.033.

H.M. Byrne. The importance of intercellular adhesion in the development of carcinomas. *Mathematical Medicine and Biology*, 14(4):305–323, 1997. doi:10.1093/imammb14.4.305.

H.M. Byrne and M.A.J. Chaplain. Modelling the role of cell-cell adhesion in the growth and development of carcinomas. *Math Comp Model*, 24(12):1–17, 1996. doi:10.1016/S0895-7177(96)00174-4.

H.M. Byrne and M.A.J. Chaplain. Free boundary value problems associated with the growth and development of multicellular spheroids. *European Journal of Applied Mathematics*, 8(6):639–658, 1997. doi:10.1017/S0956792597003264.

H.M. Byrne, M.R. Owen, T. Alarcón, and P.K. Maini. Cancer disease: integrative modelling approaches. *3rd IEEE International Symposium on Biomedical Imaging: Macro to Nano, 2006*, 1:806–809, 2006a. doi:10.1109/ISBI.2006.1625040.

H.M. Byrne, M.R. Owen, T. Alarcón, J. Murphy, P.K. Maini, and N. Bellomo. Modelling the response of vascular tumours to chemotherapy: a multiscale approach.

Mathematical Models and Methods in Applied Sciences, 16(7S):1219–1241, 2006b. doi:10.1142/S0218202506001522.

U. Cavallaro and G. Christofori. Cell adhesion and signalling by cadherins and ig-cams in cancer. *Nature Reviews Cancer*, 4(2):118–132, 2004. doi:10.1038/nrc1276.

M.A.J. Chaplain. Avascular growth, angiogenesis and vascular growth in solid tumours: The mathematical modelling of the stages of tumour development. *Mathematical and Computer Modelling*, 23(6):47–87, 1996. doi:10.1016/0895-7177(96)00019-2.

M.A.J. Chaplain. Mathematical modelling of angiogenesis. *Journal of Neuro-Oncology*, 50(1–2):37–51, 2000. doi:10.1023/A:1006446020377.

M.A.J. Chaplain and G. Lolas. Mathematical modelling of cancer cell invasion of tissue: The role of the urokinase plasminogen activation system. *Mathematical Models and Methods in Applied Sciences*, 15:1685–1734, 2005.

M.A.J. Chaplain and G. Lolas. Mathematical modelling of cancer invasion of tissue: Dynamic heterogeneity. *Networks and Heterogeneous Media*, 1:399–439, 2006.

M.A.J. Chaplain and A.M. Stuart. A mathematical model for the diffusion of tumour angiogenesis factor into the surrounding host tissue. *IMA Journal of Mathematics Applied in Medicine & Biology*, 8(3):191–220, 1991. doi:10.1093/imammb/8.3.191.

M.A.J. Chaplain, S.M. Giles, B.D. Sleeman, and R.J. Jarvis. A mathematical analysis of a model for tumour angiogenesis. *Journal of Mathematical Biology*, 33(7):744–770, 1995. doi:10.1007/BF00184647.

A. Chauviere, T. Hillen, and L. Preziosi. Modeling cell movement in anisotropic and heterogeneous network tissues. *Networks and Heterogeneous media*, 2(2):333–357, 2007.

L.L. Chen, A. Whitty, R.R. Lobb, S.P. Adams, and R.B. Pepinsky. Multiple activation states of integrin $\alpha_4\beta_1$ detected through their different affinities for a small molecule ligand. *Journal of Biological Chemistry*, 274(19):13167–13175, 1999.

M.R. Chicoine and D.L. Silbergeld. Assessment of brain tumor cell motility *in vivo* and *in vitro*. *Journal of Neurosurgery*, 82(4):615–622, 1995. doi:10.3171/jns.1995.82.4.0615.

D. Choquet, D.P. Felsenfeld, and M.P. Sheetz. Extracellumar matrix rigidity causes strengthening of integrin-cytoskeleton linkages. *Cell*, 88(1):39–48, 1997. doi:10.1016/S0092-8674(00)81856-5.

C. Cluzel, F. Saltel, J. Lussi, F. Paulhe, B.A. Imhof, and B. Wehrle-Haller. The mechanisms and dynamics of $\alpha_v\beta_3$ integrin clustering in living cells. *The Journal of Cell Biology*, 171(2):383–392, 2005. doi:10.1083/jcb.200503017.

E.A. Cox, S.K. Sastry, and A. Huttenlocher. Integrin-mediated adhesion regulates cell polarity and membrane protrusion through the rho family of gtpases. *Molecular Biology of the Cell*, 12(2):265–277, 2001.

V. Cristini, H.B. Frieboes, R. Gatenby, S. Caserta, M. Ferrari, and J. Sinek. Morphologic instability and cancer invasion. *Clinical Cancer Research*, 11(19):6772–6779, 2005. doi:10.1158/1078-0432.CCR-05-0852.

V. Cristini, X. Li, J.S. Lowengrub, and S.M. Wise. Nonlinear simulations of solid tumor growth using a mixture model: invasion and branching. *Journal of Mathematical Biology*, 58(4–5):723–763, 2009. doi:10.1007/s00285-008-0215-x.

J.C. Dallon and H.G. Othmer. A discrete cell model with adaptive signalling for aggregation of dictyostelium discoideum. *Philosophical Transactions of the Royal Society B: Biological Sciences*, 352(1351):391–417, 1997. doi:10.1098/rstb.1997.0029.

K. Danø, N. Behrendt, G. Høyer-Hansen, M. Johnsen, L.R. Lund, M. Ploug, and J. Rømer. Plasminogen activation and cancer. *Thrombosis and Haemostasis*, 93 (4):676–681, 2005. doi:10.1160/TH05-01-0054.

S. de Franciscis, H. Hatzikirou, and A. Deutsch. Analysis of lattice-gas cellular automaton models for tumor growth by means of fractal scaling. *Acta Physica Polonica B Proceedings Supplement*, 4(2):167–182, 2011. doi:10.5506/APhysPolBSupp.4.167.

C. Deroulers, M. Aubert, M. Badoual, and B. Grammaticos. Modeling tumor cell migration: From microscopic to macroscopic models. *Physical Review E*, 79(3): 031917, 2009. doi:10.1103/PhysRevE.79.031917.

P.A. DiMilla, K. Barbee, and D.A. Lauffenburger. Mathematical model for the effects of adhesion and mechanics on cell migration speed. *Biophysical Journal*, 60(1): 15–37, 1991. doi:10.1016/S0006-3495(91)82027-6.

S. Dormann and A. Deutsch. Modeling of self-organized avascular tumor growth with a hybrid cellular automaton. *In Silico Biology*, 2(3):393–406, 2002.

D. Drasdo. On selected individual-based approaches to the dynamics in multicellular systems. In W. Alt, M.A.J. Chaplain, and J. Lenz, editors, *Polymer and Cell Dynamics - Multiscale Modeling and Numerical Simulations*, Mathematics and Biosciences in Interaction, chapter III.3, pages 169–203. Birkhäuser Verlag, Basel, Switzerland, 2003.

W. Düchting and G. Dehl. A computer model for study of spatial and temporal tumor growth. *Proceedings of the Annual Symposium on Computer Applications in Medical Care*, 2:713–719, 1980a.

W. Düchting and G. Dehl. Spread of cancer cells in tissues: modelling and simulation. *International Journal of Bio-Medical Computing*, 11(3):175–195, 1980b. doi:10.1016/0020-7101(80)90044-6.

M.J. Duffy. Urokinase plasminogen activator and its inhibitor, pai-1, as prognostic markers in breast cancer: from pilot to level 1 evidence studies. *Clinical Chemistry*, 48(8):1194–1197, 2002.

M.J. Duffy and C. Duggan. The urokinase plasminogen activator system: a rich source of tumour markers for the individualised management of patients with cancer. *Clinical Biochemistry*, 37(7):541–548, 2004. doi:10.1016/j.clinbiochem.2004.05.013.

L. Edelstein-Keshet. *Mathematical Models in Biology*. SIAM, New York, 2005.

V. Ellis, C. Pyke, J. Eriksen, H. Solberg, and K. Danø. The urokinase receptor: involvement in cell surface proteolysis and cancer invasion. *Annals of the New York Academy of Sciences*, 667:13–31, 1992. doi:10.1111/j.1749-6632.1992.tb51591.x.

H. Enderling, M.A.J. Chaplain, A.R.A. Anderson, and J. Vaidya. A mathematical model of breast cancer development, local treatment and recurrence. *Journal of Theoretical Biology*, 246(2):245–259, 2007. doi:10.1016/j.jtbi.2006.12.010.

E.A. Evans. Detailed mechanics of membrane-membrane adhesion and separation. i: Continuum of molecular cross-bridges. *Biophysical Journal*, 48(1):175–183, 1985a. doi:10.1016/S0006-3495(85)83770-X.

E.A. Evans. Detailed mechanics of membrane-membrane adhesion and separation. ii: Discrete kinetically trapped molecular cross-bridges. *Biophysical Journal*, 48(1): 185–192, 1985b. doi:10.1016/S0006-3495(85)83771-1.

S. Fedotov and A. Iomin. Migration and proliferation dichotomy in tumor-cell invasion. *Physical Review Letters*, 98(11):118101, 2007. doi:10.1103/PhysRevLett.98.118101.

S. Fedotov and A. Iomin. Probabilistic approach to a proliferation and migration dichotomy in tumour cell invasion. *Physical Review E*, 77(3):031911, 2008. doi:10.1103/PhysRevE.77.031911.

I.J. Fidler. Tumor heterogeneity and the biology of cancer invasion and metastasis. *Cancer Research*, 38(9):2651–2660, 1978.

J. Folkman. Tumor angiogenesis. *Advances in Cancer Research*, 19:331–358, 1974.

J. Folkman. The vascularization of tumors. *Scientific American*, 234(5):58–73, 1976. doi:10.1038/scientificamerican0576-58.

J. Folkman and M. Klagsbrun. Angiogenic factors. *Science*, 235(4787):442–447, 1987. doi:10.1126/science.2432664.

H.B. Frieboes, X. Zheng, C.H. Sun, B. Tromberg, R. Gatenby, and V. Christini. An integrated computational/experimental model of tumor invasion. *Cancer Research*, 66(3):1597–1604, 2006. doi:10.1158/0008-5472.CAN-05-3166.

H.B. Frieboes, F. Jin, Y.L. Chuang, S.M. Wise, J.S. Lowengrub, and V. Cristini. Three-dimensional multispecies nonlinear tumor growth - ii: tumour invasion and angiogenesis. *Journal of Theoretical Biology*, 264(4):1254–1278, 2010. doi:10.1016/j.jtbi.2010.02.036.

P. Friedl and K. Wolf. Tumour-cell invasion and migration: diversity and escape mechanisms. *Nature Reviews Cancer*, 3(5):362–374, 2003. doi:10.1038/nrc1075.

M. Fussenegger, J.E. Bailey, and J. Varner. A mathematical model of caspase function in apoptosis. *Nat Biotechnol*, 18:768–774, 2000. doi:10.1038/77589.

N.D. Gallant, K.E. Michael, and A.J. García. Cell adhesion strengthening: contributions of adhesive area, integrin binding, and focal adhesion assembly. *Molecular Biology of the Cell*, 16(9):4329–4340, 2005. doi:10.1091/mbc.E05-02-0170.

J. Galle, M. Loeffler, and D. Drasdo. Modeling the effect of deregulated proliferation and apoptosis on the growth dynamics of epithelial cell populations in vitro. *Biophysical Journal*, 88(1):62–75, 2005. doi:10.1529/biophysj.104.041459.

A.J. García and D. Boettiger. Integrin-fibronectin interactions at the cell-material interface: initial integrin binding and signaling. *Biomaterials*, 20(23–24):2427–2433, 1999. doi:10.1016/S0142-9612(99)00170-2.

A.J. García, F. Huber, and D. Boettiger. Force required to break $\alpha_5\beta_1$ integrin-fibronectin bonds in intact adherent cells is sensitive to integrin activation state. *Journal of Biological Chemistry*, 273(18):10988–10993, 1998.

D.R. Garrod. Cell to cell and cell to matrix adhesion. *BMJ*, 306(6879):703–705, 1993. doi:10.1136/bmj.306.6879.703.

R.A. Gatenby and E.T. Gawlinski. A reaction-diffusion model of cancer invasion. *Cancer Research*, 56(24):5745–5753, 1996.

R.A. Gatenby and E.T. Gawlinski. The glycolytic phenotype in carcinogenesis and tumor invasion: insights through mathematical models. *Cancer Research*, 63(14): 3847–3854, 2003.

D.J. Gavaghan, J.M. Brandy, C.P. Behrenbruch, R.P. Highnam, and P.K. Maini. Breast cancer: modelling and detection. *Journal of Theoretical Medicine*, 4(1):3–20, 2002. doi:10.1080/10273660290015233.

A. Gerisch and M.A.J. Chaplain. Robust numerical methods for taxis–diffusion–reaction systems: Applications to biomedical problems. *Mathematical and Computer Modelling*, 43(1–2):49–75, 2006. doi:10.1016/j.mcm.2004.05.016.

A. Gerisch and M.A.J. Chaplain. Mathematical modelling of cancer cell invasion of tissue: Local and non-local models and the effect of adhesion. *Journal of Theoretical Biology*, 250(4):684–704, 2008. doi:10.1016/j.jtbi.2007.10.026.

P. Gerlee and A.R.A. Anderson. An evolutionary hybrid cellular automaton model of solid tumour growth. *Journal of Theoretical Biology*, 246(4):583–603, 2007. doi:10.1016/j.jtbi.2007.01.027.

P. Gerlee and A.R.A. Anderson. A hybrid cellular automaton model of clonal evolution in cancer: The emergence of the glycolytic phenotype. *Journal of Theoretical Biology*, 250(4):705–722, 2008. doi:10.1016/j.jtbi.2007.10.038.

M. Ghaemi and A. Shahrokhi. Combination of the cellular potts model and lattice gas cellular automata for simulating the avascular cancer growth. *Lecture Notes in Computer Science*, 4173:297–303, 2006. doi:10.1007/11861201_35.

F.G. Giancotti and E. Ruoslahti. Integrin signaling. *Science*, 285(5430):1028–1032, 1999. doi:10.1126/science.285.5430.1028.

J.F. Gibbs, M. Schlieman, P. Singh, R. Saxena, M. Martinick, A.D. Hutson, and J. Corasanti. A pilot study of urokinase-type plasminogen activator (upa) overexpression in the brush cytology of patients with malignant pancreatic or biliary strictures. *HPB Surgery*, 2009, 2009. doi:10.1155/2009/805971.

A. Giese, M.A. Loo, N. Tran, D. Haskett, S.W. Coons, and M.E. Berens. Dichotomy of astrocytoma migration and proliferation. *International Journal of Cancer*, 67(2):275–282, 1996. doi:10.1002/(SICI)1097-0215(19960717)67:2<275::AID-IJC20>3.3.CO;2-Y.

J.A. Glazier and F. Graner. Simulation of the differential adhesion driven rearrangement of biological cells. *Physical Review E*, 47(3):2128–2154, 1993. doi:10.1103/PhysRevE.47.2128.

J.A. Glazier, A. Balter, , and N.J. Poplawski. Magnetization to morphogenesis: a brief history of the glazier-graner-hogeweg model. In A.R.A. Anderson, M.A.J. Chaplain, and K.A. Rejniak, editors, *Single-Cell-Based Models in Biology and Medicine*,

Mathematics and Biosciences in Interaction, chapter II, pages 79–106. Birkhäuser Verlag, Basel, Switzerland, 2007.

A.S. Gobin and J.L. West. Cell migration through defined, synthetic extracellular matrix analogues. *The FASEB Journal*, 16(7):751–753, 2002. doi:10.1096/fj.01-0759fje.

F. Graner and J.A. Glazier. Simulation of biological cell sorting using a two-dimensional extended potts model. *Physical Review Letters*, 69(13):2013–2016, 1992. doi:10.1103/PhysRevLett.69.2013.

H.P. Greenspan. Models for the growth of a solid tumor by diffusion. *Studies in Applied Mathematics*, 51(4):317–340, 1972.

H.P. Greenspan. On the growth and stability of cell cultures and solid tumors. *Journal of Theoretical Biology*, 56:229–242, 1976. doi:10.1016/S0022-5193(76)80054-9.

W. Guo and F.G. Giancotti. Integrin signalling during tumour progression. *Nature Reviews Molecular Cell Biology*, 5(10):816–826, 2004. doi:10.1038/nrm1490.

W.H. Guo and Y.L. Wang. Retrograde fluxes of focal adhesion proteins in response to cell migration and mechanical signals. *Molecular Biology of the Cell*, 18(11): 4519–4527, 2007. doi:10.1091/mbc.E07-06-0582.

D.A. Hammer and D.A. Lauffenburger. A dynamical model for receptor-mediated cell adhesion to surfaces. *Biophysical Journal*, 53(3):475–487, 1987. doi:10.1016/S0006-3495(87)83236-8.

D. Hanahan and R.A. Weinberg. The hallmark of cancer. *Cell*, 100(1):57–70, 2000. doi:10.1016/S0092-8674(00)81683-9.

H. Hatzikirou, L. Brusch, C. Schaller, M. Simon, and A. Deutsch. Prediction of

traveling front behavior in a lattice-gas cellular automaton model for tumor invasion. *Computers & Mathematics with Applications*, 59(7):2326–2339, 2010. doi:10.1016/j.camwa.2009.08.041.

S. Havaki, M. Kouloukoussa, K. Amawi, Y. Drosos, L.D. Arvanitis, N. Goutas, D. Vlachodimitropoulos, S.D. Vassilaros, E.Z. Katsantoni, I. Voloudakis-Baltatzis, V. Aleporou-Marinou, C. Kittas, and E. Marinos. Altered expression pattern of integrin alphavbeta3 correlates with actin cytoskeleton in primary cultures of human breast cancer. *Cancer Cell International*, 7(1):16, 2007. doi:10.1186/1475-2867-7-16.

R.B. Hazan, G.R. Phillips, R.F. Qiao, L. Norton, and S.A. Aaronson. Exogenous expression of n-cadherin in breast cancer cells induces cell migration, invasion, and metastasis. *The Journal of Cell Biology*, 148(4):779–790, 2000. doi:10.1083/jcb.148.4.779.

I. Henneke, S. Greschus, R. Savai, M. Korfei, P. Markart, P. Mahavadi, R.T. Schermuly, M. Wygrecka, J. Stürzebecher, W. Seeger, A. Günther, and C. Ruppert. Inhibition of urokinase activity reduces primary tumor growth and metastasis formation in murine lung carcinoma model. *American Journal of Respiratory and Critical Care Medicine*, 181(6):611–619, 2010. doi:10.1164/rccm.200903-0342OC.

G.H. Heppner. Tumor heterogeneity. *Cancer Research*, 44:2259–2265, 1984.

M.A. Herrero and J.J.L Velázquez. Chemotactic collapse for the keller-segel model. *Journal of Mathematical Biology*, 35(2):177–194, 1996. doi:10.1007/s002850050049.

C. Heyder, E. Gloria-Maercker, W. Hatzmann, B. Niggemann, K.S. Zänker, and

T. Dittmar. Role of the β_1-integrin subunit in the adhesion, extravasation and migration of t24 human bladder carcinoma cells. *Clinical and Experimental Metastasis*, 22:99–106, 2005. doi:10.1007/s10585-005-4335-z.

A.V. Hill. The diffusion of oxygen and lactic acid through tissues. *Proceedings of the Royal Society London B*, 104:39–96, 1928. doi:10.1098/rspb.1928.0064.

T. Hillen. M^5 mesoscopic and macroscopic models for mesenchymal motion. *Journal of Mathematical Biology*, 53(4):585–616, 2006. doi:10.1007/s00285-006-0017-y.

T. Hillen and K.J. Painter. Global existence for a parabolic chemotaxis model with prevention of overcrowding. *Advances in Applied Mathematics*, 26(4):280–301, 2001. doi:10.1006/aama.2001.0721.

T. Hillen and K.J. Painter. A user's guide to pde models for chemotaxis. *Journal of Mathematical Biology*, 58(1–2):183–217, 2009. doi:10.1007/s00285-008-0201-3.

D.C. Hocking and C.H. Chang. Fibronectin matrix polymerization regulates small airway epithelial cell migration. *American Journal of Physiology - Lung Cellular and Molecular Physiology*, 285(1):169–179, 2003. doi:10.1152/ajplung.00371.2002.

D. Hortsmann and G. Wang. Blowup in a chemotaxis model without symmetry assumptions. *European Journal of Applied Mathematics*, 12:159–177, 2001. doi:10.1017/S0956792501004363.

Z. Horváth. Positivity of runge–kutta and diagonally split runge–kutta methods. *Applied Numerical Mathematics*, 28(2–4):309–326, 1998. doi:10.1016/S0168-9274(98)00050-6.

H.P. Hsu, Y.S. Shan, Y.T. Jin, M.D. Lai, and P.W. Lin. Loss of e-cadherin and beta-catenin is correlated with poor prognosis of ampullary neoplasms. *Journal of Surgical Oncology*, 101(5):356–362, 2010. doi:10.1002/jso.21493.

C.F. Huang, C. Lira, K. Chu, M.A. Bilen, Y.C. Lee, X. Ye, S.M. Kim, A. Ortiz, F.L.L. Wu, C.J. Logothetis, L.Y. Yu-Lee, and S.H. Lin. Cadherin-11 increases migration and invasion of prostate cancer cells and enhances their interaction with osteoblasts. *Cancer Research*, 70(11):4580–4589, 2010. doi:10.1158/0008-5472.CAN-09-3016.

A. Huttenlocher, M.H. Ginsberg, and A.F. Horwitz. Modulation of cell migration by integrin-mediated cytoskeletal linkages and ligand-binding affinity. *Journal of Cell Biology*, 134(6):1551–1562, 1996. doi:10.1083/jcb.134.6.1551.

R.O. Hynes. Integrins: bidirectional, allosteric signaling machines. *Cell*, 110(6):673–687, 2002. doi:10.1016/S0092-8674(02)00971-6.

R.B. Irby and T.J. Yeatman. Increased src activity disrupts cadherin/catenin-mediated homotypic adhesion in human colon cancer and transformed rodent cells. *Cancer Research*, 62(9):2669–2674, 2002.

J.R. Izbicki, S.B. Hosch, U. Pichlmeier, A. Rehders, C. Busch, A. Niendorf, B. Passlick, C.E. Broelsch, and K. Pantel. Prognostic value of immunohistochemically identifiable tumor cells in lymph nodes of patients with completely resected esophageal cancer. *New England Journal of Medicine*, 337(17):1188–1194, 1997. doi:10.1056/NEJM199710233371702.

W. Jäger and S. Luckhaus. On explosions of solutions to a system of partial differential equations modelling chemotaxis. *Transactions of the American Mathematical Society*, 329(2):819–824, 1992. doi:10.2307/2153966.

S.M. Janes and F.M. Watt. New roles for integrins in squamous- cell carcinoma. *Nature Reviews Cancer*, 6(3):175–183, 2006. doi:10.1038/nrc1817.

G. Jenkins. The role of proteases in transforming growth factor-β activation. *International Journal of Biochemistry and Cell Biology*, 40(6–7):1068–1078, 2008. doi:10.1016/j.biocel.2007.11.026.

W.G. Jiang. E-cadherin and its associated protein catenins, cancer invasion and metastasis. *British Journal of Surgery*, 83(4):437–446, 1996. doi:10.1002/bjs.1800830404.

Y. Jiang, J. Pjesivac-Grbovic, C. Cantrell, and J.P. Freyer. A multiscale model for avascular tumor growth. *Biophysical Journal*, 89(6):3884–3894, 2005. doi:10.1529/biophysj.105.060640.

S. Kase, K. Sugio, K. Yamazaki, T. Okamoto, T. Yano, and K. Sugimachi. Expression of e-cadherin and β-catenin in human non-small cell lung cancer and the clinical significance. *Clinical Cancer Research*, 6(12):4789–4796, 2000. doi:10.1016/S0169-5002(00)80667-4.

L.J. Kaufman, C.P. Brangwynne, K.E. Kasza, E. Filippidi, V.D. Gordon, T.S. Deisboeck, and D.A. Weitz. Glioma expansion in collagen i matrices: Analyzing collagen concentration-dependent growth and motility patterns. *Biophysical Journal*, 89 (1):635–650, 2005. doi:10.1529/biophysj.105.061994.

K. Kawakami, H. Tatsumi, and M. Sokabe. Dynamics of integrin clustering at focal contacts of endothelial cells studied by multimode imaging microscopy. *Journal of Cell Science*, 114(17):3125–3135, 2001.

J. Kawanishi, J. Kato, K. Sasaki, S. Fujii, N. Watanabe, and Y. Niitsu. Loss of e-cadherin-dependent cell-cell adhesion due to mutation of the β-catenin gene in a human cancer cell line, hsc-39. *Molecular and Cellular Biology*, 15(3):1175–1181, 1995.

E.F. Keller and L.A. Segel. Initiation of slime mold aggregation viewed as instability. *Journal of Theoretical Biology*, 26(3):399–417, 1970. doi:10.1016/0022-5193(70)90092-5.

C.B. Khatiwala, S.R. Peyton, and A.J. Putnam. Intrinsic mechanical properties of the extracellular matrix affect the behavior of pre-osteoblastic mc3t3-e1 cells. *American Journal of Physiology - Cell Physiology*, 290(6):C1640–C1650, 2006. doi:10.1152/ajpcell.00455.2005.

Y. Kim and A. Friedman. Interaction of tumour with its micro-environment: a mathematical model. *Bulletin of Mathematical Biology*, 72(5):1029–1068, 2009. doi:10.1007/s11538-009-9481-z.

Y. Kim, M.A. Stolarska, H.G. Othmer, N. Bellomo, and P.K. Maini. A hybrid model for tumor spheroid growth in vitro i: Theoretical development and early results. *Mathematical Models and Methods in Applied Sciences*, 17:1773–1798, 2007. doi:10.1142/S0218202507002479.

S.C. Kirkland and H. Ying. $\alpha_2\beta_1$ integrin regulates lineage commitment in multipotent human colorectal cancer cells. *Journal of Biological Chemistry*, 283(41):27612–27619, 2008. doi:10.1074/jbc.M802932200.

P. Koistinen and J. Heino. Integrins in cancer cell invasion. In J. Heino and V.M. Kähäri, editors, *Cell invasion*, Medical Intelligence Unit, chapter II. Landes Bioscience, 2002.

P.J. Kowalski, M.A. Rubin, and C.G. Kleer. E-cadherin expression in primary carcinomas of the breast and its distant metastases. *Breast Cancer Research*, 5(6): R217–R222, 2003. doi:10.1186/bcr651.

S. Kuphal, R. Bauer, and A-K. Bosserhoff. Integrin signaling in malignant melanoma. *Cancer and Metastasis Reviews*, 24(2):195–222, 2005. doi:10.1007/s10555-005-1572-1.

D.A. Lauffenburger and A.F. Horwitz. Cell migration: a physically integrated molecular process. *Cell*, 84(3):359–369, 1996. doi:10.1016/S0092-8674(00)81280-5.

Y.C. Lee, C.T. Wu, C.S. Chen, H.H. Hsu, and Y.L. Chang. The significance of e-cadherin and α-, β-, and γ-catenin expression in surgically treated non-small cell lung cancers of 3 cm or less in size. *Journal of Thoracic and Cardiovascular Surgery*, 123(3):502–507, 2002. doi:10.1067/mtc.2002.119334.

S. Li, J-L. Guan, and S. Chien. Biochemistry and biomechanics of cell motility. *Annual Review of Biomedical Engingeering*, 7(1):105–150, 2005. doi:10.1146/annurev.bioeng.7.060804.100340.

F. Lindemann, G. Schlimok, P. Dirschedl, J. Witte, and G. Riethmuller. Prognostic significance of micrometastatic tumour cells in bone marrow of colorectal cancer patients. *Lancet*, 340(8821):685–689, 1992. doi:10.1016/0140-6736(92)92230-D.

L.A. Liotta. Tumor invasion and metastases–role of the extracellular matrix: Rhoads memorial award lecture. *Cancer Research*, 46(1):1–7, 1986.

J.S. Lowengrub, H.B. Frieboes, F. Jin, Y-L. Chuang, X. Li, P. Macklin, S.M. Wise, and V. Cristini. Nonlinear modelling of cancer: bridging the gap between cells and tumours. *Nonlinearity*, 23(1):R1–R91, 2010. doi:10.1088/0951-7715/23/1/R01.

L.M. Machesky and A. Hall. Role of actin polymerization and adhesion to extracellular matrix in rac-and rho-induced cytoskeletal reorganization. *Journal of Cell Biology*, 138(4):913–926, 1997. doi:10.1083/jcb.138.4.913.

R. Machné, A. Finney, S. Müller, J. Lu, S. Widder, and C. Flamm. The sbml ode solver library: a native api for symbolic and fast numerical analysis of reaction networks. *Bioinformatics Applications Note*, 22(11):1406–1407, 2006. doi:10.1093/bioinformatics/btl086.

P. Macklin and J.S. Lowengrub. Nonlinear simulation of the effect of microenvironment on tumor growth. *Journal of Theoretical Biology*, 245(4):677–704, 2007. doi:10.1016/j.jtbi.2006.12.004.

P. Macklin, S. McDougall, A.R.A. Anderson, M.A.J. Chaplain, V. Cristini, and J. Lowengrub. Multiscale modelling and nonlinear simulation of vascular tumour growth. *Journal of Mathematical Biology*, 58(4–5):765–798, 2009. doi:10.1007/s00285-008-0216-9.

R.N.M. MacSween. *Muir's textbook of pathology*. Arnold, 14th Edition, 2003.

S.A. Maggelakis. The effects of tumor angiogenesis factor (taf) and tumor inhibitor factors (tifs) on tumor vascularization: A mathematical model. *Mathematical and Computer Modelling*, 23(6):121–133, 1996. doi:10.1016/0895-7177(96)00022-2.

G. Maheshwari, A. Wells, L.G. Griffith, and D.A. Lauffenburger. Biophysical integration of effects of epidermal growth factor and fibronectin on fibroblast migration. *Biophysical Journal*, 76(5):2814–2823, 1999. doi:10.1016/S0006-3495(99)77435-7.

G. Maheshwari, G. Brown, D.A. Lauffenburger, A. Wells, and L.G. Griffith. Cell adhesion and motility depend on nanoscale rgd clustering. *Journal of Cell Science*, 113(10):1677–1686, 200.

G. Maity, S. Fahreen, A. Banerji, P.R. Choudhury, T. Sen, A. Dutta, and A. Chatterjee. Fibronectinintegrin mediated signaling in human cervical cancer cells (siha). *Molecular and Cellular Biochemistry*, 336(1–2):65–74, 2009. doi:10.1007/s11010-009-0256-5.

A. Mallavarapu and T. Mitchison. Regulated actin cytoskeleton assembly at filopodium tips controls their extension and retraction. *Journal of Cell Biology*, 146(5):1097–1106, 1999. doi:10.1083/jcb.146.5.1097.

N.V. Mantzaris, S. Webb, and H.G. Othmer. Mathematical modeling of tumor-induced angiogenesis. *Journal of Mathematical Biology*, 49(2):111–187, 2004. doi:10.1007/s00285-003-0262-2.

Q. Mao, X. Zheng, K. Yang, J. Qin, Y. Bai, X. Jia, Y. Li, and L. Xie. Suppression of migration and invasion of pc3 prostate cancer cell line via activating e-cadherin expression by small activating rna. *Cancer Investigation*, 28(10):1013–1018, 2010. doi:10.3109/07357900802620844.

B.P. Marchant, J. Norbury, and J.A. Sherratt. Travelling wave solutions to a haptotaxis-dominated model of malignant invasion. *Nonlinearity*, 14(6):1653–1672, 2001. doi:10.1088/0951-7715/14/6/313.

B.P. Marchant, J. Norbury, and H.M. Byrne. Biphasic behaviour in malignant invasion. *Mathematical Medicine and Biology*, 23(3):173–196, 2006. doi:10.1093/imammb/dql007.

G. Markus. The relevance of plasminogen activators to neoplastic growth. a review of recent literature. *Enzyme*, 40(2–3):158–172, 1988.

V.L. Martins, J.J. Vyas, M. Chen, K. Purdie, C.A. Mein, A.P. South, A. Storey, J.A. McGrath, and E.A. O'Toole. Increased invasive behaviour in cutaneous squamous cell carcinoma with loss of basement-membrane type vii collagen. *Journal of Cell Science*, 122(11):1788–1799, 2009. doi:10.1242/jcs.042895.

S.R. McDougall, A.R.A. Anderson, M.A.J. Chaplain, and J.A. Sherratt. Mathematical modelling of flow through vascular networks: implications for tumour-induced angiogenesis and chemotherapy strategies. *Bulletin of Mathematical Biology*, 64(4): 673–702, 2002. doi:10.1006/bulm.2002.0293.

S.R. McDougall, A.R.A. Anderson, and M.A.J. Chaplain. Mathematical modelling of dynamic adaptive tumour-induced angiogenesis: Clinical implications and therapeutic targeting strategies. *Journal of Theoretical Biology*, 3(7):564–589, 2006. doi:10.1016/j.jtbi.2005.12.022.

D.L.S. McElwain and P.J. Ponzo. A model for the growth of a solid tumour with non-uniform oxygen consumption. *Mathematical Biosciences*, 35(3–4):267–279, 1977. doi:10.1016/0025-5564(77)90028-1.

G.J. Mizejewski. Role of integrins in cancer: survey of expression patterns. *Proceedings of the Society for Experimental Biology and Medicine*, 222(2):124–138, 1999. doi:10.1046/j.1525-1373.1999.d01-122.x.

E. Monaghan, V. Gueorguiev, and C. Wilkins-Port. The receptor for urokinase-type plasminogen activator regulates fibronectin matrix assembly in human skin fibroblasts. *Journal of Biological Chemistry*, 279(2):1400–1407, 2004. doi:10.1074/jbc.M310374200.

J. Moreira and A. Deutsch. Cellular automaton models of tumour development: a critical review. *Advances in Complex Systems (ACS)*, 5(2–3):247–267, 2002. doi:10.1142/S0219525902000572.

F.A. Moretti, A.K. Chauhan, A. Iaconcig, F. Porro, F.E. Baralle, and A.F. Muro. A major fraction of fibronectin present in the extracellular matrix of tissues is plasma-derived. *Journal of Biological Chemistry*, 282(38):28057–28062, 2007. doi:10.1074/jbc.M611315200.

J.D. Murray. *Mathematical Biology II: Spatial Models and Biomedical Applications*. Springer, New York, NY, third edition, 2003.

T.L. Ng, A.M. Gown, T.S. Barry, M.C.U. Cheang, A.K.W. Chan, D.A. Turbin, F.D. Hsu, R.B. West, and T.O. Nielsen. Nuclear beta-catenin in mesenchymal tumors. *Modern Pathology*, 18:68–74, 2005. doi:10.1038/modpathol.3800272.

T. Nishizaka, Q. Shi, and M.P. Sheetz. Position-dependent linkages of fibronectin-integrin-cytoskeleton. *Proceedings of the National Academy of Sciences (PNAS)*, 97 (2):692–697, 2000. doi:10.1073/pnas.97.2.692.

M.L. Nyström, G.J. Thomas, M. Stone, I.C. Mackenzie, I.R. Hart, and J.F. Marshall. Development of a quantitative method to analyse tumour cell invasion in organotypic culture. *Journal of Pathology*, 205(4):468–475, 2005. doi:10.1002/path.1716.

M. Ojaniemi and K. Vuori. Epidermal growth factor modulates tyrosine phosphorylation of p130cas. involvement of phophatidylinositol 3'-kinase and actin cytoskeleton. *Journal of Biological Chemistry*, 272(41):25993–25998, 1997. doi:10.1074/jbc.272.41.25993.

M.E. Orme and M.A.J. Chaplain. A mathematical model of the first steps of tumour-related angiogenesis: Capillary sprout formation and secondary branching. *IMA Journal of Mathematics Applied in Medicine and Biology*, 13(2):73–98, 1996a. doi:10.1093/imammb13.2.73.

M.E. Orme and M.A.J. Chaplain. A mathematical model of vascular tumour growth and invasion. *Mathematical and Computer Modelling*, 23(10):43–60, 1996b. doi:10.1016/0895-7177(96)00053-2.

M.E. Orme and M.A.J. Chaplain. Two-dimensional models of tumour angiogenesis and anti-angiogenesis strategies. *IMA Journal of Mathematics Applied in Medicine & Biology*, 14(3):189–205, 1997. doi:10.1093/imammb/14.3.189.

O. Oudar. Spheroids: relation between tumour and endothelial cells. *Critical Reviews in Oncology/Hematology*, 36(2–3):99–106, 2000. doi:10.1016/S1040-8428(00)00080-9.

K.J. Painter. Modelling cell migration strategies in the extracellular matrix. *Journal of Mathematical Biology*, 58(4–5):511–543, 2009. doi:10.1007/s00285-008-0217-8.

K.J. Painter and T. Hillen. Volume-filling and quorum-sensing in models for chemosensitive movement. *Canadian Applied Mathematics Quarterly*, 10(4):501–543, 2002.

K.J. Painter, N.J. Armstrong, and J.A. Sherratt. The impact of adhesion on cellular invasion processes in cancer and development. *Journal of Theoretical Biology*, 264 (3):1057–1067, 2010. doi:10.1016/j.jtbi.2010.03.033.

S.P. Palecek, J.C. Loftus, M.H. Ginsberg, D.A. Lauffenburger, and A.F. Horwitz. Integrin-ligand binding properties govern cell migration speed through cell-substratum adhesiveness. *Nature*, 385(6616):537–540, 1997. doi:10.1038/385537a0.

S.P. Palecek, A. Huttenlocher, A.F. Horwitz, and D.A. Lauffenburger. Physical and biochemical regulation of integrin release during rear detachment of migrating cells. *Journal of Cell Science*, 111(7):929–940, 1998.

S.P. Palecek, A.F. Horwitz, and D.A. Lauffenburger. Kinetic model for integrin-mediated adhesion release during cell migration. *Annals of Biomedical Engineering*, 27(2):219–235, 1999. doi:10.1114/1.176.

R. Pankov and K.M. Yamada. Fibronectin at a glance. *Journal of Cell Science*, 115 (20):3861–3863, 2002. doi:10.1242/jcs.00059.

S.L. Parsons, S.A. Watson, P.D. Brown, H.M. Collins, and R.J. Steele. Matrix metalloproteinases. *British Journal of Surgery*, 84(2):160–166, 1997. doi:10.1046/j.1365-2168.1997.02719.x.

K.A. Paschos, D.Canovas, and N.C. Bird. The role of cell adhesion molecules in the progression of colorectal cancer and the development of liver metastasis. *Cellular Signaling*, 21(5):665–674, 2009. doi:10.1016/j.cellsig.2009.01.006.

I.G. Pearce, M.A.J. Chaplain, P.G. Schofield, A.R.A. Anderson, and S.F. Hubbard. Chemotaxis-induced spatio-temporal heterogeneity in multi-species host-parasitoid systems. *Journal of Mathematical Biology*, 55(3):365–388, 2007. doi:10.1007/s00285-007-0088-4.

M.S. Pepper. Role of the matrix metalloproteinase and plasminogen activator-plasmin systems in angiogenesis. *Arteriosclerosis, Thrombosis, and Vascular Biology*, 21 (7):1104–1117, 2001. doi:10.1161/hq0701.093685.

M.S. Pepper and G. Lolas. The lymphatic vascular system in lymphangiogenesis invasion and metastasis a mathematical approach. In N. Bellomo, M.A.J. Chaplain, and E. De Angelis, editors, *Selected topics in cancer modelling: genesis, evolution, immune competition, and therapy*, Modeling and Simulation in Science, Engineering and Technology, chapter X, pages 255–276. Springer, 2008.

J.Y. Perentes, T.D. McKee, C.D. Ley, H. Mathiew, M. Dawson, T.P. Padera, L.L. Munn, R.K. Jain, and Y. Boucher. *In vivo* imaging of extracellular matrix remodeling by tumor-associated fibroblasts. *Nature Methods*, 6(2), 2009. doi:10.1038/nmeth.1295.

A.K. Perl, P. Wilgenbus, U. Dahl, H. Semb, and G. Christofori. A causal role for e-cadherin in the transition from adenoma to carcinoma. *Nature*, 392(6672):190–193, 1998.

A.J. Perumpanani, J.A. Sherratt, J. Norbury, and H.M. Byrne. Biological inferences from a mathematical model for malignant invasion. *Invasion & Metastasis*, 16(4–5): 209–221, 1996.

A.J. Perumpanani, D.L. Simmons, A.J.H. Gearing, K.M. Miller, G. Ward, J. Norbury, M. Schneemann, and J.A. Sherratt. Extracellular matrix-mediated chemotaxis can impede cell migration. *Proceedings of the Royal Society London B*, 265(1413): 2347–2352, 1998. doi:10.1098/rspb.1998.0582.

A.J. Perumpanani, J.A. Sherratt, J. Norbury, and H.M. Byrne. A two parameter family of travelling waves with a singular barrier arising from the modelling of extracellular matrix mediated cellular invasion. *Physica D: Nonlinear Phenomena*, 126(3–4): 145–159, 1999. doi:10.1016/S0167-2789(98)00272-3.

S.R Peyton and A.J. Putnam. Extracellular matrix rigidity governs smooth muscle cell motility in a biphasic fashion. *Journal of Cellular Physiology*, 204(1):198–209, 2005. doi:10.1002/jcp.20274.

M. Pignatelli. Integrins, cadherins, and catenins: molecular cross-talk in cancer cells. *Journal of Pathology*, 186(1):1–2, 1998. doi:10.1002/(SICI)1096-9896(199809)186:1<1::AID-PATH135>3.0.CO;2-T.

M. J. Plank and B. D. Sleeman. A reinforced random walk model of tumour angiogenesis and anti-angiogenic strategies. *IMA Journal of Mathematics Applied in Medicine & Biology*, 20(2):135–181, 2003. doi:10.1093/imammb/20.2.135.

M. J. Plank, B. D. Sleeman, and P.F. Jones. A mathematical model of tumour angiogenesis, regulated by vascular endothelial growth factor and the angiopoietins. *Journal of Theoretical Biology*, 229(4):435–454, 2004. doi:10.1016/j.jtbi.2004.04.012.

T.D. Pollard and M.S. Mooseker. Direct measurement of actin polymerization rate constants by electron microscopy of actin filaments nucleated by isolated microvillus cores. *Journal of Cell Biology*, 88(3):654–659, 1981. doi:10.1083/jcb.88.3.654.

N.J. Poplawski, M. Swat, J.S. Gens, and J.A. Glazier. Adhesion between cells, diffusion of growth factors, and elasticity of the aer produce the paddle shape of the chick limb. *Physica A*, 373:521–532, 2006. doi:10.1016/j.physa.2006.05.028.

N.J. Poplawski, A. Shirinifard, M. Swat, and J.A. Glazier. Simulation of single-species bacterial-biofilm growth using the glazier-graner-hogeweg model and the compucell3d modeling environment. *Mathematical Biosciences and Engineering*, 5(2): 355–388, 2008.

N.J. Poplawski, U. Agero, J.S. Gens, M. Swat, J.A. Glazier, and A.R.A. Anderson. Front instabilities and invasiveness of simulated avascular tumors. *Bulletin of Mathematical Biology*, 71(5):1189–1227, 2009. doi:10.1007/s11538-009-9399-5.

L. Preziosi. *Cancer Modelling and Simulation*. Chapman & Hall/CRC Press, 2003.

I. Ramis-Conde, D. Drasdo, A.R.A. Anderson, and M.A.J. Chaplain. Modeling the influence of the e-cadherin-*beta*-catenin pathway in cancer cell invasion: A multiscale approach. *Biophysical Journal*, 95(1):155–165, 2008. doi:10.1529/biophysj.107.114678.

I. Ramis-Conde, M.A.J. Chaplain, A.R.A. Anderson, and D. Drasdo. Multi-scale modelling of cancer cell intravasation: the role of cadherins in metastasis. *Physical Biology*, 6(1):016008–016013, 2009. doi:10.1088/1478-3975/6/1/016008.

C.M. Regen and A.F. Horwitz. Dynamics of β_1 integrin-mediated adhesive contacts in motile fibroblasts. *Journal of Cell Biology*, 119(5):1347–1359, 1992.

K.A. Rejniak and A.R.A. Anderson. Multiscale hybrid models of tumor growth. *Wiley Interdisciplinary Reviews: Systems Biology and Medicine*, 2010. doi:10.1002/wsbm.102.

D. Ribatti, A. Vacca, and M. Presta. The discovery of angiogenic factors: a historical review. *General Pharmacology*, 35:227–231, 2002. doi:10.1016/S0306-3623(01)00112-4.

B.M. Rubenstein and L.J. Kaufman. The role of extracellular matrix in glioma invasion: a cellular potts model approach. *Biophysical Journal*, 95(12):5661–5680, 2008. doi:10.1529/biophysj.108.140624.

G.M. Saidel, L.A. Liotta, and J. Kleinerman. System dynamics of a metastatic process from an implanted tumor. *Journal of Theoretical Biology*, 56(2):417–434, 1976. doi:10.1016/S0022-5193(76)80083-5.

K. Sawada, A.K. Mitra, A.R. Radjabi, V. Bhaskar, E.O. Kistner, M. Tretiakova, S. Jagadeeswaran, A. Montag, A. Becker, H.A. Kenny, M.E. Peter, V. Ramakrishnan,

S.D. Yamada, and E. Lengyel. Loss of e-cadherin promotes ovarian cancer metastasis via α_5-integrin, which is a therapeutic target. *Cancer Research*, 68:2329–2339, 2008. doi:10.1158/0008-5472.CAN-07-5167.

H. Sawai, Y. Okada, H. Funahashi, Y. Matsuo, H. Takahashi, H. Takeyama, and T. Manabe. Interleukin-1α enhances the aggressive behavior of pancreatic cancer cells by regulating the $\alpha_6\beta_1$-integrin and urokinase plasminogen activator receptor expression. *BMC Cell Biology*, 7:8, 2006. doi:10.1186/1471-2121-7-8.

M.v. Schlippe, J.F. Marshall, P. Perry, M. Stone, A.J. Zhu, and I.R. Hart. Functional interaction between e-cadherin and α_v-containing integrins in carcinoma cells. *Journal of Cell Science*, 113(3):425–437, 2000.

O. Schmalhofer, S. Brabletz, and T. Brabletz. E-cadherin, beta-catenin, and zeb1 in malignant progression of cancer. *Cancer and Metastasis Reviews*, 28(1–2):151–166, 2009. doi:10.1007/s10555-008-9179-y.

J.L. Sechler, Y. Takada, and J.E. Schwarzbauer. Altered rate of fibronectin matrix assembly by deletion of the first type iii repeats. *Journal of Cell Biology*, 134(2): 573–583, 1996. doi:10.1083/jcb.134.2.573.

J.A. Sherratt and M.A.J. Chaplain. A new mathematical model for avascular tumour growth. *Journal of Mathematical Biology*, 43(4):291–312, 2001. doi:10.1007/s002850100088.

J.A. Sherratt, S.A. Gourley, N.J. Armstrong, and K.J. Painter. Boundedness of solutions of a non-local reaction-diffusion model for adhesion in cell aggregation and cancer invasion. *European Journal of Applied Mathematics*, 20(01):123–144, 2009. doi:10.1017/S0956792508007742.

Y. Shimoyama, A. Nagafuchi, S. Fujita, M. Gotoh, M. Takeichi, S. Tsukita, and S. Hirohashi. Cadherin dysfunction in a human cancer cell line: Possible involvement of

loss of α-catenin expression in reduced cell-cell adhesiveness. *Cancer Research*, 52 (20):5770–5774, 1992.

A. Shirinifard, J.S. Gens, B.L. Zaitlen, N.J. Poplawski, M. Swat, and J.A. Glazier. 3d multi-cell simulation of tumour growth and angiogenesis. *PLoS ONE*, 4(10):e7190, 2009. doi:10.1371/journal.pone.0007190.

J. Silvestre, P.J.A. Kenis, and D.E. Leckband. Cadherin and integrin regulation of epithelial cell migration. *Langmuir*, 25(17):10092–10099, 2009. doi:10.1021/la901109e.

E.K. Sloan, N. Pouliot, K.L. Stanley, J. Chia, J.M. Moseley, D.K. Hards, and R.L. Anderson. Tumor-specific expression of $\alpha_v\beta_3$ integrin promotes spontaneous metastasis of breast cancer to bone. *Breast Cancer Research*, 8(2):R20, 2006. doi:10.1186/bcr1398.

K. Smallbone, D.J. Gavaghan, R.A. Gatenby, and P.K. Maini. The role of acidity in solid tumour growth and invasion. *Journal of Theoretical Biology*, 235(4):476–484, 2005. doi:10.1016/j.jtbi.2005.02.001.

M.B. Sporn. The war on cancer. *Lancet*, 347(9012):1377–1381, 1996. doi:10.1016/S0140-6736(96)91015-6.

E.N. Spremulli and D.L. Dexter. Human tumor cell heterogeneity and metastasis. *Journal of Clinical Oncology*, 1(8):496–509, 1983.

A. Stahl and B.M. Mueller. Melanoma cell migration on vitronectin: Regulation by components of the plasminogen activation system. *International Journal of Cancer*, 71(1):116–122, 1997. doi:10.1002/(SICI)1097-0215(19970328)71:1<116::AID-IJC19>3.3.CO;2-Z.

I.J. Stamper, H.M. Byrne, M.R. Owen, and P.K. Maini. Modelling the role of angiogenesis and vasculogenesis in solid tumour growth. *Bulletin of Mathematical Biology*, 69(8):2737–2772, 2007. doi:10.1007/s11538-007-9253-6.

A.M. Stein, T. Demuth, D. Mobley, M. Berens, and L.M. Sander. A mathematical model of glioblastoma tumor spheroid invasion in a three-dimensional in vitro experiment. *Biophysical Journal*, 92(1):356–365, 2007. doi:10.1529/biophysj.106.093468.

A. Stéphanou, S.R. McDougall, A.R.A. Anderson, and M.A.J. Chaplain. Mathematical modelling of the influence of blood rheological properties upon adaptative tumour-induced angiogenesis. *Mathematical and Computer Modelling*, 44(1–2):96–123, 2006. doi:10.1016/j.mcm.2004.07.021.

J.M. Stewart, P. Broadbridge, and J.M. Goard. Symmetry analysis and numerical modelling of invasion by malignant tumour tissue. *Nonlinear Dynamics*, 28(2):175–193, 2002. doi:10.1023/A:1015009016590.

R.M. Sutherland. Cell and environment interactions in tumor microregions: the multicell spheroid model. *Science*, 240(4849):177–184, 1988. doi:10.1126/science.2451290.

H. Suzuki, N. Masuda, T. Shimura, K. Araki, T. Kobayashi, S. Tsutsumi, T. Asao, and H. Kuwano. Nuclear β-catenin expression at the invasive front and in the vessels predicts liver metastasis in colorectal carcinoma. *Anticancer Research*, 28(3B): 1821–1830, 2008.

K.R. Swanson. Quantifying glioma cell growth and invasion in vitro. *Mathematical and Computer Modelling*, 47(5–6):638–648, 2008. doi:10.1016/j.mcm.2007.02.024.

K.R. Swanson, E.C. Alvord Jr, and J.D. Murray. A quantitative model for differential motility of gliomas in grey and white matter. *Cell Proliferation*, 33(5):317–329, 2000. doi:10.1046/j.1365-2184.2000.00177.x.

K.R. Swanson, C. Bridge, J.D. Murray, and E.C. Alvord Jr. Virtual and real brain tumours: using mathematical modelling to quantify glioma growth and invasion. *Journal of the Neurological Sciences*, 216:1–10, 2003. doi:10.1016/j.jns.2003.06.001.

M.H. Swat, S.D. Hester, R.W. Heiland, B.L. Zaitlen, and J.A. Glazier. Multi-cell simulations of development and disease using the compucell3d simulation environment. *Methods in Molecular Biology*, 500:361–428, 2009. doi:10.1007/978-1-59745-525-1_13.

Z. Szymańska, C. M. Rodrigo, M. Lachowicz, and M.A.J. Chaplain. Mathematical modelling of cancer invasion of tissue: the role and effect of nonlocal interactions. *Mathematical Models and Methods in Applied Sciences*, 19(2):257–281, 2009. doi:10.1142/S0218202509003425.

Y. Takada, X. Ye, and S. Simon. The integrins. *Genome Biology*, 8(5):215, 2007. doi:10.1186/gb-2007-8-5-215.

J.W. Tamkun and R.O. Hynes. Plasma fibronectin is synthesized and secreted by hepatocytes. *Journal of Biological Chemistry*, 258(7):4641–4647, 1983.

J.P. Thiery. Epithelial-mesenchymal transitions in tumour progression. *Nature Reviews Cancer*, 2(6):442–454, 2002. doi:10.1038/nrc822.

R.H. Thomlinson and L.H. Gray. The histological structure of some human lung cancers and the possible implications for radiotherapy. *British Journal of Cancer*, 9(4): 539–549, 1955. doi:10.1038/bjc.1955.55.

J. Tsutsui, M. Moriyama, N. Arima, H. Ohtsubo, H. Tanaka, and M. Ozawa. Expression of cadherin-catenin complexes in human leukemia cell lines. *Journal of Biochemistry*, 120:1034–1039, 1996.

T.A. Tucker, C. Dean, A.A. Komissarov, K. Koenig, A.P. Mazar, U. Pendurthi, T. Allen, and S. Idell. The urokinase receptor supports tumorigenesis of human malignant pleural mesothelioma cells. *American Journal of Respiratory Cell and Molecular Biology*, 42(6):685–696, 2010. doi:10.1165/rcmb.2008-0433OC.

S. Turner and J.A. Sherratt. Intercellular adhesion and cancer invasion: a discrete simulation using the extended potts model. *Journal of Theoretical Biology*, 216(1): 85–100, 2002. doi:10.1006/jtbi.2001.2522.

M. Uchino, H. Kojima, K. Wada, M. Imada, F. Onoda, H. Satofuka, T. Utsugi, and Y. Murakami. Nuclear β-catenin and cd44 upregulation characterize invasive cell populations in non-aggressive mcf-7 breast cancer cells. *BMC Cancer*, 10(414), 2010. doi:10.1186/1471-2407-10-414.

J. Valenciano and M.A.J. Chaplain. Computing highly accurate solutions of a tumour angiogenesis model. *Mathematical Models and Methods in Applied Sciences*, 13(5): 747–766, 2003. doi:10.1142/S0218202503002702.

I.M.M. van Leeuwen, C.M. Edwards, M. Ilyas, and H.M. Byrne. Towards a multiscale model of colorectal cancer. *World Journal of Gastroenterology*, 13(9):1399–1407, 2007.

M. Vicente-Manzanares, D.J. Webb, and A.R. Horwitz. Cell migration at a glance. *Journal of Cell Science*, 118(21):4917–4919, 2005. doi:10.1242/jcs.02662.

Z. Wang and T. Hillen. Classical solutions and pattern formation for a volume filling chemotaxis model. *Chaos*, 17:037108, 2007. doi:10.1063/1.2766864.

D.J. Webb, J.T. Parsons, and A.R. Horwitz. Adhesion assembly, disassembly and turnover in migrating cells - over and over and over again. *Nature Cell Biology*, 4 (4):E97–E100, 2002. doi:10.1038/ncb0402-e97.

S.D. Webb, J.A. Sherratt, and R.G. Fish. Alterations in proteolytic activity at low ph and its association with invasion: a theoretical model. *Clinical & Experimental Metastasis*, 17(5):397–407, 1999.

M.M. Webber and A. Waghray. Urokinase-mediated extracellular matrix degradation by human prostatic carcinoma cells and its inhibition by retinoic acid. *Clinical Cancer Research*, 1(7):755–761, 1995.

B. Wehrle-Haller. Analysis of integrin dynamics by fluorescence recovery after photobleaching. In A.S. Coutts, editor, *Adhesion Protein Protocols*, Methods in Molecular Biology, chapter 13, pages 173–201. Springer, 2007.

B. Wehrle-Haller and B.A. Imhof. Actin, microtubules and focal adhesion dynamics during cell migration. *International Journal of Biochemistry and Cell Biology*, 35 (1):39–50, 2003. doi:10.1016/S1357-2725(02)00071-7.

R.A. Weinberg. *The biology of cancer*. Garland Science, Taylor & Francis Group, LLC, 2007.

R. Weiner, B.A. Schmitt, and H. Podhaisky. ROWMAP—a ROW-code with Krylov techniques for large stiff ODEs. *Applied Numerical Mathematics*, 25(2–3):303–319, 1997. doi:10.1016/S0168-9274(97)00067-6.

I. Wierzbicka-Patynowski and J. Schwarzbauer. The ins and outs of fibronectin matrix assembly. *Journal of Cell Science*, 116(16):3269–3276, 2003. doi:10.1242/jcs.00670.

B.P. Wijnhoven, W.N. Dinjens, and M. Pignatelli. E-cadherin-catenin cell-cell adhesion complex and human cancer. *British Journal of Surgery*, 87(8):992–1005, 2000. doi:10.1046/j.1365-2168.2000.01513.x.

P.W. Wiseman, C.M. Brown, D.J. Webb, B. Hebert, N.L. Johnson, J.A. Squier, M.H. Ellisman, and A.F. Horwitz. Spatial mapping of integrin interactions and dynamics during cell migration by image correlation microscopy. *Journal of Cell Science*, 117 (23):5521–5534, 2004. doi:10.1242/jcs.01416.

Y. Xiao and G.A. Truskey. Effect of receptor-ligand affinity on the strength of endothelial cell adhesion. *Biophysical Journal*, 71(5):2869–2884, 1996. doi:10.1016/S0006-3495(96)79484-5.

W. Xue, I. Mizukami, R.F. Todd III, and H.R. Petty. Urokinase-type plasminogen activator receptors associate with β_1 and β_3 integrins of fibrosarcoma cells: dependence on extracellular matrix components. *Cancer Research*, 57(9):1682–1689, 1997.

K.M. Yamada. Cell surface interactions with extracellular materials. *Annual Review of Biochemistry*, 52:761–799, 1983. doi:10.1146/annurev.bi.52.070183.003553.

M.H. Zaman, L.M. Trapani, A.L. Sieminski, D. MacKellar, H. Gong, R.D. Kamm, A. Wells, D.A. Lauffenburger, and P. Matsudaira. Migration of tumor cells in 3d matrices is governed by matrix stiffness along with cell-matrix adhesion and proteolysis. *Proceedings of the National Academy of Sciences USA (PNAS)*, 103(29): 10889–10894, 2006. doi:10.1073/pnas.0604460103.

N.D. Zantek and M.S. Kinch. Analysis of cell migration. In Z. Darzynkiewicz, H.A. Crissman, and J.P. Robinson, editors, *Cytometry Vol 63*, Methods in Cell Biology, chapter 25, pages 549–560. Academic Press Inc, San Diego, 2001.

L. Zhang, C.A. Athale, and T.S. Deisboeck. Development of a three-dimensional multiscale agent-based tumor model: simulating gene-protein interaction profiles, cell

phenotypes and multicellular patterns in brain cancer. *Journal of Theoretical Biology*, 244(1):96–107, 2007. doi:10.1016/j.jtbi.2006.06.034.

L. Zhang, C.G. Strouthos, Z. Wang, and T.S. Deisboeck. Simulating brain tumor heterogeneity with a multiscale agent-based model: linking molecular signatures, phenotypes and expansion rate. *Mathematical and Computer Modelling*, 49(1–2): 307–319, 2009. doi:10.1016/j.mcm.2008.05.011.

X. Zheng, S.M. Wise, and V. Cristini. Nonlinear simulation of tumor necrosis, neo-vascularization and tissue invasion via an adaptive finite-element/level-set method. *Bulletin of Mathematical Biology*, 67(2):211–259, 2005. doi:10.1016/j.bulm.2004.08.001.

C-Q. Zhu, S.N. Popova, E.R.S. Brown, D. Barsyte-Lovejoy, R. Navab, W. Shih, M. Li, M. Lu, I. Jurisica, L.Z. Penn, D. Gullberg, and M-S. Tsao. Integrin α_{11} regulates igf2 expression in fibroblasts to enhance tumorigenicity of human non-small-cell lung cancer cells. *Proceedings of the National Academy of Sciences USA (PNAS)*, 104(28):11754–11759, 2007. doi:10.1073/pnas.0703040104.

Index